



**HAL**  
open science

## Study of SiGe layers submitted to ultraviolet nanosecond laser annealing

Léa Dagault

► **To cite this version:**

Léa Dagault. Study of SiGe layers submitted to ultraviolet nanosecond laser annealing. Micro and nanotechnologies/Microelectronics. Université Paul Sabatier - Toulouse III, 2021. English. NNT : 2021TOU30139 . tel-03637329v2

**HAL Id: tel-03637329**

**<https://theses.hal.science/tel-03637329v2>**

Submitted on 11 Apr 2022

**HAL** is a multi-disciplinary open access archive for the deposit and dissemination of scientific research documents, whether they are published or not. The documents may come from teaching and research institutions in France or abroad, or from public or private research centers.

L'archive ouverte pluridisciplinaire **HAL**, est destinée au dépôt et à la diffusion de documents scientifiques de niveau recherche, publiés ou non, émanant des établissements d'enseignement et de recherche français ou étrangers, des laboratoires publics ou privés.



# THÈSE

**En vue de l'obtention du  
DOCTORAT DE L'UNIVERSITÉ DE TOULOUSE  
Délivré par l'Université Toulouse 3 - Paul Sabatier**

---

**Présentée et soutenue par  
Léa DAGAULT**

Le 8 avril 2021

**Etude du comportement de couches  $\text{Si}_{1-x}\text{Ge}_x$  soumises au recuit  
laser nanoseconde ultraviolet.**

---

Ecole doctorale : **GEETS - Génie Electrique Electronique, Télécommunications et  
Santé : du système au nanosystème**

Spécialité : **MicroNano Systèmes**

Unité de recherche :

**LAAS - Laboratoire d'Analyse et d'Architecture des Systèmes**

Thèse dirigée par

**Filadelfo CRISTIANO et Sébastien Kerdiles**

Jury

**M. Dominique MANGELINCK, Rapporteur**

**M. Abdelilah SLAOUI, Rapporteur**

**Mme Caroline BONAFOS, Examinatrice**

**Mme Francesca CHIODI, Examinatrice**

**M. Fulvio MAZZAMUTO, Examineur**

**M. Filadelfo CRISTIANO, Directeur de thèse**







---

# REMERCIEMENTS

Je voudrais commencer par remercier Fuccio Cristiano, Sébastien Kerdilès et Pablo Acosta Alba, qui m'ont encadrée au cours de cette thèse. Ils ont fait montre d'une disponibilité exemplaire pour moi tout au long de cette thèse, qui s'est exprimée de multiples manières : par les nombreuses discussions, par leurs relectures des articles et du manuscrit, par leurs conseils pour la marche à suivre. J'adresse un immense merci à mon directeur, Fuccio, qui a réalisé de (très) nombreuses observations TEM, et sans qui ce manuscrit serait bien moins riche. Je n'aurais pas pu espérer beaucoup mieux comme encadrement, et j'espère que leur collaboration continuera ainsi !

Ma gratitude va aussi à tous les membres du jury, qui ont accepté d'assister à la soutenance, bien qu'elle ait lieu dans des conditions un peu particulières. Merci aux deux rapporteurs, Dominique Mangelinck et Abdelillah Slaoui, pour leur lecture attentive et leurs questions, qui ont permis de développer et préciser certaines idées. De même, je remercie Caroline Bonafos, Francesca Chiodi et Fulvio Mazzamuto pour l'intérêt porté à ce travail et pour leur nombreuse questions. J'ai fortement apprécié les discussions avec eux.

Merci aussi à toute l'équipe de SCREEN, qu'elle soit sur le site du CEA-LETI ou à l'autre bout du monde, sans qui rien de tout ça n'aurait jamais eu lieu.

Cette thèse a aussi été possible grâce au travail de nombreuses autres personnes autour de moi, que ce soit pour la fabrication des échantillons, les simulations, ou la caractérisation. Merci donc, entre autres, à Jean-Michel Hartmann, Patrice Gergaud, Jean-Paul Barnes, Nicolas Gauthier, Richard Monflier, Anne-Sophie Royet et Denis Marseilhan. Sans leur collaboration et toutes leurs réponses à mes questions, ce travail n'aurait jamais pu être aussi complet et abouti. Merci à eux pour toutes les fois où ils se sont démenés pour réaliser ce dont j'avais besoin !

Je tiens aussi à saluer l'intégralité de l'équipe du SSURF, pour la bonne humeur générale (et les croissants à la pause-café). Ils ont toujours été accueillants, et ont su maintenir un lien au cours des périodes de confinement. Cette ambiance toujours positive a été précieuse au cours de ma thèse, et je me suis toujours sentie à mon aise au sein de cette équipe. Parmi le SSURF, mon affection va particulièrement à l'équipe des « précaires » que j'ai rencontré au cours de ces trois ans : tous les jeunes du service, qu'ils soient doctorants, stagiaires ou alternants. Je remercie infiniment Laurent et Laura, qui ont été mes compagnons de rédaction : ils ont été un excellent support, et un exutoire bienvenu aux frustrations de cette période ! Ce trio va me manquer longtemps.

Un grand merci à trois autres présences constantes au cours de cette thèse : Joël Kanyandekwe, Marie Marmiesse et Jessica Lassarre. Joël, le meilleur voisin de bureau, avec qui j'ai pu discuter de tout et de rien, et qui est devenu un expert en thé au cours de ces quelques années ! Quant à Marie (ma jumelle de thèse) et Jessica, elles sont devenues de véritables amies au cours du temps, et cette thèse n'aurait pas été la même sans nos régulières discussions du midi.

---

Merci à Florian, qui m'a encouragée à poursuivre cette voie et m'a permis de me lancer dans ce qui me paraissait alors infranchissable.

Merci à Sébastien, qui m'a soutenue sans relâche pendant deux ans, et qui a enduré avec sagesse et patience la double épreuve du confinement et de la rédaction avec moi. Son soutien a été infiniment précieux au cours de cette dernière année, et continue de l'être.

Merci à Elena et Sophie, des amies si précieuses avec qui j'ai pu parler de tout et qui se sont toujours avérées de bon conseil, y compris pour me signaler que j'ai tort. Elles ont su me booster dans les périodes de creux et me donner envie de faire mieux.

Enfin, merci à tous ceux que je n'ai pas cités, tous les amis que je me suis faits au cours de ces trois années à Grenoble, tout ceux qui m'ont fait découvrir la montagne et apprécier ma vie dans cette ville.

En dernier, mais pas des moindres, je remercie ma famille. Malgré la distance et le peu d'occasions de se voir, ils m'ont toujours soutenue dans les choix et m'ont permis, par leur soutien discret et patient, d'aller au bout de cette aventure.

---

# SUMMARY

INTRODUCTION .....	1
CHAPTER I NANOSECOND LASER ANNEALING IN MICROELECTRONICS.....	5
I - MICROELECTRONIC DEVICES EVOLUTIONS AND PROCESS ADAPTATIONS .....	7
1. MOSFET device shrinking .....	7
a) MOSFET operation .....	7
b) Device shrinking and roadmaps.....	8
c) Material Modifications .....	8
d) Architecture evolutions.....	10
2. Strain and mobility engineering with Silicon-Germanium alloys .....	11
a) Strained SiGe layers formation .....	11
b) Electrical properties in strained SiGe alloys .....	13
3. Annealing processes in microelectronics .....	15
a) Heat transfer.....	15
b) Atomic diffusion within a crystalline material.....	17
i. Dopant activation and defect healing .....	17
ii. Atomic Diffusion.....	17
c) Thermal budget reduction .....	18
i. Diffusion and activation trade-off.....	18
ii. Process evolution.....	19
II - NANOSECOND LASER ANNEAL : A SURFACE ANNEAL SOLUTION .....	20
1. Heating by laser radiation absorption.....	20
a) Theoretical background.....	20
b) Laser annealing conditions .....	22
i. Industrial laser types.....	22
ii. Impact of laser properties on melt depth and solidification velocities .....	23
2. Semiconductor layers after NLA : structure and quality .....	24
a) Annealing of crystalline layers .....	24
i. Simple case.....	24
ii. Excessive crystallization velocities .....	25
b) Annealing of amorphous layers.....	25
i. Explosive melt and crystallization .....	25
ii. Second melt.....	27
3. Dopant behavior in Si or Ge upon NLA.....	28

a) Dopant redistribution .....	28
i. Typical diffusion and segregation in laser annealed samples .....	28
ii. Dopant segregation .....	29
iii. Anomalous boron diffusion .....	30
b) Dopant activation .....	31
i. Evolution with energy density .....	31
ii. Activation above the solid solubility limit .....	32
d) Deactivation .....	33
III - NANOSECOND LASER ANNEAL ON SiGe ALLOYS.....	34
1. SiGe fusion and solidification.....	35
a) SiGe layers formation by NLA.....	35
b) Germanium segregation .....	35
c) Explosive crystallization in Si <sub>1-x</sub> Ge <sub>x</sub> .....	36
2. Relaxation .....	37
3. Electrical Results .....	37
CONCLUSION .....	40
KEY INFORMATION .....	41
BIBLIOGRAPHY .....	42
CHAPTER II LASER ANNEALING ON SiGe : SAMPLES FABRICATION AND CHARACTERIZATION ..	53
I - NANOSECOND LASER ANNEALING TOOL : SCREEN LT-3100 .....	54
1. Tool description .....	54
2. Laser annealing conditions.....	56
II - Si AND SiGe SAMPLES .....	57
III - CHARACTERIZATION METHODS.....	59
1. In-situ Time Resolved Reflectivity (TRR) .....	59
3. Surface Characterizations .....	62
a) Haze measurements .....	62
b) Atomic Force Microscopy (AFM).....	63
4. Crystalline quality assessment .....	65
a) Strain and crystallinity measurements by XRD .....	65
b) Structure observations via Transmission Electron Microscopy.....	70
5. Composition and concentration profiles.....	72
a) Secondary Ion Mass Spectrometry (SIMS) .....	72
b) Energy Dispersive X-Ray Analysis (EDX).....	73
6. Electrical Characterizations.....	74
a) Sheet resistance by Four-Point-Probe .....	74
b) Hall effect measurements .....	75

---

IV – NUMERICAL SIMULATIONS.....	77
1. LIAB software .....	77
a) Simulation Model .....	77
b) Structures and solvers for Si <sub>1-x</sub> Ge <sub>x</sub> simulations .....	78
2. Segregation and elastic energy .....	78
CONCLUSION .....	82
KEY INFORMATION .....	83
BIBLIOGRAPHY .....	84
CHAPTER III ANNEALING REGIMES AND CHARACTERISTICS OF ANNEALED SiGe SAMPLES.....	89
I - REGIMES IDENTIFICATION .....	91
1. Regimes in Si <sub>1-x</sub> Ge <sub>x</sub> .....	91
a) UV-NLA on a pseudomorphic Si <sub>0.6</sub> Ge <sub>0.4</sub> crystalline layer.....	91
b) UV-NLA on an amorphous Si <sub>1-x</sub> Ge <sub>x</sub> layer .....	94
2. Extension to layers with different thicknesses and compositions .....	96
II - LAYER PROPERTIES AND IMPACT ON MELT THRESHOLD .....	98
1. Optical and thermal properties variations with composition.....	98
a) Evolution of optical indices .....	98
i. Ge concentration and temperature.....	98
ii. With B concentration and temperature.....	99
b) Evolution of thermal properties.....	101
2. Melt threshold evolution.....	101
III - SURFACE STRUCTURATIONS .....	102
1. Origin of surface roughness .....	102
a) Crystalline Si <sub>0.7</sub> Ge <sub>0.4</sub> layer.....	102
b) Amorphous Si <sub>0.7</sub> Ge <sub>0.3</sub> layer .....	104
2. Further analysis and impact of layer properties.....	105
a) Haze signal .....	105
b) Nanostructure shape: influence of concentration .....	106
c) Surface coverage by nanostructures .....	108
IV - SEGREGATION AND DIFFUSION DURING NANOSECOND LASER ANNEAL.....	110
1. Germanium segregation, a melt marker .....	110
a) Ge profiles after UV-NLA on crystalline layers .....	110
i. Observation of segregation.....	110
ii. Noticeable differences between SIMS and STEM-EDX.....	111
b) Melt depth and interface roughness .....	112
i. Melt depth evolution .....	112
ii. Maximum melt depth variability.....	114

c) Ge profiles after UV-NLA on amorphous layers .....	115
2. Segregation simulations .....	116
a) With a constant partition coefficient $k_i$ .....	117
i. Database calibration .....	117
ii. Ge segregation .....	117
b) With a variable partition coefficient $k_i$ .....	118
i. $k_i$ evolution with Ge content and solidification velocity .....	118
ii. Simulation results.....	119
V – MODIFICATIONS IN REFLECTIVITY SIGNALS.....	121
1. TRR signals on SiGe.....	121
a) Evolution with energy density .....	121
i. At high energy densities.....	121
ii. Evolution from sub-melt to full melt .....	122
iii. Origin of second slope .....	124
b) Impact of chuck temperature on signal .....	125
2. Kinetics evaluation.....	126
a) Automatic extraction.....	126
b) Melt duration evolution.....	127
c) Estimated liquid/solid interface velocities .....	128
i. Time required to melt the upper 20 nm.....	128
ii. Time required for the solidification of the upper 20 nm.....	129
CONCLUSION .....	132
KEY INFORMATION .....	133
BIBLIOGRAPHY .....	134
CHAPTER IV STRAIN EVOLUTION UPON NANOSECOND LASER ANNEALING .....	137
I – EVOLUTION OF STRAIN STATE WITH THE ANNEALING REGIMES : $\text{Si}_{0.6}\text{Ge}_{0.4}$ EXAMPLE .....	138
1. Strain state observed for each regime .....	138
2. Origin of relaxation .....	142
a) Impact of the liquid/solid interface roughness.....	142
b) Elastic energy-driven relaxation .....	143
i. Bi-layer formation at high energy densities .....	143
ii. Elastic energy density calculations .....	144
II – IMPACT OF SiGe LAYER PROPERTIES ON STRAIN RELAXATION.....	145
1. Impact of Germanium concentration and layer thickness.....	146
a) Strain relaxation in 30 nm thick layers: impact of Ge content.....	146
b) Strain relaxation in $\text{Si}_{0.7}\text{Ge}_{0.3}$ layers : impact of thickness.....	149
c) Elastic energy density limit for strain relaxation .....	151

d) Predictive calculations for elastic energy-induced relaxation.....	152
e) Conclusion on pseudomorphic undoped layers.....	153
2. Amorphous SiGe layers: comparison with epi-layers.....	153
a) Initial state.....	153
b) Relaxation for 15 nm and 30 nm thick amorphized layers .....	154
i. In explosive regime .....	154
ii. In other regimes.....	156
III – BORON IMPACT ON THE RELAXATION OF 30 NM-THICK $\text{Si}_{0.7}\text{Ge}_{0.3}$ LAYERS.....	157
1. Relaxation in pseudomorphic doped layers .....	157
2. Relaxation in amorphized doped layers.....	159
CONCLUSION .....	161
KEY INFORMATION .....	162
BIBLIOGRAPHY .....	163
CHAPTER V ELECTRICAL PROPERTIES OF BORON DOPED $\text{Si}_{0.7}\text{Ge}_{0.3}$ LASER ANNEALED LAYERS .	167
I – DOPANT ACTIVATION IN $\text{Si}_{0.7}\text{Ge}_{0.3}$ LAYERS.....	168
1. Dopant activation in pseudomorphic layers .....	168
a) Metrology .....	168
b) Initial state after epitaxy .....	168
c) Electrical properties of SiGe:B laser annealed with a single pulse .....	170
i. Boron redistribution .....	170
ii. Impact of layer quality and doping level .....	171
c) Electrical properties with single pulse at 450°C .....	174
d) Electrical properties with multiple pulses at room temperature.....	175
2. Dopant activation in initially amorphous layers.....	176
II – THERMAL STABILITY OF BORON ACTIVATION FOLLOWING A SUBSEQUENT ANNEALING STEP .....	177
1. Samples and annealing conditions.....	177
a) Selected samples .....	177
b) Furnace annealing conditions.....	178
c) Modifications assessment .....	179
2. Morphological and electrical evolutions with anneal temperature .....	180
a) Samples without laser anneal .....	180
i. Structural modifications.....	180
ii. $R_s$ evolution upon subsequent furnace anneal.....	183
b) Laser annealed samples.....	184
i. Structural modifications.....	184
ii. $R_s$ evolution upon subsequent furnace anneal.....	187

---

CONCLUSION .....	189
KEY INFORMATION .....	190
BIBLIOGRAPHY .....	191
CONCLUSION.....	195
APPENDICES .....	199
COMPORTEMENT DE COUCHES $Si_{1-x}Ge_x$ SOUMISES AU RECUIT LASER NANOSECONDE .....	205

---

## LIST OF ACRONYMS

4PP	Four Point Probe
AFM	Atomic Force Microscopy
ASGM	Aperiodic Stepwise Growth Model
CGM	Continuous Growth Model
ED	Energy density
EDX	Energy Dispersive X-ray
FLA	Flash Lamp Annealing
GILD	Gas Immersion Laser Doping
ITRS	International Technology Roadmap for Semiconductors
LIAB	LASSE Innovative Application Booster
LPER	Liquid Phase Epitaxial Regrowth
MD	Misfit Dislocation
MOSFET	Metal Oxide Semiconductor Field Effect Transistor
NLA	Nanosecond Laser Annealing → UV-NLA: UltraViolet NLA
RC	Rocking Curve
RMS	Root Mean Square
RSF	Relative Sensitivity Factor
RSM	Reciprocal Space Map
RTP	Rapid Thermal Processing
SCE	Short Channel Effects
SEM	Scanning Electronic Microscopy
SF	Stacking Fault
SIMS	Secondary Ion Mass Spectrometry → ToF-SIMS: Time-of-Flight SIMS
SOI	Silicon-On-Insulator → FD-SOI: Fully Depleted SOI
SPER	Solid Phase Epitaxial Regrowth
STEM	Scanning Transmission Electronic Microscopy → STEM-HAADF: STEM High Angle Annular Dark Field → STEM EDX: STEM Energy Dispersive X-ray
TEM	Transmission Electronic Microscopy → BFTEM: Bright Field TEM → DFTEM: Dark Field TEM
TRR	Time-Resolved Reflectometry
XRD	X-ray Diffraction
XRR	X-ray Reflectivity



# INTRODUCTION

Modern microelectronics are based on the MOSFET device, composed of a channel, source and drain junctions and a gate that controls the current flow. This device was invented in 1925, and is now widely used. In order to improve its performances and reduce its costs, the MOSFET dimensions have **regularly shrunk, following Moore's law**. Roadmaps, such as the 'International Technology Roadmap for Semiconductors' ITRS, define the objectives in terms of dimensions and performances. The size reductions however have detrimental impacts on the channel control, and require higher doping levels in the source and drain regions to maintain satisfying electrical results. Multiple evolutions in the architecture of the devices were introduced, along with the use of novel materials, to satisfy these requirements and limit side effects. These evolutions include the introduction of high-k dielectrics in the gate, rather than SiO<sub>2</sub>, to limit the short channel effects. Regarding the architecture, the development of Silicon-On-Insulator or FinFET technologies enable an improvement of the channel control.

One of the methods currently used in p-MOSFET integration path to boost the carrier mobility in the channel region is the introduction of an uniaxially tensily strained Si to form the channel. Indeed, the tensile strain improves the hole mobility. The strain in the channel is obtained by the formation of biaxially compressive strained SiGe source and drain regions on each side. The strain level can then be controlled by adjusting the Ge concentration of the source and drain regions. In addition, in the SiGe alloys the hole mobility can be improved by the increase of Ge content.

In addition to strain, high active dopant concentrations must be obtained to improve the electrical performances in ultra-shallow junctions. Forming such ultra-shallow junctions requires a high dopant activation rate, while dopant diffusion must be limited in order to control the junction depth. As both phenomena do not occur on the same timescale in solid semiconductor materials (**<1  $\mu$ s for dopant activation versus >1  $\mu$ s for dopant diffusion**), **it is then possible to use high temperatures and short duration annealing process to activate dopants while limiting the diffusion**. This is one of the reasons why a progressive evolution of annealing processes toward shorter durations and higher temperatures has been observed. Nowadays, the integration paths of current device generations leverage anneal durations close to the millisecond. As the duration of the anneal is modified, the temperature distribution in the materials also changes: while furnace anneals led to a uniform temperature over the whole wafer thickness, shorter anneals cause temperature gradients within the wafer volume. Nowadays, annealing methods below the microsecond are considered for the next device generations: they enable reaching high temperatures at the extreme surface while keeping the underlying material at much lower temperature.

Nanosecond laser anneal (NLA) is a promising method that has been widely studied in the last 50 years, for Si and Ge materials. This annealing method relies on short (typically 1-200 ns) laser pulses and a short absorption depth, whose value depends on the laser wavelength, as well as the annealed material physical parameters. The energy deposited is then transformed into heat by the light/matter interaction and diffuses. Depending on the energy density and on the stack characteristics, materials such as Si or Ge can reach their melting temperature and form liquid layers which then solidify. It was demonstrated that the Liquid Phase Epitaxial Regrowth could lead to the formation of defect-free monocrystalline layers, depending on the laser energy density and stack characteristics. Due to the short duration of the anneal, very limited diffusion of dopants is expected in the solid phases, while it can occur in the liquid layers. This allows to incorporate high concentrations of dopants in the lattice, well above the solid solubility limits.

The impact of NLA on  $\text{Si}_{1-x}\text{Ge}_x$  alloys is however not well-known, with multiple contradictory results regarding the strain state, and a lack of understanding in the dopant activation observations. Ge segregation was observed in multiple studies, and appears to be desirable for contact formation, particularly in gallium-doped layers. This work is therefore dedicated to the systematic study of the effects encountered during UV-NLA on  $\text{Si}_{1-x}\text{Ge}_x$  alloys, with Ge concentrations up to 40%. It particularly focuses on the distinction between the various annealing regimes, and how they influence the surface roughness, the germanium redistribution, the layer crystalline quality and finally the dopant activation. This work is a result of a collaboration between the CEA-LETI in Grenoble, the LAAS-CNRS laboratory in Toulouse and the equipment supplier SCREEN-LASSE, who designed, built and provided the commercially available NLA system used in this work .

The first chapter of this PhD work gives an overview of the microelectronic devices and their progressive modifications, while detailing the reasons for the evolution of annealing processes toward shorter durations and higher temperatures. The principle of nanosecond laser anneal is then explained, with insight on how pulse duration and laser wavelength may modify the results. Based on the prior art, the morphological and electrical impact on simple materials such as Si or Ge are shown, including multiple studies in which activation levels above the solid solubility limits were obtained. Finally, the current knowledge in  $\text{Si}_{1-x}\text{Ge}_x$  alloys is presented, highlighting the points where additional or unified understanding is required.

The second chapter is dedicated to the methods: it presents the  $\text{Si}_{1-x}\text{Ge}_x$  samples used during the thesis, how they were fabricated and how they were annealed. Four main series are presented, each focusing on a different parameter, either Ge content, layer thickness, boron content or amorphization. It then details the various characterization methods leveraged to analyze the impact of NLA in these different conditions. In particular, we focus on chemical redistribution (via Secondary Ion Mass Spectrometry and Energy-Dispersive X-Ray), surface morphology (via Haze, Atomic Force Microscopy and Scanning Electron Microscopy) and strain state (via X-Ray Diffraction and Transmission Electron Microscopy). Four-point probe and Hall effect measurements were also applied to doped layers to assess their electrical characteristics.

The third chapter analyzes the multiple phenomena that occur during the nanosecond laser annealing of the various  $\text{Si}_{1-x}\text{Ge}_x$  epilayers ( $0 \leq x \leq 0.4$ ), and show how they vary with the annealing regimes. It first defines the regimes that are observed when increasing the laser energy density and the techniques used in order to identify the regime limits. The following sections of the chapter each focus on a different phenomenon, its evolution with the annealing regimes and what can be inferred from the process impact on the layer from this phenomenon. This includes the surface state and appearance of surface nanostructures, the germanium segregation toward the surface and the information derived from the in-situ time-resolved reflectivity measurements.

The fourth chapter aims to give a unified understanding of the possible relaxation in initially pseudomorphic  $\text{Si}_{1-x}\text{Ge}_x$  layers submitted to NLA, using systematic X-Ray diffraction measurements and multiple TEM observations. Along with the morphological observations from the previous chapter, it presents how the layer physical parameters (Ge content and thickness) and the energy density influence the crystalline defect formation. This chapter also highlights the conditions in which a fully strained SiGe layer with a graded Ge content can be obtained.

The final chapter is dedicated to the dopant behavior in laser annealed SiGe layers, with three different boron concentrations in the  $7 \times 10^{19}$ - $2.4 \times 10^{20}$  at·cm<sup>-3</sup> range. A first section focuses on the impact of crystallinity and structural defects on the dopant distribution and activation levels. A second section focuses on the behavior of such laser annealed doped layers when submitted to additional furnace anneals, to mimic the impact of subsequent

processes. This shows clear divergences in tendencies between samples with and without nanosecond laser annealing.

---

# CHAPTER I

## NANOSECOND LASER ANNEALING IN MICROELECTRONICS

I - MICROELECTRONIC DEVICES EVOLUTIONS AND PROCESS ADAPTATIONS.....	7
1. MOSFET device shrinking.....	7
a) MOSFET operation.....	7
b) Device shrinking and roadmaps.....	8
c) Material Modifications.....	8
d) Architecture evolutions.....	10
2. Strain and mobility engineering with Silicon-Germanium alloys.....	11
a) Strained SiGe layers formation.....	11
b) Electrical properties in strained SiGe alloys.....	13
3. Annealing processes in microelectronics.....	15
a) Heat transfer.....	15
b) Atomic diffusion within a crystalline material.....	17
i. Dopant activation and defect healing.....	17
ii. Atomic Diffusion.....	17
c) Thermal budget reduction.....	18
i. Diffusion and activation trade-off.....	18
ii. Process evolution.....	19
II - NANOSECOND LASER ANNEAL : A SURFACE ANNEAL SOLUTION.....	20
1. Heating by laser radiation absorption.....	20
a) Theoretical background.....	20
b) Laser annealing conditions.....	22
i. Industrial laser types.....	22
ii. Impact of laser properties on melt depth and solidification velocities.....	23
2. Semiconductor layers after NLA : structure and quality.....	24
a) Annealing of crystalline layers.....	24
i. Simple case.....	24
ii. Excessive crystallization velocities.....	25
b) Annealing of amorphous layers.....	25
i. Explosive melt and crystallization.....	25
ii. Second melt.....	27
3. Dopant behavior in Si or Ge upon NLA.....	28
a) Dopant redistribution.....	28

i. Typical diffusion and segregation in laser annealed samples .....	28
ii. Dopant segregation .....	29
iii. Anomalous boron diffusion .....	30
b) Dopant activation .....	31
i. Evolution with energy density .....	31
ii. Activation above the solid solubility limit .....	32
d) Deactivation .....	33
III - NANOSECOND LASER ANNEAL ON SiGe ALLOYS.....	34
1. SiGe fusion and solidification.....	35
a) SiGe layers formation by NLA.....	35
b) Germanium segregation .....	35
c) Explosive crystallization in $Si_{1-x}Ge_x$ .....	36
2. Relaxation .....	37
3. Electrical Results .....	37
CONCLUSION .....	40
KEY INFORMATION .....	41
BIBLIOGRAPHY .....	42

# CHAPTER I

## NANOSECOND LASER ANNEALING IN MICROELECTRONICS

Microelectronic devices are constantly reduced to increase performance and reduce costs, hence requiring evolutions in the materials and processes used. This chapter will first detail the device operation, and how the use of novel annealing methods, as well as new materials, have participated in their evolution. A second part focuses on nanosecond laser annealing, a more recent method, with the theoretical background and some experimental results. Finally, the known impacts of this annealing method are presented for  $\text{Si}_{1-x}\text{Ge}_x$  layers.

### I - MICROELECTRONIC DEVICES EVOLUTIONS AND PROCESS ADAPTATIONS

#### 1. MOSFET device shrinking

##### a) MOSFET operation

Logic operations in microelectronic devices are performed by MOSFETs (Metal Oxide Semiconductor Field Effect Transistors), as they are cheaper and less consuming than other alternatives. The idea was first developed by Lilienfeld in 1925, but the current operation of the device was patented in 1960 by Kahng [1].

The original device is composed of a substrate, a source, a drain and a gate, each connected to a given potential or the ground, as shown in Figure I - 1. The source, drain and substrate are made of doped semiconductor materials, originally silicon, and are doped to form either n-p-n or p-n-p junctions [2]. The gate is metallic with a  $\text{SiO}_2$  oxide layer. Logic operations are performed by controlling the current flow between source and drain, coding for 1 or 0. The voltage applied to the gate,  $V_G$ , controls this flow of current.

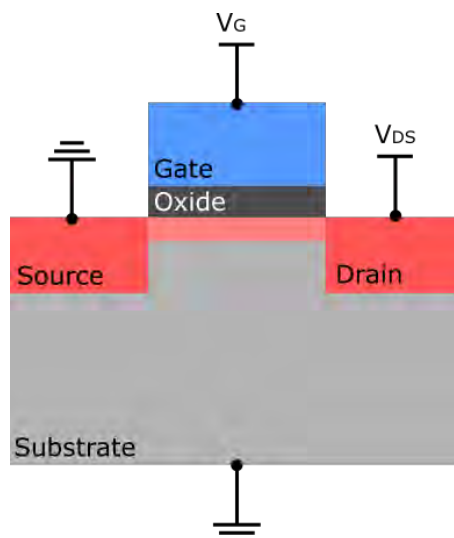


Figure I - 1. Representation of a basic MOS device in passing mode. In this case, current flows between source and drain regions.

As shown in Figure I - 1, the source and substrate are connected to the ground, while the drain is connected to a potential  $V_{DS}$ , and the gate to a potential  $V_G$ . The different regimes are determined by the gate potential  $V_G$  : in the case of an n-type MOS, the holes near the

substrate/oxide interface are progressively repulsed in the substrate as the gate voltage increases, while the negatively charged acceptors remain. This forms a depleted area. When  $V_G$  exceeds the voltage threshold  $V_T$ , electrons are attracted to the interface and an inversion region, the channel, is formed at the interface. A current therefore flows between source and drain junctions if  $V_{DS} > 0$ .

### b) Device shrinking and roadmaps

To answer the industry need for faster MOSFET devices, as well as cost reductions, the complexity of integrated circuits is consistently increasing. As predicted by Moore [3], the density of components follows an exponential growth, doubling every two years. The level of miniaturization of devices is usually classified by their gate length and is referred to as the node level, such as in Figure I - 2. It represents the evolution of the node size in production, from 1970 to 2020, and highlights the reduction of their dimensions, following the predicted exponential law.

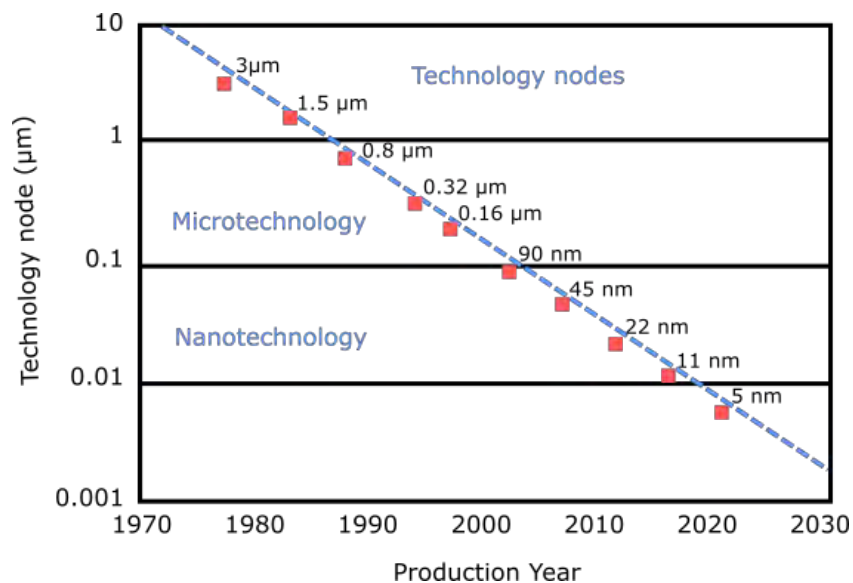


Figure I - 2. Evolution of technology nodes for devices since 1970 [4]. The node initially matched the gate length for older generations and became only indicative of the performances for recent generations.

Roadmaps were created to plan the necessary evolution of devices and follow Moore's law : the International Technology Roadmap for Semiconductors (ITRS) [5] was the guideline for production from 8 µm nodes to 45 nm nodes, reached in 2007. These reductions were accompanied by the use of larger substrates for production, further reducing the costs. Nowadays, the remaining foundries have reached nodes on the 7 nm or 5 nm scale. However, due to technological evolution, the "gate length" is only indicative of the circuit performances and does not represent the actual gate length in the circuit.

Device shrinking however led to the appearance of parasitic effects in the MOSFET performances that have to be addressed by constant evolutions in the materials and architecture used. This will be developed in the following sections.

### c) Material Modifications

Physical phenomena have interfered with the devices shrinking, such as gate tunneling, Short Channel Effects (SCE) or velocity saturation [6,7]. Those effects have led to performance degradation and leakage currents. Continuous improvement of the devices are then mandatory to limit their impact. While the active regions of devices were initially composed mainly of Si and SiO<sub>2</sub>, these evolutions required the use of novel materials. The SiO<sub>2</sub> gate oxide

was for instance replaced with high-k dielectrics : this enables to form a thick dielectric layer and avoid the tunneling of carriers between substrate and gate through the oxide, while keeping electrical performances equivalent to a thin SiO<sub>2</sub> layer [4].

The SCE are directly caused by the reduction of channel length : the channel becomes controlled by the depletion regions from the junctions [4,6]. The gate therefore loses its electrostatic control over the channel. As a result, the threshold voltage is lowered and may become dependent on the drain voltage [4] (Drain Induced Barrier Lowering). If the depletion regions join, current flows without gate voltage (Punchthrough). These effects can be reduced by forming highly doped shallow junctions [4] : it requires improvements of doping processes, such as the dopant implantation, and of the annealing processes to avoid dopant diffusion (further developed in section I - 3.).

Finally, novel materials were developed for the channel, to improve the mobilities (and thus the velocity in the channel). A wide range of materials can be considered, such as Ge, GeSn, or III-V semiconductors [4]. Another possibility is the use of strained materials, as, under specific conditions, strain improves the carrier mobility. Different processes exist to form strained Si, such as presented in Figure I - 3, by using materials with a larger lattice parameter such as SiGe [7–9]. Bi-axially tensile strained Si, as in Figure I - 3(a), is favorable for electron conduction while uniaxial compressive stress, as in Figure I - 3 (b), is favorable for hole conduction. In the first case, strained Si is grown on top of a relaxed SiGe layer, which causes biaxial strain. In the second case, uniaxial strain is formed in the channel with the presence of compressively strained SiGe source and drains. As presented in Figure I - 3(c), the uniaxial strain leads to better mobilities for a similar strain level, and is therefore more efficient. This process is commonly referred to as the "Intel process" [8,9]. It was first used in 2003, with a 18% Ge content in the source and drain, which led to performance improvements from the 45 nm node. Identical processes were used in the following nodes, with ever increasing Ge content to obtain higher strain levels [10].

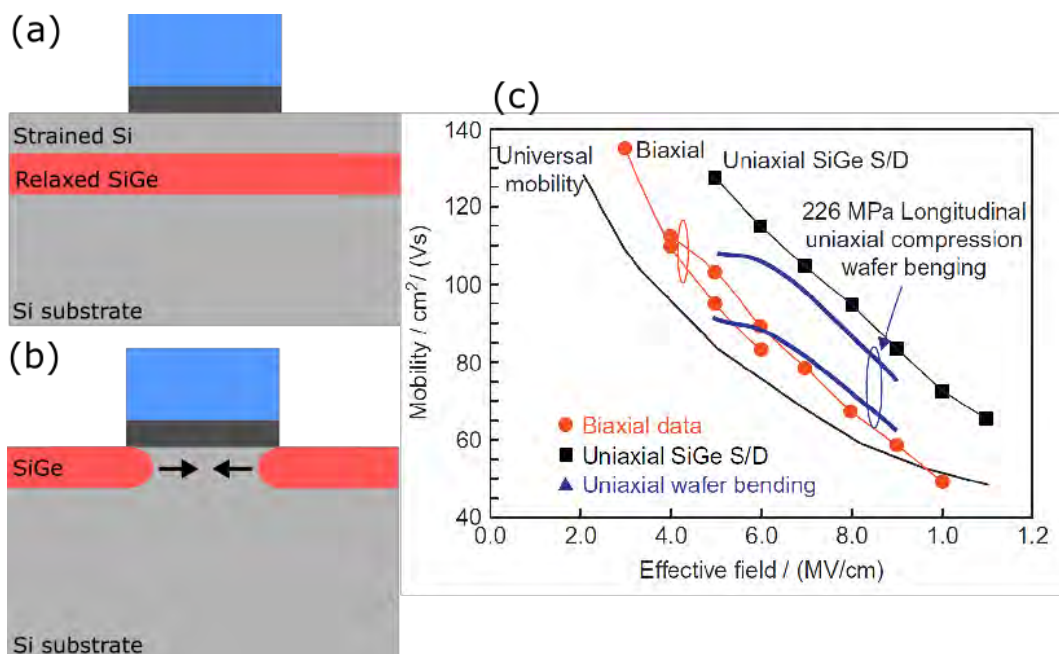


Figure I - 3. Strained Si channels obtained by growth on a relaxed SiGe layer (a) or compressively strained SiGe source and drains (b). The uniaxial strained Si formed by SiGe S/D exhibits higher hole mobilities than biaxial strain (c) [7]

## d) Architecture evolutions

Further evolutions were enabled by changes in the architecture of the devices. These improvements aim better electrostatic control of the channel and limitation of leakages.

The Silicon-On-Insulator (SOI) method consists in the fabrication of a transistor above a buried oxide layer, such as presented in Figure I - 4. The Si region on top is fully depleted for thin Si layers (Fully Depleted SOI), and the oxide layer limits the leakage. As a result, these technologies consume less power than classical devices on Si substrates [11].



Figure I - 4. Schematic representation of an SOI device with a fully depleted channel.

FinFETs, as represented in Figure I - 5, use a three dimensional gate, while source, channel and drain are formed with a single fin. The gate is "wrapped" around three sides of the channel, ensuring high control of the internal field and limiting the SCE.

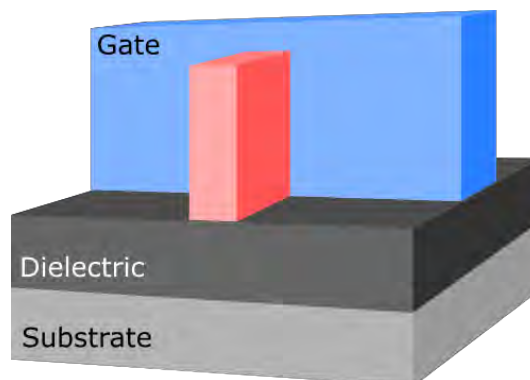


Figure I - 5. Schematic representation of a FinFET device.

In any case, these different improvements remain dependent on the properties of the materials used for the active regions. As a consequence, materials such as novel contact materials, and strained SiGe are of high interest and will likely be used in future devices.

There are also recent developments aiming to use the vertical dimension, by stacking two layers of devices on top of one another [12]. The number of devices on a given surface can therefore be doubled, and it can allow the direct integration of sensors on top of a MOSFET [13]. These architectures however require the development of "low temperature" processes, below 600°C, for the top layer, to ensure the performances of the buried devices.

There have been multiple improvements in microelectronics, driven by the need to reduce the devices dimensions. These evolutions required new materials, such as the use of SiGe source and drain regions to stress the Si channel, or new architectures. The following section focuses on the properties of strained SiGe. In order to obtain satisfying electrical performances, the alloy should be highly doped and defect-free.

## 2. Strain and mobility engineering with Silicon-Germanium alloys

### a) Strained SiGe layers formation

Silicon and germanium are both semiconductors with diamond structure (CFC) and a relatively small lattice mismatch near 4%, which allows forming  $\text{Si}_{1-x}\text{Ge}_x$  alloys. Their lattice parameters are respectively  $a_{\text{Si}}=5.43105 \text{ \AA}$  and  $a_{\text{Ge}}=5.65575 \text{ \AA}$ . They are miscible over the whole composition range, as shown in the phase diagram from Figure I - 6. The lattice parameter for an unstrained alloy can be calculated with Vegard's law, or with updated equations taking into account small deviations [14] from Vegard's law:

$$a_{\text{SiGe}}^0 = a_{\text{Si}} + 0.1988 \cdot x + 0.028 \cdot x^2 \quad \text{Eq. I - [1]}$$

Where  $x$  is the Ge content in the layer.

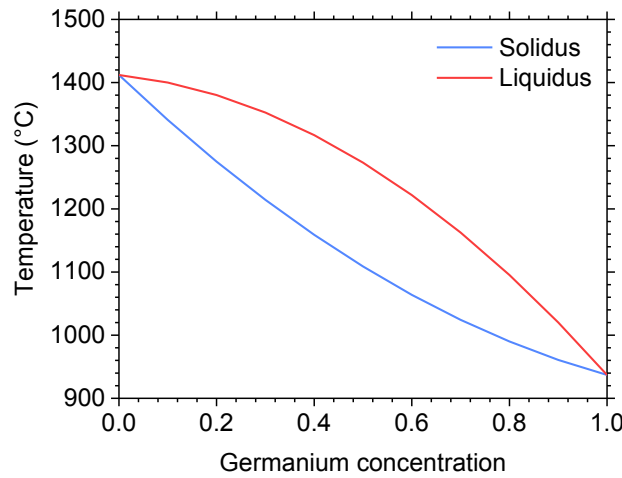


Figure I - 6. SiGe phase diagram, presenting the evolution of solidus (blue curve) and liquidus (red curve) as a function of the Ge content

$\text{Si}_{1-x}\text{Ge}_x$  can be grown pseudomorphically on Si or Ge substrates: its lattice distorts to match the substrate lattice, as presented in Figure I - 7(b). The stress caused by this deformation can be accommodated until it becomes energetically favorable to form dislocations in the layer, i.e. when the stored elastic energy is higher than the energy needed to form a defect [15]. For a layer with uniform Ge content, this limit is reached at the critical thickness  $h_c$ :

$$h_c \cong \left( \frac{1.9 \cdot 10^{-2}}{\varepsilon^2} \right) \ln \left( \frac{h_c}{4} \right) \quad \text{Eq. I - [2]}$$

where  $\varepsilon$  is the strain, defined as

$$\varepsilon = \frac{a_{\text{SiGe}} - a_{\text{Si}}}{a_{\text{Si}}} \quad \text{Eq. I - [3]}$$

Misfit dislocations may form at the interface for layers exceeding their critical thickness, which partially relaxes the lattice strain, as in Figure I - 7(c). This relaxation is accompanied by the formation of threading dislocations crossing through the SiGe layer up to the surface, bounding the misfit dislocations.

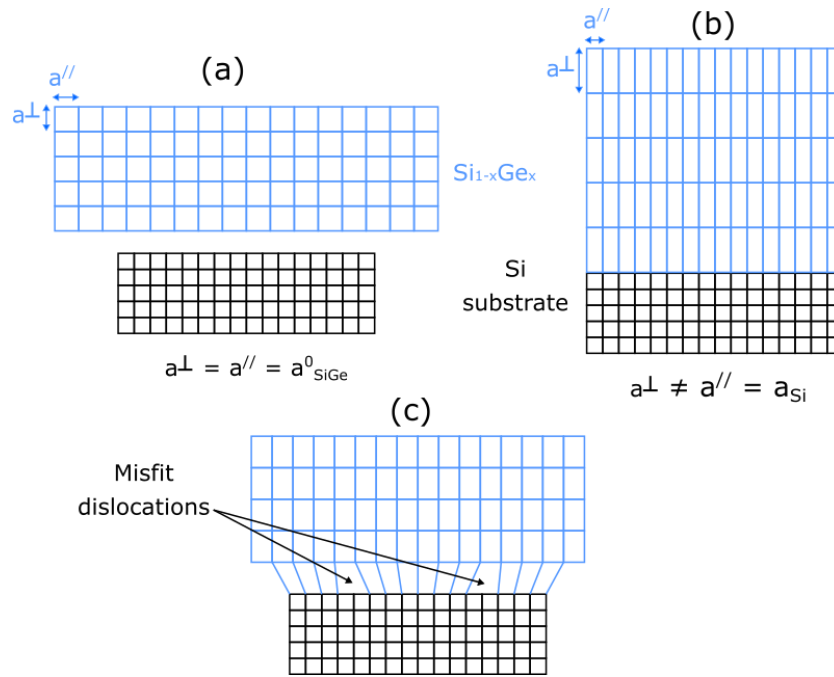


Figure I - 7. The lattice parameter of  $Si_{1-x}Ge_x$  is higher than that of Si (a), and its pseudomorphic growth on Si leads to deformation in the SiGe (b). This stress can relax via the introduction of misfit dislocations at the interface (c).

The critical thickness can however be exceeded without relaxation if the growth is performed in non-equilibrium conditions. The layers are therefore metastable. The graph in Figure I - 8 [16] highlights that lower growth temperatures enable the formation of thicker strained layers for a given Ge content. In 2011, Hartmann [14] experimentally showed that  $Si_{1-x}Ge_x$  layers could reach 200 nm and 40 nm for  $x=0.22$  and  $x=0.42$  respectively.

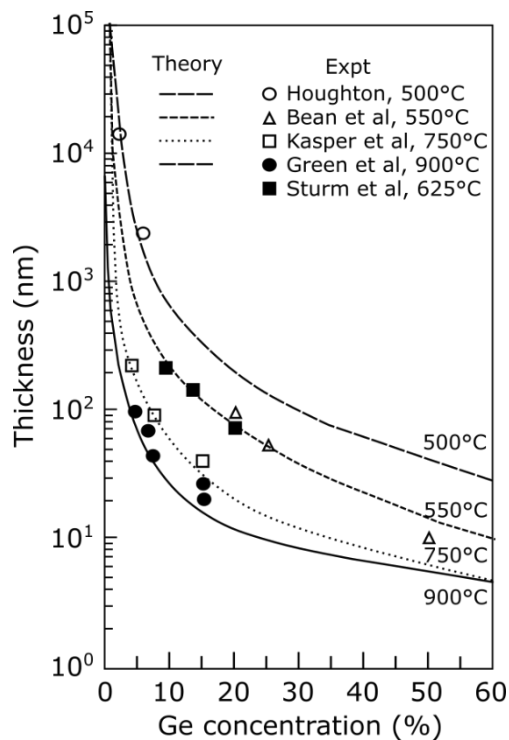


Figure I - 8. Critical thickness of  $Si_{1-x}Ge_x$  layers as a function of Ge content  $x$ , at various growth temperatures, from [16]. The critical thickness at a given content increases for lower growth temperatures.

## b) Electrical properties in strained SiGe alloys

Electronic properties of  $\text{Si}_{1-x}\text{Ge}_x$  evolve with the Ge content in the layers, and with their strain state. As Ge bandgap is smaller than the Si one (0.66 eV versus 1.12 eV),  $\text{Si}_{1-x}\text{Ge}_x$  bandgap decreases with  $x$ , as shown in Figure I - 9. Its evolution is however not linear with concentration: it reduces progressively up to Ge content ~85%, and drops abruptly for higher contents. Due to band splitting, two sets of values are presented for strained  $\text{Si}_{1-x}\text{Ge}_x$  for the heavy and light hole bands [17,18]. Both bandgaps decrease at a much faster rate with the Ge content than the unstrained material.

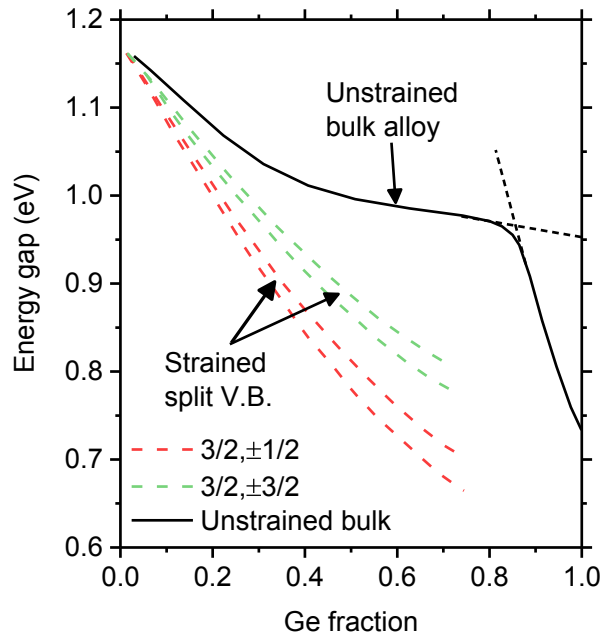


Figure I - 9. Evolution of indirect bandgap in strained and unstrained SiGe alloys. Two sets of values are shown for strained SiGe due to the valence band splitting. It is a summary of data from [17,19].

The hole mobility for boron-doped unstrained alloys can be expressed as [20]:

$$\mu_h = \mu_0 \cdot \exp\left(\frac{-p_c}{n_t}\right) + \frac{\mu_{max}}{1 + \left(\frac{n_t}{C_R}\right)^\alpha} - \frac{\mu_1}{1 + \left(\frac{C_S}{n_t}\right)^\beta} \quad \text{Eq. I - [4]}$$

Where  $n_t$  is the hole concentration, while other parameters depend on the Ge concentration.

The bands modification caused by strain leads to a reduction of the hole effective mass and therefore to an improvement of the hole mobility [21]. The evolution of mobility with increasing Ge content for strained and relaxed alloys is presented in Figure I - 10, with a distinction between the in-plane mobility  $\mu_{xx}$  and the out-of-plane mobility  $\mu_{zz}$  for strained SiGe. While the mobility slightly improves with Ge content for relaxed alloys, this enhancement is superior for strained alloys. Both  $\mu_{xx}$  and  $\mu_{zz}$  increase in a similar fashion with Ge concentration, though the mobility is somewhat higher for  $\mu_{xx}$ . The curves in Figure I - 11 summarize the calculated hole mobilities as a function of boron concentration [21]. Both tensile and compressive strain show improved values compared to unstrained alloys [22].

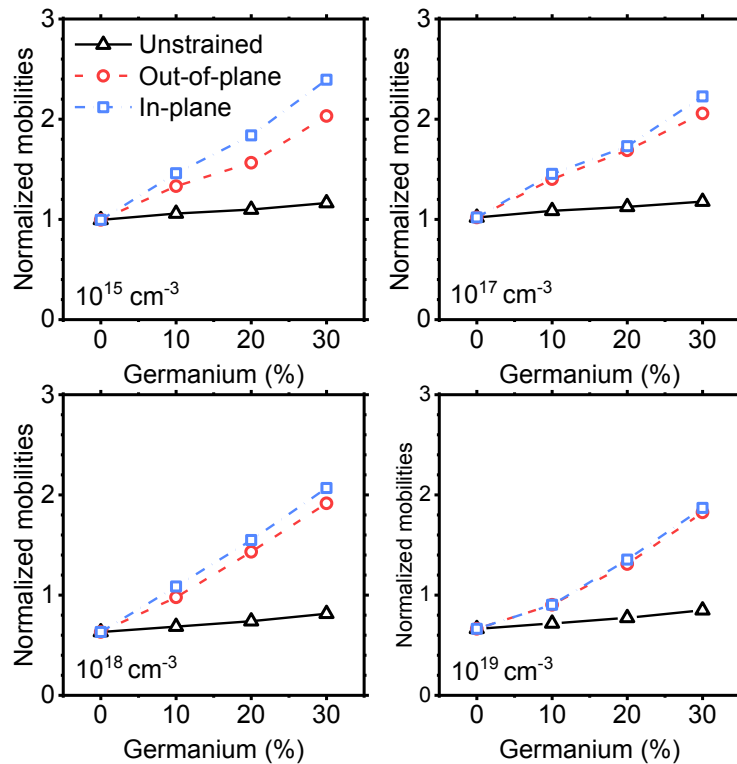


Figure I - 10. Evolution of hole mobility in strained and relaxed SiGe layers grown on Si (001), as a function of the Ge content, at different boron doping levels. These results were obtained from simulations [21]. The triangles correspond to unstrained SiGe, while squares and circles, respectively correspond to in-plane and out-of-plane mobilities in strained SiGe. These values are normalized to the mobility in relaxed Si.

The presence of defects such as the misfit and threading dislocations in relaxed alloys is detrimental to the electronic properties [23]. These dislocations cause local distortions in the lattice and thus cause additional carrier scattering, or act as trapping and recombination centers for the carriers. The resulting effects are a decrease in mobility and an increase in leakage currents, as well as poorer optoelectronic properties.

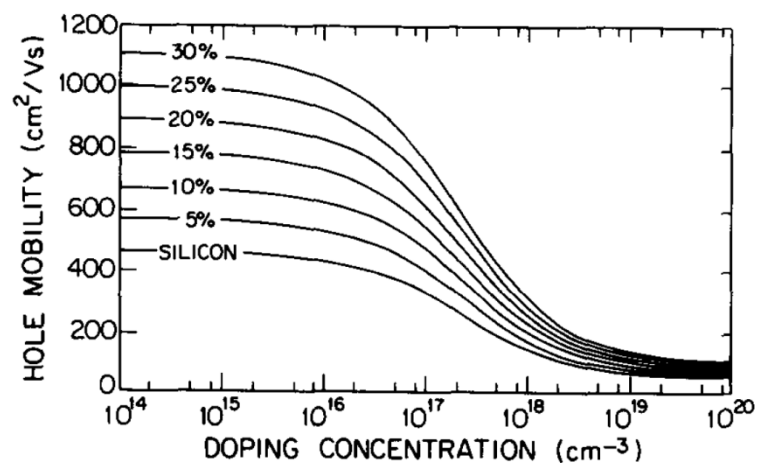


Figure I - 11. Hole mobility evolution in boron doped strained SiGe with dopant concentration, for Ge concentrations from 0% to 30% [21].

### 3. Annealing processes in microelectronics

The active regions of devices (source, channel and drain) have to be doped to obtain satisfying electrical performances. In particular, source and drain regions need high activation levels to improve sheet resistance and contact resistivity. The dopant activation process in semiconductor layers via annealing is presented in the following parts.

#### a) Heat transfer

There are three different mechanisms of heat transfer between two materials at different temperatures, called conduction, convection and radiation, as schematically presented in Figure I - 12. Conduction and convection both involve a transfer through or within a medium, while radiation can occur even without a medium (in vacuum) [24]. Conduction is a transfer within a body, or between bodies that have a physical contact. Heat flows from a hotter region to a colder one by collisions of atoms and movement of electrons. The heat flux  $W$  is proportional to the thermal gradient and can be expressed with Fourier's law for a simple one-dimensional system with no internal heat generation:

$$W = -\kappa \cdot A \cdot dT \cdot dx \quad \text{Eq. I - [5]}$$

where  $\kappa$  is the thermal conductivity expressed in  $W/m \cdot K$  and  $A$  is the exchange surface expressed in  $m^2$ . The typical length over which the material is heated corresponds to the diffusion length  $L_{HEAT}$ . It depends on the heat diffusion coefficient  $D_H$ , as well as on time.

$$L_{HEAT}(T, \tau) = 2\sqrt{D_H(T) \cdot \tau} \quad \text{Eq. I - [6]}$$

$$D_H(T) = \frac{\kappa}{\rho \cdot C_p} \quad \text{Eq. I - [7]}$$

with  $\rho$  the density and  $C_p$  is the thermal capacitance.

Heat transfer by convection is the result of motion of molecules or atoms in a fluid. Natural convection is due to temperature gradients affecting the liquid or gas density. In the case of forced convection, an external pressure gradient accelerates the motion of the fluid.

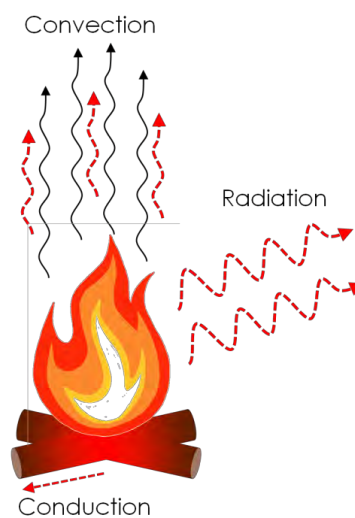


Figure I - 12. The three types of heat transfer are radiation, conduction and convection

Radiation occurs via the emission of thermal radiation from a hot body. The generation of these radiations from a hot material is caused by the thermal excitation of electrons. Photons

with an energy  $E = h \cdot \nu$  are thus emitted. A perfect emitter is a black-body, and its luminance,  $L_\lambda$ , follows Planck's law. It allows to determine the wavelength  $\lambda$  (frequency  $\nu$ ) for which the emission is maximal.

$$L_\lambda = \frac{2hc^2}{\lambda^5} \cdot \frac{1}{\exp\left(\frac{hc}{\lambda kT}\right) - 1} \quad \text{Eq. I – [8]}$$

The radiations can be either transmitted, reflected or absorbed when they reach another material. The fraction of incident light undergoing each one of these three phenomena are named absorptivity  $a$ , reflectivity  $r$  and emissivity  $t$ , and obey the following expression :

$$a + r + t = 1 \quad \text{Eq. I – [9]}$$

Reflectivity can be independent of the incident light direction and be equivalent in all directions (diffuse reflection), or depend on the incident light direction (specular reflection). In this case, the reflection angle is equal to the incident angle. Reflectivity can also be a mix of both diffuse and specular reflectivity. Absorption strongly depends on the wavelength of incident light, and the probability of finding radiation at a given depth  $z$  in the medium follows a Beer-Lambert law :

$$P(z) = \exp(-\alpha \cdot z) \quad \text{Eq. I – [10]}$$

$$\text{with } \alpha = 1/l = 4\pi k/\lambda \quad \text{Eq. I – [11]}$$

Where  $\alpha$  is the absorption coefficient ( $\text{m}^{-1}$ ),  $l$  is the absorption length (m) and  $k$  is the extinction coefficient, itself dependent on the wavelength. The absorption length thus varies with the wavelength of the incoming radiation, and varies with the material, as shown in Figure I - 13 for Si and Ge.

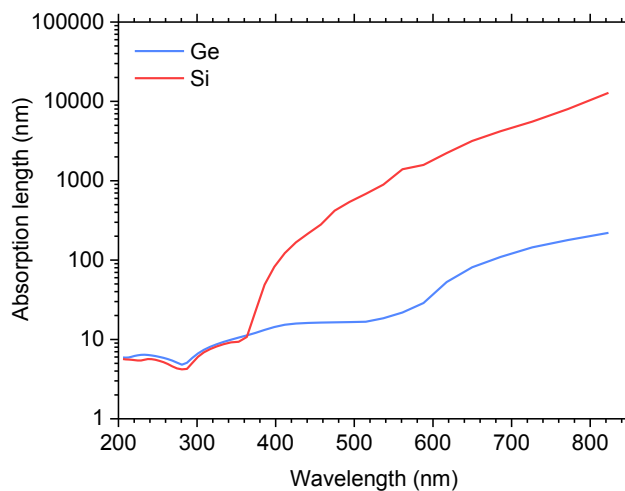


Figure I - 13. Absorption length as a function of radiation wavelength for silicon and germanium at room temperature. Radiations with short wavelength are more energetic and therefore absorbed over a shorter depth.

Materials can be heated through diffusion, convection or radiation. Depending on their physical characteristics, they will react in various ways and heat over different lengths or at different temperatures. The energy brought by an annealing process may give rise to multiple effects within a crystalline material, including the displacement of atoms by diffusion mechanisms.

## b) Atomic diffusion within a crystalline material

*i. Dopant activation and defect healing*

Semiconductor doping requires the introduction of impurities in the lattice, in order to obtain free carriers. In the case of group IV semiconductors (Si, Ge, SiGe alloys), the addition of atoms from the third column (boron, gallium) of the periodic table or from the fifth column (phosphorus, arsenic) respectively lead to conduction via holes or electrons. When these dopants are in substitutional position (i.e. located at a node of the crystalline lattice) as in Figure I - 14, they form covalent bonds with the neighboring Si atoms. This forms an additional carrier, either a hole for p-type doping or an electron for n-type doping. These carriers can be easily excited to become free carriers, as they are not on the same energy levels.

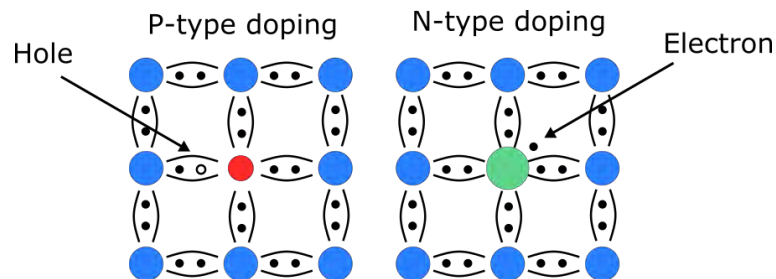


Figure I - 14. Impurities have to be introduced in the semiconductor lattice in order to produce additional carriers. These dopant elements must be in substitutional position.

The dopant introduction can be performed by multiple ways: during the growth of the material, introduced afterwards with ion implantation or with diffusion from a solid or gaseous source. In the case of ion implantation, the impinging species cause disorder in the lattice, and can cause its amorphization, such as in Figure I - 15. Diffusion of the atoms, both impurities and matrix element, is therefore required in order to move from this disordered state to a well-organized lattice, with dopants in substitutional position. The energy required can be provided by thermal energy during annealing processes.

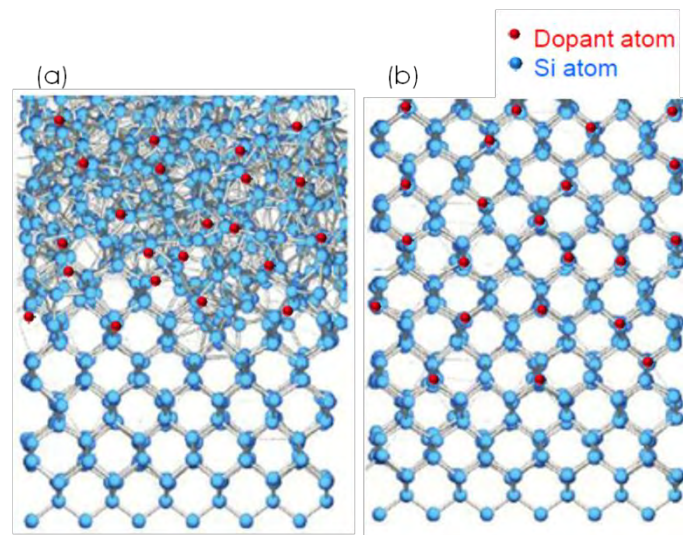


Figure I - 15. The introduction of dopants via implantation leads to disorder in the material (a). Annealing processes are used to recover an ordered lattice and activate the dopants via diffusion (b).

*ii. Atomic Diffusion*

The atomic diffusion is the transport and movement of atoms inside a lattice. If any other gradient (electrical or thermal potentials) are ruled out, the atoms movement is caused by the

presence of a concentration gradient. The relations between the diffusion flux,  $J$ , the diffusion coefficient or diffusivity  $D$  ( $\text{cm}^2/\text{s}$ ) and the concentration  $C$  can therefore be written as:

$$J(x, t) = -D(T) \cdot \frac{\partial C(x, t)}{\partial x} \quad \text{Eq. I - [12]}$$

$$\frac{\partial C(x, t)}{\partial t} = \frac{\partial}{\partial x} \left( D(T) \cdot \frac{\partial C(x, t)}{\partial x} \right) \quad \text{Eq. I - [13]}$$

Combining the transport equation (Eq. I - [13]) with the first Fick's Law (Eq. I - [12]), we obtain the second Fick's Law

$$\frac{\partial C(x, t)}{\partial t} = \frac{\partial}{\partial x} \left( D(T) \cdot \frac{\partial C(x, t)}{\partial x} \right) \quad \text{Eq. I - [14]}$$

If the diffusion coefficient  $D$  does not depend on the concentration, it can be written through a simple Arrhenius law:

$$D(T) = D_0 \cdot \exp\left(-\frac{E_a}{kT}\right) \quad \text{Eq. I - [15]}$$

where the activation energy,  $E_a$ , represents the energy required for one impurity atom to move from its site to the neighbor one. In practice,  $E_a$  varies according to the diffusion species and the corresponding diffusion mechanism.

The diffusion length  $L$  for a given species is the distance it can cover in a given time  $t$ , and depends on  $D(T)$ :

$$L(T, t) = 2\sqrt{D(T) \cdot t} \quad \text{Eq. I - [16]}$$

Diffusion relies on the naturally found point defects in the lattice, either interstitials or vacancies. An interstitial corresponds to an atom located outside of the lattice nodes, where there should be a void, while a vacancy is the lack of atom in one of the lattice nodes. The diffusion mechanism depends on how the diffusing impurity interacts with said defect, as presented in Figure I - 16 : it can be vacancy-mediated, interstitial mediated or a combination of both.

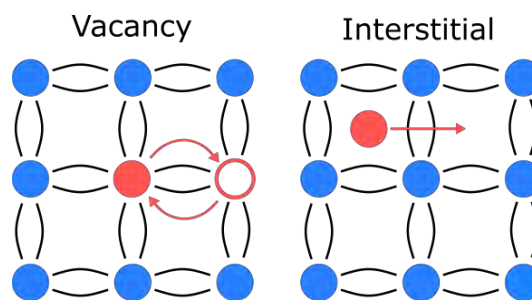


Figure I - 16. Basic diffusion mechanisms in a lattice

Dopant diffusion and activation depend on both the temperature and duration of the anneal, and modify the positions of the atoms within the lattice.

### c) Thermal budget reduction

#### i. Diffusion and activation trade-off

As mentioned previously, a junction reduction is needed to reduce the overall size of components, and must be compensated with very high level of activation. The dopant

activation must therefore be performed at high temperatures to increase the solid solubility of the impurities in the lattice and quench them during the cooling down. These high temperatures may however enable diffusion beyond the initial junction. A trade-off between the dopant activation and dopant diffusion is therefore required, as both are thermally activated phenomena. The characteristic timescales shown in Figure I - 17 (adapted from [25]) however indicate that, for similar temperatures, the activation is observed at shorter timescales than the diffusion. For more information on the BIC dissolution and on boron deactivation, see [26–28] and references therein. Anneals with duration in the  $1 \times 10^{-10}$  -  $1 \times 10^{-4}$  s range are sufficient to activate dopants (Red triangles), while significant diffusion requires the timescale to be above the millisecond (blue and green curves). It is therefore possible to activate dopants while keeping diffusion limited, by using anneals at high temperatures with very short durations, and the annealing industry in the microelectronics has evolved to satisfy these requirements.

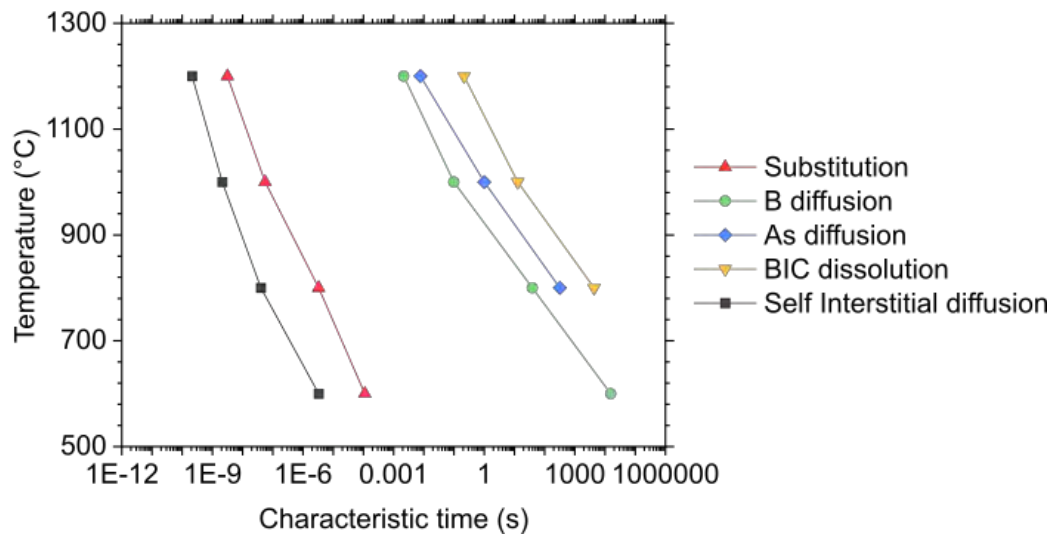


Figure I - 17. Dependence of various phenomena such as diffusion and activation upon anneal temperature and duration, in doped silicon, adapted from [25]. This shows that activation can be performed without diffusion, for annealing processes with short duration.

### ii. Process evolution

Anneals were originally performed in furnaces for several hours, which led to the formation of deep junctions due to the diffusion. In these processes, the whole volume of the samples was uniformly heated. Novel annealing methods with shorter timescales were therefore introduced to limit the dopants diffusion [29]. Rapid Thermal Processing (RTP) encompasses different annealing methods with duration in the second timescale, with typical temperatures up to 1100°C [30]. These processes are also long enough to heat the entire sample, but they can limit the dopant diffusion compared to furnace anneals, as shown in the simulated boron profiles in Figure I - 18 [31].

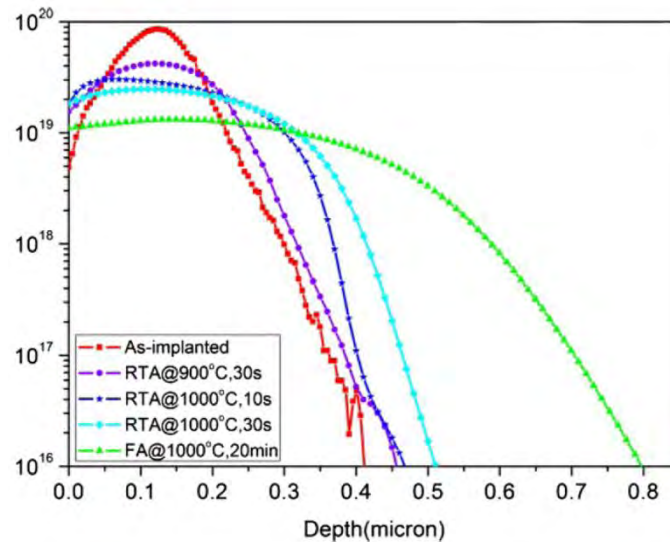


Figure I - 18. Simulated boron profiles after implantation and RTA or furnace annealing (FA), from [31].

Starting from identical as-implanted boron profiles, annealing at 1000°C with RTP for 30 seconds forms a thinner junction (~200 nm shorter) than a 20 minutes furnace anneal at the same temperature. Flash Lamp Anneal (FLA) was introduced in the 2000's, further reducing the anneal duration down to a few milliseconds by illuminating the sample with infrared lamps. In this case, a temperature gradient is formed within the sample, as in Figure I - 19 (b).

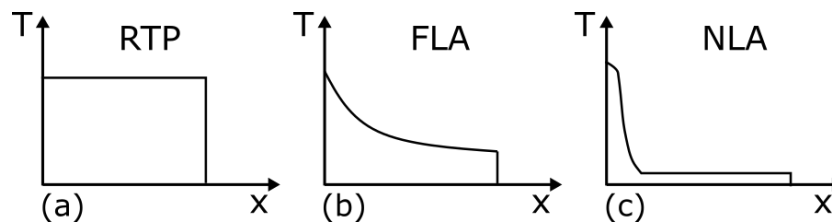


Figure I - 19. Typical temperatures profiles in material depth for different types of anneals : RTP (a) , FLA (b) and NLA (c) [29], with x the depth.

Finally, anneals in the nanosecond scale are now explored by the industry, such as the Nanosecond Laser Annealing (NLA). These anneals also use radiations to heat the samples, with pulses that last from few nanoseconds to a few hundred nanoseconds : the process is quasi-adiabatic, leading to high temperatures near the surface, potentially reaching the melt temperature, while the lower regions of the samples remain at low temperatures, as in Figure I - 19(c). For such timescales, the diffusion of dopants is almost suppressed in the solid phase of the semiconductors, while it can largely occur in the liquid phase. For these reasons, NLA is a promising method for the realization of thin and abrupt junctions.

## II - NANOSECOND LASER ANNEAL : A SURFACE ANNEAL SOLUTION

NLA is a promising technique for future annealing of semiconductors, and will likely be used for the formation of device junctions. The following sections detail its principle and main characteristics and aim at giving an overview of its impact on Si and Ge quality and doping.

### 1. Heating by laser radiation absorption

#### a) Theoretical background

NLA relies on heat transfer via radiation. When these radiations reach the annealed material and are absorbed, several phenomena take place, as described by Sundaram [32]. These effects are summarized in Figure I - 20 and detailed here:

- Carrier excitation: Single photon absorption is the dominant mechanism for exciting electrons from the valence band to the conduction band, if the photon energy is larger than the bandgap. It can be assisted by the creation of phonons if the gap is indirect. The complete process typically occurs in less than a picosecond.
- Thermalization: refers to the scattering phenomena, that can be either carrier to carrier or carrier to phonon. In this case, the scattering transfers a small amount of energy to the lattice. As scattering events multiply in the lattice, the matter reaches high temperatures. Carriers and the lattice reach thermal equilibrium in less than a picosecond [33].
- Carrier removal: free carriers in excess in the excitation region diffuse or recombine, for up to a few microseconds.
- Thermal and structural effects: depending on the reached temperature, phase changes (change to liquid phase) may happen if nucleation sites form. The lattice is simultaneously cooled by heat diffusion in the deeper regions that were not heated by the pulse. These phenomena can last up to several microseconds.

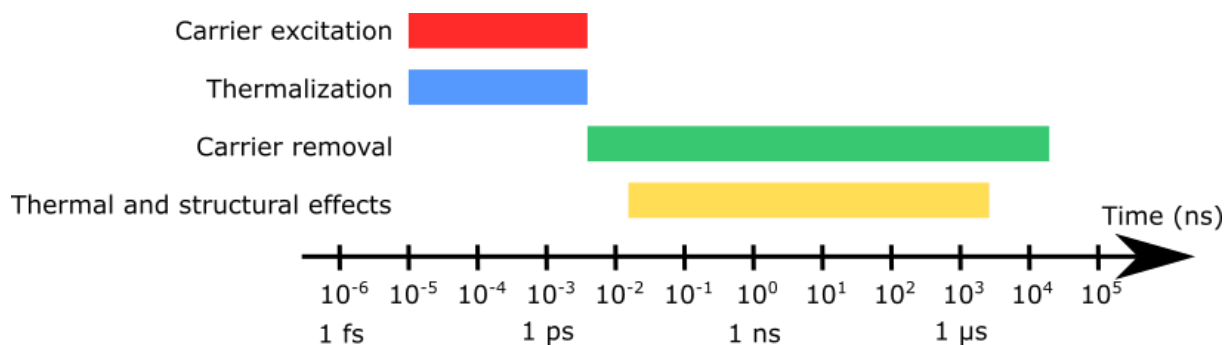


Figure I - 20. Timescale of the phenomena occurring in a semiconductor material after illumination via a pulsed laser, adapted from [32].

For a nanosecond laser, the lattice heating can be considered as immediate, as the timescale for reaching high temperatures (excitation and thermalization) is on the picosecond timescale, several orders of magnitude below the duration of the anneal itself. This consideration is not valid for picosecond laser anneals or femtosecond laser anneals, in which all these steps have to be considered [32]. Three conditions should however be fulfilled to consider the heating as immediate in a material:

- The carrier diffusion length has to be shorter than light penetration depth or the heat diffusion length during pulse duration.
- The transition from valence to conduction band should be the predominant absorption process, to produce new free carriers (negligible free carrier absorption).
- The carrier lifetime (time to recombine or scatter) should be shorter than the pulse duration.

These conditions are fulfilled in the case of silicon submitted to a nanosecond laser pulse [34].

The semiconductor is heated by the laser pulse over a depth equivalent to the largest value between the absorption length  $l = (1/\alpha)$ , where  $\alpha$  is the absorption length, or the heat diffusion length  $L_{HEAT} = 2\sqrt{D_H \cdot \tau}$  where  $D$  is the thermal diffusivity and  $\tau$  is the pulse duration [35]. The estimated heat diffusion lengths in Si and Ge are shown in Figure I - 21 as a function of pulse duration, while absorption lengths as a function of wavelength are shown in Figure I - 13. The heat diffusion length is the predominant parameter for these materials, as it is on the order of micrometer, while absorption length is on the order of the nanometer,

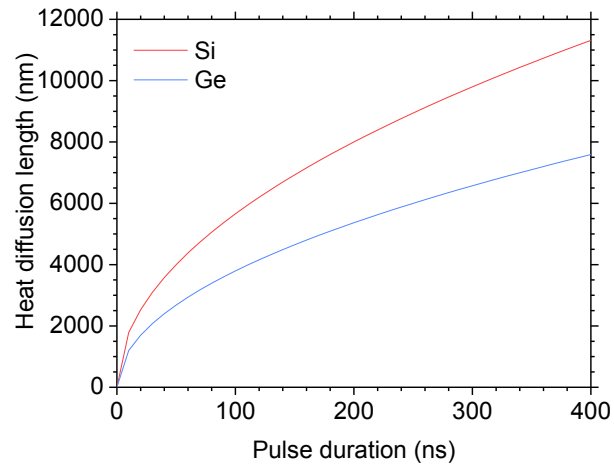


Figure I - 21. Heat diffusion length as a function of the laser pulse duration in silicon and germanium.

The surface reaches high temperatures, while the deeper regions are cooler and heated only through the heat diffusion. At the end of the laser pulse, the material cools with heat diffusion and the substrate acts as a heat-sink. The cooling rates (hence the solidification velocities) are therefore dependent on the temperature gradients: steeper gradients lead to higher cooling rates (i.e. faster solidification in case of melt).

#### b) Laser annealing conditions

##### *i. Industrial laser types*

The industrial nanosecond lasers are defined by several characteristics:

- Laser source: it can be either solid or gaseous, and defines the wavelength of the radiation. The most classical ones are indicated in Table I - 1. The absorption length strongly depends on wavelength.
- Laser pulse: its shape and time length define the anneal duration, which impacts the heated thickness. It is usually indicated with the Full Width Half Maximum (FWHM) duration of the peak, up to a few hundred nanoseconds.
- Energy density ( $J/cm^2$ ) range: amount of energy that can be deposited per surface unit in a single laser pulse. Higher energy densities lead to higher temperatures at surface.
- Repetition rate: defines the frequency with which laser pulses can be performed on a given surface. As multiple pulses can be made on the same surface area, faster rates may allow to re-heat the material before it has fully cooled.
- Coverage: either scanning mode or stepping mode, shown in Figure I - 22. Scanning lasers progressively cover the surface with a continuous movement. The beam shape is usually rather thin (a few microns large and a few mm long). In contrast, step & repeat lasers anneal a wider area ( $15 \times 15 \text{ mm}^2$  for ex.) in a single step, then move to another area.

Table I - 1. Wavelengths of lasers commonly studied for semiconductor annealing

Radiation	Ultraviolet		Visible	Infrared	
Laser type	KrF	XeCl	Frequency doubled Nd:YAG	Ruby	Nd:YAG
Wavelength	248 nm	308 nm	532 nm	694 nm	1064 nm
Typical pulse duration	20 -25 ns	20 - 200ns	20 - 80 ns ?	2 – 20 ns	

Other parameters, such as the anneal ambient (usually  $N_2$  in our experimental conditions) or the ability to heat the chuck on which the wafer is mounted at higher temperatures, may also play a role.

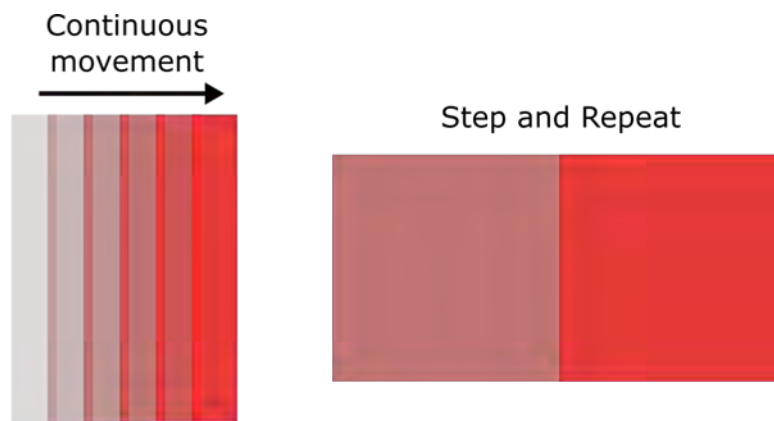


Figure I - 22. Surface illumination mode are either scanning mode, with a continuous movement across the surface or stepping mode, with a wide area annealed at each step.

### ii. Impact of laser properties on melt depth and solidification velocities

The variation of any of the laser beam features described in the previous section modifies the anneal, as it modifies the annealing temperatures and gradients. Nanosecond laser anneal can lead to sub-melt regimes or melt regimes depending on the type of laser and the energy density. Sub-melt anneals are usually performed with multiple pulses on the same area, while melt anneals tend to be performed with a single pulse. For these, the melt depth and melt duration are impacted by the wavelength, the pulse duration, the energy density, as well as the optical and thermal properties of the material itself.

For instance, for a given wavelength, a shorter pulse duration causes a reduced thermal diffusion in the material. As a result, the material reaches higher temperatures, at a given energy density. This can be observed in Figure I - 23 [36], that presents the molten depth in Si as a function of the laser energy density, after annealing with two different pulses, 25 ns (empty triangles) and 200 ns (full triangles). The melt threshold (the lowest energy density for which melting is observed) is reached at lower energy densities for the shorter pulse duration ( $-0.6 \text{ J/cm}^2$  vs  $-1.5 \text{ J/cm}^2$ ). For a given energy density, a much deeper melt is achieved for a shorter pulse. Short pulses also lead to faster solidification, as shown in Figure I - 24, due an increased temperature gradient [34]. It should be noted that higher energy densities cause a deeper melt and longer melt duration, for a given pulse duration and a given wavelength.

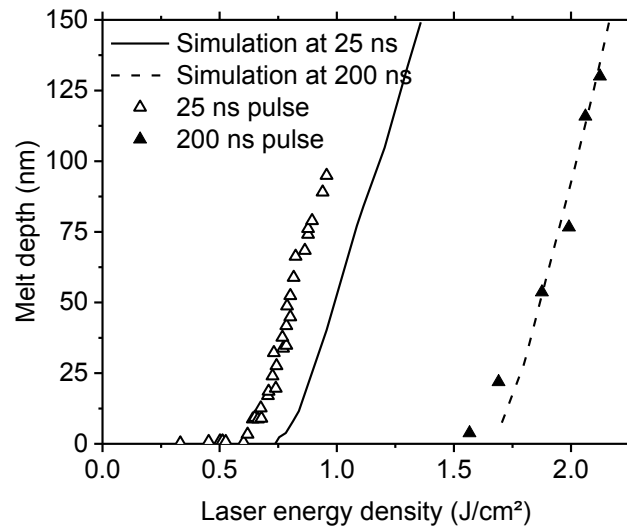


Figure I - 23. Melt depths extracted after annealing of intrinsic Si using a XeCl laser (308 nm) with a pulse duration of 25 ns (empty symbols) or 200 ns (full symbols) [36].

Similarly, a shorter wavelength causes absorption over a thinner layer of material that reaches higher temperatures. The melting point is therefore reached at lower energy densities for shorter wavelengths. This leads to higher regrowth velocities, as presented in Figure I - 24: for a given pulse duration and at a similar melt depth, the UV-NLA exhibits a much higher solidification rate than the Ruby-NLA. This behavior is observed for most semiconductor materials.

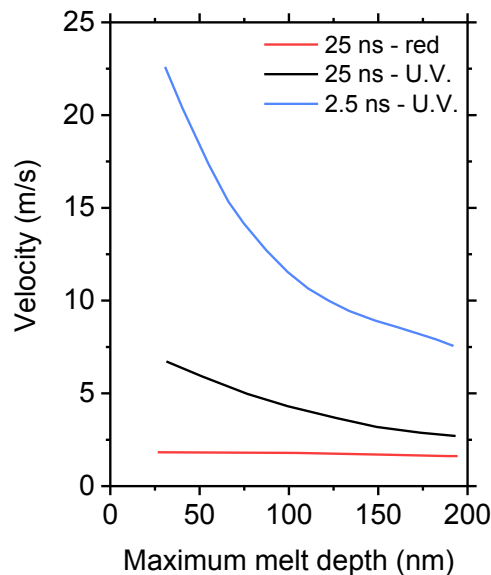


Figure I - 24. Dependence of the solidification velocity on melt depth for various laser wavelengths (Red at 694 nm or U.V. at 347 nm) and various pulse durations (25 ns vs 2.5 ns) [34].

## 2. Semiconductor layers after NLA : structure and quality

Depending on the initial sample structure, the melt depth and the solidification velocity, the resulting layers after NLA may exhibit various microstructures or morphologies.

### a) Annealing of crystalline layers

#### *i. Simple case*

The most simple laser annealing case is the melt of a Si or Ge monocrystalline layer, with the melt depth within that layer. As the seed for regrowth is crystalline, the solidifying layer will adapt to the template and regrow by following the same orientation, hence forming a perfectly crystalline layer.

### ii. Excessive crystallization velocities

Amorphization of initially crystalline semiconductors was observed upon NLA, for crystallization at high velocities due to very short laser pulses near 2-3 ns [37–39]. The formation of an amorphous phase is likely due to strong undercooling. It occurs for low energy densities (right above the melt threshold), that correspond to the highest regrowth velocities. At sufficiently high solidification velocity (typically beyond 10 m/s), the lattice is unable to restructure and an amorphous layer can be obtained. As the melt depth increases, the amorphous layer becomes thicker with increasing energy densities until the crystallization threshold is reached. The crystalline layer quality however depends on the surface orientation, as presented in Figure I - 25: monocrystalline samples are obtained for (001) surfaces, while numerous defects are observed for (111) orientations [39]. In addition, it appears that (001) and (011) surfaces can sustain higher solidification, up to 15 m/s, without amorphization.

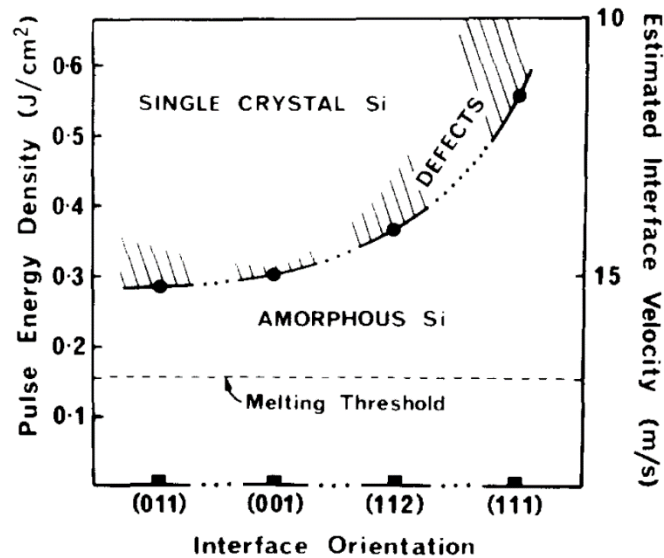


Figure I - 25. Dependence of the nature of the recrystallized layer (after NLA) on the surface orientation and liquid/solid interface velocity [39].

The range of energy densities where amorphization occurs is moreover different with the orientations, and is larger for (111) surfaces [38]. It was observed that the amorphous phase formed for regrowth velocities above 15 nm/ns (100) orientations [39] for a very short laser pulse (2.5 ns,  $\lambda=347$  nm).

## b) Annealing of amorphous layers

### i. Explosive melt and crystallization

The explosive crystallization occurs when melt NLA is applied to an amorphous layer of semiconductor. It has been very well described by Thompson [40] and Lombardo [41], and the different steps of the process are illustrated in Figure I - 26 in the case of an amorphous Si layer on top of crystalline Si.

When the melting point of the amorphous phase is reached, the surface region starts to melt (cf. Figure I - 26(b)). As amorphous Si has a lower melt temperature ( $T_m \sim 1150^\circ\text{C}$ ) than

the crystalline phase ( $T_m=1417^\circ\text{C}$ ) [40], the formed liquid layer (primary melt) is undercooled in this range of temperatures, and can be considered as a metastable phase. Therefore, it quickly solidifies into polycrystalline Si. As the phase transition from liquid to crystalline Si occurs, the released crystallization latent heat can be reabsorbed by the underlying amorphous solid material. This leads to melt of a thin layer of the underlying amorphous, as shown in Figure I - 26 (c). Being in direct contact with two solid layers (a poly-Si layer above and an amorphous layer below). This thin liquid layer is severely undercooled and solidifies at fast rate into poly-Si. Latent heat is again released during this fast re-solidification, so that a new thin liquid layer is continuously formed and crystallized in a self-sustainable manner. It propagates at extremely high velocity ( $>10\text{ m/s}$ ) until to the whole amorphous layer is crystallized (cf. Figure I - 26 (d-e)), unless the released latent heat is dissipated within the surrounding material.

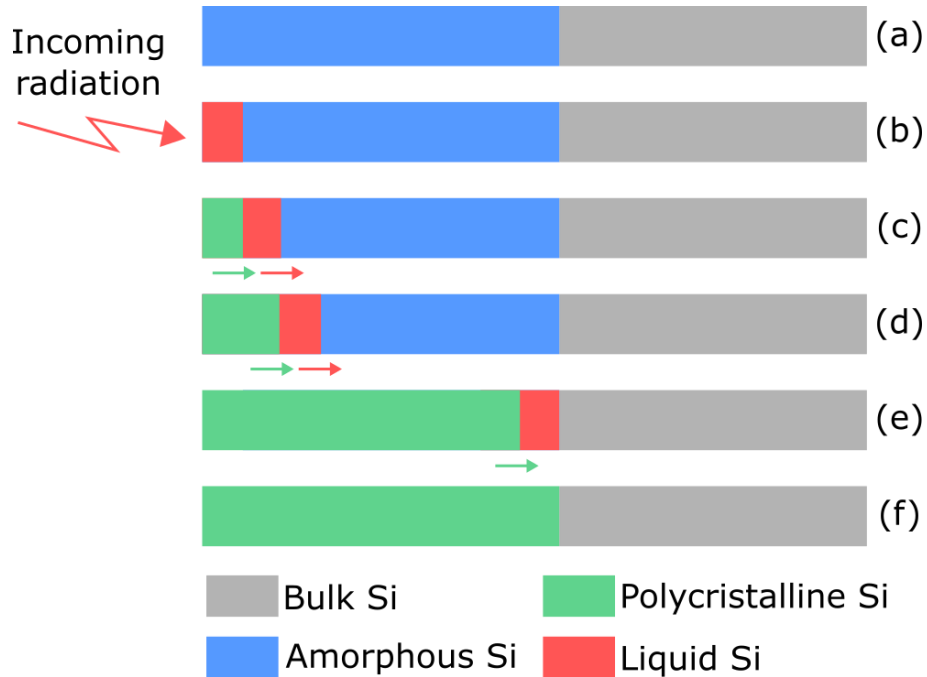


Figure I - 26. Propagation of a thin liquid layer inside an amorphous Si layer submitted to NLA, known as the explosive recrystallization phenomenon. Adapted from [41].

TEM observations, simulations and in-situ measurements can be used to compare the poly-Si depth formed by the explosive and the calculated melt depth [40], which do not match, as shown in Figure I - 27. The theoretical melt depth evolves linearly with energy density, while the poly-Si thickness is equivalent to the thickness of the initial amorphous layer for relatively low energy densities. This indicates that the explosive melt and subsequent crystallization were sustained down to the bottom of the layer, even though the laser energy density was theoretically not sufficient to melt the full layer. It should be noted that this whole process occurs in only a few nanoseconds, hence its name of explosive crystallization.

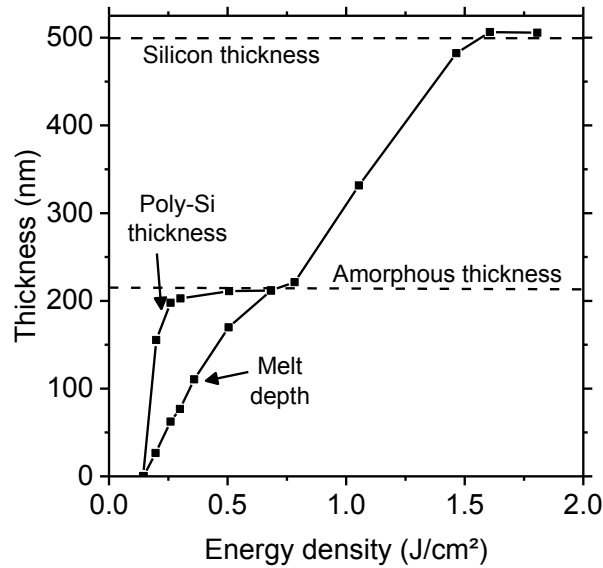


Figure I - 27. Evolution of melt depth in an amorphized Si layer annealed with a 28 ns ruby laser [40]. A discrepancy is observed between the observed thickness of polysilicon formed and the theoretical depth supposed to be directly melted by laser heating.

Studies on a-Ge [42] have proved that explosive crystallization is sustainable over several micrometers ( $\sim 7 \mu\text{m}$ ), in regions that were not directly exposed to a laser pulse.

#### ii. Second melt

A second melt occurs if the laser energy density is sufficient to melt the poly-crystalline layer formed by explosive crystallization. It can be observed with time-resolved reflectivity, as the reflectivity of the liquid layer is higher than that of the solid layer. In Figure I - 28, a sharp peak is observed in (a-b), corresponding to the explosive melt. Higher energy densities (c-d-e) exhibit a second increase in reflectivity caused by the second melt, with a duration that increases with energy density [43].

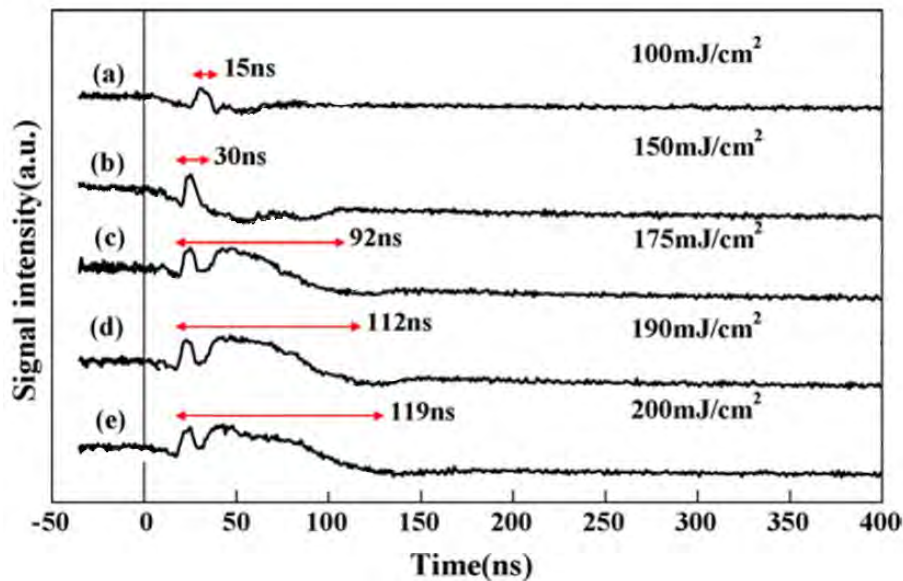


Figure I - 28. Time-resolved reflectivity signals showing the explosive melt alone at low energy densities (a-b) and followed with a second melt at higher energy densities (c-d-e). The measurements were made on an amorphous Si sample with backside annealing, through an  $\text{SiO}_2$  and a glass layer. The laser was an XeF laser with a 351 nm wavelength and a 25 ns pulse duration [43].

If the energy density of NLA is sufficient to melt the complete layer, the solidification starts from the underlying substrate. The solidification therefore starts from a monocrystalline seed and the regrown layer is monocrystalline as well [44].

### 3. Dopant behavior in Si or Ge upon NLA

#### a) Dopant redistribution

##### *i. Typical diffusion and segregation in laser annealed samples*

Depending on the type of laser and on the energy density used, NLA will cause the formation of liquid layers where the diffusion coefficients are several orders of magnitude higher than in the solid phase. A comparison between diffusion coefficient for As, B, P and Ga in Si is shown in Table I - 2, for Si at 1300°C (-100°C below the melting temperature) and in the liquid phase. The corresponding diffusion length for a 200 ns anneal is shown: diffusion is almost suppressed in the solid phase even at high temperatures, while these species can diffuse over several tens of nanometers in the liquid phase. Without impurity partition at the liquid/solid interface, the result is the formation of box-like profiles with almost uniform concentration over the whole melted depth and an abrupt decrease at the liquid-solid interface. This is true only for relatively low melt depths below 200 nm, as the anneal time is not sufficient for the dopants to diffuse over larger molten layers.

Table I - 2. Comparison of the diffusion coefficients in liquid and solid phases for Si, as well as the estimated diffusion length for a 200 ns anneal in these two phases [45].

Dopant	Solid phase at 1300°C		Liquid phase	
	Diffusion coefficient (cm <sup>2</sup> /s)	Diffusion length (nm)	Diffusion coefficient (cm <sup>2</sup> /s)	Diffusion length (nm)
As	1.70·10 <sup>-12</sup>	1.2·10 <sup>-2</sup>	1.90·10 <sup>-4</sup>	123.3
P	7.31·10 <sup>-12</sup>	2.4·10 <sup>-2</sup>	2.30·10 <sup>-4</sup>	135.6
Ga	1.44·10 <sup>-11</sup>	3.4·10 <sup>-2</sup>	2.60·10 <sup>-4</sup>	169.7
B	6.31·10 <sup>-12</sup>	2.2·10 <sup>-2</sup>	1.20·10 <sup>-4</sup>	97.9

This is observed for arsenic and phosphorus profiles in silicon [46] or in germanium [47,48], as shown in Figure I - 29 for a single pulse anneal. The melt depth increases with the energy density, leading to a phosphorus redistribution over the whole layer. At high energy densities ( $E_{TH}+0.65$  J/cm<sup>2</sup>), a box-like profile is formed with uniform content. There was however a pronounced out-diffusion between 23 and 38% [40]. For short pulses (28 ns in [46,48]), several pulses may be required to obtain a box-like profile for higher melt depths. Arsenic may also exhibit out diffusion.

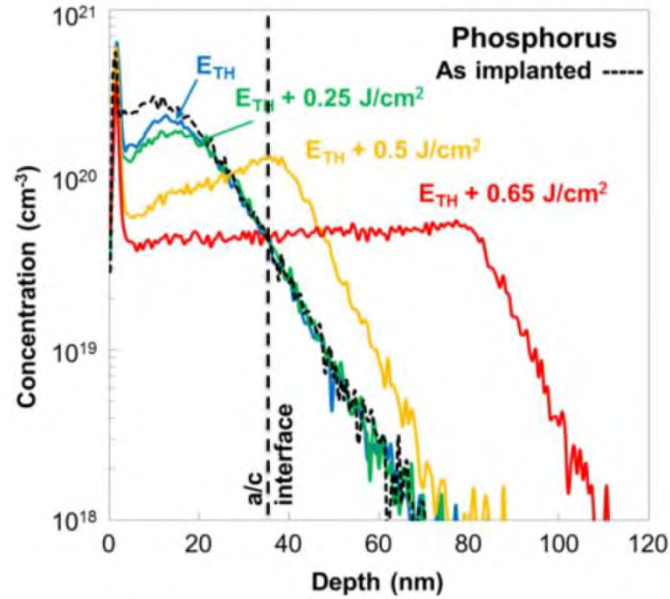


Figure I - 29. Phosphorus concentration depth profiles in germanium after laser annealing with an XeCl laser [47], obtained by SIMS measurements. The dotted line corresponds to the implantation profile, while the coloured lines corresponds to anneals at increasing energy densities, in regards to the melt threshold  $E_{TH}$ .

### ii. Dopant segregation

Partition during the solidification may also play an important role in the final profile for an impurity. At equilibrium, the partition coefficient  $k_e$  is defined as

$$k_e = \frac{\chi_s}{\chi_l} \quad \text{Eq. I - [17]}$$

where  $\chi_l$  and  $\chi_s$  are respectively the concentrations of this impurity in the liquid phase and in the solid phase at thermal equilibrium between the two phases. This equilibrium partition coefficient can be deduced from the phase diagram [49], and varies widely with the different species used as dopants [45]. Classical values in Si are 0.8 for boron, 0.35 for phosphorus, 0.008 for gallium and 0.3 for arsenic. A value lower than unity means that the solid phase will contain a lower concentration than the liquid phase, so that the dopant concentration in the liquid phase progressively increases as the solidification front moves. This causes the formation of composition gradients, with a higher concentration of impurity near the surface, such as the ones observed for Ga [50,51].

However, this coefficient is modified if the solidification is not effected at equilibrium. The effective partition coefficient  $k_i$  increases with the solidification velocity, and can be close to unity for NLA as the atoms are "trapped" in the solid phase. This explains why As in Si or Ge displays a box-like profile even though its equilibrium coefficient is below unity. There are several expressions to describe  $k_i$  dependence on velocity depending on the models considered, such as the Continuous Growth Model (CGM) or the Aperiodic Stepwise Growth Model (ASGM) [51–53]. In the CGM model, the growth is considered equivalent at any point. The coefficient is then written as:

$$k_i = \frac{k_e + v/v_D}{1 + v/v_D} \quad \text{Eq. I - [18]}$$

Where  $v_D$  is the diffusive speed defined as the ratio of dopant diffusivity at the l/s interface on the "interface thickness". In the ASGM model, the interface is considered to grow with the passage of (111) steps.  $k_i$  thus depend on the orientation and is written as:

$$k_i(\mathbf{v}, \theta) = \frac{k_e + \mathbf{v}/(v_D^T \cos\theta) \left( \frac{k_e + \mathbf{v}/v_D^L \sin\theta}{1 + \mathbf{v}/v_D^L \sin\theta} \right)}{1 + (\mathbf{v}/v_D^T \cos\theta)} \quad \text{Eq. I - [19]}$$

Where  $\theta$  is the angle between the growth direction and the (111) direction.  $v_D^T$  and  $v_D^L$  are diffusive speeds at the interface, respectively across a terrace or at a step. The ASGM model is able to reproduce the partition dependence on the growth direction for most dopants in Si [51,53].

### iii. Anomalous boron diffusion

Studies of boron-doped samples have highlighted deviations from the expected box-like profile. A boron pile-up is typically observed close to the melt depth, both in Si [54–60] and in Ge [61–63]. Typical profiles are presented in Figure I - 30: a pile-up is observed near the melt depth, while the B concentration is stable in the middle of the layer. Finally, a boron depletion is noticeable near the surface. The pile-up formation is dependent on the time allowed for diffusion: in Figure I - 30(a), the pile-up can only be observed starting from three laser pulses. This was observed in several publications, where the pile-up converges to a stable amount after 3 to 5 pulses [55]. It can even appear in the middle of the layer by combining a first pulse at high energy density (i.e. causing a deep melt and diffusion over a large layer) with a second pulse at a lower energy density : a pile-up forms at the melt depth of the second pulse [57]. Strong out-diffusion was noticed in Ge, up to 35% after 10 pulses [61].

Different theories were proposed to explain this behavior. It was suggested that variations of the partition coefficient may occur during regrowth, where  $k$  values lower than unity at the onset of regrowth would form a pile-up [57]. This was however refuted, as partition with  $k < 1$  cannot not form this kind of pile-up but rather an accumulation near the surface. Various hypothesis, such as out-diffusion, thermodiffusion and adsorption at the interface were tested [54,55] and it was concluded that adsorption was best able to reproduce the given profiles, including the depletion. This theory relies on the existence of a "wide" interface in which the dopants are adsorbed, with two partition coefficients: one, above unity (close to 2.8), for the passage from the liquid to the interface and another fixed at 0.8 for the passage from the interface to the solid phase. Simulations, such as shown in Figure I - 31(a), fit well with the experimental profiles by taking into account both an adsorbed flux and a desorbed flux at the interface.

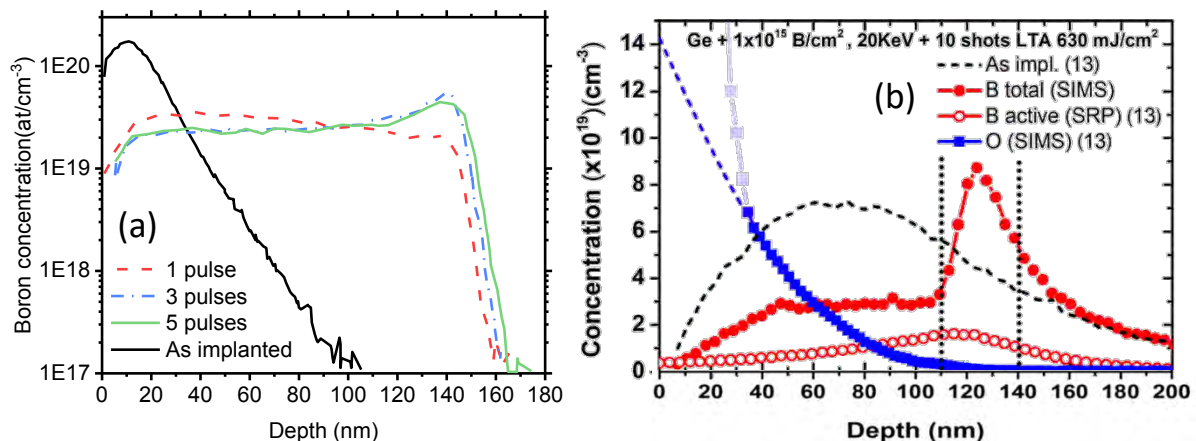


Figure I - 30. Boron concentration depth profiles in Si (a) or Ge (b) after laser annealing with single or multiple pulses [55,63].

A more widely proposed explanation is based on the existence of two types of bonds within the liquid phase [49,58]. Part of the bonds are of covalent nature, and thus correspond to a low diffusivity state, while others correspond to metallic bonding and high diffusivity state.

During regrowth, the liquid near the interface is undercooled and favors boron atoms in the low diffusivity state, which are thus attracted to the interface and form the pile-up. Simulations following this model are presented in Figure I - 31(b): they reproduce the experimental profile, except the depletion near the surface.

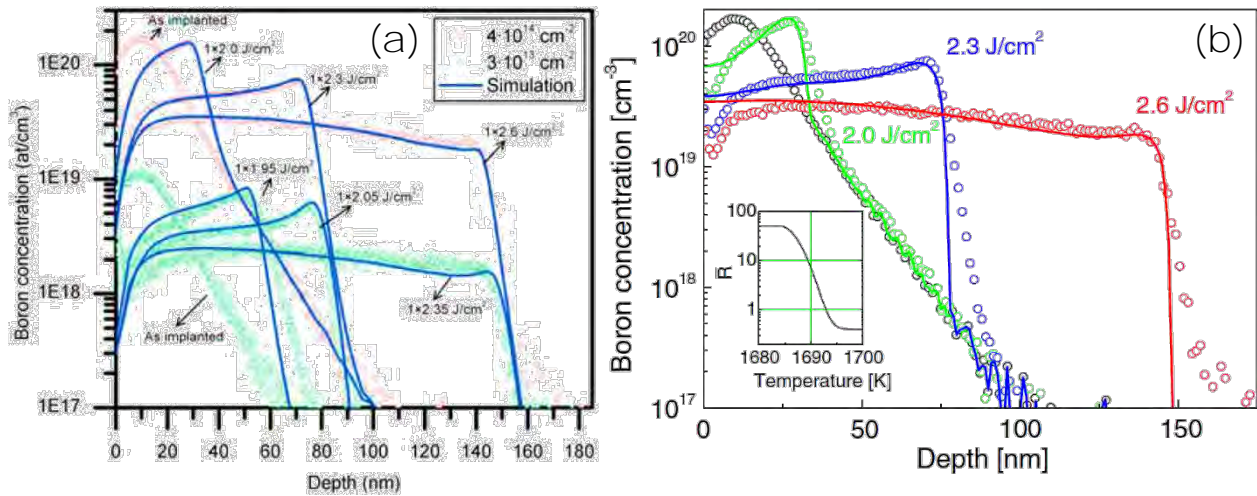


Figure I - 31. Simulations of boron depth profiles in Si following the adsorption model (a) or the liquid diffusivities model (b) [55,58]. Both reproduce fairly well the pile-up, the only difference being found near the surface for the depletion.

#### b) Dopant activation

Dopant activation using NLA is typically performed on doped layers formed by either ion implantation or by *in situ* doping during material growth. The dopant implantation can be preceded by a Pre-Amorphization Implantation (PAI), used to control the thickness of the amorphous layer formed. *In situ* doping can be implemented in different forms, such as epitaxy or deposition of an amorphous layer.

##### i. Evolution with energy density

Changes in dopant activation can be easily estimated by measuring the sheet resistance with four-point probe measurements. The sheet resistance is generally found to decrease as the energy density of the anneal increases, and its evolution can often be linked to the layer morphology, as shown in Figure I - 32 for amorphized Si [64]. In this example, Si layers were implanted with As or P to form 130 nm and 170 nm amorphous layers respectively.

As expected, the presence of an amorphous layer results in a high sheet resistance, that starts to decrease as the melt is reached. A first drop is associated with the formation of a polycrystalline layer caused by explosive melt and solidification [44,64,65]. A second, less intense decrease, can be noticed when the full melt of the layer is reached, due to the better crystalline quality that can be achieved in this case. Sheet resistance keeps lowering with energy density as the melt depth increases, since the junction becomes thicker.

Similar observations can be made for layers that were not amorphized by the implantation [66]: results on boron-implanted Si have shown better activation levels and mobilities for samples in the full melt regime, when a defect-free layer was formed.

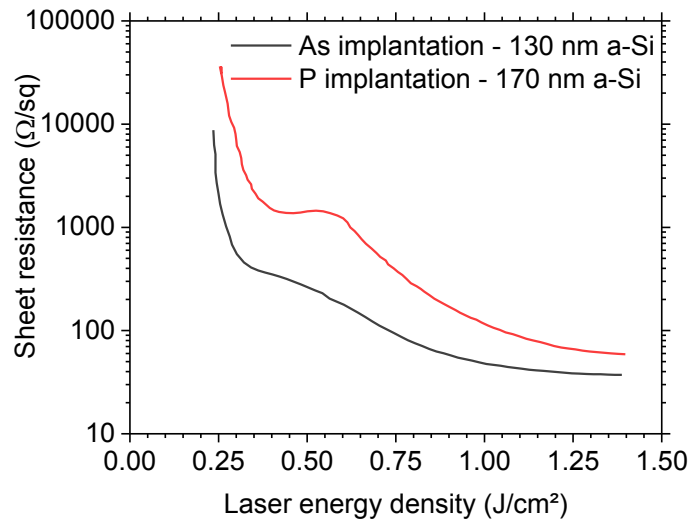


Figure I - 32. Evolution of the sheet resistance as a function of the laser energy density for Si layers doped by implantation. The black and red curves respectively correspond to a  $4 \times 10^{15} / \text{cm}^2$  As implantation at 150 keV and a  $2 \times 10^{15} / \text{cm}^2$  P implantation at 100 keV. These implantations respectively formed 130 nm and 170 nm thick amorphous layers.

*ii. Activation above the solid solubility limit*

One of the principle advantage in using nanosecond laser annealing is the possibility to reach the liquid phase over a thin layer, while the rest of the material remains solid. This enables the incorporation of a large concentration of dopants in the liquid phase, that are quenched in place during the rapid solidification, while no dopant diffusion occurs in the solid phase due to the limited duration. The aim is to obtain thin layers with high dopant concentration.

Several publications have indeed demonstrated that active dopant levels above the solubility limits were achievable with nanosecond laser annealing in Si or Ge with either boron or phosphorus. Examples are shown in Figure I - 33 for boron-doped silicon and in Figure I - 34 for phosphorus-doped silicon. For both dopants, activation levels above  $1 \times 10^{21} / \text{cm}^3$  were reached in several cases.

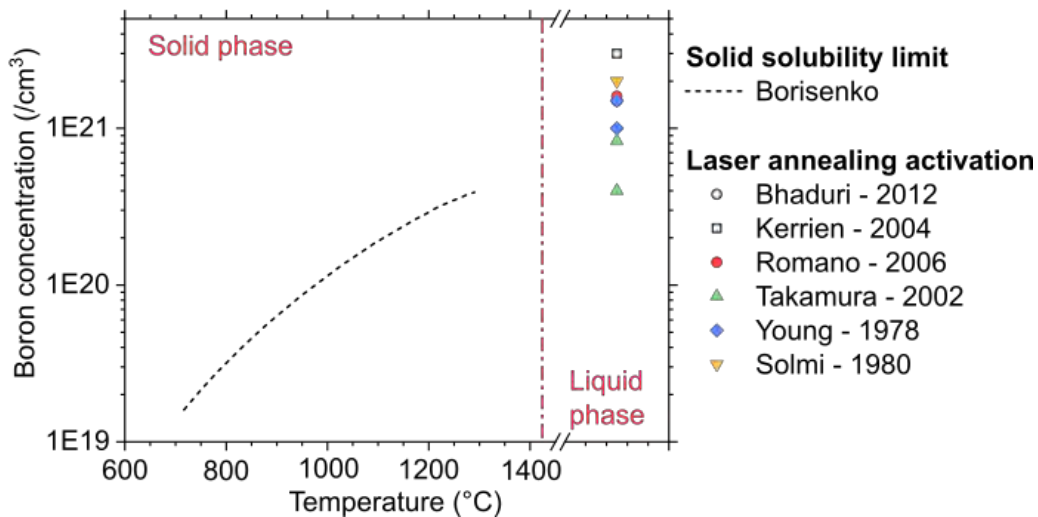


Figure I - 33. Active boron concentrations reached with nanosecond annealing in Si [67–72] compared with the estimated solid solubility limits [73,74]. Full data points correspond to activation obtained by ion implantation followed with NLA, while empty symbols correspond to the Gas Immersion Laser Doping (GILD) method in which dopants from a gaseous source are incorporated with several hundred laser pulses.

For doped Ge, boron activation levels in the  $1 \times 10^{19} - 5 \times 10^{19} / \text{cm}^3$  range were reached, even though the boron solid solubility limit in Ge is dramatically low (near  $1 \times 10^{18} / \text{cm}^3$ ). This however corresponds to only partial activation of the implanted dose [61–63]. These low activation levels are probably related to the oxygen incorporation in the layer during the anneal and to the formation of B-B complexes, as the activation improves if the oxide layer is removed before the anneal. In addition, the boron pile-up was shown to be inactive in Ge [63], while it was active for Si layers [75].

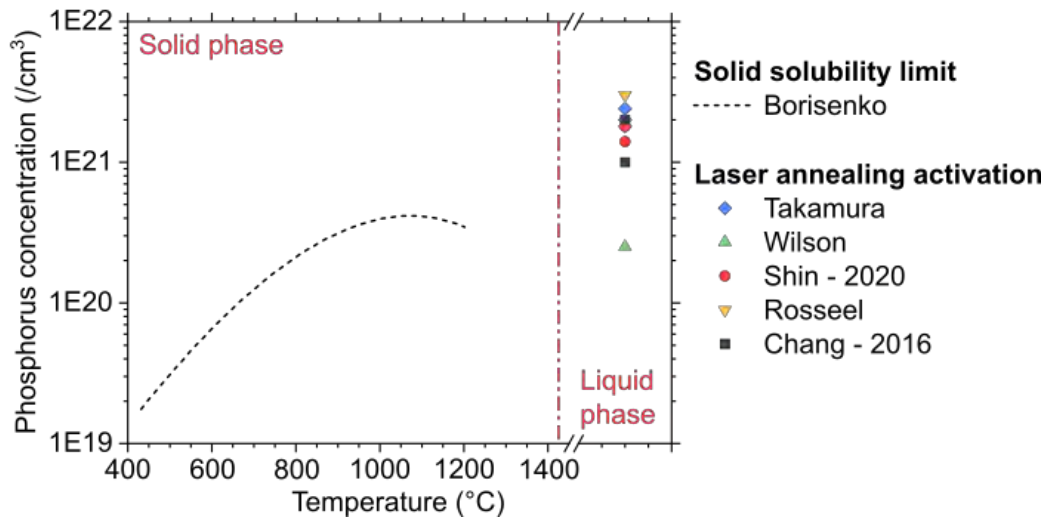


Figure I - 34. Active phosphorus concentrations reached with nanosecond annealing in Si [76–80] compared with the estimated solid solubility limits [73,74].

When active doses above the solubility limit are reached, further annealing of these layers may cause deactivation of the metastable dopants. This can be studied by submitting laser annealed layers to post-anneals with various temperatures and durations.

#### d) Deactivation

Dopants that were activated by NLA can be deactivated if they are submitted to an additional annealing (furnace or rapid thermal annealing). They may diffuse away from their substitutional positions, which deteriorates the electrical properties of the layer. Deactivation is a thermally activated process: it depends on the duration of the anneal and its temperature, as well as on the dopant type. The studies presented below were all performed after ion implantation and NLA for dopant activation in Si layers.

Boron and antimony tend to deactivate by forming precipitates [70,76,81] and their deactivation therefore requires long-distance diffusion. As a consequence, this occurs only for high temperatures and long anneals. In the case of Sb, the deactivation onset was observed near  $600^\circ\text{C}$  for 40 minutes upon furnace anneals [81], while boron seems to remain stable until  $\sim 700\text{--}800^\circ\text{C}$  [69,70,82], as presented in Figure I - 35(a) for Sb and Figure I - 35(b) for B. Other results in contradiction with these observations were obtained [82]: anneals at  $700^\circ\text{C}$  caused slight deactivation at low boron doses, while it improved the electrical results in high doses samples. This was associated with the dissolution of boron-interstitial complexes. General deactivation was however noticed near  $850^\circ\text{C}$ . Annealing at very high temperatures led to improved conductivity, associated with a carrier mobility increase induced by dopant diffusion. From the graphs presented in Figure I - 35, it can be noticed that the deactivation is dependent on the initial concentration for Sb and B. Samples with higher concentrations deactivate at lower temperatures and have higher deactivation rates: after 40 minutes at  $900^\circ\text{C}$ , the active dose is higher for the sample that initially had fewer active dopants. The formation of inactive clusters or precipitates may be facilitated for samples with a higher

concentration, leading to higher deactivation rates. This phenomena is thought to be driven by excess concentration in the samples.

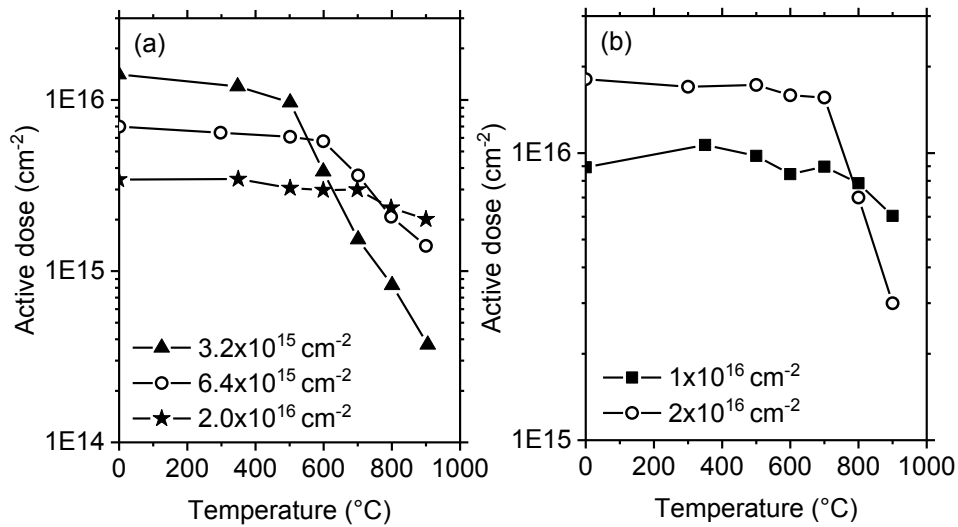


Figure I - 35. Sb (a) and B (b) deactivation after 40 min anneals as a function of temperature. Before the deactivation anneal, the samples were implanted at the indicated doses and laser annealed with a Nd:YAG (532 nm) with conditions leading to a maximum melt depth in the 110-180 nm range [70,81].

The observed phenomena are different in the case of As and P, as they are considered unstable and tend to deactivate quickly. It has been observed that deactivation started at low temperatures (450-500°C) or for short anneals [70,77], with an active dose dropping to the solid solubility limit. At 600°C, a strong P deactivation is observed after only 15 seconds, as shown in Figure I - 36. This behavior is associated with the formation of small clusters, and appears to be influenced by the initial concentration: samples with highest activation after NLA are also the ones showing stronger deactivation [77,83]. Some discrepancies between different studies still remain, with other results indicating an identical behavior for all doses [76].

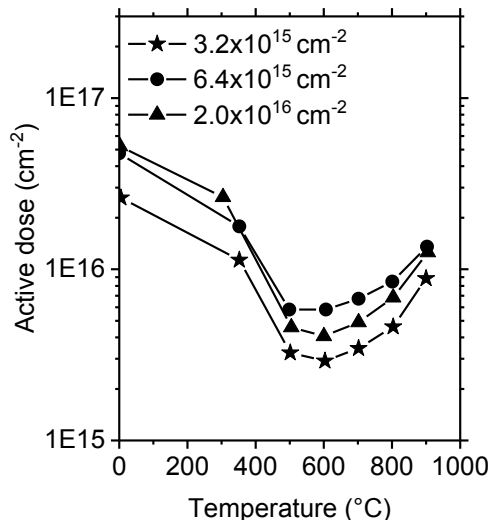


Figure I - 36. Phosphorus deactivation as a function of the temperature for 40 minutes anneals, after NLA with a frequency doubled Nd:YAG laser [76].

### III - NANOSECOND LASER ANNEAL ON SiGe ALLOYS

Thanks to its compatibility with Si technologies, and the possibilities to engineer strain and mobilities, SiGe remains a promising material for future device junctions. An understanding of the impact of NLA on SiGe layers quality and doping is therefore required.

## 1. SiGe fusion and solidification

### a) SiGe layers formation by NLA

There are several ways of forming SiGe layers using NLA, such as the deposition of a-Ge on Si [84–86], Ge ion implantation in Si [51,52] or epitaxy of SiGe followed by NLA [87,88]. The diffusion of Ge in the liquid phase enables the formation of SiGe layers with various contents and thicknesses. As mentioned earlier, SiGe properties depend on its composition and its melting temperature decreases as the Ge content increases (cf. Figure I - 6). The melt threshold is therefore expected to be lower in SiGe alloys than for pure Si, though the optical and thermal properties also impact the response to NLA. A comparison of melt depths extracted from experiments and simulations [89–91] is shown in Figure I - 37, and suggest that the melt depths are indeed higher in  $\text{Si}_{0.5}\text{Ge}_{0.5}$  than in pure Si for NLA at a given energy density with a 160 ns XeCl laser.

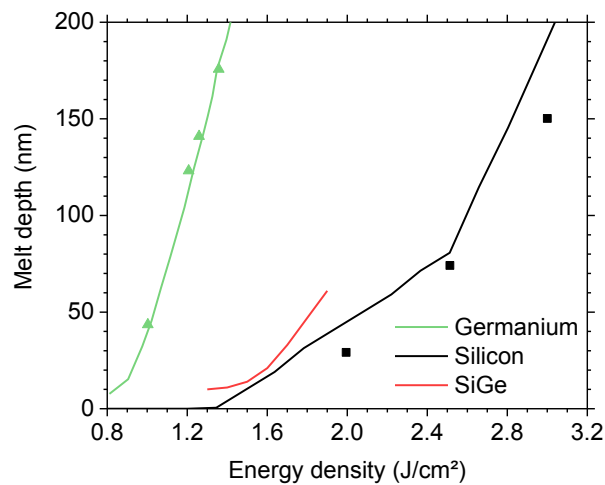


Figure I - 37. Melt depths in Si,  $\text{Si}_{0.5}\text{Ge}_{0.5}$  and Ge extracted from experimental (symbols) and simulations results (lines) after NLA with  $\lambda=308$  nm and pulse duration at 160 ns [89–92].

### b) Germanium segregation

Germanium segregation occurs during the solidification in SiGe layers, alike what occurs with dopants [88,93,94]. The resulting solid layers present a graded Ge content with a Ge-rich surface, such as in Figure I - 38(a). For a melt depth within the initial SiGe layer, a depletion is observed near the melt depth where the redistribution started, while the surface shows an enrichment. This was observed to occur in most cases, though some contradicting results with no surface enrichment exist [95].

Simulations were able to reproduce the segregation profiles [52]. As it was the case for dopants, the coefficient  $k_i$  (cf. section II.3.a.ii) depends on the solidification velocity [49,52], with an estimated equilibrium coefficient  $k_e$  near 0.4-0.45. As shown in Figure I - 38(b),  $k_i$  increases with solidification velocity, and is measured in the 0.65-0.75 range for NLA on samples from different sources with up to 10% Ge [51,52]. The influence of other parameters on the partition coefficient, such as surface orientation [51] and Ge content [52], are not fully understood yet.

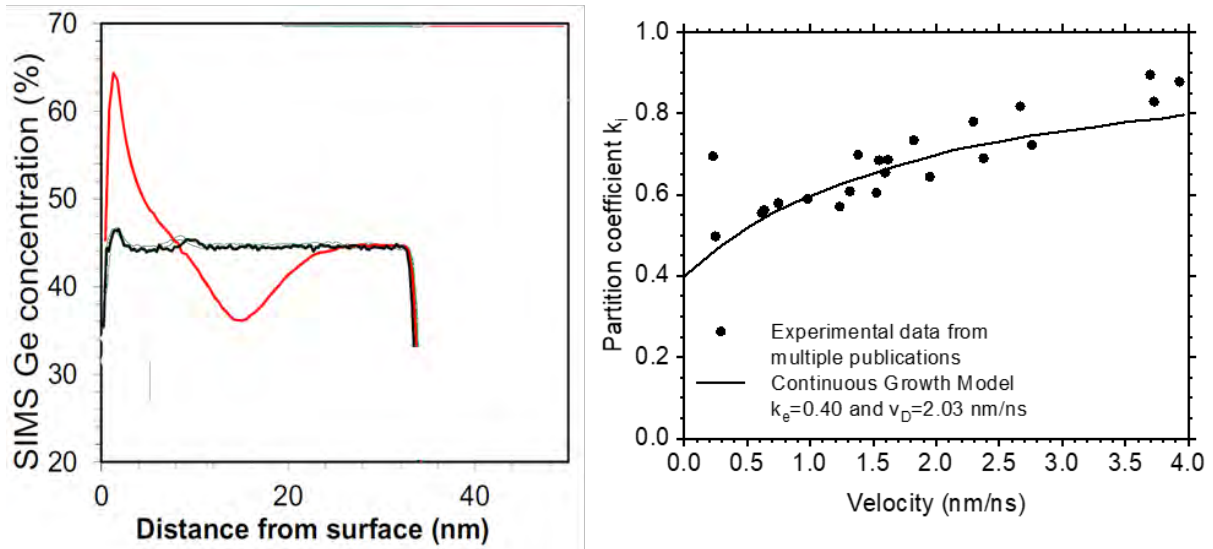


Figure I - 38. Laser annealing on an SiGe with uniform Ge concentration leads to the formation of a graded layer with high Ge concentration near the surface (a) [93]. The Ge segregation coefficient,  $k_i$ , responsible for this behavior varies with the solidification velocity (b) [52].

c) Explosive crystallization in  $\text{Si}_{1-x}\text{Ge}_x$

Explosive crystallization of amorphous  $\text{Si}_{1-x}\text{Ge}_x$  during NLA was also experimentally observed [96], with the formation of grains in thick SiGe layers. The existence of a difference in melt temperature between the a-SiGe and the c-SiGe is confirmed by the discrepancy in energy densities required to melt the two phases [97]. The solidification velocity during explosive crystallization depends on the alloy composition, as extracted from simulations and experimental results [98,99]. The solidification velocity lowers as the concentration of impurity (Si in Ge-rich layers or Ge in Si-Rich layers) increases. Simulations have indicated lowest velocities near 10 m/s for alloys in the 25%-75% Ge range, while experimental results show that the velocities drop to 5-7 m/s for alloys with a 20-40% Ge content as presented in Figure I - 39. These velocities should lead to an increase of the partition coefficient, and thus limited gradients.

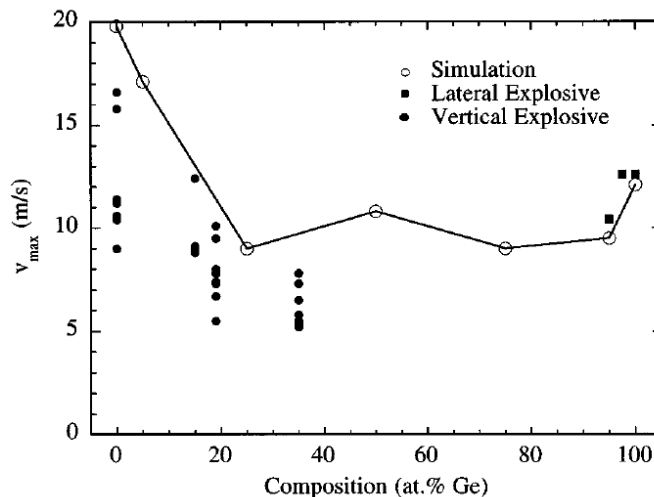


Figure I - 39. Explosive solidification velocity as a function of the germanium concentration in the amorphous layer, extracted from simulations (open circles) and experimental results (full symbols) [99].

## 2. Relaxation

Control of stress state and crystalline defects is critical for the formation of SiGe layers. As mentioned in section I.1.2.b, a layer with uniform Ge concentration may start to relax once it reaches its critical thickness by forming misfit dislocations (MDs). The presence of Ge gradients in laser annealed SiGe layers makes the critical thickness calculation meaningless.

To date, there is no general understanding of the relaxation process that occurs in these layers. Very disparate results were obtained, with observations of pseudomorphic layers in some cases [87,88,95,100,101], while partially relaxed layers (or bi-layers) [84,102] were observed in other experiments. The relaxation was attributed to excess Ge in the layers, often for values above 20% [84,85,103], and was observed to disappear for deeper melt depths (i.e. when Ge dilution within the underlying Si occurs in the liquid phase). However, several examples of strained layers with higher Ge contents [88,95] have been reported, such as shown in Figure I - 40: Ge content reaches 34%, while Reciprocal Space Maps indicate a perfectly strained layer after annealing with a KrF laser. It should be noted that all these publications did not rely on the same methods to estimate the crystalline quality and strain in their samples. They may therefore not have the same precision, and they do not provide a unified understanding of the phenomena and regimes encountered.

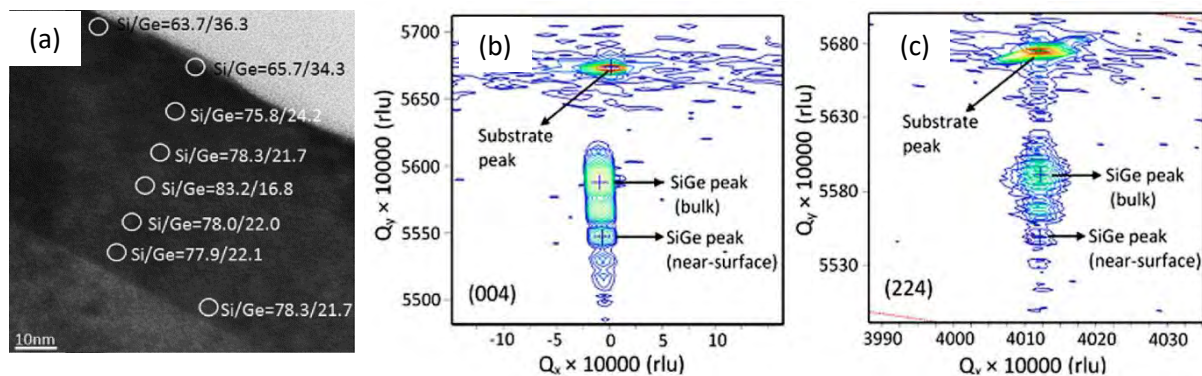


Figure I - 40. NLA on a 50 nm-thick  $\text{Si}_{0.76}\text{Ge}_{0.24}$  layer at  $0.7 \text{ J/cm}^2$  with a KrF laser causes the formation of a Ge gradient (a). The Reciprocal Space Maps, recorded for (004) and (224) Bragg reflections, indicate that the sample is strained (b-c) [88]

From this panel of results, it seems that the germanium concentration has an impact on the layers relaxation but may not be the only parameter to take into consideration.

The main part of this work focuses on a systematic study of relaxation for various samples and annealing conditions. Multiple characterizations methods are used to assess the impact of UV-NLA on the layer morphology: chemical profiles are obtained by Secondary Ion-Mass Spectrometry or Energy-Dispersive X-Rays while the surface morphology is evaluated by either SP2 Haze, Atomic Force Microscopy or Scanning Electron Microscopy. Finally, the relaxation itself is studied by X-Ray Diffraction, while defect observations rely on Transmission Electron Microscopy.

## 3. Electrical Results

The dopants attracting most interest in SiGe are boron and gallium, in order to obtain P-type layers, as mentioned in section I - 1. c. As a consequence, most publications concern these two dopants, though a few studies on As can be found.

Sheet resistance,  $R_s$ , results tend to be similar to what was observed for Si:  $R_s$  decreases with increasing laser energy density and stabilizes for the higher energy densities leading to a deeper melt [83,86,95,97,104,105]. Though we are more interested in boron or gallium doping, the evolution is particularly well described in Luong's work [95], where As was implanted in 20 nm-thick  $\text{Si}_{0.64}\text{Ge}_{0.36}$  layers, forming 7 nm of a-SiGe. The graphs reproduced in Figure I - 41 show the evolution of sheet resistance in (a) and (b), as well as active doses in (c), with increasing energy density and therefore the impact of different regimes. Explosive crystallization occurs within the amorphous layer for low energy densities, leading to a first improvement of sheet resistance. The active doses however remain low. For a melt depth in the c-SiGe layer (between 0.30 and 0.70 J/cm<sup>2</sup>), further As diffusion and activation (18% at max) are observed. Finally, the sheet resistance stabilizes when the Si melt reaches the substrate, above 0.7 J/cm<sup>2</sup>: the result is a thicker SiGe layer, with a uniform As concentration. In this case, almost complete activation of the dopants was reached. At 0.92 J/cm<sup>2</sup>, the layer formed is about 50 nm, with a chemical concentration close to  $2 \times 10^{20}$  As/cm<sup>3</sup>, and ~81% of activation.

Comparison between Ga and B doping show similar results to As doping [97]: a first decrease of sheet resistance is observed when the amorphous layer crystallizes into a polycrystalline layer (likely from explosive crystallization), and a second decrease down to ~400 Ohm/sq. occurs when the c-SiGe melts. Ga-doped layers show improvement at lower energy densities than B doped layers [104], but the final sheet resistance values are similar for both. The activation of Ga in SiGe layers is not fully understood yet [89,106], as only some results indicate an activation above the solubility limit near the surface. The near surface is rich in Ga, but presents only a partial activation of dopants.

The contact formation is improved by the presence of a Ge-rich surface [93], and contact resistivity values near or below  $10^{-9} \Omega \cdot \text{cm}^2$  (upper limit required for future devices) were observed in many studies [50,93,97,104,107]. As high dopant activation near the interface is known to improve the contact resistivity, Ga doping and segregation has attracted a lot of interest, as well as Ga and B co-doping [104,107]. Comparison between B and Ga doping has not shown clear superiority for one of them: some studies showed better performances in B-doped layers [107] while others showed improvement only in Ga-doped layers [104]. Lowest contact resistivities are obtained for intermediate energy densities, sufficient to crystallize the amorphous layer without damaging the interface or diluting the dopants [97,107]. Although dopant activation, sheet resistance and contact resistivity seem to be improved with NLA under certain conditions, the information remains superficial for B and Ga doping. In particular, their redistribution and the thermal stability of their electrical activation remain to be studied.

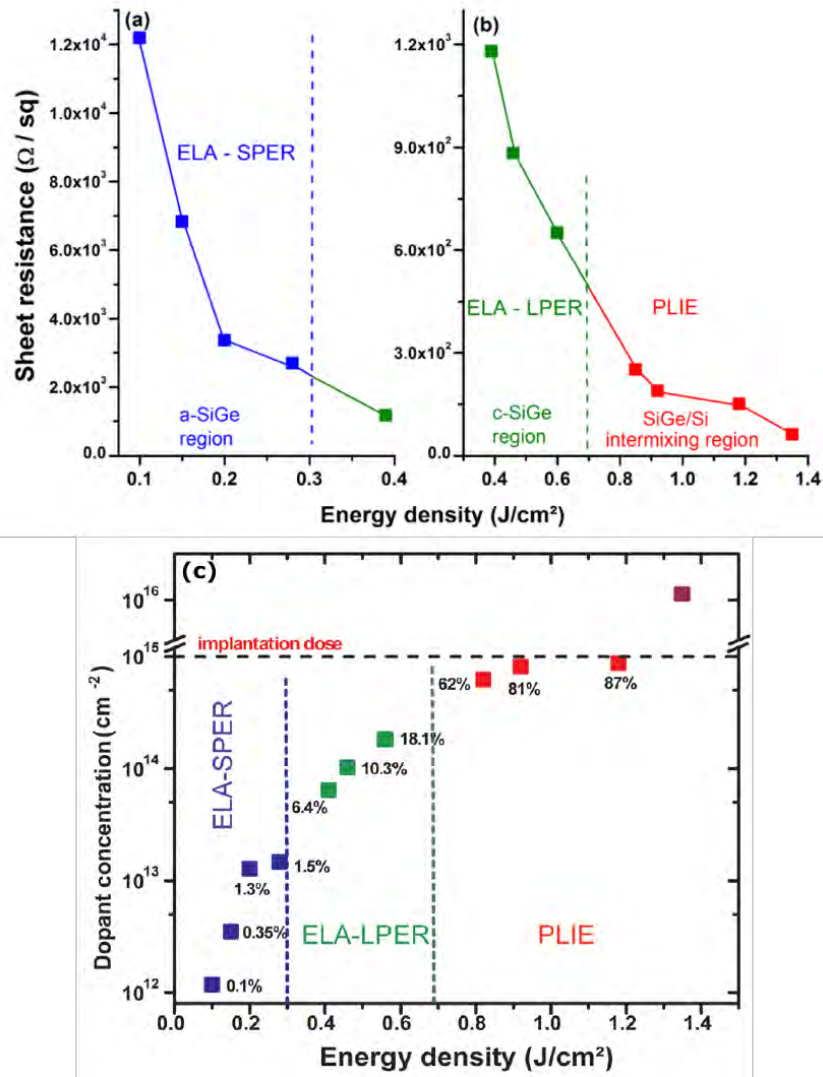


Figure I - 41. Evolution of the sheet resistance (a),(b) and active dopant dose (c) with increasing energy density, for an As implanted  $\text{Si}_{0.64}\text{Ge}_{0.36}$  layer annealed with a KrF laser (20 ns pulse duration). The graphs indicate the various regimes: below  $0.3 \text{ J}/\text{cm}^2$ , only the amorphous layer melts. Between  $0.3$  and  $0.7 \text{ J}/\text{cm}^2$ , the melt depth is within the crystalline SiGe layer. Finally, full SiGe layer melt is reached at  $0.7 \text{ J}/\text{cm}^2$  [95]

The second part of this work therefore is dedicated to the study of dopants activation and segregation within  $\text{Si}_{1-x}\text{Ge}_x$  layers submitted to UV-NLA, and how these characteristics are influenced by the laser annealing regimes encountered. Additional furnace annealing was used to understand the layers stability with thermal budget. First estimations of the doping efficiency are performed with sheet resistance measurements, with a deeper understanding provided by Hall Effect measurements and TEM observations. Once again, morphological observations (chemical profiles, strain state, surface morphology) are required to understand the layer state after UV-NLA.

## CONCLUSION

This chapter first focused on MOSFET transistors and their evolution toward shorter dimensions in order to satisfy cost and performance requirements. The shrinking has required numerous adaptations in both architecture of devices and materials used to limit parasitic effects. One of these implementations was the use of strained  $\text{Si}_{1-x}\text{Ge}_x$  in source and drain regions, therefore straining the Si channel and improving the carrier mobility in both channel and junctions. The junctions should however be highly doped to satisfy the electrical requirements and decrease the contact resistivity, while becoming ultra-thin. Annealing processes have therefore evolved toward shorter timescales to limit dopant depth diffusion and nowadays reach the sub-microsecond scale with Nanosecond Laser Annealing.

This method relies on the absorption of light emitted by a pulsed laser source, that excites the material carriers and heats the near surface region in less than a few nanoseconds, and has been extensively studied on Si and Ge. This type of annealing is considered quasi-adiabatic and causes strong temperature gradients, with high temperatures in the first nanometers of the material. It was shown to cause surface melting in semiconductor layers, with characteristics highly dependent on the material nature, the laser pulse duration, its wavelength and the incident energy density. It has been shown that monocrystalline layers were formed with NLA under specific conditions related to material nature, pulse duration and pulse wavelength in particular, and that ideal box-like profiles could be obtained for dopants with activation levels above the solid solubility limit for boron and phosphorus. These dopants however risk deactivating with further annealing at high temperatures.

NLA on  $\text{Si}_{1-x}\text{Ge}_x$  was shown to cause germanium segregation leading to high Ge concentrations near the surface, and presented sheet resistance and activation evolution similar to what was observed for Si or Ge. This knowledge however remains superficial, as the relaxation of layers and its impact on the electrical properties, as well as dopant deactivation, has barely been studied yet.

The following work focuses on the impact of UV-NLA on  $\text{Si}_{1-x}\text{Ge}_x$  layers. A first section is dedicated to the detection of the various annealing regimes on both crystalline and amorphous layers, using multiple characterizations tools, such as Haze, Atomic Force Microscopy and Secondary Ion Mass Spectrometry. It then focuses on the evolution of strain and its possible relaxation with the annealing regimes, and aims to offer a unified understanding of the mechanisms leading to defect formation during UV-NLA. This is performed with X-ray diffraction and Transmission Electron Microscopy measurements. The last section of this work addresses boron activation in  $\text{Si}_{1-x}\text{Ge}_x$  layers submitted to UV-NLA, and its subsequent deactivation with additional furnace annealing. These studies rely on sheet resistance and hall effect measurements.

KEY INFORMATION

EVOLUTIONS IN DEVICES

1. Strained SiGe junctions

- ➔ SiGe in source and drain regions
  - Higher mobilities
  - Tensile strain within the Si channel

2. Short annealing processes

- ➔ High doping levels required in Ultra-Shallow Junctions
  - Need to limit depth diffusion
  - Short anneals at high temperature to activate dopants

NANOSECOND LASER ANNEALING

1. A selective method

- ➔ Limited heat diffusion due to extremely short anneal duration
  - High temperature at surface sufficient to melt
  - No substrate heating

- ➔ Laser parameters: pulse duration, wavelength, scan mode and repetition modes

2. Morphology

- ➔ Impacted by seed crystallinity and regrowth velocity
  - Monocrystal for a monocrystalline seed
  - Polycrystalline/Nanocrystalline for an amorphous seed

3. Dopant activation

- ➔ Improves dopant activation above solubility limits
  - Box-like profile
  - Possible deactivation

IMPACT ON SIGE ALLOYS

1. Germanium segregation

- ➔ High Ge contents near the surface
  - Beneficial for contact formation
  -

2. Relaxation origin

- ➔ Likely related to Ge content
  - No clear consensus : very disparate observations

3. Dopant activation

- ➔ Seems to improve with laser energy density
  - Still incomplete for B and Ga
  - Limited fundamental understanding

- ➔ Lack of knowledge on thermal stability

Footprint reduction drives the evolution of MOSFET devices

Reduce the thermal budget with pulse duration below the microsecond

Form highly doped ultra-shallow SiGe junctions

## BIBLIOGRAPHY

- [1] D. Kahng, ELECTRIC FIELD CONTROLLED SEMICONDUCTOR DEVICE, US3102230, n.d.
- [2] K.F. Brennan, *The Physics of Semiconductors: With Applications to Optoelectronic Devices*, 1st ed., Cambridge University Press, 1999. <https://doi.org/10.1017/CBO9781139164214>.
- [3] G.E. Moore, Progress in digital integrated electronics [Technical literature, Copyright 1975 IEEE. Reprinted, with permission. Technical Digest. International Electron Devices Meeting, IEEE, 1975, pp. 11-13.], IEEE Solid-State Circuits Society Newsletter. (2006). <https://doi.org/10.1109/N-SSC.2006.4804410>.
- [4] H. Radamson, L. Thylén, *Moore's Law for Photonics and Electronics*, in: *Monolithic Nanoscale Photonics–Electronics Integration in Silicon and Other Group IV Elements*, Elsevier, 2015: pp. 121–150. <https://doi.org/10.1016/B978-0-12-419975-0.00004-0>.
- [5] International Technology Roadmap for Semiconductors 2.0, 2015. [https://www.semiconductors.org/wp-content/uploads/2018/06/0\\_2015-ITRS-2.0-Executive-Report-1.pdf](https://www.semiconductors.org/wp-content/uploads/2018/06/0_2015-ITRS-2.0-Executive-Report-1.pdf) (accessed October 5, 2020).
- [6] B. Colombeau, B. Guo, H.-J. Gossmann, F. Khaja, N. Pradhan, A. Waite, K.V. Rao, C. Thomidis, K.-H. Shim, T. Henry, N. Variam, *Advanced CMOS devices: Challenges and implant solutions*, *Physica Status Solidi (a)*. 211 (2014) 101–108. <https://doi.org/10.1002/pssa.201300169>.
- [7] H. Radamson, L. Thylén, *Metal Oxide Semiconductor Field Effect Transistors*, in: *Monolithic Nanoscale Photonics–Electronics Integration in Silicon and Other Group IV Elements*, Elsevier, 2015: pp. 1–61. <https://doi.org/10.1016/B978-0-12-419975-0.00001-5>.
- [8] S.E. Thompson, M. Armstrong, C. Auth, S. Cea, R. Chau, G. Glass, T. Hoffman, J. Klaus, Z. Ma, B. McIntyre, A. Murthy, B. Obradovic, L. Shifren, S. Sivakumar, S. Tyagi, T. Ghani, K. Mistry, M. Bohr, Y. El-Mansy, *A Logic Nanotechnology Featuring Strained-Silicon*, *IEEE Electron Device Lett.* 25 (2004) 191–193. <https://doi.org/10.1109/LED.2004.825195>.
- [9] S.E. Thompson, M. Armstrong, C. Auth, M. Alavi, M. Buehler, R. Chau, S. Cea, T. Ghani, G. Glass, T. Hoffman, C.-H. Jan, C. Kenyon, J. Klaus, K. Kuhn, Z. Ma, B. McIntyre, K. Mistry, A. Murthy, B. Obradovic, R. Nagisetty, P. Nguyen, S. Sivakumar, R. Shaheed, L. Shifren, B. Tufts, S. Tyagi, M. Bohr, Y. El-Mansy, *A 90-nm Logic Technology Featuring Strained-Silicon*, *IEEE Trans. Electron Devices.* 51 (2004) 1790–1797. <https://doi.org/10.1109/TED.2004.836648>.
- [10] C. Auth, C. Allen, A. Blattner, D. Bergstrom, M. Brazier, M. Bost, M. Buehler, V. Chikarmane, T. Ghani, T. Glassman, R. Grover, W. Han, D. Hanken, M. Hattendorf, P. Hentges, R. Heussner, J. Hicks, D. Ingerly, P. Jain, S. Jaloviar, R. James, D. Jones, J. Jopling, S. Joshi, C. Kenyon, H. Liu, R. McFadden, B. McIntyre, J. Neiryneck, C. Parker, L. Pipes, I. Post, S. Pradhan, M. Prince, S. Ramey, T. Reynolds, J. Roesler, J. Sandford, J. Seiple, P. Smith, C. Thomas, D. Towner, T. Troeger, C. Weber, P. Yashar, K. Zawadzki, K. Mistry, *A 22nm high performance and low-power CMOS technology featuring fully-depleted tri-gate transistors, self-aligned contacts and high density MIM capacitors*, in: *2012 Symposium on VLSI Technology (VLSIT)*, IEEE, Honolulu, HI, USA, 2012: pp. 131–132. <https://doi.org/10.1109/VLSIT.2012.6242496>.
- [11] J.-P. Noel, *Optimisation de dispositifs FDSOI pour la gestion de la consommation et de la vitesse: application aux mémoires et fonctions logiques*, (n.d.) 205.

- [12] P. Batude, B. Sklenard, C. Fenouillet-Beranger, B. Previtali, C. Tabone, O. Rozeau, O. Billoint, O. Turkyilmaz, H. Sarhan, S. Thuries, G. Cibrario, L. Brunet, F. Deprat, J.E. Michallet, F. Clermidy, M. Vinet, 3D sequential integration opportunities and technology optimization, in: IEEE International Interconnect Technology Conference, 2014: pp. 373–376. <https://doi.org/10.1109/IITC.2014.6831837>.
- [13] P. Batude, T. Ernst, J. Arcamone, G. Arndt, P. Coudrain, P.E. Gaillardon, 3-D Sequential Integration: A Key Enabling Technology for Heterogeneous Co-Integration of New Function With CMOS, IEEE Journal on Emerging and Selected Topics in Circuits and Systems. 2 (2012) 714–722. <https://doi.org/10.1109/JETCAS.2012.2223593>.
- [14] J.M. Hartmann, A. Abbadie, S. Favier, Critical thickness for plastic relaxation of SiGe on Si(001) revisited, Journal of Applied Physics. 110 (2011) 083529. <https://doi.org/10.1063/1.3656989>.
- [15] R. People, J.C. Bean, Calculation of critical layer thickness versus lattice mismatch for  $\text{Ge}_x\text{Si}_{1-x}/\text{Si}$  strained-layer heterostructures, Appl. Phys. Lett. 47 (1985) 322–324. <https://doi.org/10.1063/1.96206>.
- [16] D.C. Houghton, Strain relaxation kinetics in  $\text{Si}_{1-x}\text{Ge}_x/\text{Si}$  heterostructures, Journal of Applied Physics. 70 (1991) 2136–2151. <https://doi.org/10.1063/1.349451>.
- [17] D.V. Lang, R. People, C. Bean, A.M. Sergent, Measurement of the band gap of  $\text{Ge}_x\text{Si}_{1-x}/\text{Sn}$  strained-layer heterostructures, (n.d.) 3.
- [18] M.E. Levinshstein, S.L. Rumyantsev, M. Shur, Properties of advanced semiconductor materials: GaN, AlN, InN, BN, SiC, SiGe, Wiley, New York, 2001.
- [19] R. Braunstein, A.R. Moore, F. Herman, Intrinsic Optical Absorption in Germanium-Silicon Alloys, Phys. Rev. 109 (1958) 695–710. <https://doi.org/10.1103/PhysRev.109.695>.
- [20] C.D. Hansen, C.R. Johnson, Visualization handbook, Elsevier, 2011.
- [21] T. Manku, J.M. McGregor, A. Nathan, D.J. Roulston, J.-Noel, D.C. Houghton, Drift hole mobility in strained and unstrained doped  $\text{Si}_{1-x}\text{Ge}_x/\text{Si}$  alloys, IEEE Transactions on Electron Devices. 40 (1993) 1990–1996. <https://doi.org/10.1109/16.239739>.
- [22] M. Gavelle, Etude expérimentale de l'interdiffusion Ge-Si à partir de sources solides Germanium sur Silicium. Application à la formation de couches graduelles  $\text{Si}_{1-x}\text{Ge}_x$  pour les transistors pMOSFETs, n.d.
- [23] P.M. Mooney, Strain relaxation and dislocations in SiGe/Si structures, Materials Science and Engineering: R: Reports. 17 (1996) 105–146. [https://doi.org/10.1016/S0927-796X\(96\)00192-1](https://doi.org/10.1016/S0927-796X(96)00192-1).
- [24] M.J. Hurley, D. Gottuk, J.R. Hall, K. Harada, E. Kuligowski, M. Puchovsky, J. Torero, J.M. Watts, C. Wiczorek, eds., SFPE Handbook of Fire Protection Engineering, Springer New York, New York, NY, 2016. <https://doi.org/10.1007/978-1-4939-2565-0>.
- [25] H.W. Kennel, M.D. Giles, M. Diebel, P.H. Keys, J. Hwang, S. Govindaraju, M. Liu, A. Budrevich, Kinetics of Shallow Junction Activation: Physical Mechanisms, in: 2006 14th IEEE International Conference on Advanced Thermal Processing of Semiconductors, IEEE, Kyoto, 2006: pp. 85–91. <https://doi.org/10.1109/RTP.2006.367986>.
- [26] F. Cristiano, Ion Implantation-Induced extended defects: structural investigations and impact on Ultra-Shallow Junction properties, (n.d.) 127.

- [27] L. Pelaz, G.H. Gilmer, H.-J. Gossmann, C.S. Rafferty, M. Jaraiz, J. Barbolla, B cluster formation and dissolution in Si: A scenario based on atomistic modeling, *Appl. Phys. Lett.* 74 (1999) 3657–3659. <https://doi.org/10.1063/1.123213>.
- [28] M. Aboy, L. Pelaz, E. Bruno, S. Mirabella, S. Boninelli, Kinetics of large B clusters in crystalline and preamorphized silicon, *Journal of Applied Physics.* 110 (2011) 073524. <https://doi.org/10.1063/1.3639280>.
- [29] L. Rebohle, Introduction, in: *Flash Lamp Annealing*, Springer International Publishing, Cham, 2019: pp. 1–14. [https://doi.org/10.1007/978-3-030-23299-3\\_1](https://doi.org/10.1007/978-3-030-23299-3_1).
- [30] A.T. Fiory, Rapid thermal processing for silicon nanoelectronics applications, *JOM.* 57 (2005) 21–26. <https://doi.org/10.1007/s11837-005-0131-0>.
- [31] P. Liang, P. Han, F. Yujie, Y. Xing, Annealing studies of boron implanted emitters for n-silicon solar cells, *Semicond. Sci. Technol.* 29 (2014) 035011. <https://doi.org/10.1088/0268-1242/29/3/035011>.
- [32] S.K. Sundaram, E. Mazur, Inducing and probing non-thermal transitions in semiconductors using femtosecond laser pulses, *Nature Materials.* 1 (2002) 217–224. <https://doi.org/10.1038/nmat767>.
- [33] P. Brüesch, *Phonons: Theory and Experiments I*, Springer Berlin Heidelberg, Berlin, Heidelberg, 1982. <https://doi.org/10.1007/978-3-642-81781-6>.
- [34] P. Baeri, E. Rimini, Laser annealing of silicon, *Materials Chemistry and Physics.* 46 (1996) 169–177. [https://doi.org/10.1016/S0254-0584\(97\)80010-7](https://doi.org/10.1016/S0254-0584(97)80010-7).
- [35] A.V. Dvurechenskii, The Energy Pulse-Oriented Crystallization Phenomenon in Solids (Laser Annealing), in: *Advances in Semiconductor Nanostructures*, Elsevier, 2017: pp. 367–381. <https://doi.org/10.1016/B978-0-12-810512-2.00015-9>.
- [36] J. Venturini, M. Hernandez, G. Kerrien, C. Laviron, D. Camel, J.L. Santailier, T. Sarnet, J. Boulmer, Excimer laser thermal processing of ultra-shallow junction: laser pulse duration, *Thin Solid Films.* 453–454 (2004) 145–149. <https://doi.org/10.1016/j.tsf.2003.11.087>.
- [37] A.G. Cullis, H.C. Webber, N.G. Chew, J.M. Poate, P. Baeri, Transitions to defective crystal and the amorphous state induced in elemental Si by laser quenching, *Physical Review Letters.* 49 (1982) 219.
- [38] J.A. Yater, M.O. Thompson, Orientation dependence of laser amorphization of crystal Si, *Phys. Rev. Lett.* 63 (1989) 2088–2091. <https://doi.org/10.1103/PhysRevLett.63.2088>.
- [39] A.G. Cullis, N.G. Chew, H.C. Webber, D.J. Smith, Orientation dependence of high speed silicon crystal growth from the melt, *Journal of Crystal Growth.* 68 (1984) 624–638. [https://doi.org/10.1016/0022-0248\(84\)90469-X](https://doi.org/10.1016/0022-0248(84)90469-X).
- [40] M.O. Thompson, G.J. Galvin, J.W. Mayer, P.S. Peercy, J.M. Poate, D.C. Jacobson, A.G. Cullis, N.G. Chew, Melting Temperature and Explosive Crystallization of Amorphous Silicon during Pulsed Laser Irradiation, *Phys. Rev. Lett.* 52 (1984) 2360–2363. <https://doi.org/10.1103/PhysRevLett.52.2360>.
- [41] S.F. Lombardo, S. Boninelli, F. Cristiano, I. Deretzis, M.G. Grimaldi, K. Huet, E. Napolitani, A. La Magna, Phase field model of the nanoscale evolution during the explosive crystallization phenomenon, *Journal of Applied Physics.* 123 (2018) 105105. <https://doi.org/10.1063/1.5008362>.

- [42] L. Nikolova, M.J. Stern, J.M. MacLeod, B.W. Reed, H. Ibrahim, G.H. Campbell, F. Rosei, T. LaGrange, B.J. Siwick, In situ investigation of explosive crystallization in a-Ge: Experimental determination of the interface response function using dynamic transmission electron microscopy, *Journal of Applied Physics*. 116 (2014) 093512. <https://doi.org/10.1063/1.4894397>.
- [43] C.-C. Kuo, Observation of explosive crystallization during excimer laser annealing using in situ time-resolved optical reflection and transmission measurements, *Journal of Materials Processing Technology*. 209 (2009) 2978–2985. <https://doi.org/10.1016/j.jmatprotec.2008.07.003>.
- [44] P. Acosta-Alba, S. Kerdiles, B. Mathieu, R. Kachtouli, F. Mazzamuto, I. Toque-Tresonne, K. Huet, P. Besson, M. Veillerot, F. Aussenac, C. Fenouillet-Beranger, Nanosecond Laser Annealing for Phosphorous Activation in Ultra-Thin Implanted Silicon-On-Insulator Substrates, in: 2016 21st International Conference on Ion Implantation Technology (IIT), 2016: pp. 1–4. <https://doi.org/10.1109/IIT.2016.7882896>.
- [45] J.P. Garandet, *New Determinations of Diffusion Coefficients for Various Dopants in Liquid Silicon*, (n.d.) 19.
- [46] E.V. Monakhov, B.G. Svensson, M.K. Linnarsson, A.L. Magna, V. Privitera, M. Camalleri, G. Fortunato, L. Mariucci, Excimer laser annealing of shallow As and B doped layers, *Materials Science and Engineering: B*. 114–115 (2004) 352–357. <https://doi.org/10.1016/j.mseb.2004.07.062>.
- [47] M. Shayesteh, D.O. Connell, F. Gity, P. Murphy-Armando, R. Yu, K. Huet, I. Toqué-Tresonne, F. Cristiano, S. Boninelli, H.H. Henrichsen, P.F. Nielsen, D.H. Petersen, R. Duffy, Optimized Laser Thermal Annealing on Germanium for High Dopant Activation and Low Leakage Current, *IEEE Transactions on Electron Devices*. 61 (2014) 4047–4055. <https://doi.org/10.1109/TED.2014.2364957>.
- [48] R. Milazzo, E. Napolitani, G. Impellizzeri, G. Fiscaro, S. Boninelli, M. Cuscunà, D. De Salvador, M. Mastromatteo, M. Italia, A. La Magna, G. Fortunato, F. Priolo, V. Privitera, A. Carnera, N-type doping of Ge by As implantation and excimer laser annealing, *Journal of Applied Physics*. 115 (2014) 053501. <https://doi.org/10.1063/1.4863779>.
- [49] S.F. Lombardo, S. Boninelli, F. Cristiano, G. Fiscaro, G. Fortunato, M.G. Grimaldi, G. Impellizzeri, M. Italia, A. Marino, R. Milazzo, E. Napolitani, V. Privitera, A. La Magna, Laser annealing in Si and Ge: Anomalous physical aspects and modeling approaches, *Materials Science in Semiconductor Processing*. 62 (2017) 80–91. <https://doi.org/10.1016/j.mssp.2016.10.047>.
- [50] L.L. Wang, H. Yu, M. Schaekers, J.L. Everaert, A. Franquet, B. Douhard, L. Date, J. del A. Borniquel, K. Hollar, F.A. Khaja, W. Aderhold, A.J. Mayur, J.Y. Lee, H. van Meer, D. Mocuta, N. Horiguchi, N. Collaert, K.D. Meyer, Y.L. Jiang, Comprehensive study of Ga activation in Si, SiGe and Ge with 5 #x00D7; 10 #x2212;10 #x03A9; #x00B7;cm<sup>2</sup> contact resistivity achieved on Ga doped Ge using nanosecond laser activation, in: 2017 IEEE International Electron Devices Meeting (IEDM), 2017: p. 22.4.1-22.4.4. <https://doi.org/10.1109/IEDM.2017.8268441>.
- [51] R. Reitano, P.M. Smith, M.J. Aziz, Solute trapping of group III, IV, and V elements in silicon by an aperiodic stepwise growth mechanism, *Journal of Applied Physics*. 76 (1994) 1518–1529. <https://doi.org/10.1063/1.357728>.
- [52] D.P. Brunco, M.O. Thompson, D.E. Hoglund, M.J. Aziz, H. -J. Gossmann, Germanium partitioning in silicon during rapid solidification, *Journal of Applied Physics*. 78 (1995) 1575–1582. <https://doi.org/10.1063/1.360251>.

- [53] R. Reitano, P.M. Smith, M.J. Aziz, Trends in Solute Segregation Behavior During Silicon Solidification, MRS Online Proceedings Library Archive. 321 (1993). <https://doi.org/10.1557/PROC-321-479>.
- [54] M. Hackenberg, K. Huet, R. Negru, J. Venturini, G. Fiscaro, A. La Magna, P. Pichler, Modeling boron profiles in silicon after pulsed excimer laser annealing, AIP Conference Proceedings. 1496 (2012) 241–244. <https://doi.org/10.1063/1.4766533>.
- [55] M. Hackenberg, K. Huet, R. Negru, G. Fiscaro, A. La Magna, N. Taleb, M. Quillec, P. Pichler, Simulation of the boron build-up formation during melting laser thermal annealing, Phys. Status Solidi C. 11 (2014) 89–92. <https://doi.org/10.1002/pssc.201300156>.
- [56] P.C. Lill, M. Dahlinger, J.R. Köhler, Boron Partitioning Coefficient above Unity in Laser Crystallized Silicon, Materials. 10 (2017) 189. <https://doi.org/10.3390/ma10020189>.
- [57] K.K. Ong, K.L. Pey, P.S. Lee, A.T.S. Wee, X.C. Wang, Y.F. Chong, Dopant distribution in the recrystallization transient at the maximum melt depth induced by laser annealing, Applied Physics Letters. 89 (2006) 172111. <https://doi.org/10.1063/1.2364834>.
- [58] G. Fiscaro, K. Huet, R. Negru, M. Hackenberg, P. Pichler, N. Taleb, A. La Magna, Anomalous Impurity Segregation and Local Bonding Fluctuation in I-Si, Phys. Rev. Lett. 110 (2013) 117801. <https://doi.org/10.1103/PhysRevLett.110.117801>.
- [59] E.V. Monakhov, B.G. Svensson, M.K. Linnarsson, A. La Magna, M. Italia, V. Privitera, G. Fortunato, M. Cuscunà, L. Mariucci, Boron distribution in silicon after excimer laser annealing with multiple pulses, Materials Science and Engineering: B. 124–125 (2005) 228–231. <https://doi.org/10.1016/j.mseb.2005.08.058>.
- [60] E.V. Monakhov, B.G. Svensson, A. La Magna, P. Alippi, M. Italia, V. Privitera, G. Fortunato, L. Mariucci, F. Tumisto, K. Kuitunen, Excimer Laser Annealing of Ion-Implanted Silicon: Dopant Activation, Diffusion and Defect Formation, in: 2007 15th International Conference on Advanced Thermal Processing of Semiconductors, IEEE, Cannizzaro, Catania, Italy, 2007: pp. 31–35. <https://doi.org/10.1109/RTP.2007.4383815>.
- [61] G. Impellizzeri, E. Napolitani, R. Milazzo, S. Boninelli, M. Cuscunà, G. Fiscaro, A. La Magna, G. Fortunato, F. Priolo, V. Privitera, Role of oxygen on the electrical activation of B in Ge by excimer laser annealing, Phys. Status Solidi A. 211 (2014) 122–125. <https://doi.org/10.1002/pssa.201300308>.
- [62] G. Impellizzeri, E. Napolitani, S. Boninelli, G. Fiscaro, M. Cuscunà, R. Milazzo, A.L. Magna, G. Fortunato, F. Priolo, V. Privitera, B-doping in Ge by excimer laser annealing, Journal of Applied Physics. 113 (2013) 113505. <https://doi.org/10.1063/1.4795268>.
- [63] R. Milazzo, G. Impellizzeri, D. Piccinotti, A. La Magna, G. Fortunato, D. De Salvador, A. Carnera, A. Portavoce, D. Mangelinck, V. Privitera, E. Napolitani, Impurity and defect interactions during laser thermal annealing in Ge, Journal of Applied Physics. 119 (2016) 045702. <https://doi.org/10.1063/1.4940737>.
- [64] A.G. Cullis, H.C. Webber, N.G. Chew, Correlation of the structure and electrical properties of ion-implanted and laser-annealed silicon, Applied Physics Letters. 36 (1980) 547–550. <https://doi.org/10.1063/1.91575>.
- [65] G. Kerrien, M. Hernandez, C. Laviron, T. Sarnet, D. Débarre, T. Noguchi, D. Zahorski, J. Venturini, M.N. Semeria, J. Boulmer, Optical characterization of laser processed ultra-shallow junctions, Applied Surface Science. 208–209 (2003) 277–284. [https://doi.org/10.1016/S0169-4332\(02\)01354-5](https://doi.org/10.1016/S0169-4332(02)01354-5).

- [66] F. Cristiano, Y. Qiu, E. Bedel-Pereira, K. Huet, F. Mazzamuto, G. Fisicaro, A.L. Magna, M. Quillec, N. Cherkashin, H. Wang, S. Duguay, D. Blavette, Extended defects in ion-implanted Si during nanosecond laser annealing, in: 2014 International Workshop on Junction Technology (IWJT), 2014: pp. 1–6. <https://doi.org/10.1109/IWJT.2014.6842019>.
- [67] A. Bhaduri, T. Kociniewski, F. Fossard, J. Boulmer, D. Débarre, Optical and electrical properties of laser doped Si:B in the alloy range, *Applied Surface Science*. 258 (2012) 9228–9232. <https://doi.org/10.1016/j.apsusc.2011.10.077>.
- [68] G. Kerrien, T. Sarnet, D. Débarre, J. Boulmer, M. Hernandez, C. Laviron, M.-N. Semeria, Gas immersion laser doping (GILD) for ultra-shallow junction formation, *Thin Solid Films*. 453–454 (2004) 106–109. <https://doi.org/10.1016/j.tsf.2003.11.151>.
- [69] L. Romano, A.M. Piro, V. Privitera, E. Rimini, G. Fortunato, B.G. Svensson, M. Foad, M.G. Grimaldi, Mechanism of de-activation and clustering of B in Si at extremely high concentration, *Nuclear Instruments and Methods in Physics Research Section B: Beam Interactions with Materials and Atoms*. 253 (2006) 50–54. <https://doi.org/10.1016/j.nimb.2006.10.012>.
- [70] Y. Takamura, S.H. Jain, P.B. Griffin, J.D. Plummer, Thermal stability of dopants in laser annealed silicon, *Journal of Applied Physics*. 92 (2002) 230–234. <https://doi.org/10.1063/1.1481975>.
- [71] R.T. Young, J. Narayan, Laser annealing of diffusion-induced imperfections in silicon, *Appl. Phys. Lett.* 33 (1978) 14–16. <https://doi.org/10.1063/1.90164>.
- [72] S. Solmi, E. Landi, F. Baruffaldi, High-concentration boron diffusion in silicon: Simulation of the precipitation phenomena, *Journal of Applied Physics*. 68 (1990) 3250–3258. <https://doi.org/10.1063/1.346376>.
- [73] F.A. Trumbore, Solid solubilities of impurity elements in germanium and silicon, *The Bell System Technical Journal*. 39 (1960) 205–233. <https://doi.org/10.1002/j.1538-7305.1960.tb03928.x>.
- [74] V.E. Borisenko, S.G. Yudin, Steady-state solubility of substitutional impurities in silicon, *Physica Status Solidi (a)*. 101 (1987) 123–127.
- [75] G. Fisicaro, L. Pelaz, M. Aboy, P. Lopez, M. Italia, K. Huet, F. Cristiano, Z. Essa, Q. Yang, E. Bedel-Pereira, M. Quillec, A. La Magna, Kinetic Monte Carlo simulations of boron activation in implanted Si under laser thermal annealing, *Appl. Phys. Express*. 7 (2014) 021301. <https://doi.org/10.7567/APEX.7.021301>.
- [76] Y. Takamura, P.B. Griffin, J.D. Plummer, Physical processes associated with the deactivation of dopants in laser annealed silicon, *Journal of Applied Physics*. 92 (2002) 235–244. <https://doi.org/10.1063/1.1481974>.
- [77] S.R. Wilson, W.M. Paulson, R.B. Gregory, G. Tam, C.W. White, B.R. Appleton, A.K. Rai, P.P. Pronko, Thermal stability of electrically active dopants in laser annealed silicon films, *Journal of Applied Physics*. 54 (1983) 5004–5013. <https://doi.org/10.1063/1.332768>.
- [78] H. Shin, M. Lee, E. Ko, H. Ryu, S. Park, E. Kim, D.-H. Ko, Dopant Activation of In Situ Phosphorus-Doped Silicon Using Multi-Pulse Nanosecond Laser Annealing, *Physica Status Solidi (a)*. 217 (2020) 1900988. <https://doi.org/10.1002/pssa.201900988>.
- [79] E. Rosseel, S.K. Dhayalan, A.Y. Hikavy, R. Loo, H.B. Profijt, D. Kohen, S. Kubicek, T. Chiarella, H. Yu, N. Horiguchi, D. Mocuta, K. Barla, A. Thean, G. Bartlett, J. Margetis, N. Bhargava, J. Tolle, Selective Epitaxial Growth of High-P Si:P for Source/Drain Formation in

- Advanced Si nFETs, ECS Transactions. 75 (2016) 347–359. <https://doi.org/10.1149/07508.0347ecst>.
- [80] R.-D. Chang, C.-H. Lin, Activation and deactivation of phosphorus in silicon-on-insulator substrates, *Materials Science in Semiconductor Processing*. 42 (2016) 219–222. <https://doi.org/10.1016/j.mssp.2015.09.008>.
- [81] Y. Takamura, A. Vaillonis, A.F. Marshall, P.B. Griffin, J.D. Plummer, Dopant deactivation in heavily Sb doped Si (001): A high-resolution x-ray diffraction and transmission electron microscopy study, *Journal of Applied Physics*. 92 (2002) 5503–5507. <https://doi.org/10.1063/1.1510953>.
- [82] W. Luo, S. Yang, P. Clancy, M.O. Thompson, Deactivation kinetics of supersaturated boron:silicon alloys, *Journal of Applied Physics*. 90 (2001) 2262–2268. <https://doi.org/10.1063/1.1385360>.
- [83] T.-K. Chang, F.-T. Chu, C.-W. Lin, C.-H. Tseng, H.-C. Cheng, A novel germanium doping method for fabrication of high-performance p-channel poly-Si<sub>1-x</sub>Ge<sub>x</sub> TFT by excimer laser crystallization, *IEEE Electron Device Letters*. 24 (2003) 233–235. <https://doi.org/10.1109/TCSI.2003.811423>.
- [84] T. Kociniewski, F. Fossard, J. Boulmer, D. Bouchier, Synthesis of strained SiGe on Si(100) by pulsed laser induced epitaxy, *Thin Solid Films*. 518 (2010) 2542–2545. <https://doi.org/10.1016/j.tsf.2009.09.154>.
- [85] S. Lombardo, P.M. Smith, M.J. Uttormark, D.P. Brunco, K. Kramer, M.O. Thompson, Demonstration of laser-assisted epitaxial deposition of Ge<sub>x</sub>Si<sub>1-x</sub> alloys on single-crystal Si, *Appl. Phys. Lett.* 58 (1991) 1768–1770. <https://doi.org/10.1063/1.105085>.
- [86] A. Slaoui, C. Deng, S. Talwar, J. Kramer, T.W. Sigmon, Slaoui1994; Fabrication and doping of poly-SiGe using excimer-laser processing, *Applied Physics A: Materials Science & Processing*. 59 (1994) 203–207.
- [87] R. Larciprete, M.G. Grimaldi, E. Borsella, S. Cozzi, S. Martelli, S. Pieretti, I. Vianey, Larciprete1998; KrF laser epitaxy of silicon germanium alloy layers by irradiation of Si(1-x)Ge<sub>x</sub>/Si (100) structures, *Journal of Vacuum Science & Technology B: Microelectronics and Nanometer Structures Processing, Measurement, and Phenomena*. 16 (1998) 1589–1594. <https://doi.org/10.1116/1.589944>.
- [88] C.Y. Ong, K.L. Pey, X. Li, X.C. Wang, C.M. Ng, L. Chan, Laser annealing induced high Ge concentration epitaxial SiGe layer in Si<sub>1-x</sub>Ge<sub>x</sub> virtual substrate, *Appl. Phys. Lett.* 93 (2008) 041112. <https://doi.org/10.1063/1.2962991>.
- [89] T. Tabata, J. Aubin, K. Huet, F. Mazzamuto, Segregation and activation of Ga in high Ge content SiGe by UV melt laser anneal, *Journal of Applied Physics*. 125 (2019). <https://doi.org/10.1063/1.5096889>.
- [90] K. Huet, F. Mazzamuto, T. Tabata, I. Toqué-Tresonne, Y. Mori, Doping of semiconductor devices by Laser Thermal Annealing, *Materials Science in Semiconductor Processing*. 62 (2017) 92–102. <https://doi.org/10.1016/j.mssp.2016.11.008>.
- [91] K. Huet, J. Aubin, P.-E. Raynal, B. Curvers, A. Verstraete, B. Lespinasse, F. Mazzamuto, A. Sciuto, S.F. Lombardo, A. La Magna, P. Acosta-Alba, L. Dagault, C. Licitra, J.-M. Hartmann, S. Kerdilès, Pulsed laser annealing for advanced technology nodes: Modeling and calibration, *Applied Surface Science*. (2019) 144470. <https://doi.org/10.1016/j.apsusc.2019.144470>.

- [92] K. Huet, G. Fiscaro, J. Venturini, H. Besaucèle, A. La Magna, Defect kinetics and dopant activation in submicrosecond laser thermal processes, *Appl. Phys. Lett.* 95 (2009) 231901. <https://doi.org/10.1063/1.3268472>.
- [93] C.N. Ni, Y.C. Huang, S. Jun, S. Sun, A. Vyas, F. Khaja, K.V. Rao, S. Sharma, N. Breil, M. Jin, C. Lazik, A. Mayur, J. Gelatos, H. Chung, R. Hung, M. Chudzik, N. Yoshida, N. Kim, PMOS contact resistance solution compatible to CMOS integration for 7 nm node and beyond, in: 2016 International Symposium on VLSI Technology, Systems and Application (VLSI-TSA), 2016: pp. 1–2. <https://doi.org/10.1109/VLSI-TSA.2016.7480531>.
- [94] G. Fiscaro, A. La Magna, G. Piccitto, V. Privitera, Laser annealing of SiGe and Ge based devices, *Microelectronic Engineering.* 88 (2011) 488–491. <https://doi.org/10.1016/j.mee.2010.09.014>.
- [95] G.V. Luong, S. Wirths, S. Stefanov, B. Holländer, J. Schubert, J.C. Conde, T. Stoica, U. Breuer, S. Chiussi, M. Goryll, D. Buca, S. Mantl, Study of dopant activation in biaxially compressively strained SiGe layers using excimer laser annealing, *Journal of Applied Physics.* 113 (2013) 204902. <https://doi.org/10.1063/1.4807001>.
- [96] S. Sedky, M. Gromova, T. Van der Donck, J.-P. Celis, A. Witvrouw, Characterization of KrF excimer laser annealed PECVD Si<sub>1-x</sub>Ge<sub>x</sub> for MEMS post-processing, *Sensors and Actuators A: Physical.* 127 (2006) 316–323. <https://doi.org/10.1016/j.sna.2006.01.035>.
- [97] O. Gluschenkov, H. Wu, K. Brew, C. Niu, L. Yu, Y. Sulehria, S. Choi, C. Durfee, J. Demarest, A. Carr, S. Chen, J. Willis, T. Thanigaivelan, F. Lie, W. Kleemeier, D. Guo, External Resistance Reduction by Nanosecond Laser Anneal in Si/SiGe CMOS Technology, in: 2018 IEEE International Electron Devices Meeting (IEDM), 2018: p. 35.3.1-35.3.4. <https://doi.org/10.1109/IEDM.2018.8614628>.
- [98] E.J. Albenze, M.O. Thompson, P. Clancy, Molecular Dynamics Study of Explosive Crystallization of SiGe and Boron-Doped SiGe Alloys, *Ind. Eng. Chem. Res.* 45 (2006) 5628–5639. <https://doi.org/10.1021/ie051361w>.
- [99] Q. Yu, M.O. Thompson, P. Clancy, Solidification kinetics in SiGe alloys, *Phys. Rev. B.* 53 (1996) 8386–8397. <https://doi.org/10.1103/PhysRevB.53.8386>.
- [100] L. Vincent, F. Fossard, T. Kociniewski, L. Largeau, N. Cherkashin, M.J. Hÿtch, D. Debarre, T. Sauvage, A. Claverie, J. Boulmer, D. Bouchier, Nanoscale concentration and strain distribution in pseudomorphic films Si<sub>1-x</sub>Ge<sub>x</sub>/Si processed by pulsed laser induced epitaxy, *Applied Surface Science.* 258 (2012) 9208–9212. <https://doi.org/10.1016/j.apsusc.2011.07.074>.
- [101] F. Liu, H.S. Wong, K.W. Ang, M. Zhu, X. Wang, D.M.Y. Lai, P.C. Lim, Y.C. Yeo, Laser Annealing of Amorphous Germanium on SiliconGermanium Source/Drain for Strain and Performance Enhancement in pMOSFETs, *IEEE Electron Device Letters.* 29 (2008) 885–888. <https://doi.org/10.1109/LED.2008.2001029>.
- [102] N. Frangis, J. Van Landuyt, R. Larciprete, S. Martelli, E. Borsella, S. Chiussi, J. Castro, B. León, High resolution electron microscopy and x-ray photoelectron spectroscopy studies of heteroepitaxial Si<sub>1-x</sub>Ge<sub>x</sub> alloys produced through laser induced processing, *Applied Physics Letters.* 72 (1998) 2877–2879. <https://doi.org/10.1063/1.121487>.
- [103] K. -Josef Kramer, S. Talwar, T.W. Sigmon, K.H. Weiner, Crystallinity, strain, and thermal stability of heteroepitaxial Si<sub>1-x</sub>Ge<sub>x</sub>/Si (100) layers created using pulsed laser induced epitaxy, *Appl. Phys. Lett.* 61 (1992) 769–771. <https://doi.org/10.1063/1.107793>.

- [104] J.L. Everaert, M. Schaekers, H. Yu, L.L. Wang, A. Hikavy, L. Date, J. del A. Borniquel, K. Hollar, F.A. Khaja, W. Aderhold, A.J. Mayur, J.Y. Lee, H. van Meer, Y.L. Jiang, K.D. Meyer, D. Mocuta, N. Horiguchi, Sub-10E-9 Ohm.cm<sup>2</sup> contact resistivity on p-SiGe achieved by Ga doping and nanosecond laser activation, in: 2017 Symposium on VLSI Technology, 2017: pp. T214–T215. <https://doi.org/10.23919/VLSIT.2017.7998176>.
- [105] C.Y. Ong, K.L. Pey, K.K. Ong, D.X.M. Tan, X.C. Wang, H.Y. Zheng, C.M. Ng, L. Chan, A low-cost method of forming epitaxy SiGe on Si substrate by laser annealing, *Applied Physics Letters*. 94 (2009) 082104. <https://doi.org/10.1063/1.3086881>.
- [106] T. Tabata, J. Aubin, K. Huet, F. Mazzamuto, Y. Mori, A.L. Magna, L.M. Rubin, P. Kopalidis, H. Tsai, D. Roh, R. Reece, Super Activation of Highly Surface Segregated Dopants in High Ge Content SiGe Obtained by Melt UV Laser Annealing, in: 2018 22nd International Conference on Ion Implantation Technology (IIT), 2018: pp. 353–356. <https://doi.org/10.1109/IIT.2018.8807912>.
- [107] C.Y. Chang, F.A. Khaja, K.E. Hollar, K.V. Rao, C. Lazik, M. Jin, H. Zhou, R. Hung, Y.C. Huang, H. Chung, A. Mayur, N. Kim, Ultra-low (1.2E-9 ohmcm<sup>2</sup>) p-Si<sub>0.55</sub>Ge<sub>0.45</sub> contact resistivity using nanosecond laser anneal for 7nm nodes and beyond, in: 2017 17th International Workshop on Junction Technology (IWJT), 2017: pp. 23–26. <https://doi.org/10.23919/IWJT.2017.7966504>.

---



# CHAPTER II

## LASER ANNEALING ON SiGe : SAMPLES FABRICATION AND CHARACTERIZATION

I - NANOSECOND LASER ANNEALING TOOL : SCREEN LT-3100.....	54
1. Tool description .....	54
2. Laser annealing conditions.....	56
II - Si AND SiGe SAMPLES .....	57
III - CHARACTERIZATION METHODS.....	59
1. In-situ Time Resolved Reflectivity (TRR) .....	59
3. Surface Characterizations .....	62
a) Haze measurements .....	62
b) Atomic Force Microscopy (AFM).....	63
4. Crystalline quality assessment .....	65
a) Strain and crystallinity measurements by XRD .....	65
b) Structure observations via Transmission Electron Microscopy.....	70
5. Composition and concentration profiles.....	72
a) Secondary Ion Mass Spectrometry (SIMS) .....	72
b) Energy Dispersive X-Ray Analysis (EDX) .....	73
6. Electrical Characterizations.....	74
a) Sheet resistance by Four-Point-Probe .....	74
b) Hall effect measurements .....	75
IV – NUMERICAL SIMULATIONS.....	77
1. LIAB software .....	77
a) Simulation Model .....	77
b) Structures and solvers for Si <sub>1-x</sub> Ge <sub>x</sub> simulations .....	78
2. Segregation and elastic energy .....	78
CONCLUSION .....	82
KEY INFORMATION .....	83
BIBLIOGRAPHY .....	84

## CHAPTER II

# LASER ANNEALING ON SiGe : SAMPLES FABRICATION AND CHARACTERIZATION

This chapter aims to present the experimental procedure for the study of the SiGe samples from their fabrication to their UV nanosecond laser annealing (UV-NLA) treatment, as well as the multiple characterization methods that were used to extract information on their initial and final state after nanosecond laser annealing. Various characterizations were performed, aiming to gain an overview of the samples chemical composition via SIMS and EDX measurements, strain state with X-ray diffraction analysis and electrical performances with sheet resistance and hall effect measurements. Transmission electron microscopy observations were performed on multiple samples. Numerical simulations were used as a comparison mean with experimental data.

### I - NANOSECOND LASER ANNEALING TOOL : SCREEN LT-3100

The nanosecond laser annealing system used during this work is described in the following section. As the theoretical background for this method was described in Chapter I, only the specificities of the tool used are presented, including the optical line and pulse properties.

#### 1. Tool description

UV-NLA was performed with an industrial LT-3100 tool from SCREEN. The laser annealing system, fabricated by SCREEN-LASSE, a French subsidiary of SCREEN, is based on a XeCl laser source, enabling anneals at  $\lambda=308$  nm with a FWHM of 160 ns pulse duration as presented in Figure II - 1. This pulse duration can be slightly modified by changing the gas mixture within the laser source.

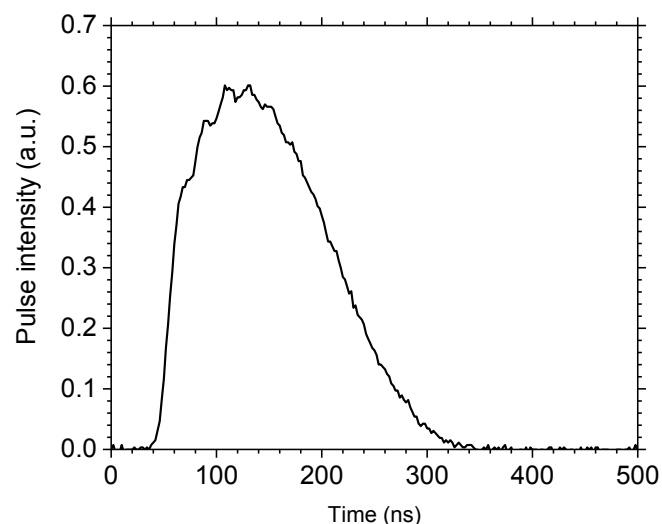


Figure II - 1. LT-3100 laser pulse profile as a function of time. The profile is controlled to obtain a 160 ns FWHM duration.

A simplified representation of the tool is shown in Figure II - 2. The laser cavity is filled with a gaseous mixture of mainly Ne, along with Xe, HCl, et H<sub>2</sub>. The final energy density depends on the voltage applied the top and bottom electrodes, and is adjusted by the attenuator along

the optical line. This attenuator is formed by semi-reflecting plates that dampen the incoming beam depending on their configuration [1].

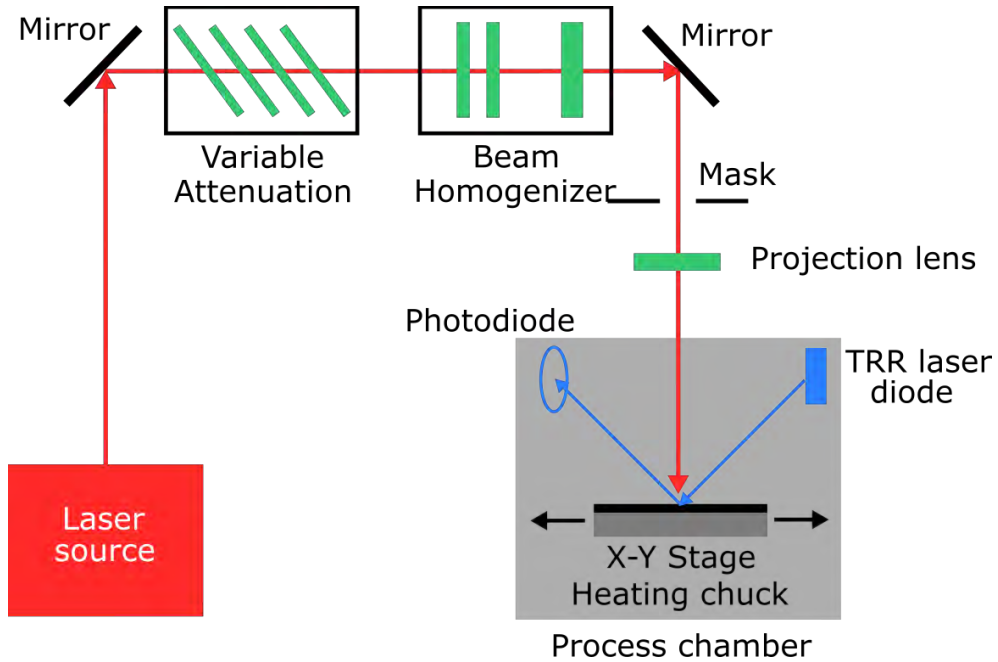


Figure II - 2. Schematic representation of the typical optical line for a nanosecond laser annealing tool.

The beam homogenizer consists of a single microlens array and a Fourier lens [2] : the microlens array splits the incident beam into beamlets that subsequently pass through a spherical lens and overlap at the homogenization plane. In the case of the SCREEN LT-3100 system, the final beam, shown in Figure II - 3, is a rectangle flat-top or 'Top-hat' with a 26x33 mm<sup>2</sup> maximum size. The microlens array can be modified to form final beams of smaller dimensions, therefore shifting the available range of energy densities to higher energy densities.

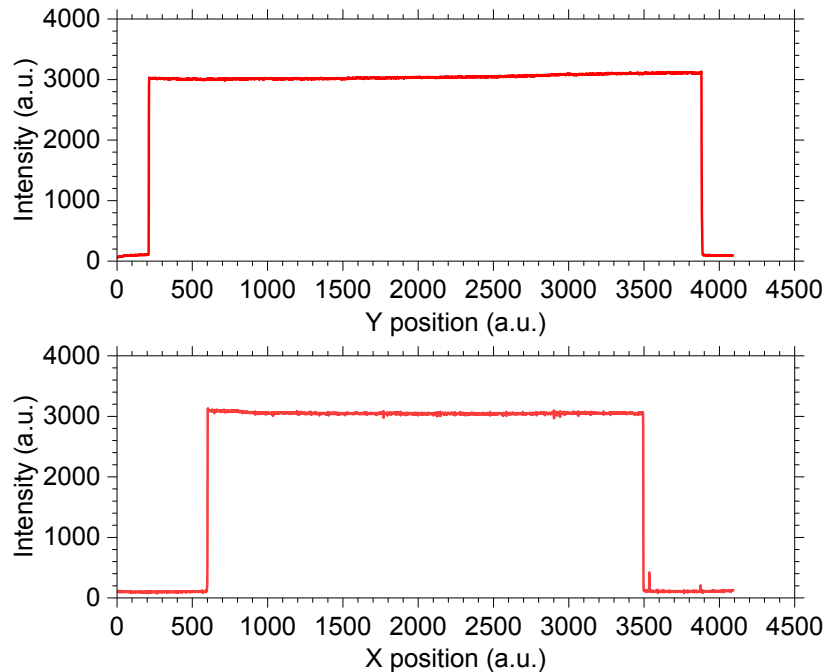


Figure II - 3. Spatial profile of the laser beam along the X (a) and Y (b) directions for a 26x33 mm<sup>2</sup> shot, exhibiting a top-hat profile with sharp edges.

The typical beam uniformity achieved is below +/-3% ( $U=(max-min)/(max+min)$ ). An example for a 15×15 mm<sup>2</sup> shot is shown in Figure II - 4. Several masks are also available to define the final size of the projected beam onto the surface. The experiments presented here were strictly made with a 15×15 mm<sup>2</sup> mask that allowed energy densities from 0.30 to 3.60 J/cm<sup>2</sup>. More details on the laser annealing tool can be found in [3], [4].

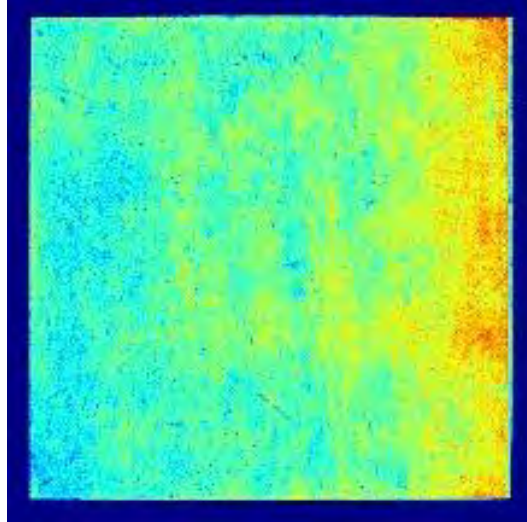


Figure II - 4. Shot uniformity measurement for a 15×15 mm<sup>2</sup> mask. The measured homogeneity was 2.09%.

The tool automatically handles 200 mm and 300 mm wafers, and uses the step-and-repeat mode defined in Chapter I, by displacing the stage on which the wafer is mounted underneath the beam. Each laser shot is monitored by Time-Resolved Reflectivity, an integrated metrology that is defined later in this chapter.

## 2. Laser annealing conditions

The laser annealing system installed at LETI enables automatic handling of 200 and 300 mm diameter substrates. In this study, the 300 mm wafers with SiGe epilayers were brought in the annealing chamber automatically after notch alignment to control wafer orientation. The anneals were performed under an N<sub>2</sub> ambient. The chuck on which the wafer lies is made of ceramic and can be heated up to 450°C to uniformly heat the wafer if required. The heating chuck requires up to 45 minutes to reach a stable temperature and must be started before the wafer enters the annealing chamber. In this study, most of the samples were laser annealed at room temperature (RT) and some samples were irradiated on a chuck at 450°C.

During the anneal, the wafer is maintained on the chuck by a vacuum system. The chuck moves to position the wafer under the nanosecond laser beam as indicated in pre-made recipes, with an accuracy of a few microns. Single exposure or multiple laser annealing shots can be performed at the same location, following the typical cartography shown in Figure II - 5, including 129 shot positions. The wafer is then brought back to its carrier, with a step at a cooling station if the heating chuck was used.

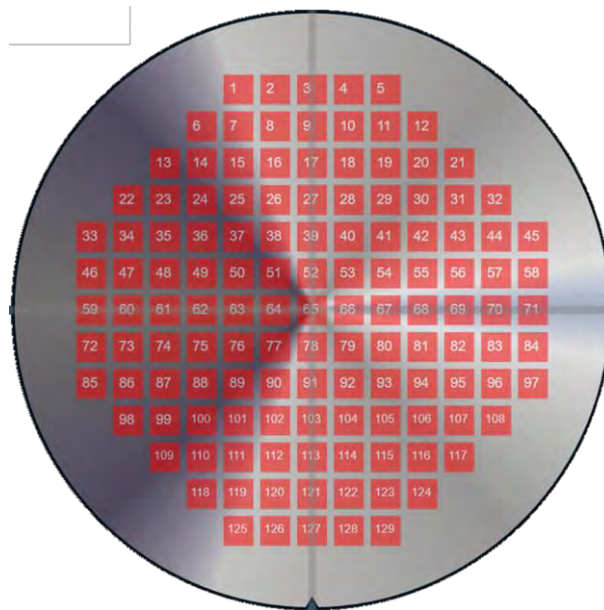


Figure II - 5. Typical shot pattern used for 300 mm wafers for 15×15 mm<sup>2</sup> shots, with 129 shot locations.

## II - Si AND SiGe SAMPLES

### 1. Samples series

Different series of samples were produced in order to study the impact of UV-NLA on Si<sub>1-x</sub>Ge<sub>x</sub> thin epilayers. Most of these samples were grown on Si (001) by Reduced Pressure Chemical Vapour Deposition in a 300 mm Epsilon 3200 tool from ASM. The Si (001) surfaces were prepared with a "HF-last" wet cleaning followed by an in-situ H<sub>2</sub> bake at 1100°C. GeH<sub>4</sub> was the Ge gaseous precursor. For undoped series of Si<sub>1-x</sub>Ge<sub>x</sub> samples, SiH<sub>4</sub> or Si<sub>2</sub>H<sub>6</sub> were used as the Si precursor for x = 0.3 and 0.4 or x ≤ 0.2, respectively. For doped samples, SiH<sub>2</sub>Cl<sub>2</sub> was used as the Si precursor. The boron precursor for doped samples was B<sub>2</sub>H<sub>6</sub>. The thicknesses and growth temperatures for each sample (wafer) were chosen in order to obtain pseudomorphic layers [5], [6]. The thickness of our epilayers were thus chosen in the 20-45 nm range with most of the layers being 30 nm thick. For the boron-doped samples, three different boron concentrations respectively nominated A, B, C were obtained. The medium concentration, B, is estimated near 2×10<sup>20</sup> B/cm<sup>3</sup>, while A and C respectively correspond to slightly lower and higher concentrations.

Detailed description of samples can be found in Table II-1. As shown in this table, three main series of samples were made : these will be named the "30 nm"-thick series, the "Si<sub>0.7</sub>Ge<sub>0.3</sub>" series and the "Boron doped" series for the rest of the manuscript. Each line corresponds to a type of wafer used - there were sometimes several identical wafers, that are not indicated here. For the "Boron doped series", the Si<sub>1-x</sub>Ge<sub>x</sub> growth was preceded by a 100 nm n-type doped Si layer, in order to enable electrical measurements by forming a p-n junction. Bulk Si (100) wafers or thick (5 μm) Ge layers were used as references for pure Si and pure Ge in some studies.

Table II - 1. Growth conditions used for crystalline Si<sub>1-x</sub>Ge<sub>x</sub> layers

Series name	Ge content	Thickness (nm)	Doping	Growth temperature (°C)	Pressure (Torr)	Precursors
30 nm series	0	30	-	550	20	Si <sub>2</sub> H <sub>6</sub>
	0.1	30	-	550	20	Si <sub>2</sub> H <sub>6</sub> - GeH <sub>4</sub>
	0.2	30	-	550	20	Si <sub>2</sub> H <sub>6</sub> - GeH <sub>4</sub>
	0.3	30	-	550	20	SiH <sub>4</sub> - GeH <sub>4</sub>
	0.4	30	-	550	20	SiH <sub>4</sub> - GeH <sub>4</sub>
Si <sub>0.7</sub> Ge <sub>0.3</sub> series	0.3	20	-	650	20	SiH <sub>2</sub> Cl <sub>2</sub> - GeH <sub>4</sub>
	0.3	30	-	650	20	SiH <sub>2</sub> Cl <sub>2</sub> - GeH <sub>4</sub>
	0.3	45	-	650	20	SiH <sub>2</sub> Cl <sub>2</sub> - GeH <sub>4</sub>
Doped series	0.3	30	Boron - A	650	20	SiH <sub>2</sub> Cl <sub>2</sub> - GeH <sub>4</sub> - B <sub>2</sub> H <sub>6</sub>
	0.3	30	Boron - B	650	20	SiH <sub>2</sub> Cl <sub>2</sub> - GeH <sub>4</sub> - B <sub>2</sub> H <sub>6</sub>
	0.3	30	Boron - C	650	20	SiH <sub>2</sub> Cl <sub>2</sub> - GeH <sub>4</sub> - B <sub>2</sub> H <sub>6</sub>

Additional samples were used for studies involving implantation. Several undoped 30 nm-thick Si<sub>0.7</sub>Ge<sub>0.3</sub> were amorphized by Ge implantation to obtain 15 nm and 30 nm thick a-SiGe layers and study the explosive crystallization in SiGe. The growth and implantation conditions are presented in Table II - 2.

Table II - 2. Growth and implantation conditions used for amorphized Si<sub>1-x</sub>Ge<sub>x</sub> layers

Process step	Sample	(1)	(2)	(3)
Epitaxy	Ge ratio	0.3	0.3	0.3
	Thickness (nm)	30	30	30
	Doping	-	-	Boron - B
	Growth temperature (°C)	650	650	650
	Pressure (Torr)	20	20	20
	Precursors	SiH <sub>2</sub> Cl <sub>2</sub> - GeH <sub>4</sub>	SiH <sub>2</sub> Cl <sub>2</sub> - GeH <sub>4</sub>	SiH <sub>2</sub> Cl <sub>2</sub> - GeH <sub>4</sub> - B <sub>2</sub> H <sub>6</sub>
	Implantation	Ge dose (at/cm <sup>2</sup> )	1.5×10 <sup>15</sup>	1.5×10 <sup>15</sup>
Energy (keV)		6	16	6
Amorphized thickness (nm)		15	30	15

## 2. Laser annealing conditions

These wafers were annealed with the SCREEN LT-3100 tool, at laser energy density values chosen to study all annealing regimes from sub-melt, regime in which the Si<sub>1-x</sub>Ge<sub>x</sub> layer

does not melt, up to the full melt, in which the complete layer and part of the underlying Si substrate melt. These ranges differ for each sample, as the thermal and optical properties depend on the thickness, composition and phase of the materials, and are presented in Table II - 3.

It should be noted that samples from the 30 nm series were annealed with a 146 ns FWHM laser pulse duration, while other series were annealed with a 160 ns pulse duration.

Table II - 3. Main laser processing conditions used for the annealing of  $\text{Si}_{1-x}\text{Ge}_x$

Series	Germanium content	Thickness (nm)	Energy density range ( $\text{J}/\text{cm}^2$ )	Energy density step ( $\text{J}/\text{cm}^2$ )	Chuck temperature	Laser pulse FWHM (ns)
30 nm series	0	30	1.60 – 2.60	Variable	RT	146
	0.1	30	1.51 – 2.48	Variable	RT	146
	0.2	30	1.40 – 2.38	Variable	RT	146
	0.3	30	1.31 – 2.28	Variable	RT	146
	0.4	30	1.21 – 2.18	Variable	RT	146
$\text{Si}_{0.7}\text{Ge}_{0.3}$ series	0.3	20	1.11 – 2.51	0.02	RT	160
	0.3	30	1.11 – 2.53	0.02	RT	160
	0.3	45	1.10 – 2.51	0.02	RT	160
Doped series	0.3	30	1.21 – 2.42	0.025	RT	160
	0.3	30	0.90 – 2.12	0.025	450°C	160
	0.3	30	1.21 – 2.41	0.025	RT	160
	0.3	30	0.80 – 2.01	0.025	450°C	160
	0.3	30	1.20 – 2.40	0.025	RT	160
	0.3	30	0.81-2.01	0.025	450°C	160

For each wafer in these series, several shots in different annealing regimes were selected and characterized. The different techniques used to study the surface, the structure and the composition are detailed in the following paragraphs.

### III - CHARACTERIZATION METHODS

As the NLA process induces many changes in the structure and composition of  $\text{Si}_{1-x}\text{Ge}_x$  layers, a wide variety of characterization methods is required to gain a complete understanding.

#### 1. In-situ Time Resolved Reflectivity (TRR)

##### a) Measurement principle

As the refraction indexes of materials evolve with temperature and phase changes, the reflectivity of a layer stack exhibits changes when submitted to UV-NLA [7]. It is possible to record these reflectivity variations by probing the annealed surface with laser light during the UV-NLA treatment. The intensity of the reflected light is recorded with a sampling in the nanosecond timescale. The data obtained is an arbitrary intensity rather than the exact reflectivity value, though it follows the same evolution.

The measurement is performed in-situ, with a laser diode ( $\lambda=638$  nm) integrated within the UV-NLA tool. The probing laser beam is oriented at a 45° angle as shown in Figure II - 6, while the nanosecond laser beam is normal to the surface. A  $5 \times 10$  mm<sup>2</sup> elliptical spot is probed on the sample by the diode laser, smaller than the  $15 \times 15$  mm<sup>2</sup> annealed area for  $\text{Si}_{1-x}\text{Ge}_x$  layers. The reflected beam intensity is recorded by a photodiode. For a single UV-NLA shot, a data point can be obtained every two nanoseconds, providing a precise evolution of the signal over durations as long as 1200 ns. This ensures that the complete heating, melting, solidification

and cooling down can be recorded. The signal is expressed in arbitrary units through this document : as the polarization of the laser probe is not controlled, it does not correspond to the absolute reflectivity.

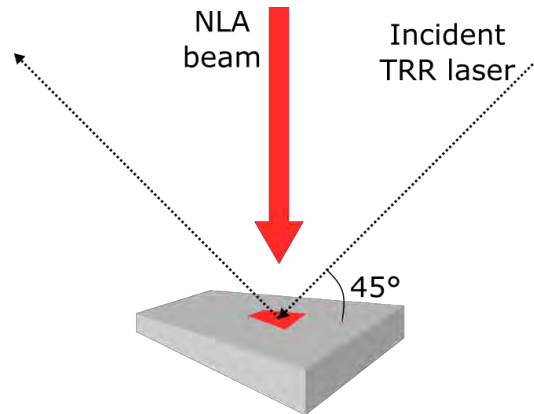


Figure II - 6. TRR signal is obtained with the reflection of a laser diode laser on the annealed surface during the nanosecond laser shot.

#### b) Observations on Si and Ge and limits

For a simple layer of Si, Ge or SiGe on top of a Si substrate, the reflectivity increases with temperature. As presented in Figure II - 7, the following steps may be observed for a laser energy density high enough to cause the surface melting :

- Before the laser pulse ①, the intensity is stable : it corresponds to a cold layer ;
- After the onset of the laser shot (and during a few nanoseconds), the evolution of optical parameters in the solid phase with the temperature results in a rise of the stack reflectivity indicating that the structures heats up ②;
- A change in slope and further increase in intensity ③ indicates the appearance of a molten layer with higher reflectivity.
- The signal intensity is proportional to the liquid layer thickness: it intensifies as the molten layer grows until it reaches a plateau ④. It corresponds to the reflectivity of a semi-infinite liquid layer, i.e. the signal level characteristic of the liquid phase as the molten layer became thick enough to appear semi-infinite at the sensing wavelength. No information can be obtained from below. For Si and Ge, this critical liquid thickness is near 20 nm [8], which roughly corresponds to twice the absorption length in liquid [9].
- The plateau finishes, and the intensity drops ⑤ after the end of the laser pulse, indicating that the material is solidifying, and that less than 20 nm of liquid remain.
- Once the solidification front reaches the surface (the whole structure solidifies), the slow evolution of the intensity at the end ⑥ corresponds to the cooling of the solid layer.

Only part of these elements may be observed for lower energy densities. If the layer does not melt, only a bump related to heating and then cooling is observed. For energy densities leading to melt depths lower than ~20 nm, the maximum intensity is lower and the plateau is not observed.

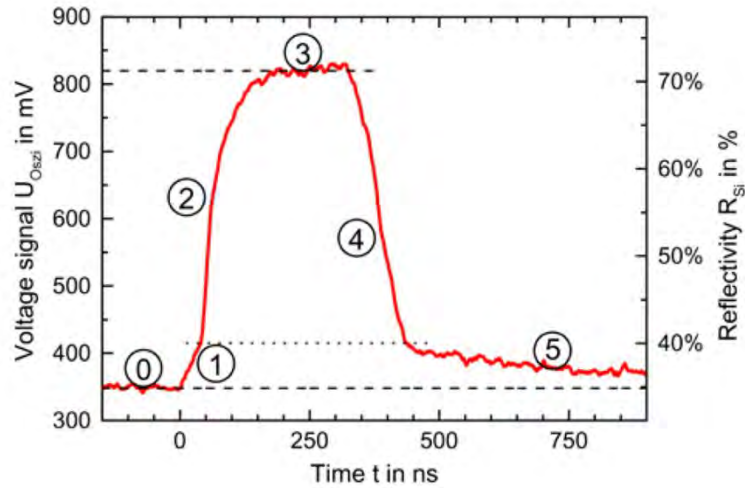


Figure II - 7. Typical TRR signal obtained on a n-type Si (001) surface caused by a 300 ns single laser pulse at  $\lambda=532$  nm. The numbers indicate the various annealing steps [10].

It is possible to determine the melt start and duration, as well as the cooling rates and reflectivity evolution with temperature [10].

## 2. Layer thickness measurement

### a) Spectroscopic ellipsometry principle

Ellipsometry is a widely used method for thickness and optical indices ( $n$ ,  $k$ ) measurement in thin layers. The refractive index  $n$  is defined as the ratio of light velocity in the material compared to the vacuum, while the extinction coefficient  $k$  defines the light lost due to scattering and absorption in the material. Rather than a direct measurement, it relies on the interaction of polarized light with a given sample, which modifies the  $s$  and  $p$  components of the reflected beam, as shown in Figure II - 8. This enables non-destructive control.

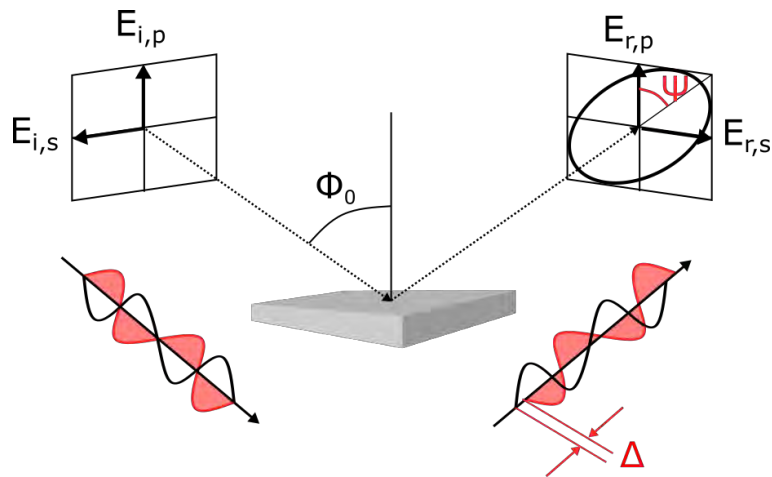


Figure II - 8. Ellipsometry measurements rely on changes in light polarization after interaction with the samples, which enable to estimate thickness and optical indices.

The values measured are  $\Delta$  and  $\psi$ , respectively the phase difference and amplitude ratio for  $s$  and  $p$  polarization of the reflected beam, which gives the following equation [11]

$$\tan \psi e^{i\Delta} = r_p / r_s \quad \text{Eq. II - [1]}$$

Where  $r_p$  and  $r_s$  are the reflection coefficients respectively within the sample plan and normal to the sample plan. As these coefficients depend on the sample nature, it is possible to extract the wanted parameters. The measurements can be performed with multiple wavelengths and various incidence angles  $\Phi_0$

In practice, a theoretical model is established for well-known samples. During a measurement, the desired parameters are modified to match the theoretical model with the experimental data, thus indicating the best set of thickness/optical indices for the measured stack of layers. Our measurements were performed on a Nanometrics spectroscopic ellipsometer (in the 200-1700 nm spectral range), and primarily aimed to estimate the  $\text{Si}_{1-x}\text{Ge}_x$  layer thickness and uniformity.

#### b) Uniformity

Thickness uniformity was evaluated by ellipsometry for the "Doped series" before laser annealing, with 49 measurement points on a 300 mm wafer. A typical mapping for a 30 nm-thick  $\text{Si}_{0.7}\text{Ge}_{0.3}$  layer with low boron doping is shown in Figure II - 9. The SiGe layer thickness was lower at the center and at the edge of the wafer. The maximum range between the thinnest and thickest point were 2.78 nm, 2.22 nm and 1.69 nm for the A, B and C doped layers.

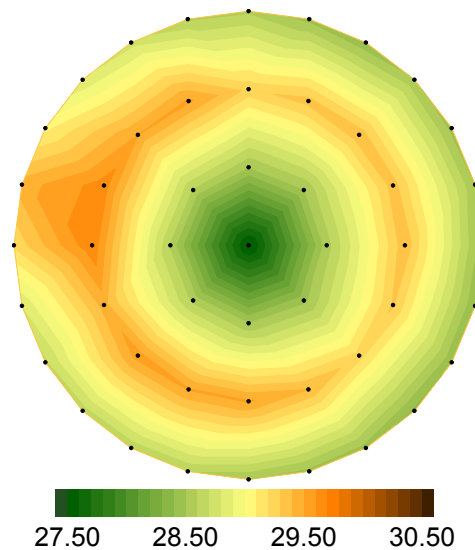


Figure II - 9. Thickness (nm) mapping for a 30 nm-thick  $\text{Si}_{0.7}\text{Ge}_{0.3}$  boron doped layer, at medium doping levels. The layer is slightly thinner in the centre and at the edge of the wafer.

In cases where several identical wafers were made, the results showed very little discrepancies between the various wafers. They are therefore considered identical.

### 3. Surface Characterizations

#### a) Haze measurements

A SP2 system from KLA-Tencor, usually dedicated to surface defects and particles counting, has been used for haze measurements presented in this work. SP2 Haze measurements rely on light scattering from a surface to gain information on its morphology [12]. Laser light illuminates the sample with normal or oblique ( $70^\circ$  from the normal) incidence, as in Figure II - 10. The light scattered by either the surface itself or particles is collected by two different channels, narrow or wide depending on the direction of scattered light [13]. The resulting signal is a mix of the haze (the background noise corresponding to the surface) and spikes caused by surface particles.

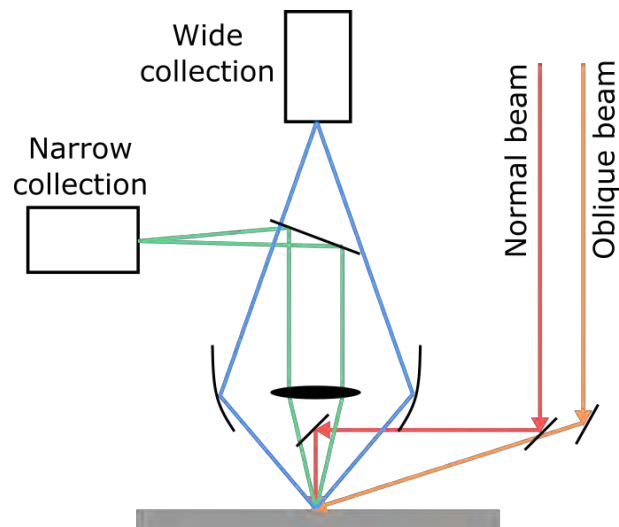


Figure II - 10. Haze measurement principle, with narrow and wide collection. Red and orange arrows respectively correspond to the normal and oblique incident beams.

The haze value highly depends on surface roughness, and varies with grain size in case of polycrystalline layers, film morphology and crystallinity. This non-destructive technique enables a fast collection of qualitative information on the surface state of the whole 300 mm wafer. In this work, laser annealed wafers were submitted to such measurement with a UV laser (360 nm) using oblique incidence and wide channel collection to estimate the haze level for each region irradiated with various laser process conditions. A typical SP2 haze map is shown in Figure II - 11.

These observations were completed with AFM scans, to evaluate the origins of surface modifications.

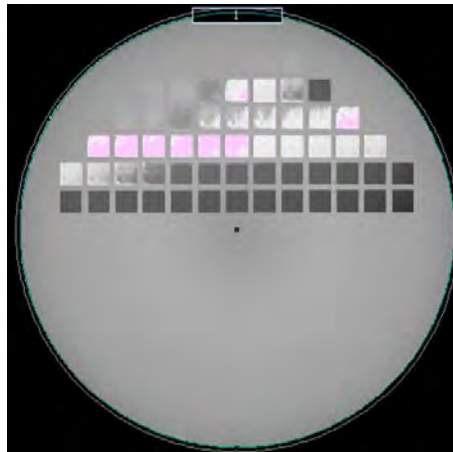


Figure II - 11. Haze cartography after NLA on a 30 nm-thick Si layer grown on Si (001). The change in intensity is caused by changes in surface roughness.

## b) Atomic Force Microscopy (AFM)

### i. Imaging principle

Atomic Force Microscopy (AFM) relies on the interactions between a sharp tip and the sample surface to obtain information on the surface topography [14]. These interactions can be approximated with a Lennard-Jones potential, if only the interaction between two atoms

are considered. In this case, the contributions are the repulsive Coulomb forces at the shorter distances, and the attractive Van der Waals forces at "longer" distances. In practice, several atoms from the tip and from the surface are simultaneously submitted to these forces and the resulting interaction is more complex.

The tip is attached to a cantilever, such as in Figure II - 12. This cantilever is able to bend, and interactions between the tip and the surface will cause a deflection  $\delta$ . A laser beam reflected on the cantilever enables the measurement of this deflection. A four quadrants photodiode is used to collect the signal and measure the deviation at a given point.

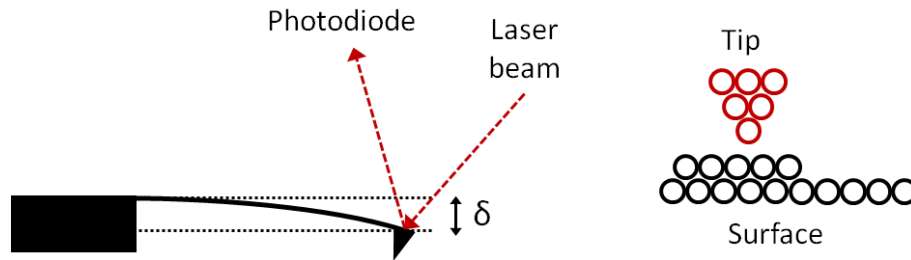


Figure II - 12. Deflection of an AFM cantilever and interactions between tip and surface.

There are different imaging modes, either contact mode or dynamic mode. In contact mode, the tip is dragged across the surface, and remains at a constant distance or at constant force. In dynamic mode, such as the tapping mode, the cantilever is forced to oscillate at its resonance frequency, with a chosen amplitude setpoint. As the tip is submitted to interactions with the surface, it will modify this amplitude. In this case, the tip is withdrawn or brought closer to the surface until the amplitude is equal to the amplitude setpoint.

#### ii. Conditions and measured values

The AFM results presented in this manuscript were obtained with the tapping mode using a Fast-Scan Bruker in-line tool. The tip curvature was usually in the 5 to 10 nm range. The scans size ranged from  $1 \times 1 \mu\text{m}^2$  to  $10 \times 10 \mu\text{m}^2$ , and the topography could be measured for features from 0.5 nm to  $2 \mu\text{m}$ . The  $10 \times 10 \mu\text{m}^2$  scans were used to obtain the Root Mean Square roughness (RMS), written as:

$$RMS = \sqrt{\frac{\sum_{i=1}^N (Z_i - \bar{Z})^2}{N}} \quad \text{Eq. II - [2]}$$

where  $N$  is the number of points in the image,  $Z_i$  is the height at a given point  $i$ , and  $\bar{Z}$  is the average height. For example, the scan presented in Figure II - 13 corresponds to the reference (i.e. without laser annealing) for the 45 nm-thick  $\text{Si}_{0.7}\text{Ge}_{0.3}$  layer, and showed RMS roughness at 0.104 nm and maximum height at 0.983 nm.

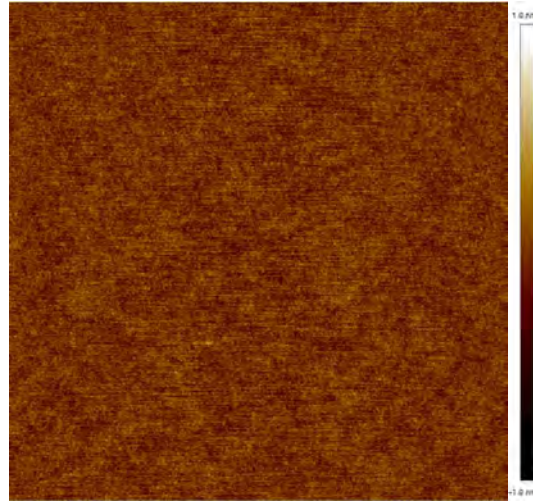


Figure II - 13. 10×10 μm<sup>2</sup> AFM scan on a 45 nm-thick Si<sub>0.7</sub>Ge<sub>0.3</sub> layer post epitaxy (no anneal)

#### 4. Crystalline quality assessment

##### a) Strain and crystallinity measurements by XRD

##### *i. X-Ray diffraction from a crystalline structure*

X-rays are electromagnetic radiations with wavelengths in the range between 10 pm and 10 nm, hence close to inter-atomic spacing. These radiations may therefore interact with matter and provide information on its structure. Diffraction phenomena refer to the constructive interference of monochromatic X-rays after interaction with a crystalline sample [15]. The interaction of X-rays with a single atom can lead to elastic scattering, i.e. to the reemission of an X-ray wave at the same wavelength but in a different direction, such as in Figure II - 14. In case of interaction with a periodic structure such as a crystal, the numerous scattered waves can interfere with each other. In order to obtain constructive interferences, the path difference between two radiations must be a multiple of the wavelength. This condition is summarized in Bragg's law, as follows [16]:

$$n\lambda = 2d_{hkl}\sin(\theta_B) \quad \text{Eq. II - [3]}$$

Where  $n$  is an integer (diffraction order),  $\lambda$  the X-ray wavelength,  $d_{hkl}$  the inter-atomic spacing between two crystallographic planes of a given  $\{hkl\}$  family and  $\theta$  the diffracted Bragg angle.  $d_{hkl}$  can be easily calculated for a cubic lattice, with  $a$  the lattice parameter :

$$d_{hkl} = \frac{a}{\sqrt{h^2 + k^2 + l^2}} \quad \text{Eq. II - [4]}$$

The diffracting set of lattice plans therefore depends on the angle. This condition must be satisfied to obtain diffraction at a given angle, but the intensity is not equivalent in all cases, as it is modulated by the structure factor. This factor takes into account the non-homogeneous electronic density within the material, and corresponds to the contribution from a single lattice cell. It is expressed as [17]

$$F(hkl) = \sum_{j=1}^n f_{i,\theta} \exp[i2\pi(hx_j + ky_j + lz_j)] \quad \text{Eq. II - [5]}$$

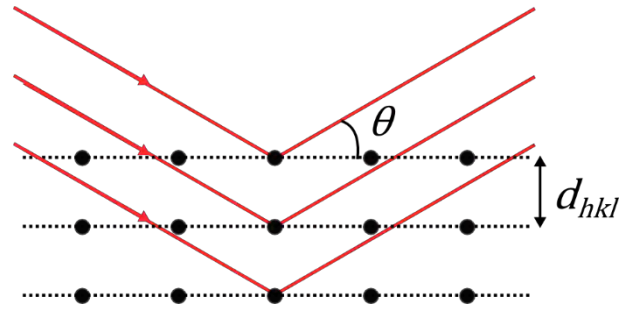


Figure II - 14. X-ray diffraction by a set of plans parallel to the surface, with spacing  $d_{hkl}$  between planes.

$\vec{k}_i$  and  $\vec{k}_d$  are respectively the incident and diffracted wave vectors, shown in Figure II - 15.  $\vec{q}$  is the scattering vector, defined as  $\vec{q} = \vec{k}_d - \vec{k}_i$ . A measurement is considered symmetrical if  $\vec{q}$  is normal to the sample surface. In this case, only the planes parallel to the surface are assessed. Asymmetrical measurements, where  $\vec{q}$  is not normal to surface, enable to gain information on tilted planes.

### ii. Diffractometers

The main components of a diffractometer are the x-ray source, the stage with the sample and the detection system [18], [19]. In our experimental conditions, X-rays are produced by the excitation of a copper anode, which emits  $K_{\alpha 1}$ ,  $K_{\alpha 2}$  and  $K_{\beta}$  radiations. An optical system formed with mirrors and monochromators is used to avoid polychromy and reduce divergence. After interaction with the sample, diffracted X-rays are collected by the detection system, often a scintillator. There are different types of detectors : 0D, 1D or 2D. A 0D punctual detector counts the incident photons for a given position, while 1D and 2D simultaneously collect photons from different angles, therefore reducing the measurements duration.

There are four rotation axes, as presented in Figure II - 15, to orient the sample as wanted.  $\omega$  corresponds to the angle between the incident radiation and the surface, while  $2\theta$  is the angle between incident and diffracted beams. The angles of rotation around the directions normal to the surface and in the plane are respectively  $\varphi$  and  $\psi$ .

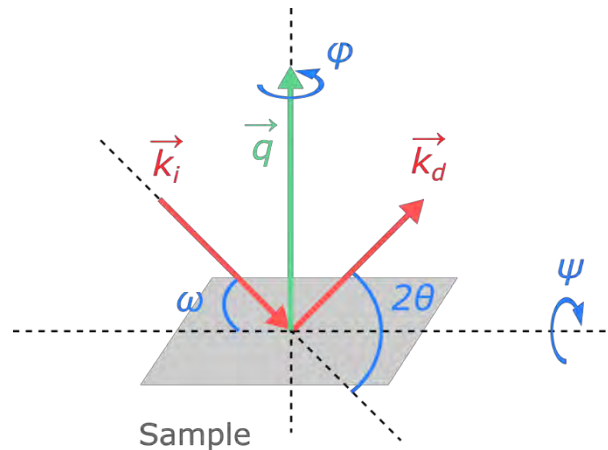


Figure II - 15. Rotation axes on a diffractometer, with the incident and diffracted beams in a case where  $\omega = \theta$ .

The diffractometers used were an X'PERT PRO from Pan'Analytical and a DELTA-XM from BRUKER, both with a copper source. The optical lines were not identical, with different slits and monochromators, respectively a four reflection Ge(220) crystal and a double reflection

Ge(004) crystal. The slits on the diffracted optical path were usually 2 mm wide to improve the resolution.

### iii. Reciprocal lattice

The reciprocal lattice is the Fourier transform of the crystalline lattice, allowing to study the material and its diffraction in wave vector terms rather than physical distances. Three reciprocal lattice vectors ( $\vec{a}^*$ ,  $\vec{b}^*$ ,  $\vec{c}^*$ ) are defined from the main vectors of the lattice [20], with :

$$\vec{a}^* = 2\pi \frac{\vec{b} \times \vec{c}}{\vec{a} \cdot (\vec{b} \times \vec{c})} \quad \text{Eq. II - [6]}$$

$$\vec{b}^* = 2\pi \frac{\vec{c} \times \vec{a}}{\vec{a} \cdot (\vec{b} \times \vec{c})} \quad \text{Eq. II - [7]}$$

$$\vec{c}^* = 2\pi \frac{\vec{a} \times \vec{b}}{\vec{a} \cdot (\vec{b} \times \vec{c})} \quad \text{Eq. II - [8]}$$

In this space, each family of planes ( $hkl$ ) can be represented by a node and a vector  $\vec{d}_{hkl}^*$ . This vector, normal to the corresponding lattice planes, is written as

$$\vec{d}_{hkl}^* = h \cdot \vec{a}^* + k \cdot \vec{b}^* + l \cdot \vec{c}^* \quad \text{Eq. II - [9]}$$

$$\|\vec{d}_{hkl}^*\| = \frac{2\pi}{d_{hkl}} \quad \text{Eq. II - [10]}$$

This reciprocal lattice representation can be combined with a representation in the wave vector space, as a function of the scattering vector  $\vec{q}$ , such as in Figure II - 16. The set of reciprocal lattice vectors determines the possible X-ray reflections (diffraction conditions [21]).

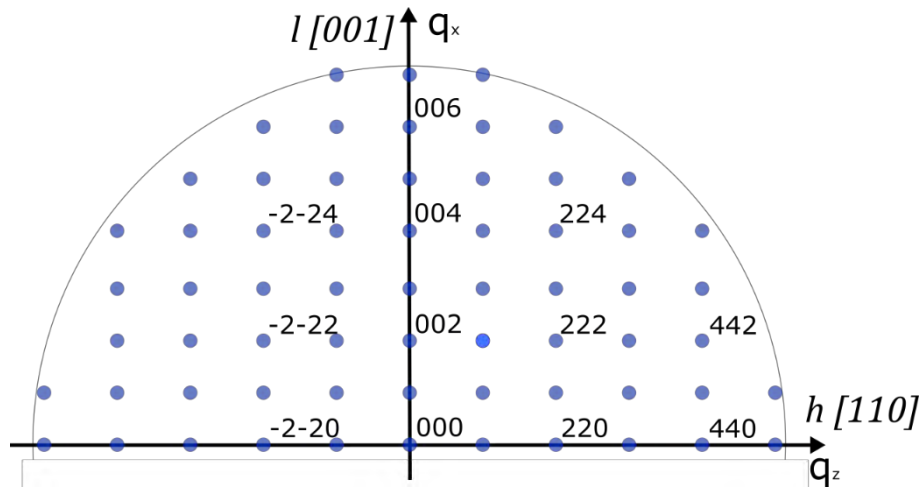


Figure II - 16. Reciprocal lattice representation for a cubic structure.

For an infinite and perfectly crystalline material, a family of planes is observed as an intense dirac peak. This is not the case for thin layers used in microelectronics, which present a broadening of the peak. These peaks associated to thin layers also exhibit thickness fringes around the peak, formed by interferences between beams from the layer and from the substrate.

The following discussion focuses on Si<sub>1-x</sub>Ge<sub>x</sub> layers grown on Si substrates. The diffraction spot position depends on the strain and composition of the layer. Figure II - 17 presents the position of a spot associated to a Si<sub>1-x</sub>Ge<sub>x</sub> layer (green) compared to a relaxed Si layer (blue), for both asymmetrical and symmetrical scans. As symmetrical measurements are influenced solely by  $a^+$  (lattice parameter for planes parallel to the surface), the position of the Si<sub>1-x</sub>Ge<sub>x</sub> spot is only modified on the  $q_z$  axis. Asymmetrical measurements are however influenced by both  $a^+$  and  $a^{\parallel}$ , therefore showing evolutions on  $q_x$  and  $q_z$  axis.  $a^+$  and  $a^{\parallel}$  both differ if the layers

are relaxed, while the spots have identical  $q_x$  values for pseudomorphic SiGe on Si. Composition also modifies the position of diffraction peaks, as it changes lattice parameters.

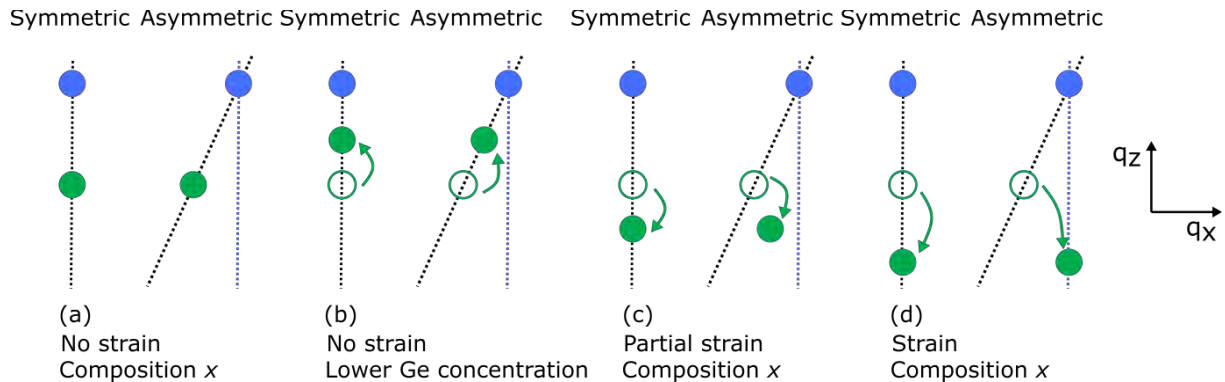


Figure II - 17. Impact of strain and composition on the position of diffraction spots in the reciprocal space for a  $\text{Si}_{1-x}\text{Ge}_x$  layer (green) compared to relaxed Si (blue), for symmetrical and asymmetrical measurements. The positions corresponding to relaxed SiGe (a) change if the composition varies (b) or if the layer is partially strained (c) or fully strained (d) [22].

The respective positions of the peaks can be measured with Reciprocal Space Maps (RSMs), as shown in Figure II - 18 for measurement along the (2 2 4) diffraction peak, which corresponds to an asymmetric measurement. It is therefore possible to evaluate the relaxation in the layer. The maps presented here are the typical maps obtained after NLA on  $\text{Si}_{1-x}\text{Ge}_x$ , and will serve as references in the following chapters. The Si peak corresponds to the bright red spot in the upper part of the image, while the SiGe peak is the second most-intense peak. Its position, shape and intensity vary depending on the layer quality.

Fully strained layers are presented in Figure II - 18 (a,b) : the SiGe peak is vertically aligned with the bright red Si peak in the upper part of the images. The sample from (a) is a layer with a uniform Ge content and uniform strain gradient, leading to the appearance of thickness fringes around the SiGe peak. This is however not visible in (b), as this layers presents a Ge gradient. The following maps (c) and (d) respectively correspond to partially relaxed and fully relaxed layers, as the SiGe peak is not vertically aligned with the Si peak. In (d), the position of the peak along the tilted line indicates full relaxation.

Finally, some samples may show multiple SiGe peaks in a RSM, indicating the formation of a bilayer, such as in Figure II - 18 (e,f). In (e), a first peak is aligned with the vertical line, indicating that part of the SiGe layer is strained, while the other peak shows partial relaxation. In (f), one peak is along the tilted line, indicating that part of the layer is fully relaxed. The other peak shows that the rest of the layer is partially relaxed.

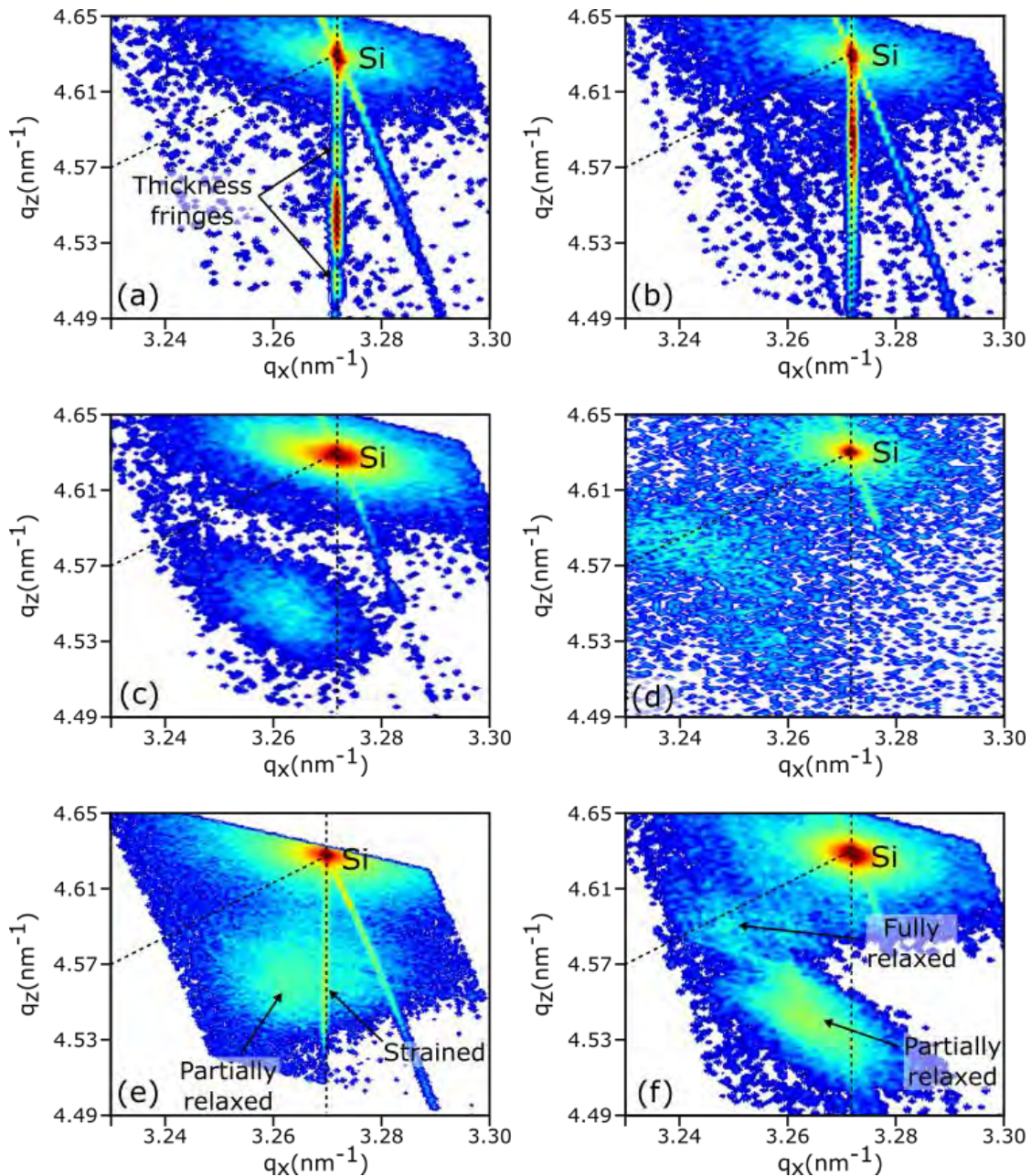


Figure II - 18. Typical reciprocal space maps obtained after NLA of  $\text{Si}_{1-x}\text{Ge}_x$  layers along the (2 2 4) diffraction peak. The tilted and vertical lines respectively indicate the fully relaxed and fully strained peak positions expected (see Figure II - 17 for an asymmetric measurement). Maps in (a,b) correspond to fully strained layers with (b) or without (a) Germanium gradient. Map (c) is a partially relaxed layer, while (d) is a fully relaxed layer. Maps (e,f) are bilayers : (e) shows a strained component and a relaxed component, while (f) shows two relaxed components.

#### iv. Performed scans

XRD measurements were used on laser annealed  $\text{Si}_{1-x}\text{Ge}_x$  layers to estimate their composition and strain. Rocking Curves along the (004) directions (RC004), and Reciprocal Space Maps around the (004) or (224) Bragg reflections (RSM004 and RSM224) were performed. Ge concentration and thickness of the layers were extracted from the rocking curves for pseudomorphic layers by measuring the position and width of the peak. This was mainly used for non-annealed samples with uniform Ge distribution. Similar measurements were performed on both diffractometers, with punctual detectors and  $\omega$  varying from  $33^\circ$  to  $35^\circ$  (Si peak at  $34.5635^\circ$ ).

Strain relaxation level assessment however required asymmetric measurements, with RSM along the (224) direction [23]. As mentioned previously, the coordinates in the reciprocal space of the Si<sub>1-x</sub>Ge<sub>x</sub> (224) reflection depend on both composition and relaxation. By measuring  $q_z$  and  $q_x$  directly on the map, it is possible to calculate the lattice parameters  $a^\perp$  and  $a^\parallel$ , as well as the corresponding relaxed lattice parameter  $a_{SiGe}^0$  :

$$a^\perp = 2\pi \cdot \frac{4}{q_z} \quad \text{Eq. II - [11]}$$

$$a^\parallel = 2\pi \cdot \frac{2\sqrt{2}}{q_x} \quad \text{Eq. II - [12]}$$

$$a_{SiGe}^0 = \frac{a^\perp + \alpha \cdot a^\parallel}{1 + \alpha} \quad \text{Eq. II - [13]}$$

Where  $\alpha$  depends on the elastic coefficients  $C_{11}$  and  $C_{12}$ , themselves depending on the Ge concentration [24]

$$\alpha = \frac{2C_{12}}{C_{11}} \quad \text{Eq. II - [14]}$$

Finally, the macroscopic level of strain relaxation  $R$  and the apparent germanium concentration  $x$  are calculated using [5], [25]:

$$R = \frac{a^\parallel - a_{Si}}{a_{SiGe}^0 - a_{Si}} \quad \text{Eq. II - [15]}$$

$$a_{SiGe}^0 = a_{Si} + 0.1988 \cdot x + 0.028 \cdot x^2 \quad \text{Eq. II - [16]}$$

These measurements were performed with similar conditions on both diffractometers, with a 1D detector. They were obtained in grazing emergence conditions, with an incident beam almost perpendicular to the sample surface, to ensure a thinner diffracted beam and therefore higher resolution.  $\omega$  varied from  $-78.70^\circ$  to  $79.60^\circ$ , while  $2\theta$  ranges differed on the two diffractometers, with respectively  $85.88^\circ$  to  $88.39^\circ$  and  $82.65^\circ$  to  $92.84^\circ$  for the Pan'Analytical and Bruker tools.

## b) Structure observations via Transmission Electron Microscopy

Transmission Electron Microscopy (TEM) is widely used to observe the microstructure and crystalline quality of samples. The short wavelength of electrons used in TEM enables minimal resolutions near 0.25-0.30 nm [26]. These electrons are accelerated toward a thin lamella extracted from the sample, where they interact with the matter. The lamella must be thin enough for electrons to be transmitted through. The various effects resulting from the interactions between atoms and electron beam enable to gain information on the sample composition, structure and its crystalline defects. Conventional TEM (CTEM) and Scanning TEM (STEM) were used in this work to observe crystalline defects, surface and interface roughness and extract information such as film thickness or melted depth after laser annealing.

### i. TEM principle and sample characteristics

The electrons are produced at the top of the TEM column by an electron gun, based on thermionic emission or, for the most advanced microscopes, on field emission. The emitted electrons are accelerated with voltages in the 100-400 kV range. The electron beam is then focused toward the sample by a set of electromagnetic lenses called the condenser lenses : they are responsible for the formation of a thin and coherent beam and define the spot size. The beam transmitted through the sample is collected first by the objective lens, focusing the beam to form an image and finally by the projector lens. This final lens enlarges the image and projects the electron beam toward a fluorescent phosphor screen. The whole column is under vacuum as low as  $1 \times 10^{-10}$  Torr to avoid arc generation and to reduce the frequency of collisions between electrons and gas atoms.

Top view or cross section observations are possible. The lamellae must be thin in order to enable transmission, typically below 100 nm. They are prepared either “manually” (sample cutting, mechanical grinding and ion milling with a Ar<sup>+</sup> beam) or using a Ga focused ion beam (FIB). Most of the results presented in the following thesis were obtained on cross section samples prepared by FIB. The TEM observations were either performed at LETI (TECNAI OSIRIS) or at the Raimond Castaing Platform of Toulouse (JEOL JEM-ARM200F, JEOL JEM2100F).

### ii. Imaging modes

The electron beam hits the thinned sample and either passes through the specimen or interacts with it by undergoing either elastic (without energy losses) or inelastic (with energy losses) scattering, and therefore deviate slightly from their original direction. In most cases, the sample is so thin that a single scattering event can be detected. As the electrons can be diffracted by interaction with the atoms, it is either possible to observe a diffraction pattern at the objective focal point, or an image at the image plan, as in Figure II - 19. A given spot on the diffraction pattern is caused by the redirection of part of the electron beam after interaction with a given set of crystalline planes : the presence of the diffraction pattern allows to study the sample crystallinity [26], [27].

In CTEM, the electrons beam is normal to the surface and covers a relatively large area at once, as in Figure II - 19 (a-b). The resulting images are either bright field, as in Figure II - 19 (a), or dark field, as in Figure II - 19 (b). Bright field corresponds to the transmitted beam, with no detectable deviation, with a contrast corresponding to the density of the presence of defects. Dark field images are obtained by placing a diaphragm so that the image is formed with the electrons coming from a given diffraction spot, rather than the central direct spot: it highlights the crystalline defects or crystalline planes corresponding to this orientation [28]. Weak Beam images can also be obtained by using weakly excited electron beams. These are particularly useful for defect imaging localisation.

In STEM, the electron beam is focused on a single point on sample surface, forming a probe that scans the whole sample as in Figure II - 19 (c). This mode was used to obtain STEM-High Angle Annular Dark Field (STEM-HAADF) images. For these images, the contrast is caused by the difference in atomic number between the atoms, and therefore allows differentiating light and heavy elements. For elements with a higher Z, more electrons are scattered at high angles, causing them to appear brighter in the resulting image.

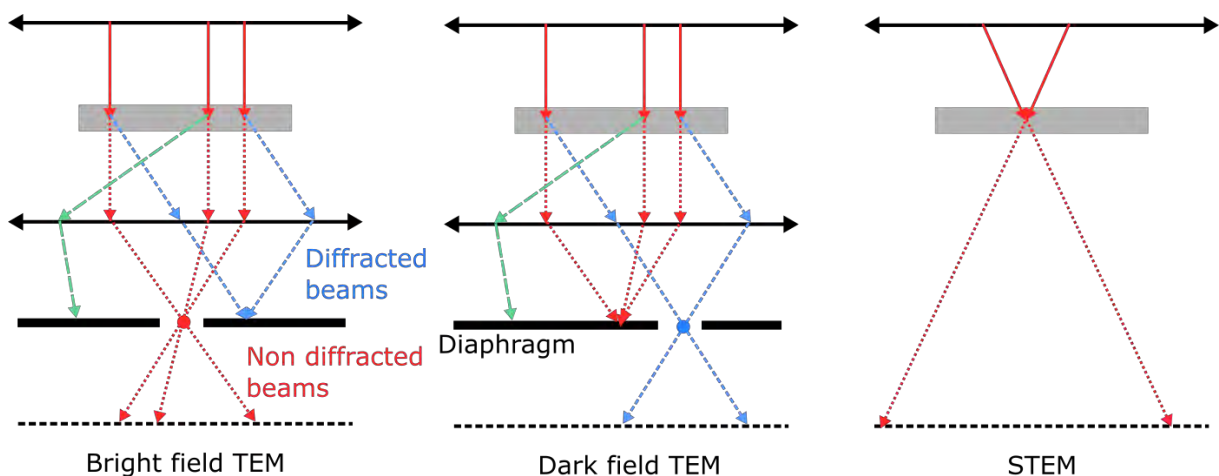


Figure II - 19. TEM setup for bright field, dark field or STEM observations. Bright field (a) images are obtained with the central transmitted spot, while dark field (b) images are formed with diffracted beams.

## 5. Composition and concentration profiles

### a) Secondary Ion Mass Spectrometry (SIMS)

Secondary Ion Mass Spectrometry (SIMS) is used to analyze the chemical composition of a sample. To do so, the material is bombarded with a primary ion beam, which sputters the particles (atoms or molecules) at surface, such as in Figure II - 20. A small part of the sputtered particles are ionized and form the secondary ion beam. These secondary ions are accelerated toward an analyzer by a given potential [29]. In classical SIMS, the analysis is performed with a mass spectrometer, which sorts the atoms and molecules depending on their mass and energy: an ionic current is obtained for each species. Time of Flight SIMS (ToF-SIMS) is slightly different: two primary ion beams are used, as represented in Figure II - 21. A low energy ion beam is used for sputtering, while a high energy ion beam is used for the analysis. This allows slower sputtering and therefore a better depth resolution, and allows to alternate both, as shown in [30]. The ions from the secondary ion beam are sorted in a free flight chamber rather than with a mass spectrometer, as the free flight duration depends mainly on the mass, which enables to analyze more species simultaneously. SIMS measurements are performed in vacuum, with a polarized sample.

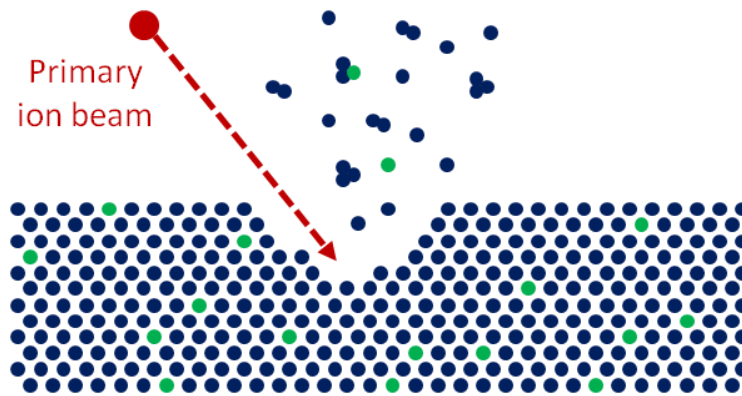


Figure II - 20. Surface sputtering by a primary ion beam during SIMS analysis. Part of the emitted particles are ions that can be used for the chemical analysis.

At the end of the measurements, the current intensity for a given species is obtained as a function of time. Several operations are required to convert this data to concentration of the species as a function of depth. Conversion from time scale to depth scale is rather straightforward if the sputtering rate is constant, and the analyzed depth is relatively large. In this case, the depth is simply proportional to the time, and the sputtering rate can be estimated by using a well-known reference. A change in composition, such as in graded  $\text{Si}_{1-x}\text{Ge}_x$ , can however modify the sputtering rate. This requires to adapt the sputtering rate for each section of the material, by using known references corresponding to the different materials present in the analyzed samples.

Finally, the conversion from intensity to concentration for a given element (quantification) is performed by normalizing the signal obtained for this element with the signal obtained from the principal element of the material, and correcting with the Relative Sensitivity Factor (RSF). The RSF is obtained by performing the same analysis on a standard sample where the concentration of this element is well known.

$$[X] = \text{RSF} \cdot \frac{\text{Intensity}(X)}{\text{Intensity}(\text{matrix element})} \quad \text{Eq. II - [17]}$$

The obtained signal from the first nanometers of the surface is usually less accurate due to the unstable sputtering rate on thin layers and to the presence of an oxide layer.

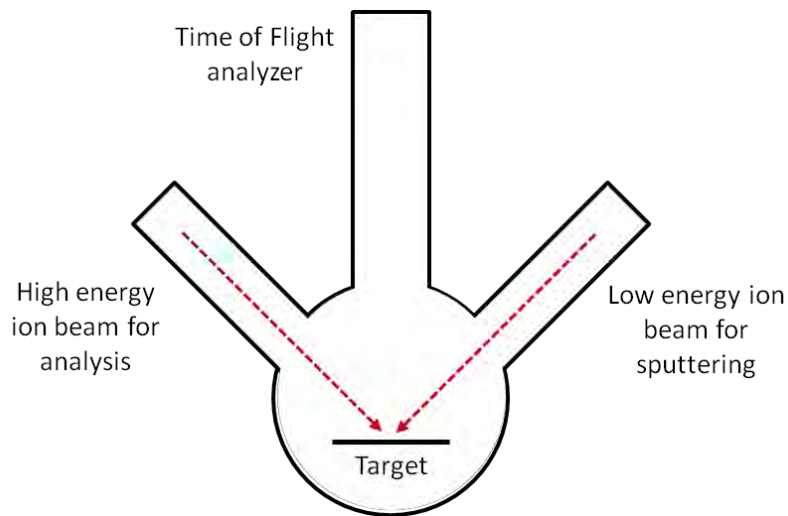


Figure II - 21. Typical ToF-SIMS system, with one ion beam to sputter the surface, and one ion beam for analysis.

The ToF-SIMS analysis presented in this manuscript were performed with a ToF-SIMS V tool from Ion ToF, where the sputtering is performed with O or Cs ions, while the analysis is made with Bi ions. Further information on this tool and on the quantification techniques can be found in [30]. The typical dimensions of the sputtering area and analyzed area are respectively 250  $\mu\text{m}$  and 70  $\mu\text{m}$  wide.

#### b) Energy Dispersive X-Ray Analysis (EDX)

STEM-EDX images and composition depth profiles were obtained on multiple samples. The STEM method is identical to what is described in section III - 3. b) ii, with a focused electron beam on the sample and a detector located above the sample surface as shown in Figure II - 22. X-rays are emitted by the atoms during their de-excitation after interaction with the electron beam. As these X-Rays are characteristic of the energy levels of the emitting atom, they can be used for spectrometry to obtain the chemical information on the observed region of the sample. A map of the atomic species can thus be collected for the area that was scanned, or the data can be compiled in a profile.

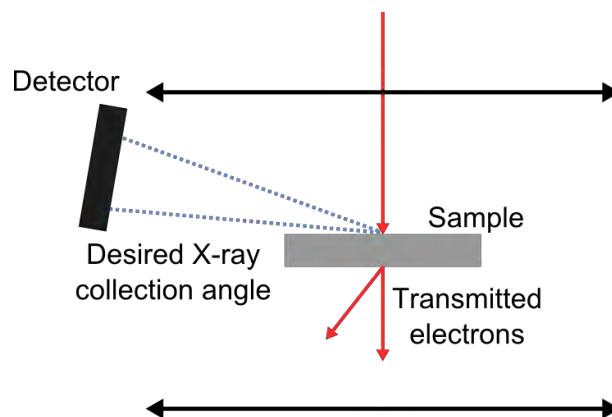


Figure II - 22. X-ray detection for EDX observations in TEM

As the dimension area scanned by the probe is on the nanometer scale, it is possible to observe chemical composition variations on a very small scale. In this work, we specifically

collected Ge concentration maps or depth profiles for samples before and after laser annealing at various energy densities. These measurements were performed at the Raimond Castaing Platform of Toulouse.

## 6. Electrical Characterizations

### a) Sheet resistance by Four-Point-Probe

The sheet resistance  $R_s$  ( $\Omega/sq$ ) is often used to evaluate the electrical properties of uniform thin films of semiconductors or metals. It corresponds to the resistance through a square of material, and is expressed in  $\Omega/sq$  rather than  $\Omega$ , though it corresponds to the same dimension. This resistance per square enables to easily compare different measurements, as the result is independent of the square size.

It is often measured by four-point probe measurements (4PP), where four tips are in contact with the surface, such as presented in Figure II - 23. These points are aligned and uniformly spaced with a distance  $L$ . If the layer thickness,  $t$ , is much lower than the distance  $L$  between two points, and the lateral size of the measured sample is sufficient,  $R_s$  can be written as:

$$R_s = \frac{\rho}{t} = \Gamma \cdot \frac{V_{mes}}{I_{inj}} \quad \text{Eq. II - [18]}$$

Where  $\rho$  is the film resistivity,  $I_{inj}$  the injected current,  $V_{mes}$  the measured voltage and  $\Gamma$  is a factor related to the points layout. For uniformly spaced points :

$$\Gamma = \ln 2 / \pi \quad \text{Eq. II - [19]}$$

This type of measurement for the sheet resistance eliminates the impact of the contact resistances and of the wire resistances if the substrate resistance is high enough, and thus enables to study only the thin film.

These measurements were performed with a WS3000 tool from NAPSON. The tips are equally distributed, with 1 mm spacing in between, and their curvature radius is about 150  $\mu m$ . Before each measurement on a sample of interest, a calibration check was performed on a wafer with known sheet resistance to detect potential drifts. The reference was a 300 mm Si(100) wafer with boron implantation and anneal, leading to sheet resistances in the 400-450  $\Omega/sq$  range.

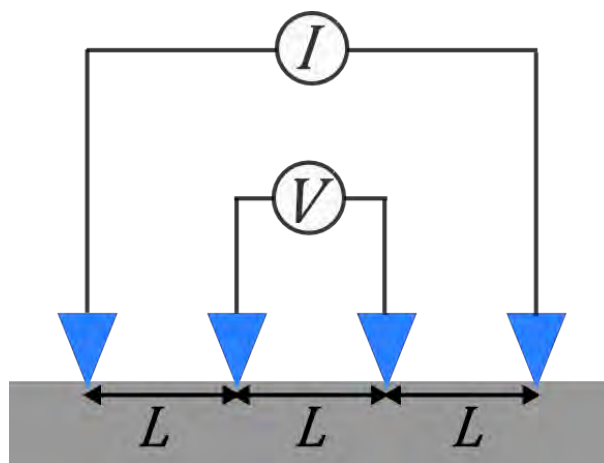


Figure II - 23. Four-point probe measurement with uniform spacing  $L$  between the probes.

Sheet resistance maps were used as uniformity estimation for boron-doped layers, using 121 or 129 data points on a wafer. The map in Figure II - 24 used a concentric mapping with 121 points for a boron doped wafer at the B-level. It corresponds to the wafer shown in Figure II - 24, and exhibits lower  $R_s$  in thinner regions: it is therefore considered that the boron concentration is uniform, and that changes in  $R_s$  are only related to the thickness. Average  $R_s$  values corresponding to wafers with doping levels A, B, and C were respectively found around 323  $\Omega/\text{sq}$ , 234  $\Omega/\text{sq}$  and 199  $\Omega/\text{sq}$ , with maximum ranges of 44  $\Omega/\text{sq}$ , 31  $\Omega/\text{sq}$  and 28  $\Omega/\text{sq}$ .

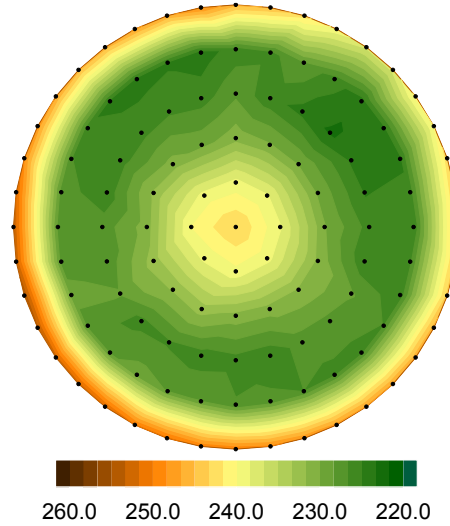


Figure II - 24. Sheet resistance mapping for a 30 nm-thick  $\text{Si}_{0.7}\text{Ge}_{0.3}$  boron doped layer (level B). The area with lower sheet resistance corresponds to the thinner areas observed by ellipsometry (cf. Figure II - 9).

#### b) Hall effect measurements

The Hall effect appears when a slice of material is submitted to a magnetic field while a current goes through it in perpendicular direction, such as in Figure II - 25. The charge carriers within the material are subjected to a Lorentz force  $\vec{F} = q\vec{v} \times \vec{B}_z + q\vec{E}$ , in a direction orthogonal to both magnetic field and electric field and accumulate on one side of the material, depending on their type. This causes the appearance of an electric field along the  $y$  direction, compensating the Lorentz force: at equilibrium, the forces compensate each other and no more charge movement is observed [31]. In that case, the Hall voltage  $V_H$  is written as:

$$V_H = -\frac{1}{nq} \cdot \frac{I_x B_z}{d} \quad \text{Eq. II - [20]}$$

where  $q$  is the carrier charge (either positive or negative depending on the carrier type),  $n$  the carrier density,  $d$  the material thickness along the  $z$  direction,  $B_z$  is the magnetic field and  $I_x$  the current flowing through the material.

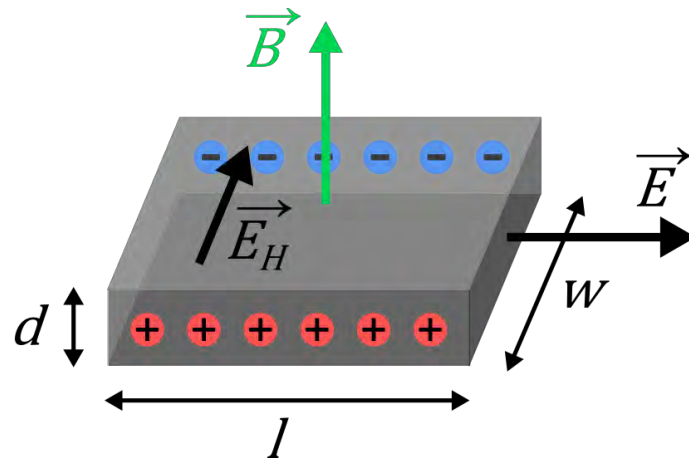


Figure II - 25. Schematic representation of the Hall effect in a semiconductor material, causing a charge displacement.

$V_H$  measurement allows to deduce three parameters : Hall coefficient  $R_H$ , Hall mobility  $\mu_H$  and Hall concentration  $n_H$ , with

$$R_H = \frac{1}{q n} \quad \text{Eq. II - [21]}$$

$$n_H = \frac{1}{q R_H} \quad \text{Eq. II - [22]}$$

$$\mu_H = \frac{R_H}{\rho} \quad \text{Eq. II - [23]}$$

Where  $\rho$  is the resistivity of the material with  $\rho = d \cdot R_s$ , with  $R_s$  the sheet resistance.

These equations were established for an ideal sample, with an uniform dopant distribution, as well as no scattering events. In reality, numerous scattering events can occur. Calculations must therefore take into account the probability of scattering events, and consider the dopant distribution within the samples [32], [33]. The calculated parameters are the Hall surface coefficient  $R_{Hs}$ , the Hall dose  $N_H = d \cdot n_H$  and the Hall mobility  $\mu_H$ .

$$R_{Hs} = \frac{r_H \int_0^d n(z) \langle \mu^2(z) \rangle dz}{q \left[ \int_0^d n(z) \langle \mu(z) \rangle dz \right]^2} \quad \text{Eq. II - [24]}$$

$$N_H = \frac{1}{q d R_H} = \frac{\left[ \int_0^d n(z) \langle \mu(z) \rangle dz \right]^2}{r_H \int_0^d n(z) \langle \mu^2(z) \rangle dz} \quad \text{Eq. II - [25]}$$

$$\mu_H = \frac{R_H}{\rho} = \frac{r_H \int_0^d n(z) \langle \mu^2(z) \rangle dz}{\int_0^d n(z) \langle \mu(z) \rangle dz} \quad \text{Eq. II - [26]}$$

Where  $\langle \mu(z) \rangle$  is the mean mobility and  $r_H$  the scattering coefficient defined as  $r_H = \langle \tau^2 \rangle / \langle \tau \rangle^2$  with  $\tau$  the mean time between two scattering events. This coefficient is also used to estimate the total active dose in the sample, with  $n_H = n / r_H$ .

The measurements were performed in LAAS facilities with a HL5500PC Nanometrics bench with 0.3 T magnet, with several measurements for each sample at various currents from 10  $\mu$ A to 1 mA. The samples were processed to obtain Van der Pauw cross or square structures identical to the ones shown in Figure II - 26, from [32]. The expected error on mobility is ~5%.

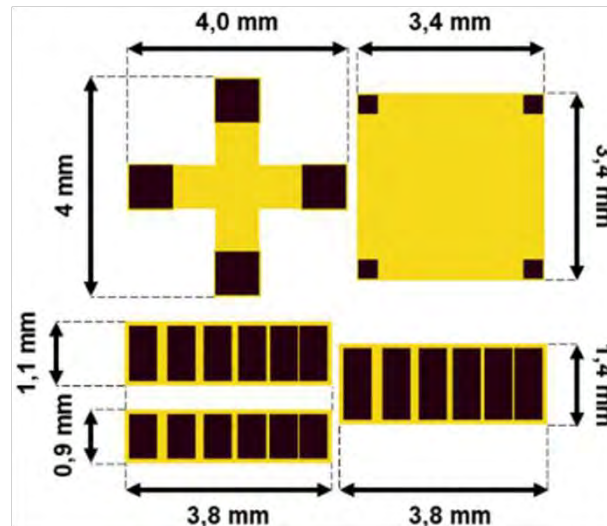


Figure II - 26. Hall measurements structures on a  $1 \times 1 \text{ mm}^2$  sample [34]. The metallic contacts are shown in black.

#### IV – NUMERICAL SIMULATIONS

Simulations were used throughout this work for different purposes. A software developed by SCREEN-LASSE and adapted to UV-NLA was used for complete annealing simulations. The final objective of these simulations is to predict the result of laser annealing on the  $\text{Si}_{1-x}\text{Ge}_x$  layers, such as the melt depth, Ge redistribution and melt duration. This requires the calibration of all physical parameters for  $\text{Si}_{1-x}\text{Ge}_x$  at various concentrations, by matching results from simulations with the experimental data. In addition, simulations can be used to extract partition coefficients by calculating the final Ge distribution accurately, and offer insight on the real melt and solidification velocities for well-matching results.

Other codes were developed on Matlab® to reproduce the segregated Ge profiles, without taking into account the laser parameters.

##### 1. LIAB software

###### a) Simulation Model

The software is based on a Lagrange type finite element method, where the dimension (1D / 2D / 3D) and the mesh sizes are chosen by the user. Calculations are performed by coupling a time harmonic solution of Maxwell equations for the heat source with heat diffusion equations. As the material parameters evolve with temperature, hence modifying the light absorption, multiple loops are performed between these equations. This system cannot be modified by the user.

There are two “solver modes” available, which differ by the way phase is calculated. On one hand, the enthalpic solver is the simpler one, where the phase change depends only on the temperature: phase changes are considered to occur precisely at the melt or solidification temperature. On the other hand, the Phase Field solver is more complex, with a phase depending on more parameters, where undercooling can occur. More details, along with the exact equations used to define the system can be found in publications from SCREEN-LASSE or their partners [35]–[38]. This solver requires longer calculation times, but enables the simulation of the chemical diffusion and segregation, and take into account the evolution of optical and thermal parameters with this diffusion. As a result, it was the most used for SiGe layers, as the Ge segregation strongly impacts the solidification. However, the liquid phase nucleation requires a very short time-step with this type of solver, and it is therefore not

compatible with an industrial software. To avoid this problem, the liquid phase nucleation is made with the enthalpic model, and the calculation mode is switched from enthalpic to phase field once a thin liquid layer is obtained. An identical solution is used for the end of solidification, when the solver switches from phase field to enthalpic model.

#### b) Structures and solvers for Si<sub>1-x</sub>Ge<sub>x</sub> simulations

The structures for simulations were 1D structures, with adapted mesh sizes for each layer, as follows:

- Si<sub>1-x</sub>Ge<sub>x</sub> layer: epilayer with thickness matching the experimental thickness measured for the references and a 0.5 nm mesh. The material is defined as an alloy, so that segregation and modification of properties upon laser annealing is taken into account.
- Si<sub>0.99</sub>Ge<sub>0.01</sub> layer: 100 nm-thick SiGe layer with a 0.5 nm mesh, defined as an alloy with very low Ge content, to enable the simulation and segregation of Ge within the underlying Si in case the melting front goes beyond the initial Si<sub>1-x</sub>Ge<sub>x</sub> epilayer.
- Si buffer: 50 nm Si layer with mesh size at 5 nm, used to gradually adapt the mesh size from 0.5 nm to 50 nm.
- Si Substrate: 500 nm thick layer with a 50 nm mesh size.

The generic structure is shown in Figure II - 27.

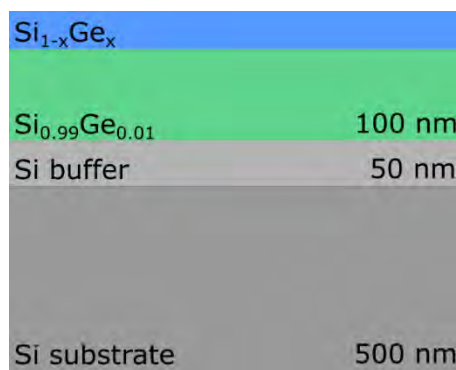


Figure II - 27. Stack used for LIAB simulation of laser annealing of SiGe layers.

The phase field solver was a 1D solver with a 7 μm-thick substrate that serves as a heat sink. It is defined as a coarse mesh for a short length and simple heat resistor for lower parts to facilitate calculations. At the onset of melt, the threshold thickness value of the liquid phase at which the solver switches from enthalpy to phase fields is ideal at 7 nm, while at the end of solidification, the switch from phase field to enthalpy occurs for a 0.001 nm-thick liquid layer. Finally, an artificial interface is defined between the solid and liquid regions in order to avoid abrupt changes in the physical parameters. Its thickness was fixed at 1 nm for the complete duration of calculations. The laser pulse profile was modified to match the real pulse duration at either 146 ns or 160 ns, by importing the recorded experimental pulse profile.

## 2. Segregation and elastic energy

### a) Segregation dependent on Ge concentration

The Ge partition coefficient depends on the solidification velocity and, to a lesser extent, on the Ge concentration in the layer [39], [40]. As simulations with LIAB cannot take this concentration dependence into account and necessitate rather complex calibration processes, a simpler code was developed using MATLAB® to reproduce final Ge concentration depth profiles. The physical phenomena leading to layer melt are overlooked, and calculations

of light absorption, heat diffusion, or phase field are not performed. The calculations only consider the basic mechanism of partition : the input parameters are the melt depth, the initial Ge concentration, the mean solidification velocity and the liquid/solid interface roughness, defined as the range from minimum melt depth to maximum melt depth at a given energy density.

The layer is divided in multiple sublayers with constant thickness (chosen by user). The ones "above" melt depth are defined as liquid, and the others as solid, as in Figure II - 28. The first step is to evaluate the amount of Ge in the liquid layer  $Ge_L$ . The calculation then proceeds sublayer by sublayer :

- If the maximum melt depth is within the depth of the initial solid layer, then  $Ge_L$  is equal to the initial concentration, as no redistribution occurs yet.
- If the stack melts beyond the SiGe layer, the Ge is redistributed in depth and the average content in the liquid layer is reduced. As we consider relatively low melt depths, it can be assumed that Ge has sufficient time to diffuse over the whole liquid layer, and that its concentration is homogeneous. The concentration in the liquid can therefore be calculated with a simple cross product.
- The partition coefficient  $k_i$  is calculated : it depends on both the Ge concentration at the interface and on the solidification velocity (indicated by user)
- The first sub-layer solidifies : the amount of Ge  $x_s^{i+1}$  incorporated in the new sublayer  $i+1$  is written as  $x_s^{i+1} = k_i \cdot x_l^i$ , where  $i$  designates the underneath sublayer.
- As only part of the Ge is incorporated in the solid layer, the liquid layer is enriched and its new content is :

$$x_l^{i+1} = \frac{x_l^i \cdot t_l^i - x_s^{i+1} \cdot h}{t_l^i - h} \quad \text{Eq. II - [27]}$$

Where  $t_l^i$  is the thickness of the liquid layer at time  $i$  and  $h$  is the sublayer thickness.

This loop is performed for every sublayer until the surface is reached, as shown in Figure II - 28. For a flat interface (i.e. equal to the sublayer thickness), a single profile is calculated. For a rough interface (often experimentally observed), multiple profiles are calculated with melt depths varying within the range indicated by user (=roughness).

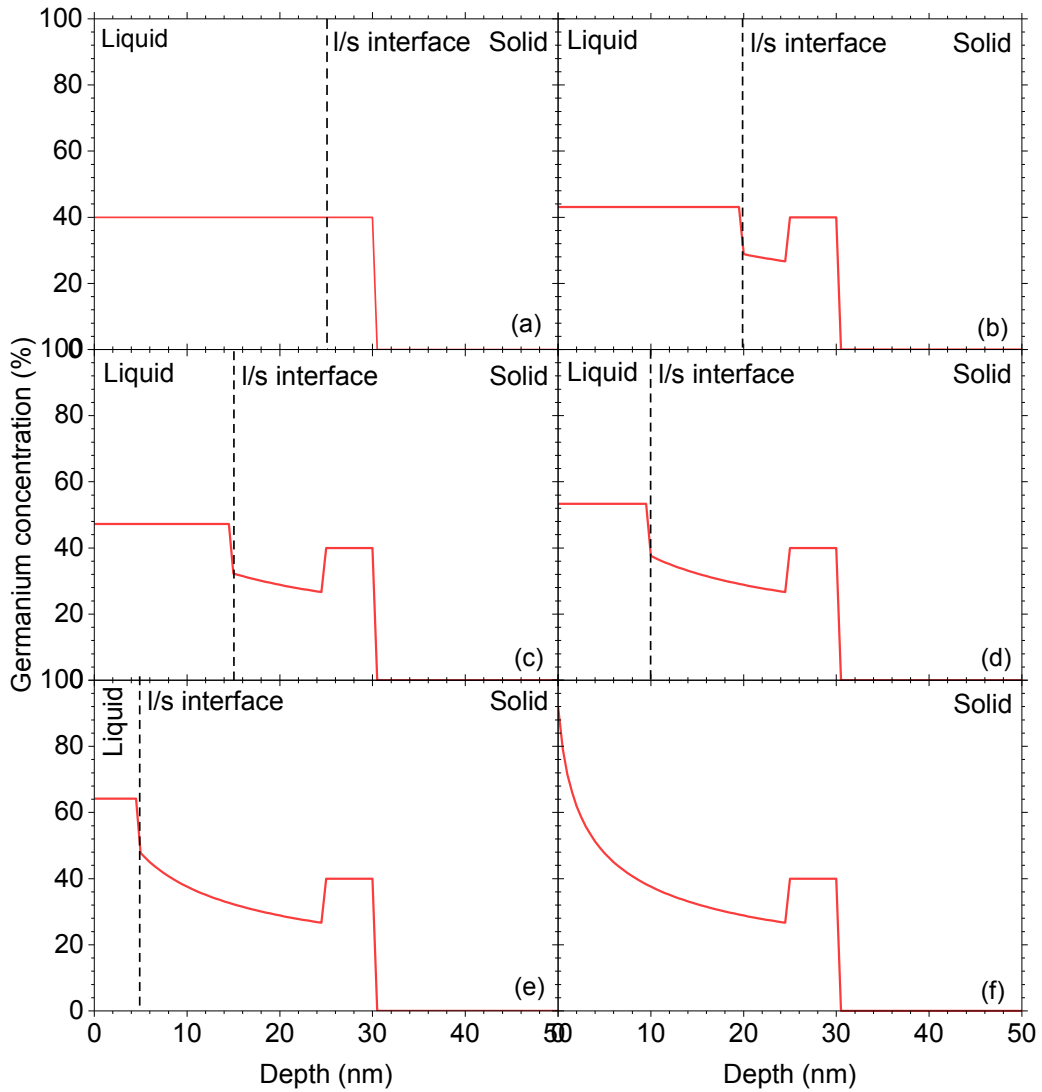


Figure II - 28. Calculation of the germanium concentration profile for an initially 30 nm thick  $\text{Si}_{0.6}\text{Ge}_{0.4}$  layer, with a melt depth at 25 nm. The solidification velocity was 1 nm/ns, and the sublayer thickness was 0.5 nm.

The partition coefficient is updated for every sublayer as it depends on the Ge amount near the interface. The data points are derived from literature [39], with an additional point at 100% at.Ge where  $k_i$  is taken equal to 1. The results allow to reproduce the experimental Ge profile and to evaluate the solidification velocity, as it required to fit the profile.

#### b) Elastic energy calculations

These calculations are performed to estimate the elastic energy density stored in the layer,  $E_{el}$  in  $\text{mJ}/\text{m}^2$ , akin to the critical thickness calculations for layers with a constant Ge content. As the Ge distribution exhibits strong gradients after UV-NLA, this calculation must be done by dividing the SiGe layer into multiple sublayers, with each a fixed Ge concentration, as in Figure II - 29. The thickness of a sublayer was chosen to be constant at 0.5 nm. The energy density of each individual sublayer is calculated separately, and cumulated to others to obtain the theoretical total energy density stored in the whole layer. It can be expressed as [41]:

$$E_{EL} = \int_{z=0}^{z=z_{max}} B \cdot \varepsilon(x)^2 \cdot dz \quad \text{Eq. II - [28]}$$

$$B = 2\mu(z) \cdot \frac{1 + \nu(z)}{1 - \nu(z)} \quad \text{Eq. II - [29]}$$

$$\varepsilon(z) = \frac{a_{SiGe} - a_{Si}}{a_{Si}} \quad \text{Eq. II - [30]}$$

Where  $z_{max}$  is the thickness of the SiGe layer,  $\varepsilon(z)$  is the strain,  $\mu(z)$  the shear modulus and  $\nu(z)$  the Poisson's ratio.  $a_{SiGe}$  and  $a_{Si}$  are respectively the lattice parameters of relaxed SiGe and Si. The strain, shear modulus and Poisson's ratio are all dependant on the Ge content in the sublayer, and thus on depth. They were derived from the elastic constants  $C_{11}$  and  $C_{12}$  [24].  $a_{SiGe}$  is calculated with :

$$a_0 = 5.43105 + 0.1988 \cdot x + 0.028 \cdot x^2 \quad \text{Eq. II - [31]}$$

With  $x$  the Ge content in the considered sublayer. This Ge content could be calculated either by modelling the experimental Ge profile, taking a point every 0.5 nm, or by using the data produced after simulation of the segregation, following the method presented in the previous section.

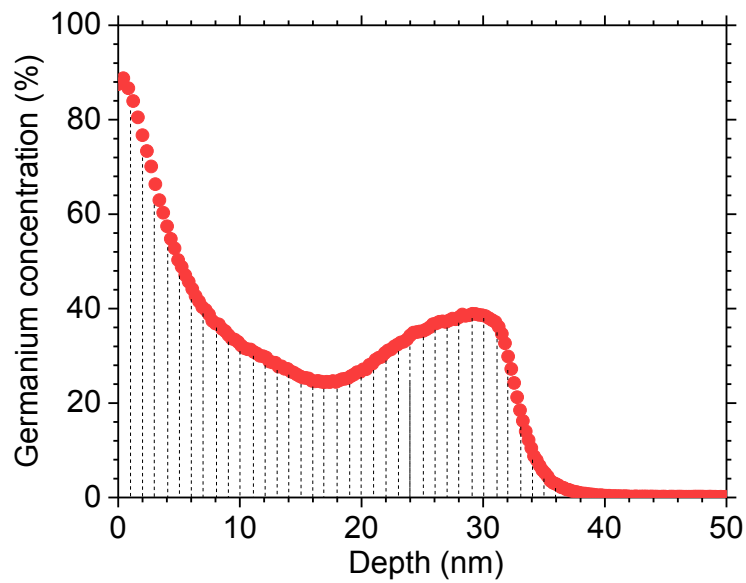


Figure II - 29. Slicing of a segregated Ge profile in multiple sublayers to calculate the elastic energy density in each sublayer. The step was chosen equal to 0.5 nm.

## CONCLUSION

Ultraviolet nanosecond laser annealing was performed with a LT3100 step-and-repeat tool from SCREEN-LASSE, using a 308 nm wavelength and a pulse duration at either 146 ns or 160 ns. The anneals were single pulse and performed at room temperature in most cases. Four series of samples were annealed with this tool, named "30 nm series", "Si<sub>0.7</sub>Ge<sub>0.3</sub> series", "Doped series" and "Amorphous series". Each series included several samples with varying parameters, either thickness or composition. The three first series of samples were prepared exclusively by RP-CVD in an Epsilon tool, while the last series included an additional implantation step. The NLA energy densities were chosen individually for each sample, to obtain conditions from the sub-melt up to the complete melt of the Si<sub>1-x</sub>Ge<sub>x</sub> layer.

The annealed layers were studied with multiple characterization methods, to gain insight on its surface state, chemical composition and redistribution, as well as crystalline and strain state. In-situ Time-Resolved Reflectivity was used during the anneal to record changes in reflectivity caused by the melt and solidification, while other characterizations were performed afterwards. Surface state was evaluated in all cases by SP2 Haze, with complementary information from AFM or SEM images. Strain and crystallinity were mainly assessed by X-ray diffraction and with TEM studies whenever possible, while composition was studied by SIMS and EDX.

Finally, 1D numerical simulation were performed using LIAB software and a homemade code via MATLAB. These simulations enabled to reproduce then predict Ge concentration depth profiles, Ge partition coefficients, melt depths as well as solidification velocities.

KEY INFORMATION

NLA tool LT3100	Industrial Nanosecond Laser Annealing Tool
1. Tool description	<ul style="list-style-type: none"> <li>➔ Produced by SCREEN-LASSE                             <ul style="list-style-type: none"> <li>○ XeCl laser with a 308 nm wavelength</li> <li>○ Pulse duration near 160 ns</li> <li>○ Step and repeat mode</li> </ul> </li> </ul>
2. Conditions	<ul style="list-style-type: none"> <li>➔ Controlled N<sub>2</sub> atmosphere, at room temperature</li> <li>➔ 129 laser shots on a 300 mm wafer</li> </ul>
Si and SiGe samples	Multiple samples to compare impact of thickness and composition
1. Samples	<ul style="list-style-type: none"> <li>➔ Grown in RP-CVD chamber at 20 Torr</li> <li>➔ Four series of samples                             <ul style="list-style-type: none"> <li>○ 30 nm series                      variable Ge content from 0 to 40%</li> <li>○ Si<sub>0.7</sub>Ge<sub>0.3</sub> series variable thicknesses</li> <li>○ Doped series                      variable boron concentration</li> <li>○ Amorphous series                variable amorphized thicknesses</li> </ul> </li> </ul>
2. Laser conditions	➔ Energy density ranges adapted for each sample
Characterization	Assessment of modifications caused by UV-NLA in Si <sub>1-x</sub> Ge <sub>x</sub>
1. Time resolved reflectivity	<ul style="list-style-type: none"> <li>➔ In-situ method</li> <li>➔ Records reflectivity changes caused by melt and solidification</li> </ul>
2. Surface state	<ul style="list-style-type: none"> <li>➔ Detect changes in surface roughness                             <ul style="list-style-type: none"> <li>○ Haze measurement on all samples</li> <li>○ AFM and SEM on selected samples for morphology</li> </ul> </li> </ul>
3. Crystalline quality	<ul style="list-style-type: none"> <li>➔ Relaxation level measured by XRD</li> <li>➔ Defect observations by TEM</li> </ul>
4. Composition	➔ In-depth composition profiles measured by SIMS and EDX
5. Electric	<ul style="list-style-type: none"> <li>➔ For boron-doped layers                             <ul style="list-style-type: none"> <li>○ Sheet resistance on all samples to study evolution</li> <li>○ Hall effect on selected samples for active dose estimation</li> </ul> </li> </ul>
Simulations	Calibration & simulation of the Ge segregated profiles
1. Predictions with LIAB	<ul style="list-style-type: none"> <li>➔ Software dedicated to UV-NLA simulations                             <ul style="list-style-type: none"> <li>○ Predictions for all annealing steps</li> <li>○ Ge profiles reproduction with constant partition coefficient <math>k_i</math></li> </ul> </li> </ul>
2. Composition and elastic energy	<ul style="list-style-type: none"> <li>➔ Developed during the Ph.D                             <ul style="list-style-type: none"> <li>○ Ge profiles reproduction with variable partition coefficient <math>k_i</math></li> <li>○ Calculation of stored elastic energy</li> </ul> </li> </ul>

## BIBLIOGRAPHY

- [1] R. Delmdahl et R. Pätzel, « Excimer laser technology trends », *J. Phys. D: Appl. Phys.*, vol. 47, n° 3, p. 034004, déc. 2013, doi: 10.1088/0022-3727/47/3/034004.
- [2] Y. Jin, Y. Zhao, et Y. Jiang, « Microlens beam homogenizer for excimer laser processing », *Journal of Laser Applications*, vol. 28, n° 2, p. 022601, mars 2016, doi: 10.2351/1.4944448.
- [3] K. Huet, I. Toqué-Tresonne, F. Mazzamuto, T. Emeraud, et H. Besaucèle, « Laser Thermal Annealing: A low thermal budget solution for advanced structures and new materials », in *2014 International Workshop on Junction Technology (IWJT)*, mai 2014, p. 1-6, doi: 10.1109/IWJT.2014.6842020.
- [4] K. Huet, F. Mazzamuto, T. Tabata, I. Toqué-Tresonne, et Y. Mori, « Doping of semiconductor devices by Laser Thermal Annealing », *Materials Science in Semiconductor Processing*, vol. 62, p. 92-102, mai 2017, doi: 10.1016/j.mssp.2016.11.008.
- [5] J. M. Hartmann, A. Abbadie, et S. Favier, « Critical thickness for plastic relaxation of SiGe on Si(001) revisited », *Journal of Applied Physics*, vol. 110, n° 8, p. 083529, oct. 2011, doi: 10.1063/1.3656989.
- [6] J. M. Hartmann et M. Veillerot, « HCl  $\text{+}$  GeH<sub>4</sub> etching for the low temperature cyclic deposition/etch of Si, Si:P, tensile-Si:P and SiGe(:B) », *Semicond. Sci. Technol.*, vol. 35, n° 1, p. 015015, nov. 2019, doi: 10.1088/1361-6641/ab52ec.
- [7] D. H. Auston, C. M. Surko, T. N. C. Venkatesan, R. E. Slusher, et J. A. Golovchenko, « Time-resolved reflectivity of ion-implanted silicon during laser annealing », *Appl. Phys. Lett.*, vol. 33, n° 5, p. 437-440, sept. 1978, doi: 10.1063/1.90369.
- [8] J. Boneberg et P. Leiderer, « On the Interpretation of Time-Resolved Surface Reflectivity Measurements during the Laser Annealing of Si Thin Films », *physica status solidi (a)*, vol. 166, n° 2, p. 643-650, doi: 10.1002/(SICI)1521-396X(199804)166:2<643::AID-PSSA643>3.0.CO;2-L.
- [9] D. H. Auston, J. A. Golovchenko, A. L. Simons, C. M. Surko, et T. N. C. Venkatesan, « Dynamics of Q-switched laser annealing », *Appl. Phys. Lett.*, vol. 34, n° 11, p. 777-779, juin 1979, doi: 10.1063/1.90670.
- [10] M. Diez, M. Ametowobla, et T. Graf, « Time-resolved reflectivity and temperature measurements during laser irradiation of crystalline silicon », *Journal of Laser Micro Nanoengineering*, vol. 12, n° 3, p. 230-234, 2017, doi: 10.2961/jlmn.2017.03.0010.
- [11] H. G. Tompkins et E. A. Irene, Éd., *Handbook of ellipsometry*. Norwich, NY : Heidelberg, Germany: William Andrew Pub. ; Springer, 2005.
- [12] V. Kanniah, E. A. Grulke, et T. Druffel, « The effects of surface roughness on low haze ultrathin nanocomposite films », *Thin Solid Films*, vol. 539, p. 170-180, juill. 2013, doi: 10.1016/j.tsf.2013.04.126.
- [13] E. Nolot et al., « Laser Scattering: a Fast, Sensitive, In-Line Technique for Advanced Process Development and Monitoring », *AIP Conference Proceedings*, vol. 931, n° 1, p. 116-120, sept. 2007, doi: 10.1063/1.2799354.
- [14] « Overview of AFM », in *Atomic Force Microscopy*, John Wiley & Sons, Ltd, 2012, p. 1-32.
- [15] C. Kittel, *Introduction to Solid State Physics*, 8<sup>e</sup> éd. Berkeley: Wiley, 2005.

- [16] C. Suryanarayana et M. G. Norton, « Lattices and Crystal Structures », in *X-Ray Diffraction: A Practical Approach*, C. Suryanarayana et M. G. Norton, Éd. Boston, MA: Springer US, 1998, p. 21-62.
- [17] M. Ladd et R. Palmer, *Structure Determination by X-ray Crystallography: Analysis by X-rays and Neutrons*, 5<sup>e</sup> éd. Springer US, 2013.
- [18] K. Inaba, « X-ray thin film measurement techniques 1 Overview », *The Rigaku Journal*, vol. 24, n° 1, p. 10-15, 2008.
- [19] S. Kobayashi et K. Inaba, « X-ray thin film measurement techniques 8 Detectors and series », *The Rigaku Journal*, vol. 28, n° 1, p. 8-13, 2012.
- [20] G. Mussler, « X-Ray diffraction of semiconductor heterostructures », 2020, [En ligne]. Disponible sur: [https://www.fz-juelich.de/SharedDocs/Downloads/PGI/PGI-3/Gruppe2/NanoelectronicCourseLab/Experiments/V11Script.pdf?\\_\\_blob=publicationFile](https://www.fz-juelich.de/SharedDocs/Downloads/PGI/PGI-3/Gruppe2/NanoelectronicCourseLab/Experiments/V11Script.pdf?__blob=publicationFile).
- [21] A. DURAND, « Characterization and industrial control of local stress in microelectronics », Theses, Ecole doctorale de Physique, 2016.
- [22] S. A. Speakman, « Introduction to High Resolution X-Ray Diffraction of Epitaxial Thin Films », Massachusetts Institute of Technology, [En ligne]. Disponible sur: <http://prism.mit.edu/xray/oldsite/Introduction%20to%20HRXRD.pdf>.
- [23] T. Konya, « X-ray thin film measurement techniques 3 High resolution diffractometry », *The Rigaku Journal*, vol. 25, n° 2, p. 1-26, 2009.
- [24] M. E. Levinshteĭn, S. L. Romyantsev, et M. Shur, *Properties of advanced semiconductor materials: GaN, AlN, InN, BN, SiC, SiGe*. New York: Wiley, 2001.
- [25] A. Rodríguez, T. Rodríguez, A. Kling, J. C. Soares, M. F. da Silva, et C. Ballesteros, « Strain and defects depth distributions in undoped and boron-doped Si<sub>1-x</sub>Ge<sub>x</sub> layers grown by solid phase epitaxy », *Journal of Applied Physics*, vol. 82, n° 6, p. 2887-2895, sept. 1997, doi: 10.1063/1.366121.
- [26] D. B. Williams et C. B. Carter, « The Instrument », in *Transmission Electron Microscopy: A Textbook for Materials Science*, D. B. Williams et C. B. Carter, Éd. Boston, MA: Springer US, 2009, p. 141-171.
- [27] D. B. Williams et C. B. Carter, « Diffraction in TEM », in *Transmission Electron Microscopy: A Textbook for Materials Science*, D. B. Williams et C. B. Carter, Éd. Boston, MA: Springer US, 2009, p. 197-209.
- [28] D. B. Williams et C. B. Carter, « Amplitude Contrast », in *Transmission Electron Microscopy: A Textbook for Materials Science*, D. B. Williams et C. B. Carter, Éd. Boston, MA: Springer US, 2009, p. 371-388.
- [29] A. V. Walker, « Secondary Ion Mass Spectrometry », in *Encyclopedia of Spectroscopy and Spectrometry (Third Edition)*, J. C. Lindon, G. E. Tranter, et D. W. Koppenaal, Éd. Oxford: Academic Press, 2017, p. 44-49.
- [30] M. Py, « Study of interfaces and nanometric structures by ToF-SIMS: upon a spatially resolved quantitative analysis », p. 277.
- [31] R. A. Dunlap, *Electrons in Solids*. IOP Publishing, 2019.

- [32] R. Daubriac, « Characterization of alternative ion implantation techniques for the optimization of the source-drain module of FDSOI 28 nm technology », Theses, INSA de Toulouse, 2018.
- [33] F. J. Morin et J. P. Maita, « Electrical Properties of Silicon Containing Arsenic and Boron », *Phys. Rev.*, vol. 96, n° 1, p. 28-35, oct. 1954, doi: 10.1103/PhysRev.96.28.
- [34] R. Daubriac, « Characterization of alternative ion implantation techniques for the optimization of the source-drain module of FDSOI 28 nm technology », Theses, INSA de Toulouse, 2018.
- [35] K. Huet et al., « Pulsed laser annealing for advanced technology nodes: Modeling and calibration », *Applied Surface Science*, p. 144470, nov. 2019, doi: 10.1016/j.apsusc.2019.144470.
- [36] S. F. Lombardo et al., « Phase field model of the nanoscale evolution during the explosive crystallization phenomenon », *Journal of Applied Physics*, vol. 123, n° 10, p. 105105, mars 2018, doi: 10.1063/1.5008362.
- [37] A. La Magna, P. Alippi, V. Privitera, G. Fortunato, M. Camalleri, et B. Svensson, « A phase-field approach to the simulation of the excimer laser annealing process in Si », *Journal of Applied Physics*, vol. 95, n° 9, p. 4806-4814, avr. 2004, doi: 10.1063/1.1690861.
- [38] G. Fisicaro et A. La Magna, « Modeling of laser annealing », *J Comput Electron*, vol. 13, n° 1, p. 70-94, mars 2014, doi: 10.1007/s10825-013-0545-9.
- [39] D. P. Brunco, M. O. Thompson, D. E. Hoglund, M. J. Aziz, et H. -J. Gossmann, « Germanium partitioning in silicon during rapid solidification », *Journal of Applied Physics*, vol. 78, n° 3, p. 1575-1582, août 1995, doi: 10.1063/1.360251.
- [40] M. Arivanandhan, R. Gotoh, K. Fujiwara, S. Uda, et Y. Hayakawa, « Segregation of Ge in B and Ge codoped Czochralski-Si crystal growth », *Journal of Alloys and Compounds*, vol. 639, p. 588-592, août 2015, doi: 10.1016/j.jallcom.2015.03.155.
- [41] A. I. Zhmakin, « Strain relaxation models », *arXiv preprint arXiv:1102.5000*, 2011.

---



# CHAPTER III

## ANNEALING REGIMES AND CHARACTERISTICS OF ANNEALED SiGe SAMPLES

I - REGIMES IDENTIFICATION .....	91
1. Regimes in Si <sub>1-x</sub> Ge <sub>x</sub> .....	91
a) UV-NLA on a pseudomorphic Si <sub>0.6</sub> Ge <sub>0.4</sub> crystalline layer.....	91
b) UV-NLA on an amorphous Si <sub>1-x</sub> Ge <sub>x</sub> layer .....	94
2. Extension to layers with different thicknesses and compositions .....	96
II - LAYER PROPERTIES AND IMPACT ON MELT THRESHOLD .....	98
1. Optical and thermal properties variations with composition.....	98
a) Evolution of optical indices .....	98
i. Ge concentration and temperature.....	98
ii. With B concentration and temperature.....	99
b) Evolution of thermal properties.....	101
2. Melt threshold evolution.....	101
III - SURFACE STRUCTURATIONS .....	102
1. Origin of surface roughness .....	102
a) Crystalline Si <sub>0.7</sub> Ge <sub>0.4</sub> layer.....	102
b) Amorphous Si <sub>0.7</sub> Ge <sub>0.3</sub> layer.....	104
2. Further analysis and impact of layer properties.....	105
a) Haze signal .....	105
b) Nanostructure shape: influence of concentration .....	106
c) Surface coverage by nanostructures .....	108
IV - SEGREGATION AND DIFFUSION DURING NANOSECOND LASER ANNEAL.....	110
1. Germanium segregation, a melt marker .....	110
a) Ge profiles after UV-NLA on crystalline layers .....	110
i. Observation of segregation.....	110
ii. Noticeable differences between SIMS and STEM-EDX .....	111
b) Melt depth and interface roughness.....	112
i. Melt depth evolution .....	112
ii. Maximum melt depth variability.....	114
c) Ge profiles after UV-NLA on amorphous layers .....	115
2. Segregation simulations .....	116
a) With a constant partition coefficient k <sub>i</sub> .....	117
i. Database calibration .....	117

ii. Ge segregation .....	117
b) With a variable partition coefficient $k_l$ .....	118
i. $k_l$ evolution with Ge content and solidification velocity .....	118
ii. Simulation results .....	119
V – MODIFICATIONS IN REFLECTIVITY SIGNALS .....	121
1. TRR signals on SiGe .....	121
a) Evolution with energy density .....	121
i. At high energy densities .....	121
ii. Evolution from sub-melt to full melt .....	122
iii. Origin of second slope .....	124
b) Impact of chuck temperature on signal .....	125
2. Kinetics evaluation .....	126
a) Automatic extraction .....	126
b) Melt duration evolution .....	127
c) Estimated liquid/solid interface velocities .....	128
i. Time required to melt the upper 20 nm .....	128
ii. Time required for the solidification of the upper 20 nm .....	129
CONCLUSION .....	132
KEY INFORMATION .....	133
BIBLIOGRAPHY .....	134

# CHAPTER III

## ANNEALING REGIMES AND CHARACTERISTICS OF ANNEALED SiGe SAMPLES

This chapter aims to present the different annealing regimes that were identified for laser annealed  $\text{Si}_{1-x}\text{Ge}_x$  layers when progressively increasing the energy density. The structural characteristics of each regime are detailed, with a focus on Ge segregation, surface morphology and information derived from Time-Resolved Reflectometry. Their dependence upon the layer features is explored, taking into account the thickness, the germanium content and/or the dopant concentration. The first section gives a brief overview of the regimes observed, and the laser energy density range for each series. The following sections are dedicated to the physical phenomena encountered on each regime, and how the initial samples characteristics are modified.

### I - REGIMES IDENTIFICATION

The regimes and their distinctive characteristics are described in subsection 1.a) for a pseudomorphic 30 nm-thick  $\text{Si}_{0.6}\text{Ge}_{0.4}$  layer submitted to laser annealing with various energy densities. Then, additional regimes observed when NLA is performed on a partially amorphized 30 nm-thick  $\text{Si}_{0.7}\text{Ge}_{0.3}$  layer (See Chapter I) will be described in subsection 1.b). These observations will then be extended to the other sample series to study their evolution with composition and thickness (subsection 2).

#### 1. Regimes in $\text{Si}_{1-x}\text{Ge}_x$

##### a) UV-NLA on a pseudomorphic $\text{Si}_{0.6}\text{Ge}_{0.4}$ crystalline layer

At low laser energy density, the first regime encountered is the sub-melt, in which the  $\text{Si}_{0.6}\text{Ge}_{0.4}$  layer remains solid though it is heated by the laser pulse. When increasing the ED, the reached maximum temperature increases as well. When the energy density is high enough, the SiGe can be melted. This transition can be detected thanks to the in-situ Time-Resolved Reflectometry (TRR), as the reflectivity of the liquid SiGe is higher than that of the solid. Several recorded TRR profiles are plotted in Figure III - 1, along with the corresponding laser pulse intensity as a function of the time.

At  $1.25 \text{ J/cm}^2$ , in Figure III - 1(a), the slight increase of the TRR signal is caused by changes in optical properties when the material temperature raises. However, the emergence of a peak, highlighted by a blue arrow, is observed at  $1.35 \text{ J/cm}^2$  in Figure III - 1(b), which corresponds to the onset of the melt. At higher energy densities, such as  $1.60 \text{ J/cm}^2$  and  $2.00 \text{ J/cm}^2$  in Figure III - 1 (c-d), the peak on the TRR signal lasts longer and becomes more intense, indicating that the melt duration and melt depth both increase. The TRR signals can be plotted as a colourmap, as shown in Figure III - 2. In this figure, the horizontal axis represents the time during the anneal, the vertical axis represents the energy density for each laser shot, while the colour scale represents the intensity of the TRR signal. This colormap therefore enabled to observe the evolution of the melt with both time and energy density: the melt threshold was detected by TRR near  $1.35 \text{ J/cm}^2$ , as seen on the individual profile. The melt threshold is followed by the surface melt regime, which is characterised by an increased surface roughness. The origin of the surface modifications leading to this increased roughness will be discussed in detail in section III of this chapter.

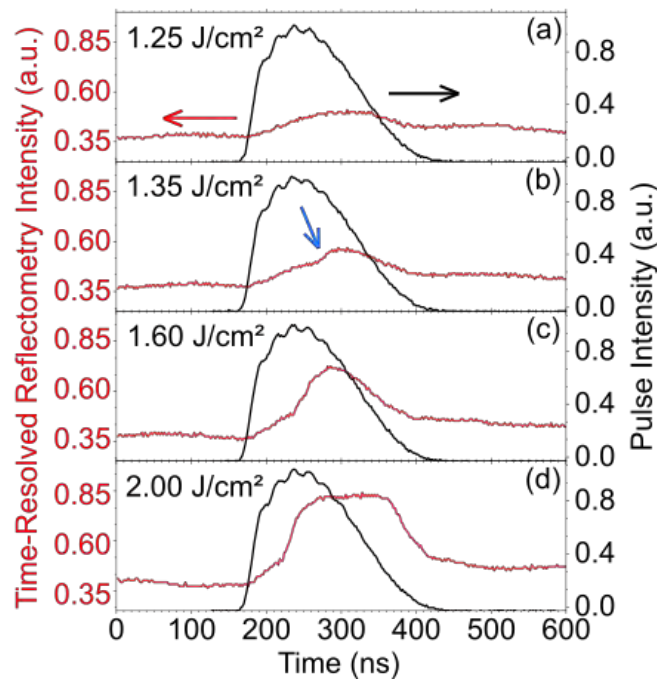


Figure III - 1. Time-Resolved Reflectometry profiles (red) and laser pulse (black) recorded during UV-NLA on a 30 nm-thick Si<sub>0.6</sub>Ge<sub>0.4</sub> layer at various energy densities. At 1.25 J/cm<sup>2</sup> (a), there is no trace of melt, while it appears above 1.35 J/cm<sup>2</sup> (b). The intensity increases for higher energy densities (c) and finally reaches a plateau (d).

Here, we report in Figure III - 3 the surface roughness values measured as a function of the laser energy density either by SP2 Haze (red squares) or AFM (RMS, black circles). Indeed, an increase is detected at 1.31 J/cm<sup>2</sup> on SP2 Haze, i.e. near the TRR melt threshold of the layer. Starting from a value of 0.3 nm after epitaxy, the surface roughness measured by AFM also increases up to 1.91 nm at 1.60 J/cm<sup>2</sup>, and then decreases for higher energy densities. Both signals stabilize for high energy densities, above 1.72 J/cm<sup>2</sup>. The surface roughness however remains slightly higher than its initial level (after epitaxy). The energy density interval corresponding the surface roughness increase therefore defines the extent of this surface melt regime.

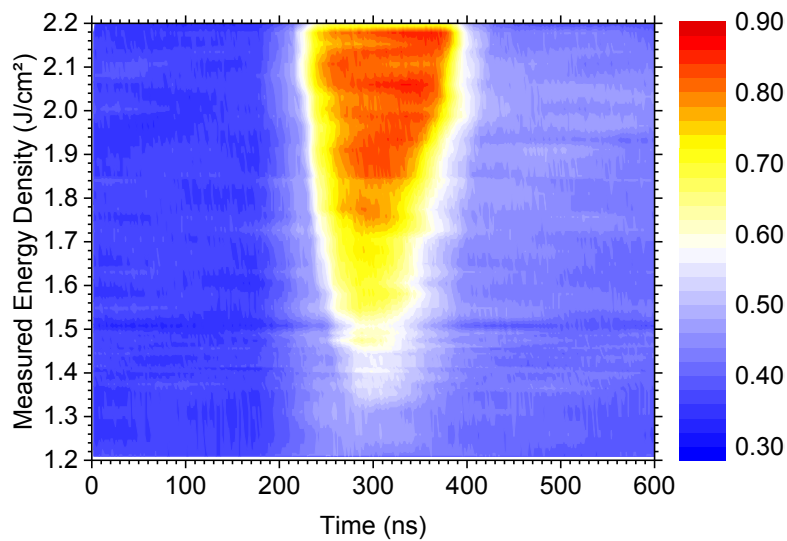


Figure III - 2. TRR colormap illustrating the evolution of the TRR signal as a function of time and laser energy density between 1.20 and 2.20 J/cm<sup>2</sup>, for a 30 nm-thick Si<sub>0.6</sub>Ge<sub>0.4</sub> layer submitted to UV-NLA. The melt threshold is found close to 1.35 J/cm<sup>2</sup>. The maximum energy density step was 50 mJ/cm<sup>2</sup>, and was as low as 10 mJ/m<sup>2</sup> near the melt threshold to study the transition.

When increasing further the energy density, the following regimes are partial melt and full melt, which can be distinguished by the melt depth. The maximum melt depth is located within the initial SiGe layer for the partial melt regime, while it extends beyond the initial SiGe/Si interface for the full melt regime. These regimes can be distinguished thanks to Ge concentration depth profiles, as the partition causes Ge redistribution starting from the liquid/solid interface. Such profiles are obtained by SIMS and showed in Figure III - 4.

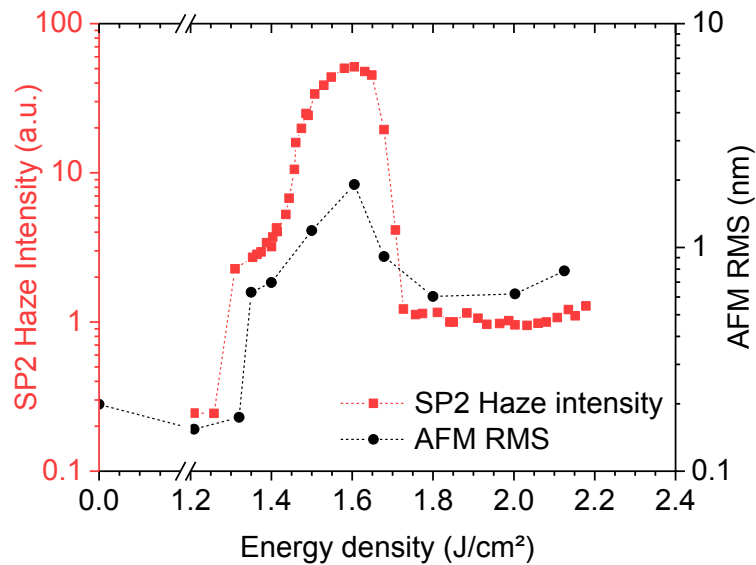


Figure III - 3. SP2 Haze (red squares) and AFM RMS roughness (black circles) as a function of the laser energy density. Both signals follow a similar trend, with an increase between 1.31 J/cm<sup>2</sup> and 1.72 J/cm<sup>2</sup>

The reference profile is flat, and is identical to the profile at 1.35 J/cm<sup>2</sup>. Variations in the SiGe/Si interface depths can be observed. These variations, up to ~3 nm, are likely due to layer non-uniformities, as they roughly correspond to the thickness variation range observed with ellipsometry (see Figure II – 9). Errors in the sputtering rate correction may also occur during the SIMS analysis, but they do not appear to have a strong impact.

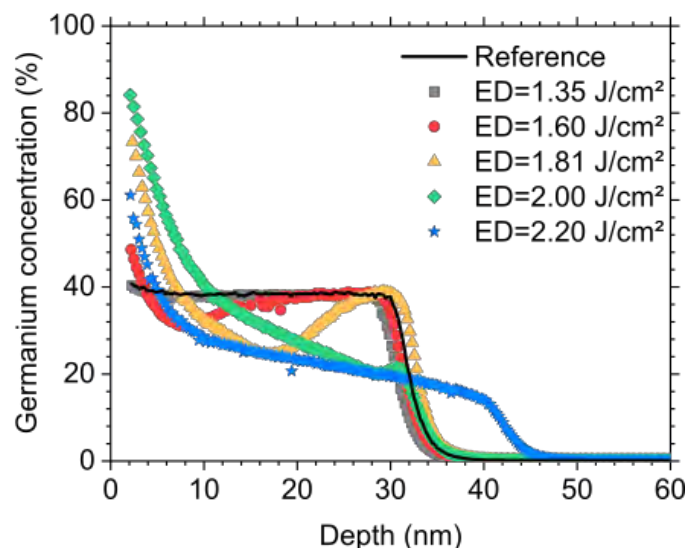


Figure III - 4. ToF-SIMS germanium concentration depth profiles for 30 nm thick Si<sub>0.6</sub>Ge<sub>0.4</sub> samples annealed at laser energy densities from 1.35 J/cm<sup>2</sup> to 2.20 J/cm<sup>2</sup>.

During the solidification, the partition causes an accumulation of germanium near the surface, leading to the gradients observed at 1.81, 2.00 and 2.20 J/cm<sup>2</sup>. At 1.81 and 2.00 J/cm<sup>2</sup>, the SiGe/Si interface is still located 34 nm-deep, near its original position: these resulting samples

are in the partial melt regime. In contrast, the Ge diffused beyond the original interface for the sample annealed at  $2.20 \text{ J/cm}^2$ , indicating that the full melt was reached. In that case, the melt depth was 45 nm. The transition from partial to full melt can also be deduced from TRR measurements, as a discontinuity in melt duration can be observed. This was however not observed for the 30 nm-thick  $\text{Si}_{0.6}\text{Ge}_{0.4}$  layer, due to an imperfect diode calibration at the time, which has improved since then. An example is shown in Figure III - 6, for a 30 nm-thick  $\text{Si}_{0.7}\text{Ge}_{0.3}$  layer that was amorphized over 15 nm by Ge implantation. A slight inflection can be observed in the red and yellow pattern at around  $2.20 \text{ J/cm}^2$  ( $t \sim 270 \text{ ns}$ ).

In summary, when annealing a 30 nm thick pseudomorphic SiGe layer grown on a Si substrate with increasing laser energy densities, the various regimes encountered are : (i) the sub-melt, as long as SiGe remains in the solid phase; (ii) the surface melt regime in which the very first nanometers are melted and the surface exhibits a high roughness; (iii) the partial melt regime ending when the maximum melt depth reaches the initial SiGe/Si interface; (iv) the full melt regime corresponding to a melting front that entered into the underlying substrate.

#### b) UV-NLA on an amorphous $\text{Si}_{1-x}\text{Ge}_x$ layer

30 nm-thick  $\text{Si}_{0.7}\text{Ge}_{0.3}$  were amorphized by Ge implantation to obtain 15 nm and 30 nm thick a-SiGe layers, using  $1.5 \times 10^{15} \text{ at/cm}^2$  doses for both and respectively 6 keV and 16 keV. The laser annealing regimes introduced previously slightly differ for a stack with an amorphous layer, due to the melt of the amorphous SiGe (a-SiGe) at lower temperature than crystalline SiGe (c-SiGe). This results in the formation of an undercooled SiGe liquid layer and its subsequent explosive crystallization. The explosive threshold, i.e. the lowest energy density for which melt and solidification of the a-SiGe occurs, as well as the onset of a second melt, are detected by TRR as shown in Figure III - 5. In the sub-melt regime, Figure III - 5 (a), the TRR slightly increases due to the change in optical parameters with temperature, as it does for crystalline layers.

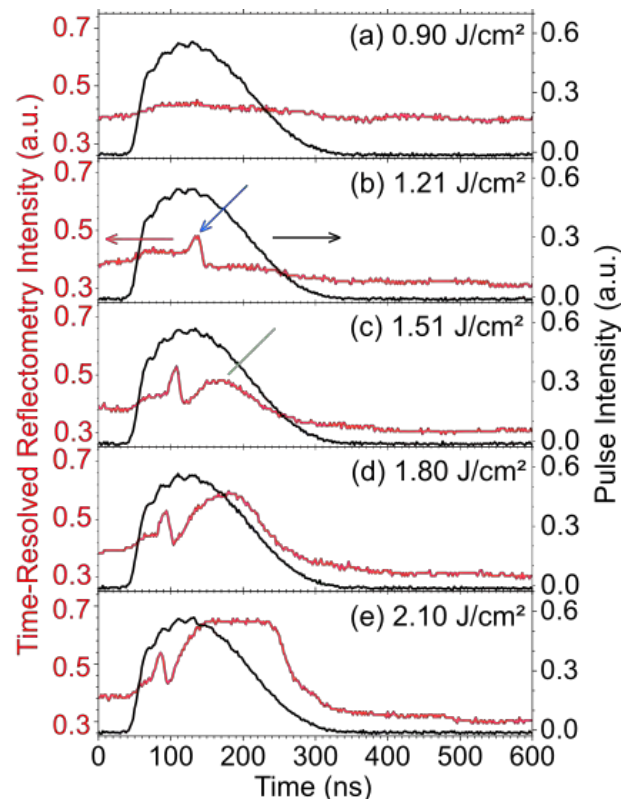


Figure III - 5. TRR profiles measured during UV-NLA of a 30 nm-thick  $\text{Si}_{0.7}\text{Ge}_{0.3}$  layer, amorphized over 15 nm by Ge implantation. The profiles correspond to annealing with a single laser pulse at  $0.90 \text{ J/cm}^2$  (a),  $1.21 \text{ J/cm}^2$  (b),  $1.51 \text{ J/cm}^2$  (c),  $1.80 \text{ J/cm}^2$  (d) and  $2.10 \text{ J/cm}^2$  (e).

The a-SiGe melt is indicated by a sharp peak in TRR signal, for only a few nanoseconds, as shown in Figure III - 5(b) by the blue arrow. It occurs first at 1.05 J/cm<sup>2</sup> and this is the beginning of the 'explosive regime'. During the explosive crystallization, the liquid resulting from the melt of the amorphous layer solidifies at high velocities, forming a nano- or poly-crystalline SiGe layer. At higher energy densities, it becomes possible to melt this layer a second time within the same laser pulse: this is the second melt, visible on Figure III - 5(c-d-e), with a green arrow on (c). The onset of the second melt corresponds to the end of the 'explosive' regime and the beginning of the 'surface melt' regime. It can also be observed on the TRR color map shown in Figure III - 6. It occurred at 1.35 J/cm<sup>2</sup> for this layer. This second melt can then extend through the newly formed polycrystalline layer, which leads to the increased intensity as seen in Figure III - 5(d-e). The plateau is reached when more than 20 nm melt.

Concerning the colormap, it should be noted that the photodiode calibration procedure differed between the Figure III - 2 and Figure III - 6. The intensity values cannot therefore be directly compared. In addition, the timescale was corrected, as a 126 ns delay was introduced in the signal due to optical line and electronics delays, to compensate the time required for light to be transmitted to the process module and back to the oscilloscope. In Figure III - 6, the pulse starts near 35 ns, whereas in Figure III - 2 it corresponds to ~160 ns.

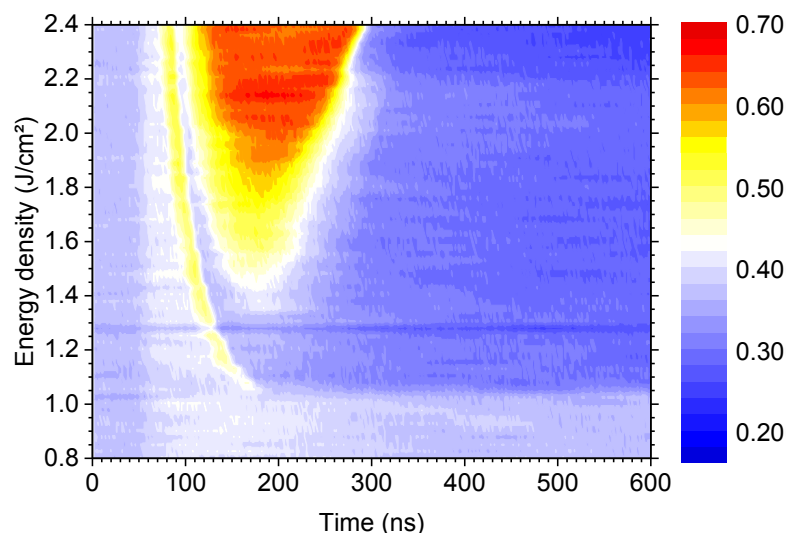


Figure III - 6. TRR signal colormap for a 30 nm-thick Si<sub>0.7</sub>Ge<sub>0.3</sub> layer, amorphized over 15 nm by Ge implantation and submitted to UV-NLA at energy densities from 0.80 J/cm<sup>2</sup> to 2.40 J/cm<sup>2</sup>. Amorphous SiGe melt and the subsequent explosive crystallization are detected from 1.05 J/cm<sup>2</sup>, second melt from 1.35 J/cm<sup>2</sup>, while the full melt occurs between 2.10 and 2.33 J/cm<sup>2</sup>.

The melt is accompanied by an increase in surface roughness detected by SP2 Haze intensity, as soon as the explosive crystallization occurs, as shown in Figure III - 7 with the SP2 Haze intensity. This peak is observed from 1.05 J/cm<sup>2</sup> (explosive regime onset) and continues up to 1.88 J/cm<sup>2</sup>, i.e. until the end of the surface melt regime, similarly to the case of an initially crystalline SiGe layer. A drop in Haze intensity is observed after 1.05 J/cm<sup>2</sup>, before returning to high values. Its origin remains unknown, and may be related to a change in the melt propagation at the onset of the explosive regime. During the explosive regime, only the amorphous layer melts. Once the second melt is reached (within the surface melt regime), the melt depth can progressively extend through the polycrystalline SiGe layer, the monocrystalline SiGe layer and finally the bulk Si. The partial and full melt regimes can be distinguished by either Ge depth profiles or TRR measurements, as it was done for crystalline layers.

In summary, compared to the case of an initially crystalline SiGe layer, the presence of an amorphous layer at the surface of the SiGe layer leads to an additional regime between the sub-melt and the surface melt: the explosive regime characterized by the melt of the

amorphous layer (only) and its subsequent explosive crystallization. The other regimes encountered at higher laser energy density values, namely the surface melt, the partial melt and the full melt regimes can happen as well, but during a second melt after the explosive recrystallization occurring during the first part of the laser pulse.

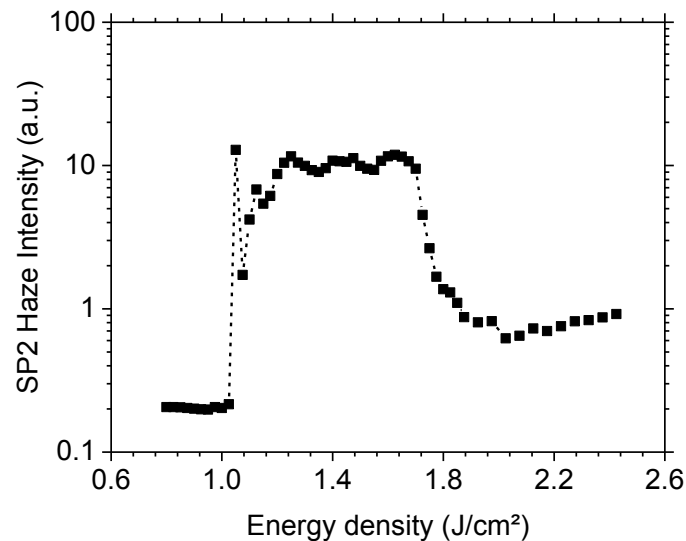


Figure III - 7. SP2 Haze intensity as a function of the laser energy density for a 30 nm-thick  $\text{Si}_{0.7}\text{Ge}_{0.3}$  layer, amorphized over 15 nm by Ge implantation, showing a peak between 1.05  $\text{J}/\text{cm}^2$  and 1.88  $\text{J}/\text{cm}^2$ .

## 2. Extension to layers with different thicknesses and compositions

The sub-melt, surface melt, partial melt and full melt regimes can be observed in every  $\text{Si}_{1-x}\text{Ge}_x$  sample, with different energy density ranges depending on the layer composition and/or thickness. The limits for each series of samples are presented in Figure III - 8, where each regime corresponds to a given color. The exact energy density values for the limits are directly given on the graphs. For comparison, the regimes observed after laser annealing on bulk silicon are also provided. It should be noted that the anneals for the "30 nm series" were performed with a 146 ns pulse duration, while all the other series were performed with a 160 ns laser pulse duration. This explains the slight differences in regimes between the 30 nm-thick  $\text{Si}_{0.7}\text{Ge}_{0.3}$  samples from the "30 nm series" and the " $\text{Si}_{0.7}\text{Ge}_{0.3}$  series". For easier understanding, whenever possible, the samples characteristics will be discussed as part of a regime rather than with respect to their exact energy density. As various characterizations can be used for regime limit determination, the origin of the values indicated on Figure III - 8 are detailed below:

- 30 nm series - Figure III - 8 (a): the melt threshold, as well as the end of surface melt, were determined by SP2 Haze. The melt threshold could also be measured with TRR. The limit between partial and full melt in  $\text{Si}_{1-x}\text{Ge}_x$  was obtained from the ToF-SIMS germanium concentration depth profiles.
- Amorphous series - Figure III - 8 (b): the explosive regime onset was inferred from both SP2 Haze and TRR, with almost identical results. The limit between the purely explosive regime and the surface melt regime was also derived from TRR, with the appearance of the second melt peak. The upper limit of the surface melt regime was inferred from SP2 Haze measurements, while the transition from partial to full melt was obtained from TRR maps (melt duration variations).
- Doped series - Figure III - 8 (c) and  $\text{Si}_{0.7}\text{Ge}_{0.3}$  series - Figure III - 8 (d): the melt threshold was measured with both TRR and SP2 Haze and the surface melt regime with SP2 Haze. The transition from partial to full melt was deduced from both SIMS observations and TRR signals. The graphs show the TRR results.

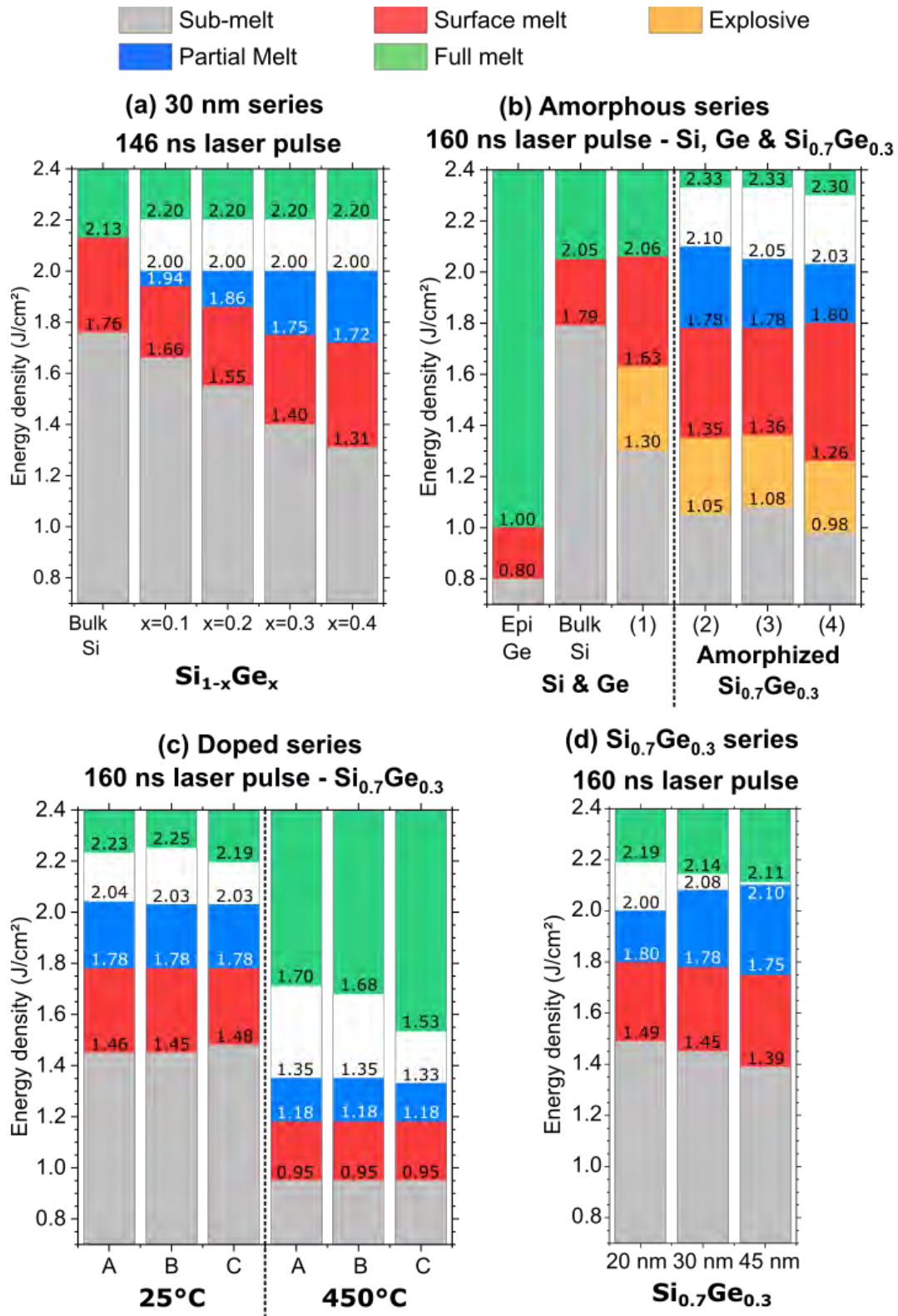


Figure III - 8. Summary of the laser annealing regimes observed for all the investigated samples. (a) 30 nm series with various Ge contents. (b) Amorphous series (Si or 30 nm-thick  $\text{Si}_{0.7}\text{Ge}_{0.3}$  layers). All samples are undoped except sample (3) (Boron doped). Si sample (1) and  $\text{Si}_{0.7}\text{Ge}_{0.3}$  samples (2, 3) are amorphized over 15 nm, while  $\text{Si}_{0.7}\text{Ge}_{0.3}$  sample (4) is amorphized to 30 nm. (c) Doped series. Laser annealing was performed while the samples were in contact with a chuck at 25°C (default value) or 450°C. (d)  $\text{Si}_{0.7}\text{Ge}_{0.3}$  series with different layer thickness.

These regimes, their different characteristics and their origins are detailed in the following sections, with comparison between the various samples.

## II - LAYER PROPERTIES AND IMPACT ON MELT THRESHOLD

As seen on Figure III - 8, modifications in the SiGe layer lead to a change in the melt threshold. This section focuses on detailing how the thermal and optical properties are modified by changes in composition and temperature, and how it impacts the melt threshold.

### 1. Optical and thermal properties variations with composition

#### a) Evolution of optical indices

##### i. Ge concentration and temperature

The evolution of optical indices with both Ge concentration and temperature was elucidated with ellipsometry. Samples from the “30 nm series” were submitted to spectroscopic ellipsometry while being heated from room temperature up to 600°C. The calculated  $n$  and  $k$  coefficients (see Chapter III section III – 2.) for  $\lambda=308$  nm (nanosecond laser wavelength) and  $\lambda=635$  nm (in-situ TRR wavelength) are presented in Figure III - 9 as a function of temperature.

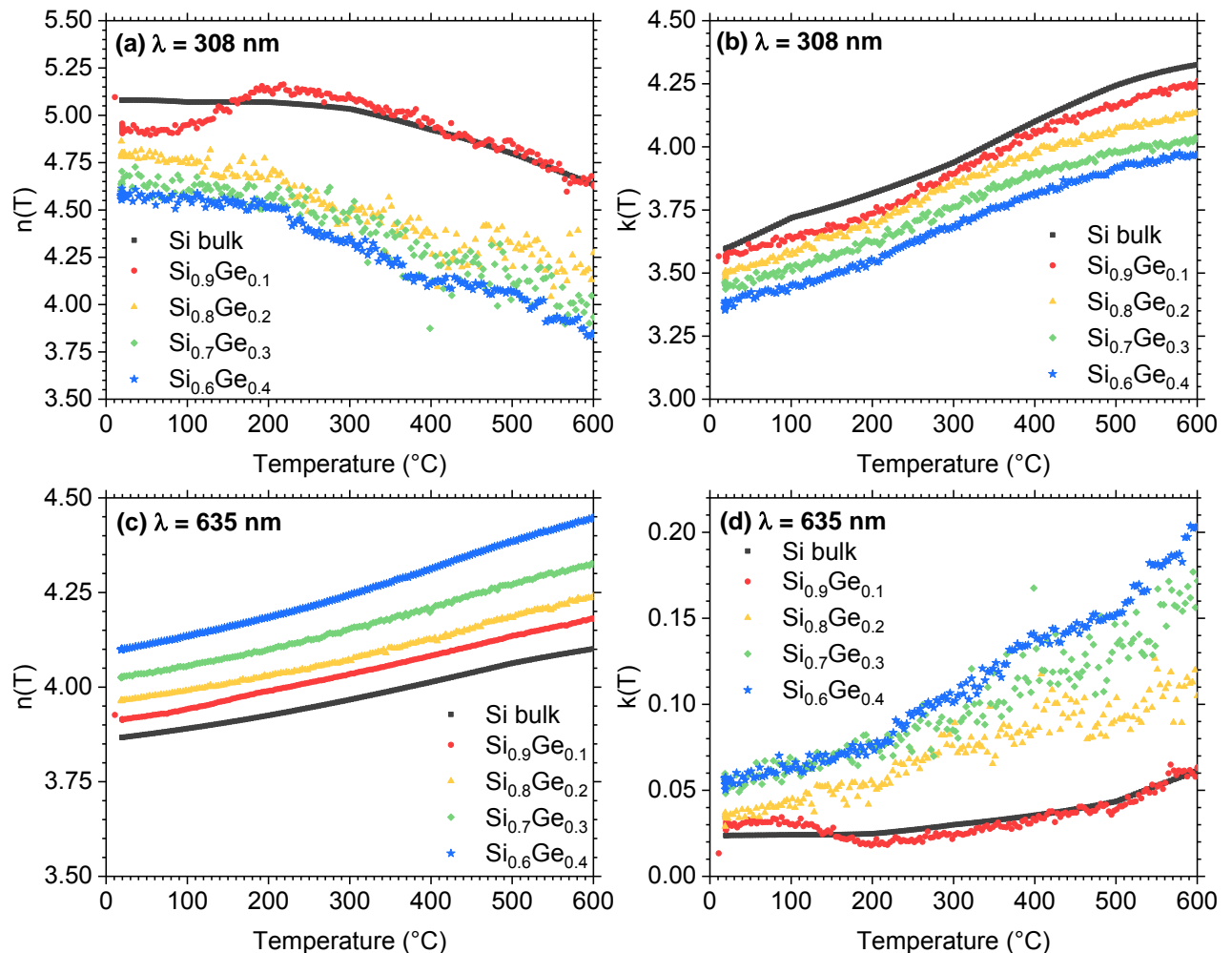


Figure III - 9. Refractive index  $n$ , (a,c) and extinction coefficient  $k$  (b,d) as a function of temperature for Si<sub>1-x</sub>Ge<sub>x</sub> layers ( $x=\{0, 0.1, 0.2, 0.3, 0.4\}$ ) for the laser annealing wavelength at 308 nm (a,b) and probing laser at 635 nm (c,d).

For a 308 nm wavelength (Figure III - 9(a-b)) at room temperature, both indices show a decrease when increasing the Ge content. “Cold” Ge-rich layers have therefore a lower

intrinsic reflectivity, and a higher absorption length. With increasing temperature,  $n(T)$  tends to decrease in a similar way for all concentrations, except for  $\text{Si}_{0.9}\text{Ge}_{0.1}$ .  $k(T)$  however increases with temperature for all concentrations. These measured  $n$  &  $k$  values in the 25-600°C range were also extrapolated using a second order polynomial fit up to the  $\text{Si}_{1-x}\text{Ge}_x$  melting point and used for the numerical simulations published in [1,2] and detailed in Chapter II, section IV – 1. For a 635 nm wavelength (Figure III - 9(c-d)) at room temperature, the situation is reversed. Both  $n(T)$  and  $k(T)$  increase with the Ge content, leading to a higher reflectivity and lower absorption lengths for Ge-rich alloys.

The evolution of reflectivity with Ge concentration was confirmed by TRR observations on samples at room temperature. As the TRR measurement started 126 ns before the laser pulse reached the sample surface, it was possible to obtain a mean value of the TRR intensity by averaging the 50 first data points. This was performed for each of the 46 laser shots at every concentration for the 30 nm series: the graph in Figure III - 10 presents the mean value with these 46 values at each concentration. The obtained intensity increases linearly with the Ge concentration, which supports the previous ellipsometry measurements at 635 nm.

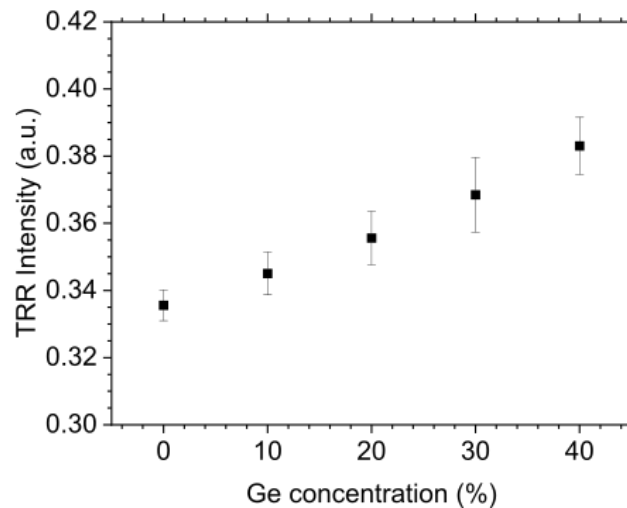


Figure III - 10. Evolution of the TRR signal (635 nm) measured at room temperature for the '30 nm series', i.e.  $\text{Si}_{1-x}\text{Ge}_x$  layers ( $x=\{0, 0.1, 0.2, 0.3, 0.4\}$ ). An increase of reflectivity is observed as the Ge concentration becomes higher.

#### ii. With B concentration and temperature

Identical experiments were performed on the "Doped Series", with boron-doped 30 nm thick  $\text{Si}_{0.7}\text{Ge}_{0.3}$  layers. Three high boron concentrations ( $\sim 10^{20}$  B/cm<sup>3</sup>) were studied, as detailed in Chapter II. The results of spectroscopic ellipsometry as a function of the temperature for  $\lambda=308$  nm and  $\lambda=635$  nm are displayed in Figure III - 11. The three doped samples show almost identical results for both  $n(T)$  and  $k(T)$  and for both wavelengths. They however differ from the indices obtained for undoped  $\text{Si}_{0.7}\text{Ge}_{0.3}$  at 308 nm,  $n(T)$  increases with the B concentration and a slight increase of  $k(T)$  is observed with B level, up to 300°C. The values vary with temperature:  $n(T)$  remains almost stable up to 600°C and  $k(T)$  increases.

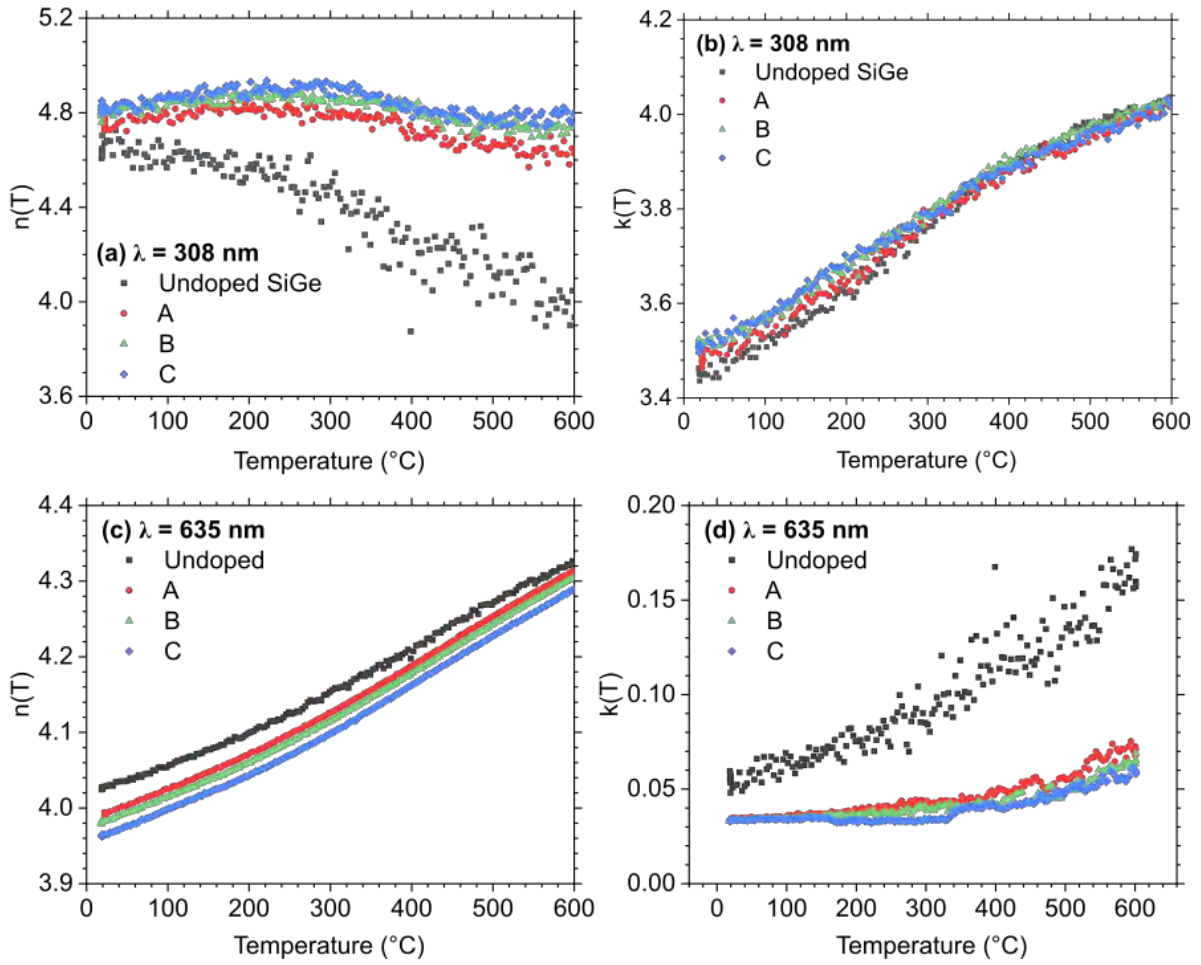


Figure III - 11. Refractive index  $n$  (a,c) and extinction coefficient  $k$  (b,d) as a function of temperature for boron doped  $\text{Si}_{0.7}\text{Ge}_{0.3}$  layers for the annealing wavelength at 308 nm (a,b) and TRR probing wavelength 635 nm (c,d).

At 635 nm, at all temperatures, the refractive index  $n$  slightly decreases when the B concentration increases, while  $k(T)$  is identical for each concentration. The very slight change in reflectivity can be observed from the TRR on samples at room temperature, as shown in Figure III - 12.

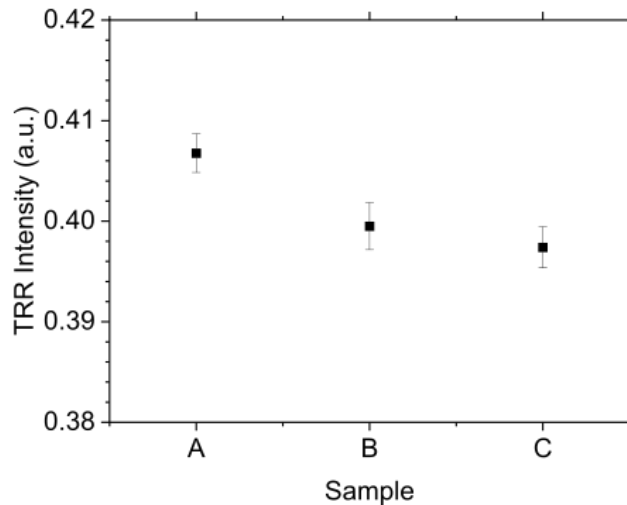


Figure III - 12. Evolution of TRR intensity for boron doped  $\text{Si}_{0.7}\text{Ge}_{0.3}$  layers at room temperature, with various boron concentrations. An decrease of reflectivity is observed as the B concentration becomes higher. These results cannot be compared with the results in Figure III - 10 due to changes in the photodiode calibration.

## b) Evolution of thermal properties

Thermal properties also vary with the Ge content in the layer. As mentioned in Chapter I, the melt temperature decreases for increasing Ge content, with liquidus  $T_L$  and solidus  $T_s$  evolutions as follows:

$$T_L = 1412 - 738 \cdot x + 236 \cdot x^2$$

$$T_s = 1412 - 80 \cdot x - 395 \cdot x^2$$

The thermal conductivity  $\kappa$  (in  $\text{W}\cdot\text{cm}^{-1}\cdot\text{K}^{-1}$ ) is known for Ge content between  $x=0.2$  and  $x=0.85$ , and can be expressed as:

$$\kappa = 0.046 + 0.084 \cdot x$$

It slightly increases with Ge content, but remains lower than the values for pure Si or pure Ge.

The evolution of optical and thermal parameters with temperature was studied, including the variations caused by the Ge or B content. These measurements are particularly useful for simulation calibration.

## 2. Melt threshold evolution

The evolution of melt threshold with Ge concentration, layer thickness or doping level is presented in Figure III - 13. The results from both TRR and SP2 Haze techniques follow an identical trend, though the melt threshold detection occurs at systematically lower energy densities with SP2 Haze. This is likely due to the higher sensitivity of the SP2 Haze technique to the presence of surface nanostructures able to scatter light and resulting from isolated molten regions, whereas a larger molten volume is most likely necessary in order to generate a detectable TRR signal (molten volume estimated to be equivalent to 4 nm thin layer on bulk Si).

In the 30 nm series, the energy density necessary to reach the melt decreased as the germanium content in the epi-layer increased. This is consistent with the lower melt temperature of a Ge-rich alloy. Besides, according to Fresnel formula in case of normal incidence, the reflection coefficient is all the more important that the refractive index of the SiGe layer is high. The decreasing refractive index at 308 nm when increasing the Ge content (Figure III - 9(a)) thus likely contributes to reduce the required laser energy density to reach the melting point, but this effect may be minor compared to the reduction of the melting temperature itself at higher Ge concentrations and both contributions cannot be deconvoluted here. The increase in layer thickness (Figure III - 13 (b)) also leads to lower melt thresholds. As there are no changes in melt temperature, this is probably due to the reduced heat conductivity in  $\text{Si}_{0.7}\text{Ge}_{0.3}$  compared to Si, though the thickness variations may also modify the stack reflectivity. For comparison, open symbols corresponding to the  $\text{Si}_{0.7}\text{Ge}_{0.3}$  layer from the 30 nm series were added in Figure III - 13(b). A slight discrepancy in melt threshold can be noticed between the 30 nm-thick  $\text{Si}_{0.7}\text{Ge}_{0.3}$  layers from the "30 nm series" and " $\text{Si}_{0.7}\text{Ge}_{0.3}$  series", with respectively 1.40 J/cm<sup>2</sup> and 1.45 J/cm<sup>2</sup> (with the Haze measurement). The value observed with TRR are however identical. This is attributed to the difference in pulse duration, as it modifies the energy deposition. Finally, there is no obvious modification of melt threshold with the boron concentration, even when compared to undoped layers.

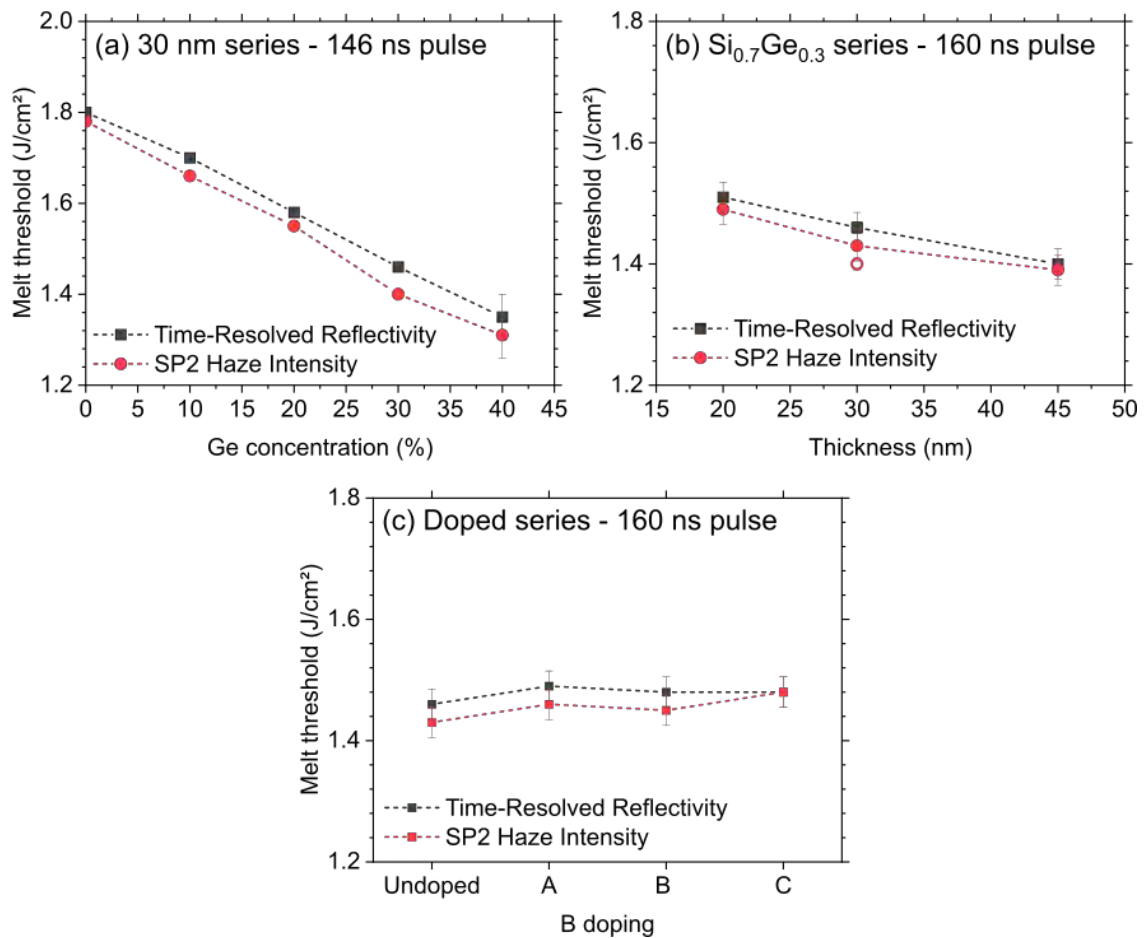


Figure III - 13. Evolution of melt threshold as a function of different SiGe layer parameters for various sample series. (a) "30 nm series": melt threshold vs. Ge concentration. (b) "Si<sub>0.7</sub>Ge<sub>0.3</sub> series": melt threshold vs. layer thickness. Empty symbols correspond to the 30 nm-thick Si<sub>0.7</sub>Ge<sub>0.3</sub> layer from the "30 nm series" for comparison. (c) "Doped series": melt threshold vs. Boron concentration. TRR and SP2 Haze measurements show good agreement in all cases.

### III - SURFACE STRUCTURATIONS

The second regime, occurring after sub-melt, is characterized by a strong increase in surface roughness. This section aims to explain its origins and evolution with energy density and/or layer composition.

#### 1. Origin of surface roughness

##### a) Crystalline Si<sub>0.7</sub>Ge<sub>0.4</sub> layer

STEM-HAADF observations were performed on the 30 nm-thick Si<sub>0.6</sub>Ge<sub>0.4</sub> layer ("30 nm series") presented in I – 1.a), after annealing at 1.40 J/cm<sup>2</sup> and 1.60 J/cm<sup>2</sup>, within the surface melt regime. STEM-HAADF of both samples are shown in Figure III - 14 : multiple bright hillocks are visible near the surface in both images, and appear more defined at 1.60 J/cm<sup>2</sup>. Figure III - 15 (a) shows one of the micrographs collected at 1.60 J/cm<sup>2</sup>, where some of the surface hillocks can be noticed on the sides. The centre of the observed area was flat, with a uniform contrast, while both sides showed hillocks with chemical contrast variations. Identical hillocks could be seen on the whole TEM cross-section and on the sample annealed with a lower energy density (1.40 J/cm<sup>2</sup>).

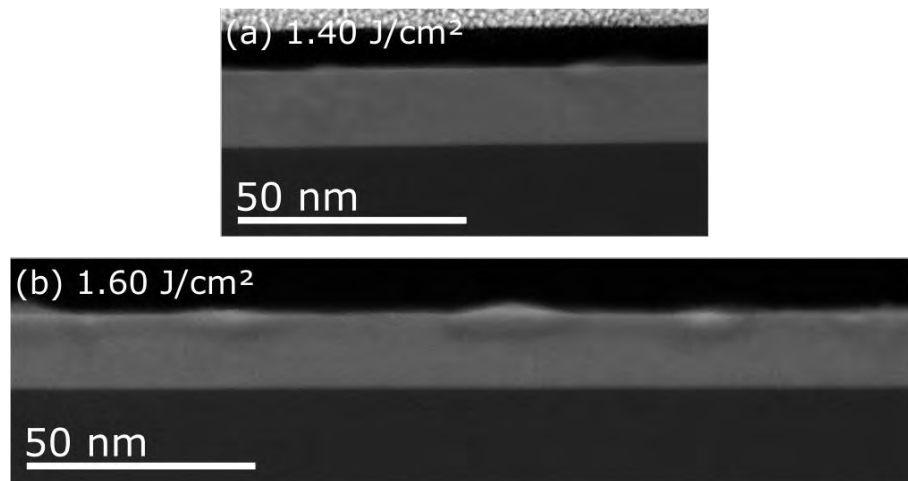


Figure III - 14. STEM-HAADF images on a 30 nm-thick  $\text{Si}_{0.6}\text{Ge}_{0.4}$  sample annealed at (a)  $1.40 \text{ J/cm}^2$  and (b)  $1.60 \text{ J/cm}^2$ . Both images present bright hillocks near the layer surface. They are more visible after annealing at  $1.60 \text{ J/cm}^2$ .

Germanium concentration profiles collected by STEM EDX were performed on the areas corresponding to the red and green squares: they are plotted as a function of depth in Figure III - 15 (b). The green profile, with an almost constant Ge content ( $\sim 40\%$ ), corresponds to the flat area in the centre. It therefore corresponds to an unmelted area since no segregation occurred (See Chapter I for segregation). In contrast, the red profile obtained along the hillock showed that the layer has been melted down to almost 10 nm in this area during the laser anneal, with significant Ge surface segregation. Isolated melted islands were thus formed on the surface, rather than a continuous liquid layer at these energy densities slightly above the melt threshold. This annealing regime can therefore be referred to as a “surface melt” regime.

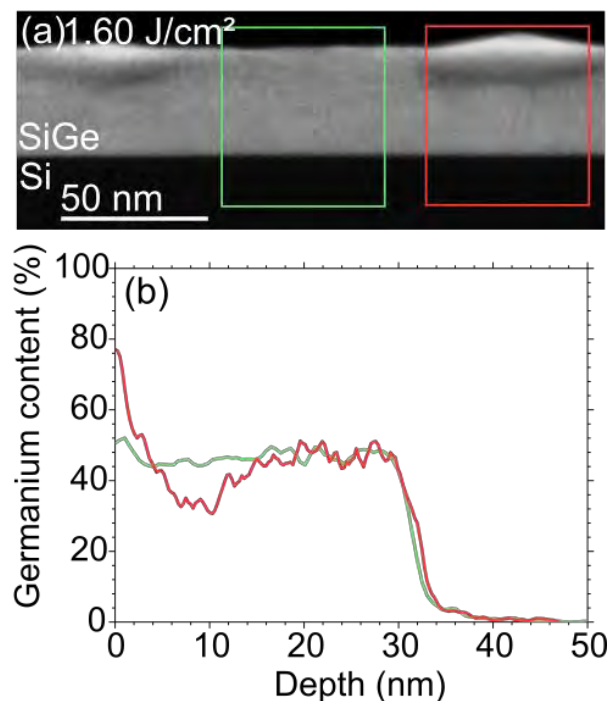


Figure III - 15. STEM-HAADF (a) image after laser annealing at  $1.60 \text{ J/cm}^2$  on a 30 nm-thick  $\text{Si}_{0.6}\text{Ge}_{0.4}$  layer, causing the formation of hillocks on the surface. STEM-EDX Ge concentration profiles (b) show that these hillocks present Ge segregation, while the flat region does not.

The AFM images shown in Figure III - 16 give more insight on these structures and their evolution. At  $1.32 \text{ J/cm}^2$ , AFM scans show some hillocks (groups of aligned white dots) a few nanometers above the initially flat epilayer. With increasing laser energy density, these nanostructures become wider, more numerous, and start merging. At  $1.60 \text{ J/cm}^2$ , about 50% of the surface is covered by hillocks. The average size of hillocks is in good agreement with what is observed by cross-sectional TEM for a sample at a close energy density ( $1.60 \text{ J/cm}^2$ ). The few hillocks were found  $70 \text{ nm}$  wide and  $6 \text{ nm}$  high by TEM. Meanwhile,  $\sim 60$  structures were investigated by AFM, which had a mean width of  $\sim 80 \text{ nm}$  and a mean height of  $\sim 4 \text{ nm}$ . Hence, it can be concluded that the nanostructures detected by AFM are those observed by TEM and that they are due to the same phenomenon: the progressive melting and covering of the surface by isolated melted islands. Similar surface structures have already been observed at the early stages of melting induced by NLA of Si and Ge [3,4] or millisecond Flash Lamp Annealing of Si, Ge and SiC [5–7]. Similarly to our case, these structures have also been interpreted as the consequence of a local melt of the material at the beginning of the melting process.

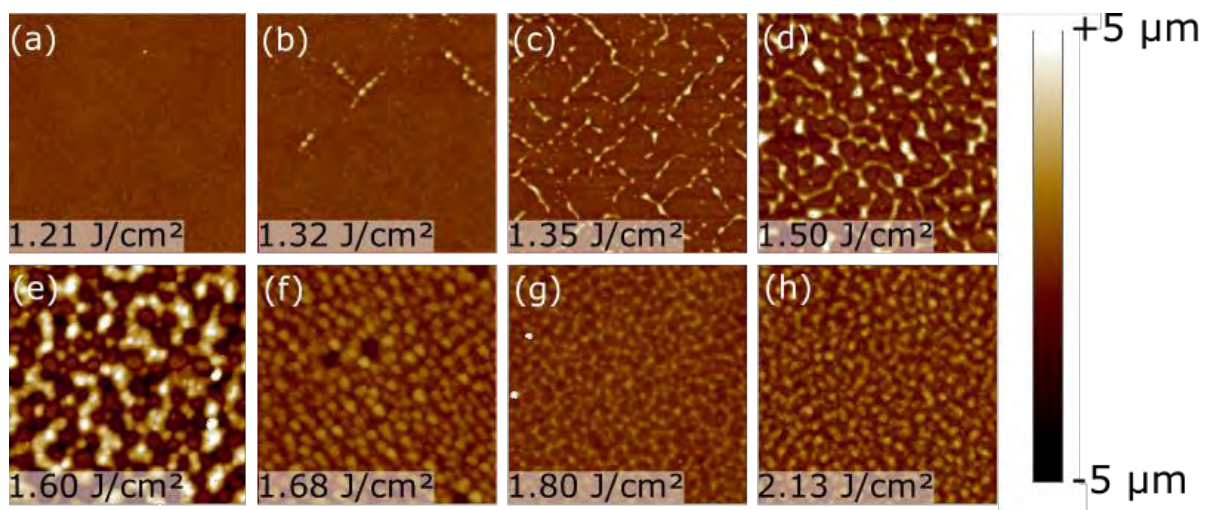


Figure III - 16.  $1 \times 1 \mu\text{m}^2$  AFM scans on a  $30 \text{ nm}$ -thick  $\text{Si}_{0.6}\text{Ge}_{0.4}$  layer after UV-NLA at  $1.21 \text{ J/cm}^2$  (a),  $1.32 \text{ J/cm}^2$  (b),  $1.35 \text{ J/cm}^2$  (c),  $1.50 \text{ J/cm}^2$  (d),  $1.60 \text{ J/cm}^2$  (e),  $1.68 \text{ J/cm}^2$  (f),  $1.80 \text{ J/cm}^2$  (g) and  $2.13 \text{ J/cm}^2$  (h).

However, it is important to note that, in these previous studies, the occurrence of local surface melt was indirectly inferred from time-resolved ellipsometry or transient diffraction measurements recorded during the anneal or after the anneal with the modified surface morphology. In contrast, in this work, thanks to the Ge partition mechanism occurring during the re-solidification of SiGe layers, the TEM observations provide a direct evidence that the melting process starts with the formation of isolated liquid islands. As for the origin of the observed local melting, this is most probably due to the nucleation occurring during the first-order solid-liquid phase transition [5], although laser radiation variability has also been proposed as a possible explanation [3]. In addition, it is known that the free surface may provide sites for heterogeneous nucleation to occur, allowing surface melt nucleation at temperatures lower than the melting temperature of the bulk solid [8].

#### b) Amorphous $\text{Si}_{0.7}\text{Ge}_{0.3}$ layer

A similar increase in SP2 Haze was observed on amorphous layers. As discussed in section I – 1.b), explosive crystallization is observed upon melt onset, prior to the occurrence of a second melt. Classical regimes (surface melt, partial melt and full melt) are observed after this second melt.  $1 \times 1 \mu\text{m}^2$  SEM micrographs on a  $30 \text{ nm}$ -thick  $\text{Si}_{0.7}\text{Ge}_{0.3}$  are presented in Figure III - 17, after amorphization over  $15 \text{ nm}$  and UV-NLA. As expected, the surface was smooth in sub-melt (a). Nanostructures were observed on the surface during the explosive crystallization

regime, even below the second melt threshold (b-c). They however differ from the structures observed on crystalline SiGe layers and do not present well defined shapes as it was observed on the other samples. Their origin remains to be studied. The start of the second melt is indicated by the appearance of additional contrast on the images, as an additional roughness is added (d-e-f). It seems to reduce and disappear with increasing energy density: only a few “dark areas” can be observed in (f), and none in (g), after the end of the Haze peak. The final morphology (g-h) is identical to the results on crystalline  $\text{Si}_{1-x}\text{Ge}_x$ .

The contrast in images (d-e-f) is likely due to the progressive surface melting. For these samples, it occurs on the polycrystalline layer formed by the explosive crystallization. Similarly to initially crystalline layers, the surface of the amorphized samples would, after the conversion of the a-SiGe layer into polycrystalline by the explosive crystallization, melt locally leading to the formation of isolated molten islands (surface melt regime). When increasing the energy density, such nanostructures would progressively coalesce leading to a continuous molten layer in the partial melt regime.

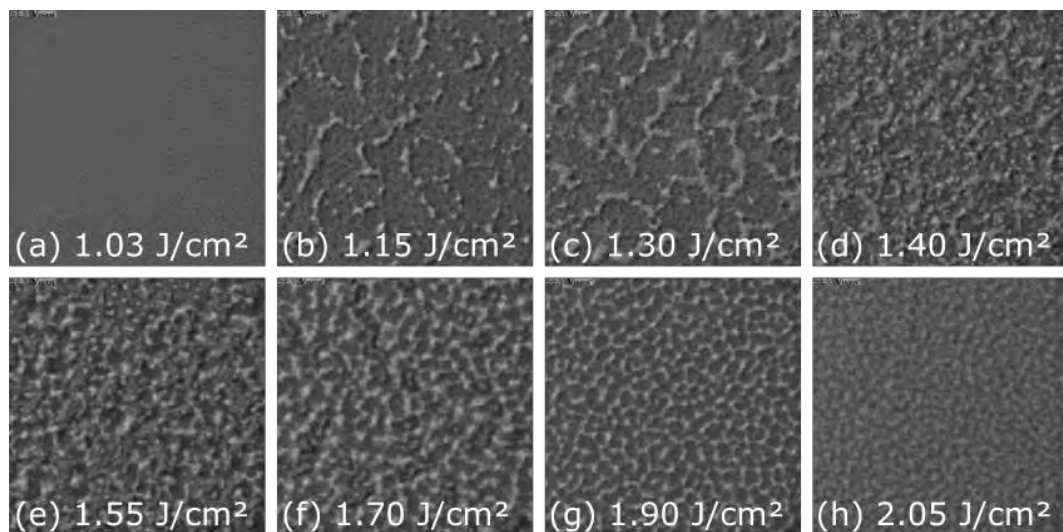


Figure III - 17.  $1 \times 1 \mu\text{m}^2$  SEM micrographs on a 30 nm-thick  $\text{Si}_{0.7}\text{Ge}_{0.3}$  layer, amorphized over 15 nm and submitted to UV-NLA. The images correspond to annealing at (a)  $1.03 \text{ J/cm}^2$ , (b)  $1.15 \text{ J/cm}^2$ , (c)  $1.30 \text{ J/cm}^2$ , (d)  $1.40 \text{ J/cm}^2$ , (e)  $1.55 \text{ J/cm}^2$ , (f)  $1.70 \text{ J/cm}^2$ , (g)  $1.90 \text{ J/cm}^2$  and (h)  $2.05 \text{ J/cm}^2$ .

## 2. Further analysis and impact of layer properties

### a) Haze signal

Haze measurements have otherwise shown that the peak is observed for all Ge concentrations and thicknesses, including bulk silicon, as shown in Figure III - 18. This proved that the local melt phenomena is not specifically related to the presence of germanium, or to the alloy properties. It is however modified by the layer properties. The evolution of the SP2 haze signal is plotted in Figure III - 18(a) as a function of the energy density for the samples from the '30 nm series' with various Ge contents. Figure III - 18(a) shows that the maximum intensity lowers for Ge-rich layers. Figure III - 18(b) shows the SP2 haze variations for the  $\text{Si}_{0.7}\text{Ge}_{0.3}$  series. Except for a slight shift in the energy density due to melt threshold changes upon thickness, there is no visible impact of the thickness on the haze signal in the 20-45 nm range. The similar plot for the doped series (Figure III - 18(c)) does not evidence any effect of the boron doping level. The SP2 haze variations as a function of the laser energy density for the amorphous series are presented in Figure III - 18(d). An initial sharp peak is detected at the onset of the explosive regime. The haze level remains high from this threshold up to  $\sim 1.80 \text{ J/cm}^2$  (beginning of the partial melt), which does not enable to distinguish the start of the second melt. A higher haze level is

detected for the sample with thicker amorphous layer. All signals exhibit a drop in Haze intensity after the explosive threshold, which is not yet understood.

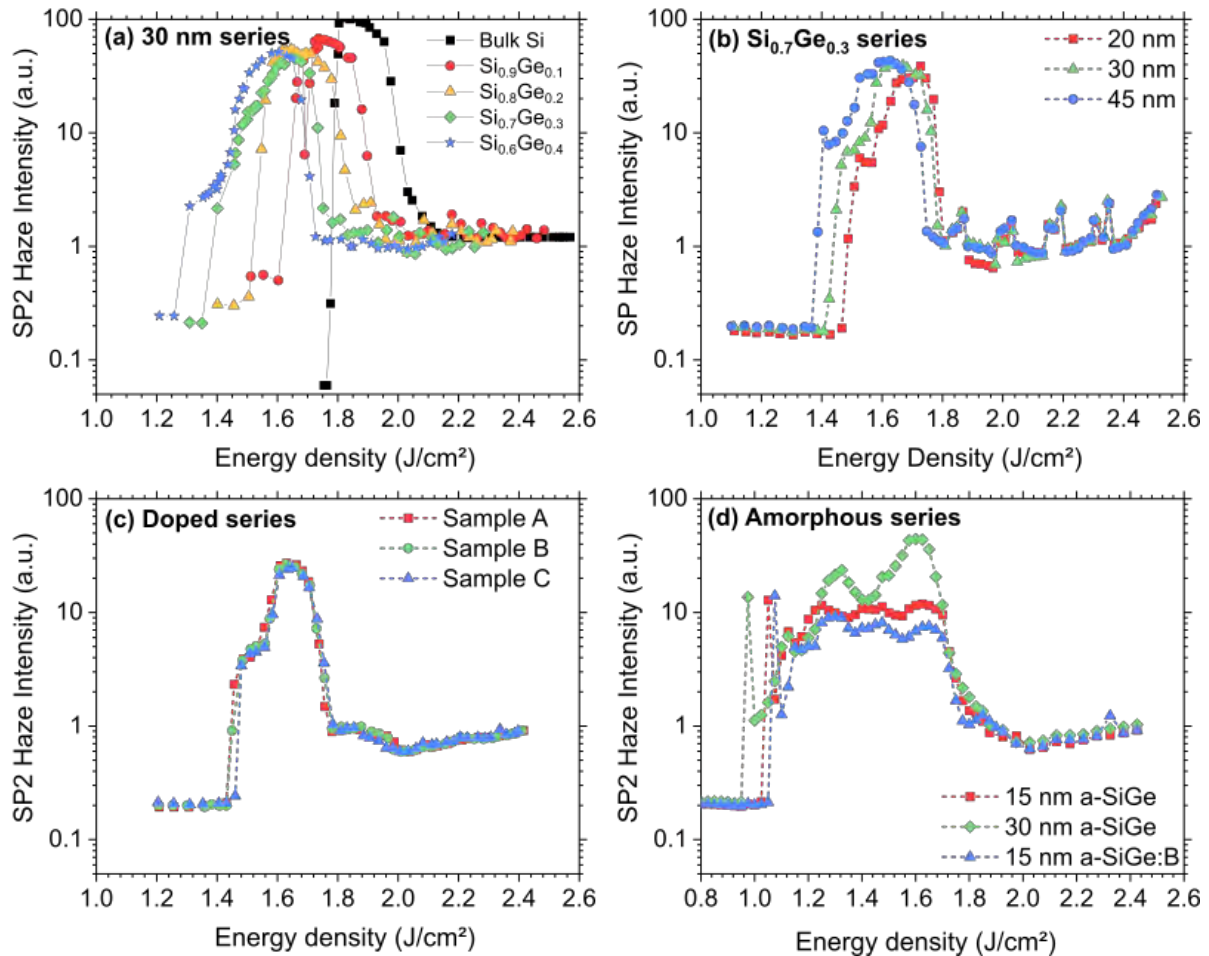


Figure III - 18. SP2 Haze intensity as a function of laser energy density for (a) the 30 nm-thick series, (b) the  $\text{Si}_{0.7}\text{Ge}_{0.3}$  series, (c) the doped series and (d) the amorphous series.  $\text{Si}_{0.7}\text{Ge}_{0.3}$  series signals exhibit measurement artefacts at high energy densities, with sharp peaks that are related to the position of the shot on the wafer.

#### b) Nanostructure shape: influence of concentration

$1 \times 1 \mu\text{m}^2$  AFM scans corresponding to the very beginning of the surface melt regime can be seen in Figure III - 19, for all Ge concentrations studied. The sides of the scans are parallel to the  $\langle 110 \rangle$  crystallographic directions. Isolated nanostructures are evidenced, with shape noticeable differences from bulk Si to  $\text{Si}_{0.6}\text{Ge}_{0.4}$  epilayer. As the Ge content increased, the nanostructures were found to be smaller and exhibited a star-like shape rather than a square one. In addition, the height and width of the hillocks decreased as the Ge content increased.

Additional SEM observations were performed on bulk Si and  $1.3 \mu\text{m}$ -thick Ge relaxed epilayers. Results after annealing at  $1.88 \text{ J/cm}^2$  and  $0.83 \text{ J/cm}^2$  are shown in Figure III - 20, for Si and Ge respectively. The structures exhibited a similar square shape on both materials. There was no assessment of height for Ge, as no AFM scans were performed on these samples.

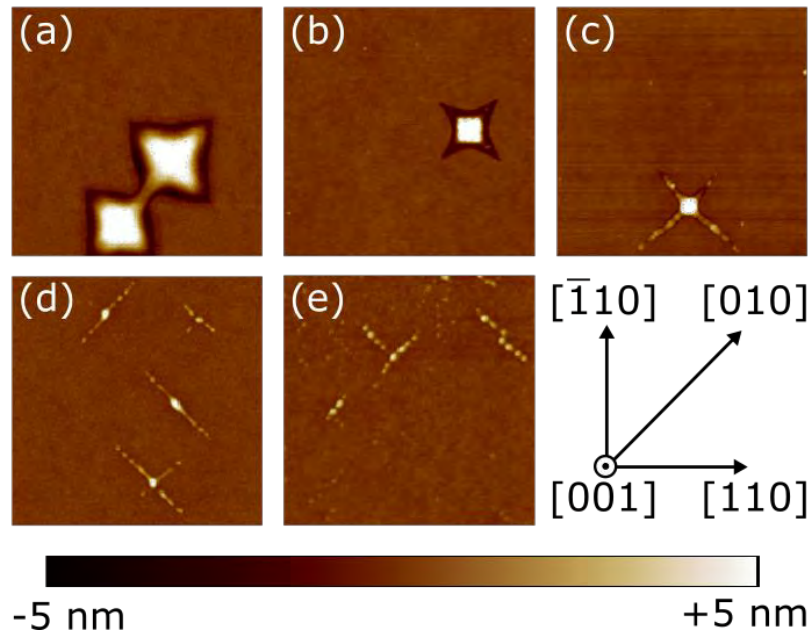


Figure III - 19.  $1 \times 1 \mu\text{m}^2$  AFM scans after laser annealing of (a) bulk Si at  $1.78 \text{ J/cm}^2$ , (b)  $\text{Si}_{0.9}\text{Ge}_{0.1}$  at  $1.66 \text{ J/cm}^2$ , (c)  $\text{Si}_{0.8}\text{Ge}_{0.2}$  at  $1.55 \text{ J/cm}^2$ , (d)  $\text{Si}_{0.7}\text{Ge}_{0.3}$  at  $1.45 \text{ J/cm}^2$  and (e)  $\text{Si}_{0.6}\text{Ge}_{0.4}$  at  $1.32 \text{ J/cm}^2$ . These energy density values correspond to the first one for which nanostructures could be observed on the surface by AFM. Scan sides are parallel to  $\langle 110 \rangle$  directions.

For the bulk Si surface or the thick Ge epilayer, the square faceted nanostructures (see Figure III - 20) are very likely the result of the anisotropy of both melting and recrystallization. In both pure and relaxed Si or Ge, melting proceeds slowest normal to dense packed lattice planes and therefore each isolated molten island has a chance to become highly faceted [5]. Upon cooling, anisotropy is also expected to play a role since crystallization velocity from the melt also proceeds slowest normal to the dense planes for both bulk Si and Ge [9,10]. Crystal growth rate on the various faces are expected in the order  $V_{G(100)} > V_{G(110)} > V_{G(111)}$ . This implies that the slowest growth velocity surface (111) forms a liquid-solid interface. Assuming a round initial molten nucleus on a (100) Si surface, further melting is expected to lead to an inverted pyramidal molten region with (111) buried faces and a square base whose edges are parallel to (110) directions.

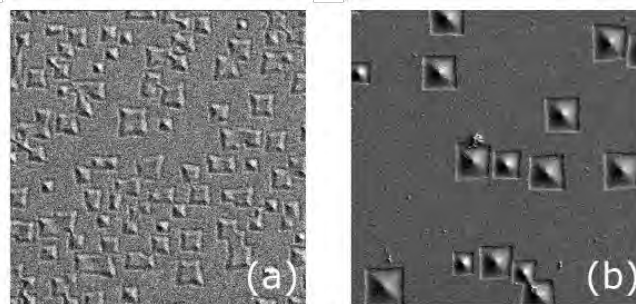


Figure III - 20.  $5 \times 5 \mu\text{m}^2$  SEM micrographs after laser annealing of (a) bulk Si at  $1.88 \text{ J/cm}^2$ , (b) 1300 nm-thick Ge epilayer on Si at  $0.83 \text{ J/cm}^2$ , within the surface melt regime.

Nevertheless, due to the much higher reflectivity of molten Si or Ge compared to the solid phase, the melt depth may be limited to a few nanometers, as can be observed on the STEM observation in Figure III - 15 for  $\text{Si}_{0.6}\text{Ge}_{0.4}$ . The top surface of this molten volume is supposed to be slightly below the initial surface level since liquid Si and liquid Ge densities are respectively 10% and 5% higher than their solid counterpart [11]. The suggested evolution of the molten area during solidification is shown in Figure III - 21. Assuming a Si molten volume with an inverted pyramid shape, truncated at a depth of 15 nm and a 100 nm basal edge, the expected step at the solid/liquid interface can be estimated to be around 1 nm. Upon solidification, this step

is expected to be the perimeter of the squares observed by SEM and AFM, and the molten region is supposed to shrink, keeping its shape and trapping the liquid in the middle. The displaced matter from the edges inevitably builds a bump in the center of the region.

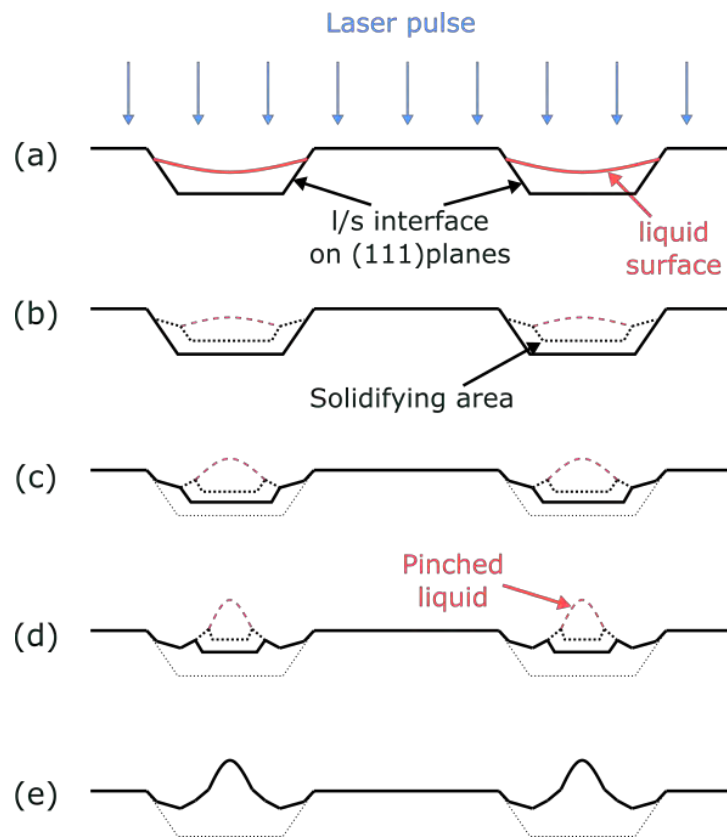


Figure III - 21. Evolution of the nanostructure shape during resolidification, starting from a truncated inverted pyramid (a) and showing the pinched liquid as the solidification proceeds from the solid edges. The final result corresponds to a hillock with low edges (e).

When increasing the Ge content from 0 to 40%, the nanostructures shape progressively changes from squares with edges along the (110) direction to stars elongated along the (010) directions. This likely reflects an inversion in the order of the melting and solidification velocities for the various crystallographic orientations. Such change could be an alloy effect and/or a strain effect. As the l/s interfaces correspond to free surfaces, the stress in the layers may inhibit the melt in given directions, causing the star-shaped structures. The various thicknesses or B-doping levels in  $\text{Si}_{0.7}\text{Ge}_{0.3}$  did not lead to detectable changes in the structures shape and distribution on the surface.

### c) Surface coverage by nanostructures

The surface covered by the hillocks (i.e. the melted regions) was inferred from  $10 \times 10 \mu\text{m}^2$  AFM scans. Figure III - 22 presents  $1 \times 1 \mu\text{m}^2$  AFM scans for surface coverage near 25%, 50% and 75% on a 30 nm-thick  $\text{Si}_{0.7}\text{Ge}_{0.3}$  layer. The covered surface ratio is plotted for each series in Figure III - 23 as a function of the laser energy density. There is always an almost linear increase of the covered surface as a function of energy density. The starting point shifted towards lower energy densities when increasing the Ge content or the layer thickness. This is due to the modification of melt threshold mentioned previously. Doping level had however no impact. The energy density interval between 0% and 100% surface coverage, i.e. the surface melt regime extension, increases with the Ge content: it is equal to 0.33, 0.35, 0.43 and  $0.47 \text{ J/cm}^2$  for 10%, 20%, 30% and 40% of Ge.

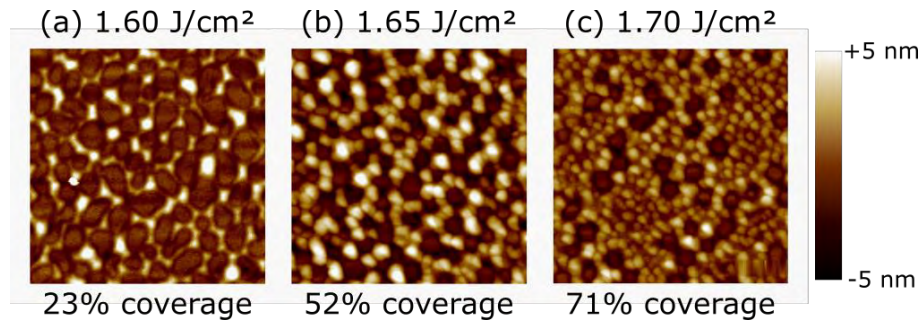


Figure III - 22.  $1 \times 1 \mu\text{m}^2$  AFM scans on a 30 nm-thick  $\text{Si}_{0.7}\text{Ge}_{0.3}$  layer annealed at  $1.60 \text{ J/cm}^2$  (a),  $1.65 \text{ J/cm}^2$  (b) and  $1.70 \text{ J/cm}^2$  (c). These energy densities cause molten surfaces near 23%, 52% and 71%.

This suggests that the nucleation rate of the surface islands or their growth rate (or both) decreases with higher Ge contents. This may be related to the SiGe phase diagram: the solidus and liquidus lines appear further apart as the Ge content increases from 0% to 50%. This means that a larger temperature range is required to reach a fully molten material, which translates into a larger energy density range in our case. This transition from isolated islands to fully molten surface may also depend on the structure shape (itself variable with the Ge content): the cross-shaped structures found in  $\text{Si}_{0.6}\text{Ge}_{0.4}$  are not as efficient to cover the surface than the squared-shaped structures on pure Si or pure Ge. There is however almost no change in the range covered by the surface melt regime when the layer thickness is increased or with various doping levels.

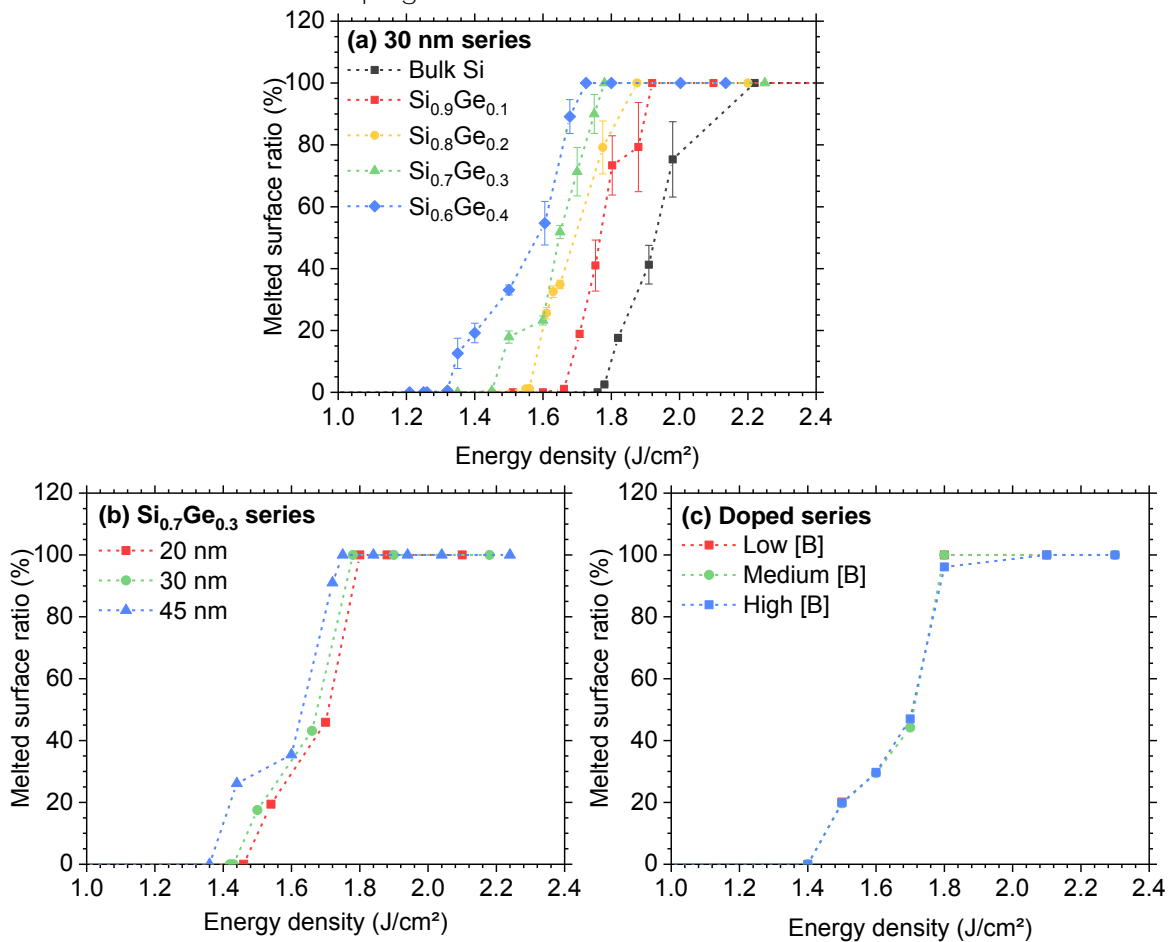


Figure III - 23. Evolution of the melted surface coverage as a function of energy density for all Ge concentrations for 30 nm-thick layers (a), for varying  $\text{Si}_{0.7}\text{Ge}_{0.3}$  thickness (b) and for various B doping levels in  $\text{Si}_{0.7}\text{Ge}_{0.3}$  (c). Data extracted from  $10 \times 10 \mu\text{m}^2$  AFM images. Additional points were taken from SP2 haze measurements: the last point before SP2 Haze increase is considered to have 0% of melted surface, while the first point after the end of the peak is supposed to be 100%.

## IV - SEGREGATION AND DIFFUSION DURING NANOSECOND LASER ANNEAL

Segregation is observed in layers that have reached their melting point, and lead to redistribution of germanium, silicon and boron. The final Ge concentration profiles were investigated with either ToF-SIMS or STEM-EDX, with additional STEM-HAADF images for the visualisation of the I/s interface. The profiles and images were used to extract information on melt depth, interface roughness and to enable simulation calibration.

### 1. Germanium segregation, a melt marker

#### a) Ge profiles after UV-NLA on crystalline layers

##### i. Observation of segregation

As mentioned in Chapter I, as well as in the first section of Chapter III, the solidification of liquid  $\text{Si}_{1-x}\text{Ge}_x$  leads to Ge segregation, thus forming a Ge-rich surface layer (see Figure III - 4 for  $\text{Si}_{0.6}\text{Ge}_{0.4}$ ). This behaviour was observed for every series: multiple examples are shown in Figure III - 24 and Figure III - 25. Figure III - 24 presents STEM-EDX profiles for the 30 nm-thick series, which are perfectly consistent with SIMS obtained profiles.

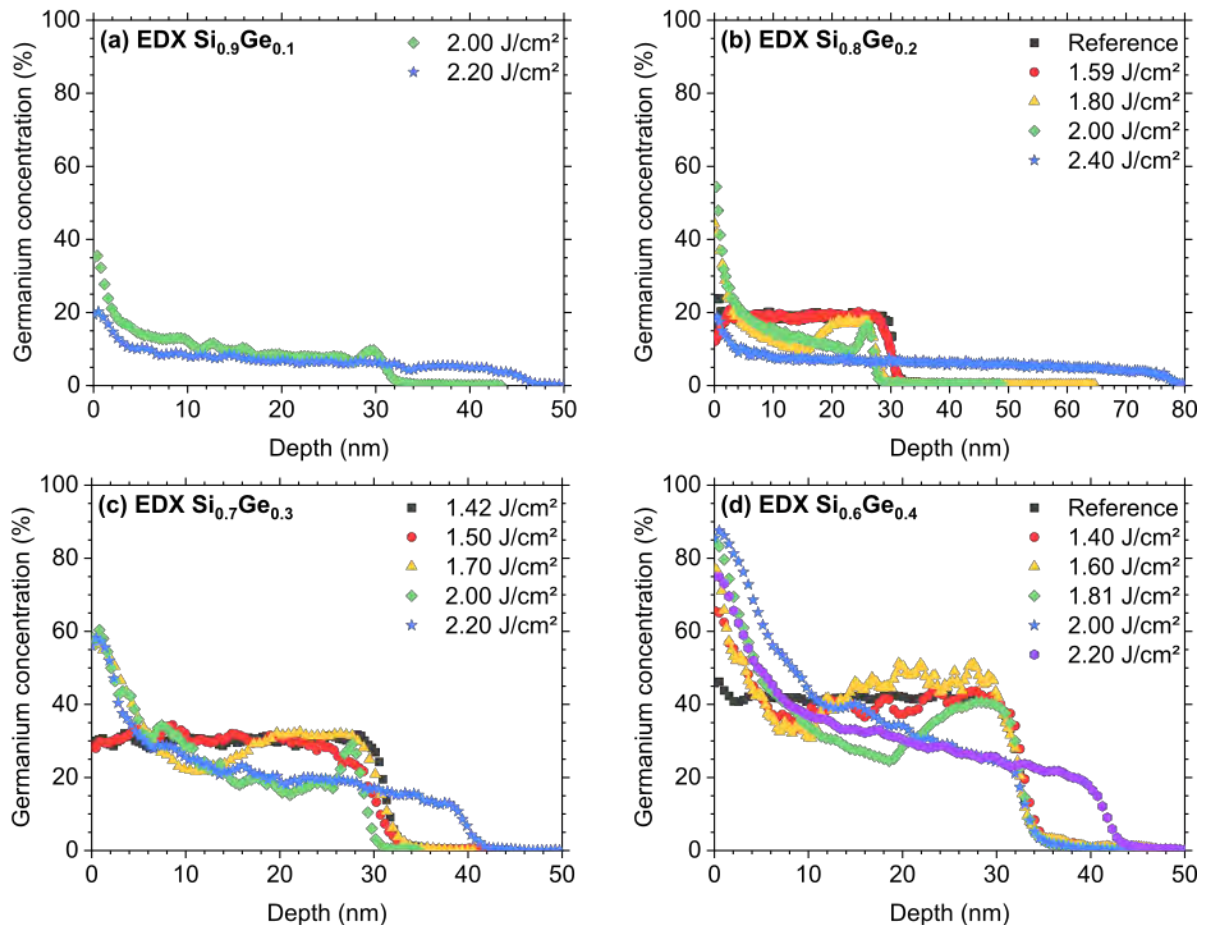


Figure III - 24. Ge concentration profiles as a function of depth, measured by STEM-EDX after laser treatment with various energy densities on 30 nm-thick layers of (a)  $\text{Si}_{0.9}\text{Ge}_{0.1}$ , (b)  $\text{Si}_{0.8}\text{Ge}_{0.2}$ , (c)  $\text{Si}_{0.7}\text{Ge}_{0.3}$  and (d)  $\text{Si}_{0.6}\text{Ge}_{0.4}$ . The profiles at 1.40 J/cm<sup>2</sup> and 1.60 J/cm<sup>2</sup> on (d) were taken on molten islands.

Partial melt led to the formation of several regions within the  $\text{Si}_{1-x}\text{Ge}_x$  layer, from depth to surface: (i) the deeper, unmelted region has an unchanged Ge profile and is followed by (ii) a region with decreasing Ge content, corresponding to the maximum melt depth. Finally, a progressive increase of Ge concentration (iii) is observed, up to the surface. In surface melt

regime, similar profiles are observed if the molten surface percentage is sufficient. For low molten surface percentage, the profiles remain identical to the as-epi reference. This is the case for  $1.80 \text{ J/cm}^2$  on  $\text{Si}_{0.8}\text{Ge}_{0.2}$  (b) and  $1.70 \text{ J/cm}^2$  on  $\text{Si}_{0.7}\text{Ge}_{0.3}$  (c). On  $\text{Si}_{0.6}\text{Ge}_{0.4}$ , the profiles at  $1.40 \text{ J/cm}^2$  and  $160 \text{ J/cm}^2$  were specifically measured on a single hillock. Otherwise, the profile measured in the unmelted areas remain identical to the initial profile. In the full melt regime, both the SiGe layer and the upper part of the underlying Si substrate melted (typically down to a depth of 40-80 nm according to the corresponding EDX profiles in Fig.III.21), leading to Ge diffusion and dilution in the liquid phase. The overall Ge content is thus lower but segregation remains clearly observable, with a richer surface.

Similar observations were performed on the  $\text{Si}_{0.7}\text{Ge}_{0.3}$  series (Figure III - 25(a)), as well as the doped series, (Figure III - 25(b)). As the result are similar for each sample in these series, only one is presented in this chapter. The remaining profiles are plotted for all samples in Appendix – I. In Figure III - 25(a), the profiles are shown for the 45 nm-thick layer from the  $\text{Si}_{0.7}\text{Ge}_{0.3}$  series: apart from the melt threshold discrepancy observed, the segregation behaviour is similar for all samples. In Figure III - 25(b), the profiles are presented for the level B sample from the doped series, which again highlights the Ge segregation toward the surface. It does not seem to be highly influenced by the B presence. A slight difference in melt depth is observed with increasing boron concentration (see Appendix – I for other profiles), as the sample C reaches the full melt at  $2.10 \text{ J/cm}^2$ , earlier than samples A and B.

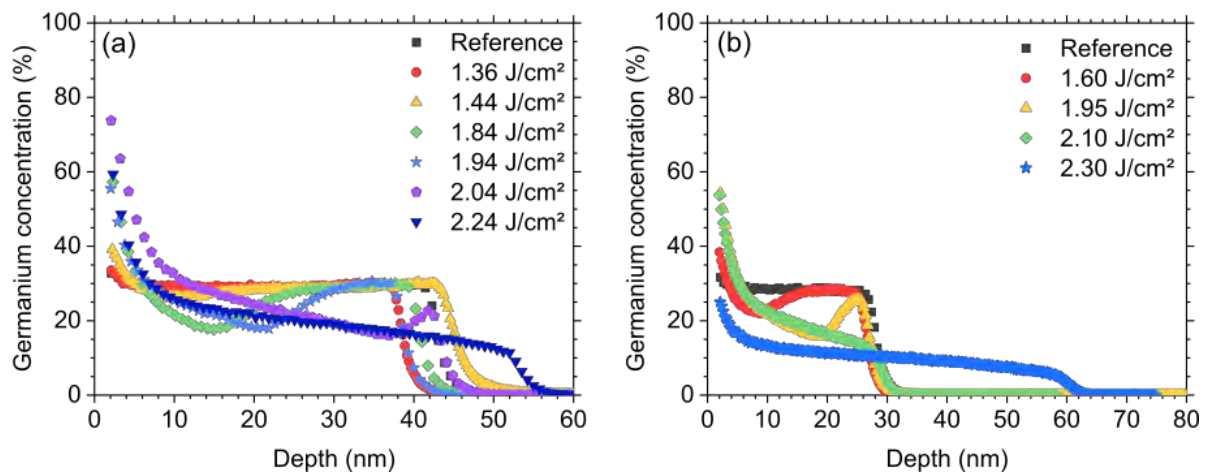


Figure III - 25. ToF-SIMS Ge profiles as a function of depth at various laser energy densities for a 45 nm-thick  $\text{Si}_{0.7}\text{Ge}_{0.3}$  layer (a) and a 30 nm-thick  $\text{Si}_{0.7}\text{Ge}_{0.3}$  layer with medium boron doping.

#### ii. Noticeable differences between SIMS and STEM-EDX

Figure III - 26(a) presents three Ge concentration depth profiles from a 30 nm-thick  $\text{Si}_{0.6}\text{Ge}_{0.4}$  profiles annealed at  $1.81 \text{ J/cm}^2$ . One was measured by ToF-SIMS (red squares), while the two others were obtained by STEM-EDX (green circles and blue triangles), on the areas shown on the micrograph from Figure III - 26(b). It can first be noticed that the SIMS profile is less noisy, though all profiles exhibit similar trends. The EDX profiles appear sharper and are not identical to each other. The green profile, from the left part of the micrograph, exhibits a minimum  $\sim 28 \text{ at.}\% \text{ Ge}$  for a depth near 16 nm, while the minimum for the blue profile reaches  $\sim 20 \text{ at.}\% \text{ Ge}$  for a depth near 20 nm. The slope at the end of the profile is also different. This is associated with local melt depth variations within a given sample, visible on the STEM micrograph. Otherwise, the remaining unmelted SiGe layer appears in brighter colours at the bottom of the SiGe layer, and is several nanometers thicker on the left part of the image. Hence, the STEM-EDX profiles are only representative of the region where the measurement was performed and can differ from each other. SIMS profiles however integrate a much wider area ( $\sim 10^7$  larger area) and thus present an average of these small-scale variations, which

results in the smoother appearance of the red profile. The progressive decrease from 40 at.% Ge at 30 nm to 26 at.% Ge at 17 nm can be considered as a qualitative indication of the liquid/solid interface roughness, while the average melt depth is taken at mid-slope.

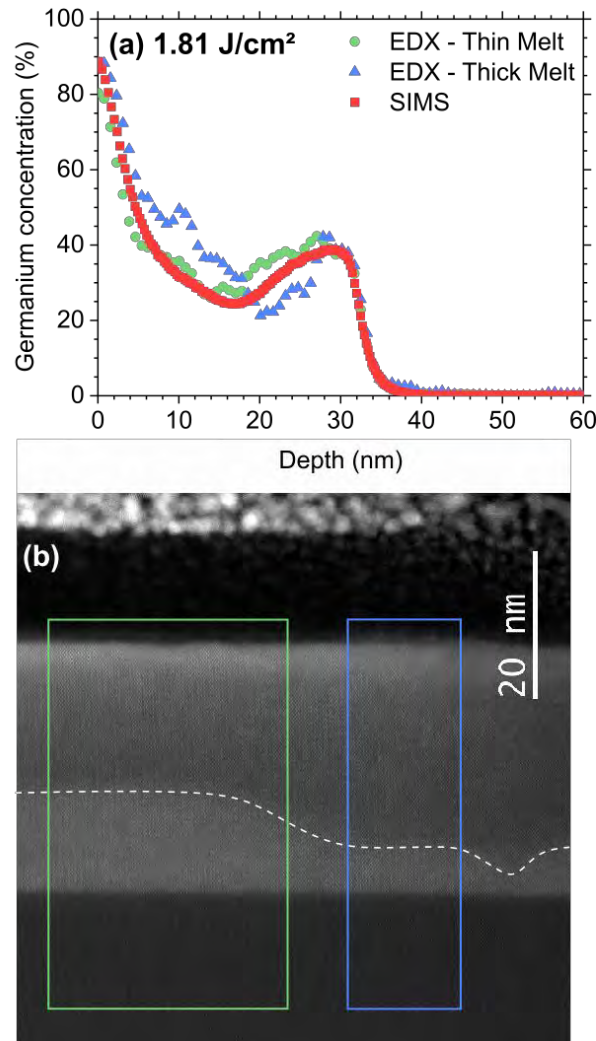


Figure III - 26. Comparison of ToF-SIMS (red) and EDX (green, blue) Ge concentration depth profiles (a), with the STEM-HAADF micrograph corresponding to the EDX profiles (b). Green and blue rectangles indicate the regions where the EDX profiles were respectively measured, while the liquid/solid interface is highlighted with a white dotted line. Si<sub>0.6</sub>Ge<sub>0.4</sub> sample laser annealed with 1.81 J/cm<sup>2</sup> process condition.

## b) Melt depth and interface roughness

### i. Melt depth evolution

Melt depth measurements for series with fully crystalline layers are presented in Figure III - 27. As detailed in the previous section, the average melt depth is measured at mid slope, while the error bars correspond to the range between the minimum melt depth and the maximum melt depth, and are therefore indicative of the liquid/solid interface roughness. The values extracted in the surface melt regime are therefore not reliable, as part of the surface did not melt. When EDX measurements correspond to a molten area, for a sample in the surface melt regime, the value indicated corresponds to the melt depth measured in this area weighted by the ratio of melted surface. This may lead to differences between the melt depths measured by SIMS and EDX.

On the 30 nm-thick series (Figure III - 27 (a)), the measured melt depths follow similar evolution for all Ge concentrations, with a roughly linear increase once the melt threshold is exceeded. As the initially higher Ge content layers reach their melt threshold for lower energy densities, they overall present deeper melt depths for a given energy density. This discrepancy however reduces near the full melt regime at  $2.20 \text{ J/cm}^2$ : once in the full melt regime, all samples presented melt depths close to each other, near 40-45 nm. This is likely related to the impact of the pure Si substrate on the melt depth. The evolution slightly varies with the thickness (20, 30 and 45 nm-thick layers) in the  $\text{Si}_{0.7}\text{Ge}_{0.3}$  series (Figure III - 27(b)), with two distinct behaviours. At low energy densities, typically below  $1.80\text{-}1.90 \text{ J/cm}^2$ , the melt depth increases at a lower rate. This may be due to the remaining unmolten areas that are observed up to  $1.80 \text{ J/cm}^2$ : the calculated melt depth corresponds only to part of the surface, and it may not be reliable. Once the complete surface becomes liquid, the melt depth is observed to increase at a faster rate with energy density.

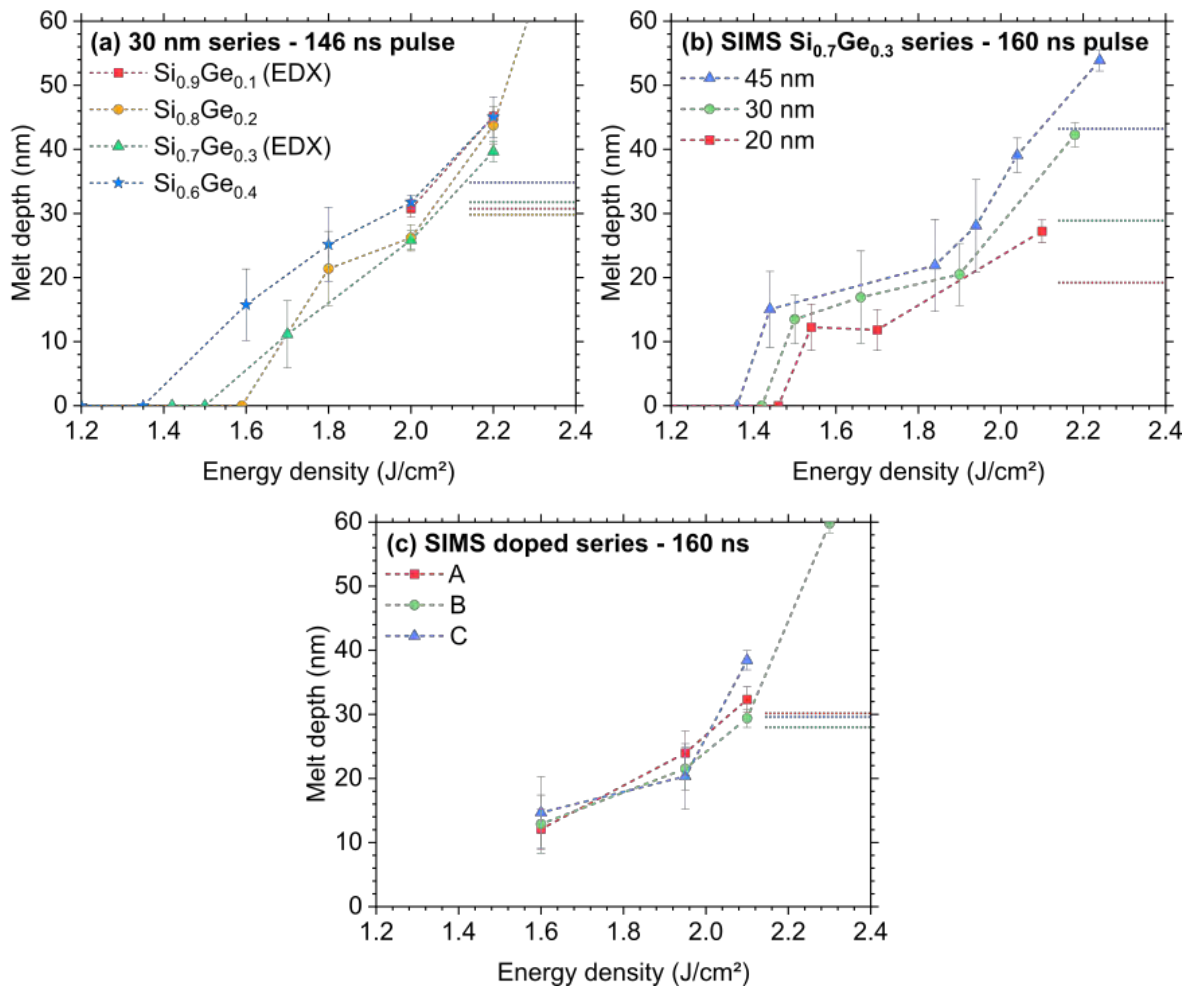


Figure III - 27. Measured melt depths as a function of energy density for the 30 nm series (a), as well as the  $\text{Si}_{0.7}\text{Ge}_{0.3}$  series (b) and the doped series (c), from SIMS and EDX measurements. The error bars are indicative of the interface roughness. For EDX measurements (a) that correspond to samples in the surface melt regime, the value indicated corresponds to the melt depth measured on a melted area weighted by the ratio of melted surface (see Figure III - 23). For each sample, a dotted line indicates the corresponding average layer thickness before laser anneal.

Similarly to the 30 nm series with various initial Ge contents, increasing the  $\text{Si}_{0.7}\text{Ge}_{0.3}$  thickness from 20 to 45 nm leads not only to a lower melt threshold but to a deeper fusion for a given energy density. In contrast, in the case of the doped series (30 nm thick  $\text{Si}_{0.7}\text{Ge}_{0.3}$  samples, cf. Figure III - 27 (c)), there is little difference in the melt depth for the three tested boron doping concentrations: the only variation is observed at  $2.10 \text{ J/cm}^2$ , where the sample C presents a

slightly higher melt depth than the other two. As it occurred for the 30 nm series, the layer that melted for lower energy densities showed deeper melt depths.

*ii. Maximum melt depth variability*

Figure III - 27 also highlights the changes in interface roughness, thanks to the error bars associated to each experimental point, although it is only qualitative. It can be observed that the measured interface range remains large for low energy densities, and only reduces for melt depths equivalent to the initial layer thickness. This is detected by both SIMS and EDX measurements, and is confirmed by STEM-HAADF micrographs, as presented in Figure III - 28. The observations were performed on samples from the 30 nm series with 20%, 30% and 40% germanium contents. The first column (a, d, f) corresponds to samples either in the surface or partial melt regime, with a visible unmelted region (brighter region) between the Si substrate (bottom part) and the melted SiGe (upper part). The visible former liquid/solid interface (l/s interface) appears rough. It however becomes smoother for samples with a deeper melt, as illustrated in the second column (b-g) : a thin (2-4 nm) unmelted region remains distinguishable at the bottom, but the interface appears smoother. Finally, samples in the full melt regime (c; e; h) present a perfectly flat liquid/solid interface.

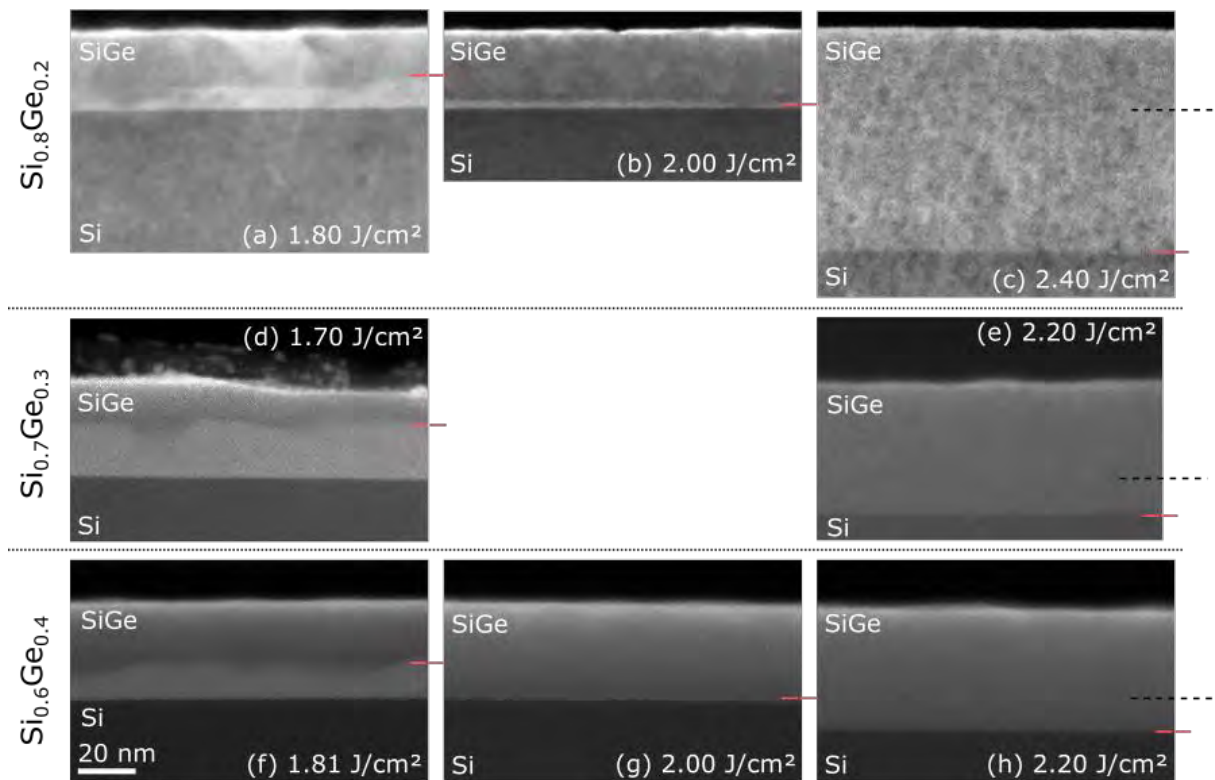


Figure III - 28. STEM-HAADF micrographs corresponding to initially 30 nm-thick undoped layers with various Ge concentrations, (a,b,c)  $\text{Si}_{0.8}\text{Ge}_{0.2}$ , (d,e)  $\text{Si}_{0.7}\text{Ge}_{0.3}$  and (f,g,h)  $\text{Si}_{0.6}\text{Ge}_{0.4}$ , annealed with increasing laser energy densities. The scale is identical in all images, and is shown in (f). Black lines on the right of each line indicate the initial SiGe/Si interface depth, while red lines show the melt depth observed on each sample.

The former l/s interface roughness during the partial melt regime likely originates from the inhomogeneous melt at the surface. The formation of molten islands at the beginning of the laser pulse likely introduces strong variations in the melt depth, between 0 nm (unmelted region) and up to 10 nm (molten islands). Later during the laser pulse, even when a continuous liquid layer is formed, the l/s interface would keep memory of part of this initial roughness in the partial melt regime. This interface roughness is reduced when the melt front approaches an interface with a material with higher melt temperature, allowing the melt front to slow down or

stop at the Si/SiGe interface. It is possible that this melt front would naturally flatten even for deep melt depth within thick  $\text{Si}_{1-x}\text{Ge}_x$  layers, but it could not be observed with these experiments even in the 45 nm-thick  $\text{Si}_{0.7}\text{Ge}_{0.3}$  layer.

c) Ge profiles after UV-NLA on amorphous layers

SIMS profiles were obtained for the undoped amorphized layers presented in Chapter II. The as-implanted Ge concentration profiles are presented in Figure III - 29: the blue and red curves correspond to the 15 nm and 30 nm amorphization respectively. The amorphizations were performed with a  $1.5 \times 10^{15}$  Ge implantation at respectively 6 keV and 16 keV. As already explained, there is an overestimation near the surface caused by the native oxide presence, though it does not seem more pronounced than in pseudomorphic layers. The concentration remains close to 30% in both cases.

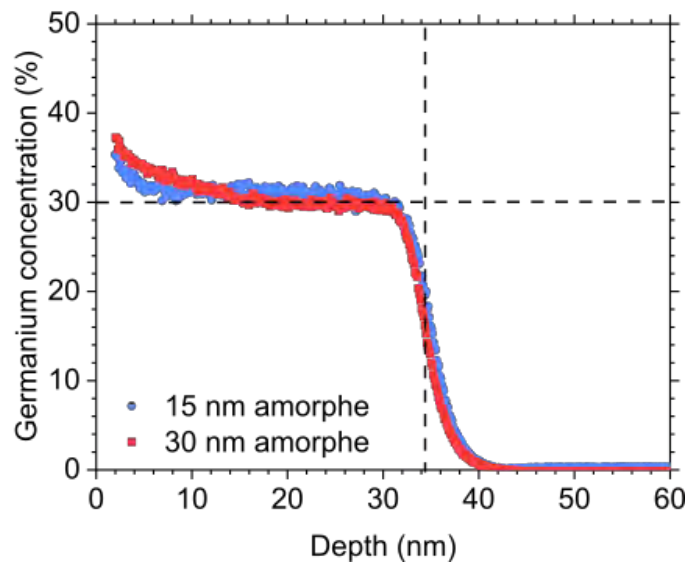


Figure III - 29. As-implanted Ge depth profiles for two 30 nm-thick  $\text{Si}_{0.7}\text{Ge}_{0.3}$  layers that were amorphized over 15 nm (blue) and 30 nm (red).

Profiles from Figure III - 30 were obtained after laser annealing of the same samples with energy densities leading to explosive crystallization of the amorphous layer, with no observed second melt yet (explosive regime). As already shown in Fig. III.8, the explosive threshold were detected respectively at  $1.05 \text{ J/cm}^2$  and  $0.98 \text{ J/cm}^2$  for the 15 nm and 30 nm amorphization. The red profiles therefore correspond to the onset of the explosive regime. Ge redistribution is already observed for these samples, and is visible over the whole initially amorphized layer: the entire amorphous layer melted even at the onset of the explosive regime. In addition, the profiles at slightly higher energy densities (in yellow) are identical: the explosive melt is identical in both cases, and leads to the same melt depth. For the samples initially amorphized down to 15 nm and laser annealed at  $1.10$  and  $1.25 \text{ J/cm}^2$  (Fig. III.28.a), a small Ge build-up is observed 10 to 15 nm below the surface, i.e. right above the initial amorphous/crystalline SiGe interface. For these same samples, there is no Ge concentration change observed in the crystalline layer, indicating that it has not melted. Similarly, the profiles for the 30 nm amorphization in Figure III - 30(b) present a slight accumulation of Ge at 25 nm, near the bottom of the former amorphous layer. This Ge redistribution suggests that the segregation occurred towards the bottom of the SiGe amorphous layer, implying that the thin liquid layer moved from top to bottom during the explosive crystallization, in agreement with [12]. The Ge redistribution due to the explosive recrystallization is much more limited than that observed previously (Figure III - 24, Figure III - 25 & Appendix I). This would confirm the hypothesis of an extremely fast solidification starting at the top and going down to the crystalline layer, as suggested by the literature [13,14]. The

limited amplitude of the Ge build-up would result from a high partition coefficient  $k_i$  slightly below unity, characteristic of a solidification velocity so high that segregation is reduced.

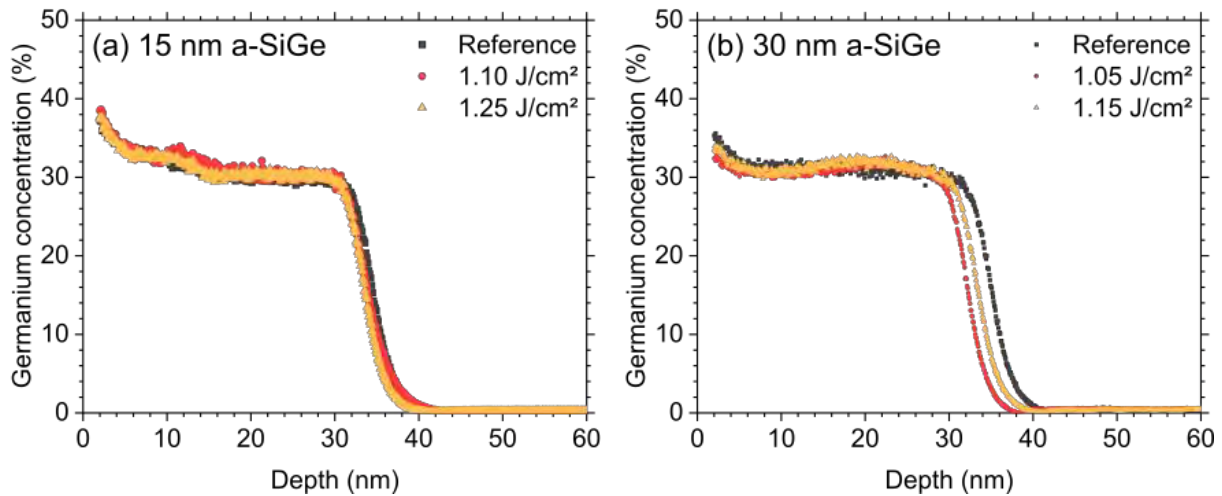


Figure III - 30. ToF-SIMS Ge concentration depth profiles after Ge implantation and UV-NLA at energy densities leading only to explosive melt within the amorphous layer. The graphs (a) and (b) correspond to 15 nm and 30 nm amorphizations respectively.

Figure III - 31 illustrates the behaviour of these same partially amorphized samples exposed to higher laser energy densities leading not only to the amorphous melt and explosive crystallization, but also to a second melt during the laser pulse. The second melt led to typical Ge profiles with expected segregation, and indicated that the full melt was reached near  $2.10 \text{ J/cm}^2$  for the 15 nm amorphization. This stronger segregation, compared to that in the explosive regime, results from a slower solidification velocity, characterized by a lower partition coefficient.

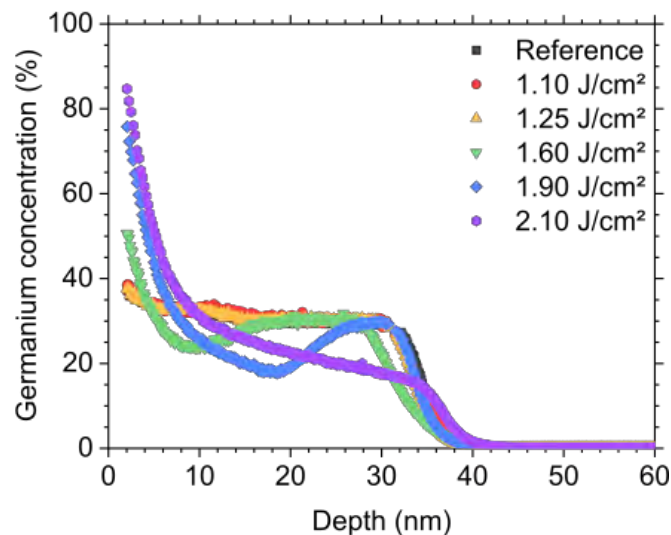


Figure III - 31. ToF-SIMS Ge concentration depth profiles after Ge implantation and UV-NLA with increasing energy density for the  $\text{Si}_{0.7}\text{Ge}_{0.3}$  layer 15 nm amorphization.

## 2. Segregation simulations

The segregated Ge profiles can be reproduced by simulations, with two methods already presented in Chapter II. The first method is based on the LIAB software, that simulates the complete laser anneal process with all the physical phenomena that take place within the material. In that case, a constant partition coefficient  $k_i$  is set in the database. A second simplified method was used, where only the solidification is considered. The calculations do not

take into account the thermal diffusion or light absorption. In that case, the partition coefficient can be defined as a variable that depends on both the Ge content and the solidification velocity.

a) With a constant partition coefficient  $k_i$

The simulations performed with LIAB consider the light absorption, thermal diffusion and chemical diffusion within the material to simulate the melt and regrowth phenomena. As such, fitting Ge profiles can only be obtained once all physical parameters are calibrated, and the Ge profiles were therefore used to validate the physical parameters in the database. All profiles were slightly modified to have the SiGe/Si interface at an identical depth (30 nm for  $\text{Si}_{0.8}\text{Ge}_{0.2}$  and 34 nm for  $\text{Si}_{0.6}\text{Ge}_{0.4}$ ) to enable the use of batch simulations. The profiles shown in this section are therefore not strictly identical to the ones presented earlier. The stack used for the simulation is presented in Chapter II.

#### *i. Database calibration*

Several sets of simulation were performed to progressively adjust different physical parameters, by matching the experimentally measured melt depths to the calculated ones for samples from the 30 nm series [1,2]. The first run of simulations used parameters extracted from the literature, and linear approximations between Si and Ge values when no literature was found. These parameters did not lead to satisfying prediction of the experimental results.

As the parameters with the highest influence on the results are the melt temperature and the permittivity, the following simulations focused on these parameters. In order to adjust the melt threshold, variations in melt temperature (either following the solidus, the liquidus or a linear evolution) and solid phase permittivities were considered. The best results were obtained using a linear evolution of melt temperature as a function of Ge content, and an extrapolation of the ellipsometry results previously presented for the permittivities (see Figure III - 9). The final permittivities (real and imaginary parts) after multiple iterations are functions of the Ge concentration  $x$  and the temperature  $T$ , as follows:

$$\text{Re}(\epsilon c) = -1.59 * 10^{-2} \cdot (T - 300) + 8276.3 \cdot x^6 - 5555.7 \cdot x^5 + 359.78 \cdot x^4 + 411.64 \cdot x^3 - 107.45 \cdot x^2 + 12.75 \cdot x + 12.72$$

$$\text{Im}(\epsilon c) = 9.8 * 10^{-3} \cdot (T - 300) - 192.07 \cdot x^4 + 133.18 \cdot x^3 - 19.146 \cdot x^2 - 15.19 \cdot x + 37.25$$

These changes enabled a satisfying correspondence with the experimental melt depths. Identical melt depths were obtained by modifying the simulated energy densities within the experimental error range ( $\pm 3\%$ ). A last set of simulations was performed to match the Ge segregated profiles with the SIMS profiles by changing the diffusivities and the partition coefficients.

#### *ii. Ge segregation*

The final simulated Ge profiles are presented in Figure III - 32 along with the corresponding experimental SIMS profiles for  $\text{Si}_{0.8}\text{Ge}_{0.2}$  and  $\text{Si}_{0.6}\text{Ge}_{0.4}$  30 nm thick layers. All curves show high concordance of the melt depth with the experiments, indicating that the calibration is sufficient to use the LIAB simulator as a prediction tool for future experiments.

The simulated Ge profiles reproduce fairly well the experimental profiles, with high Ge content near the surface. Perfect match cannot be obtained, as the software does not consider the interface roughness: simulated profiles always appear sharper than SIMS profiles. This is particularly obvious on the sample annealed at 1.80 J/cm<sup>2</sup> for  $\text{Si}_{0.8}\text{Ge}_{0.2}$  (a) and 1.81 J/cm<sup>2</sup> for  $\text{Si}_{0.6}\text{Ge}_{0.4}$  (b). All the profiles were obtained with the same partition coefficient  $k_i$ , fixed at

0.45. This leads to acceptable segregated Ge profiles in all cases, highlighting that in this range of concentration and solidification velocities, the partition coefficient does not vary much.

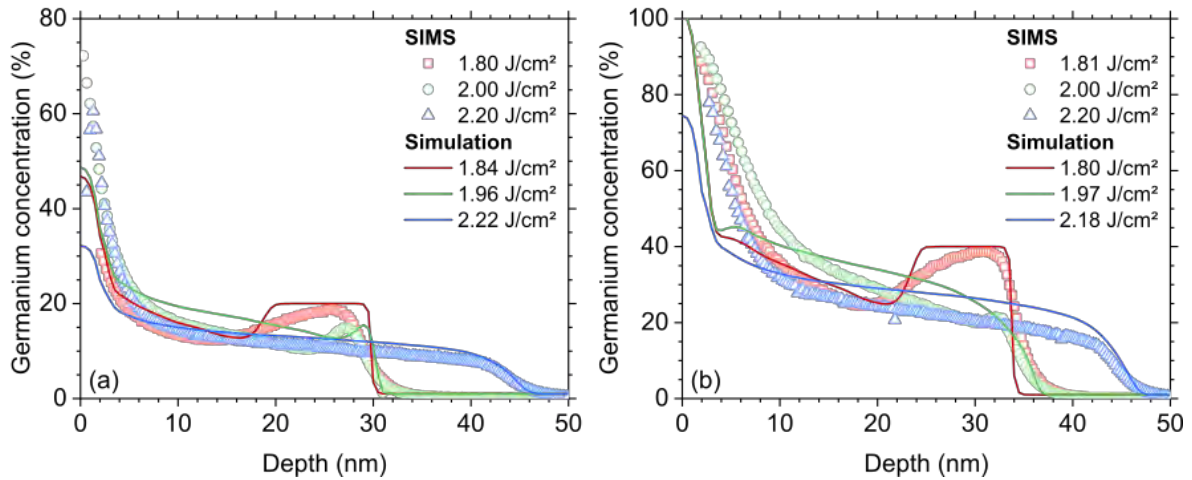


Figure III - 32. Simulated Ge profiles after NLA on a 30 nm thick  $\text{Si}_{0.8}\text{Ge}_{0.2}$  (a) and  $\text{Si}_{0.6}\text{Ge}_{0.4}$  (b) layers, with a partition coefficient of 0.45.

b) With a variable partition coefficient  $k_i$

The Ge profiles were also reproduced using a simpler method, described in Chapter II. This method considers only a liquid and a solid phase, with a flat interface between the two phases.

*i.  $k_i$  evolution with Ge content and solidification velocity*

The amount of Ge incorporated in the solid region is defined as  $\chi_s = k_i \cdot \chi_L$  where  $k_i$  is itself dependent on the Ge content near the interface and on the regrowth velocity. The dependence of  $k_i$  is extracted from the literature (Figure 6 from [15]), which shows changes for concentrations between 10% and 40% (in the solid phase). The data points extracted from these curves are replotted as a function of concentration for various solidification velocities, as presented in Figure III - 33. We consider that the partition coefficient must be unity for pure Ge and have therefore added the corresponding point in each curve.

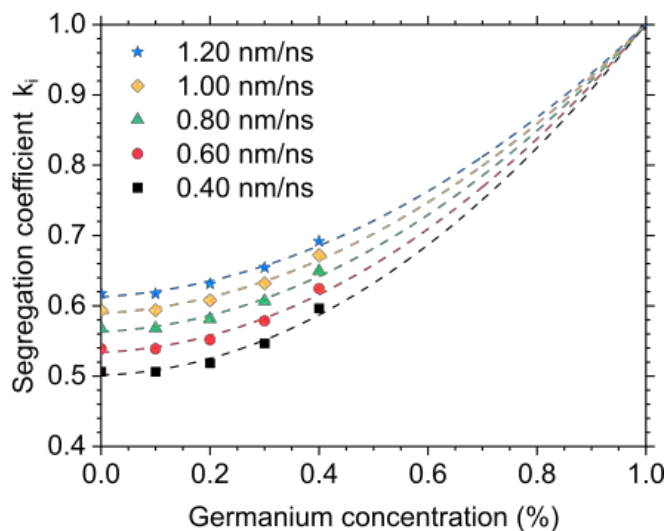


Figure III - 33. Evolution of the partition coefficient as a function of the germanium content in the solid phase near the interface, for various solidification velocities, extracted from [15].

These curves were used to obtain polynomial equations describing the evolution of  $k_i$  as a function of concentration for a few selected velocities between 0.2 nm/ns and 1.2 nm/ns.

In order to account for the interface non-uniformities that were experimentally observed, an “interface roughness” parameter was added in the simulation. The simulation then calculates multiple segregated profiles, corresponding to various melt depths within the interface roughness range. The final profile returned to the user corresponds to an averaged profile extracted from these. Some examples are shown in Figure III - 34 for an initially 30 nm-thick  $\text{Si}_{0.6}\text{Ge}_{0.4}$  layer that melted down to 25 nm in average : the various profiles correspond to an abrupt interface, or rough interfaces that were 2, 6 or 10 nm wide.

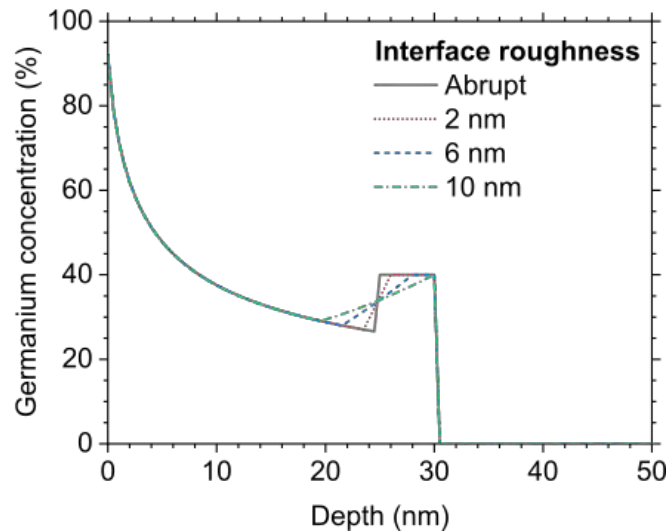


Figure III - 34. Simulated Ge concentration depth profiles after NLA on a 30 nm-thick  $\text{Si}_{0.6}\text{Ge}_{0.4}$  layer, considering various interface roughness, from abrupt to 10 nm wide.

Simulations are therefore performed by indicating a set of fixed parameters for each SIMS profiles : the melt depth, the interface roughness and the average estimated velocity during regrowth. The velocity does not vary during the solidification calculation, and multiple calculations are performed to find the best fit in the 0.4-1.2 nm/ns range. The partition coefficient evolves constantly as the Ge concentration near the interface is modified.

#### ii. Simulation results

The results are shown in Figure III - 35 and Figure III - 36 for the  $\text{Si}_{0.7}\text{Ge}_{0.3}$  series and the 30 nm series and compared with the corresponding SIMS datas. The simulations were able to reproduce the experimental profiles with high accuracy in most cases, supporting the idea that the partition coefficient evolves with Ge content. Profiles for samples with a low percentage of melted surface could however not be well reproduced. All these profiles were obtained with solidification velocities between 0.4 and 1.2 nm/ns, indicating that the average velocity does not vary much with the energy density and will thus have a limited impact on the partition coefficient [15]

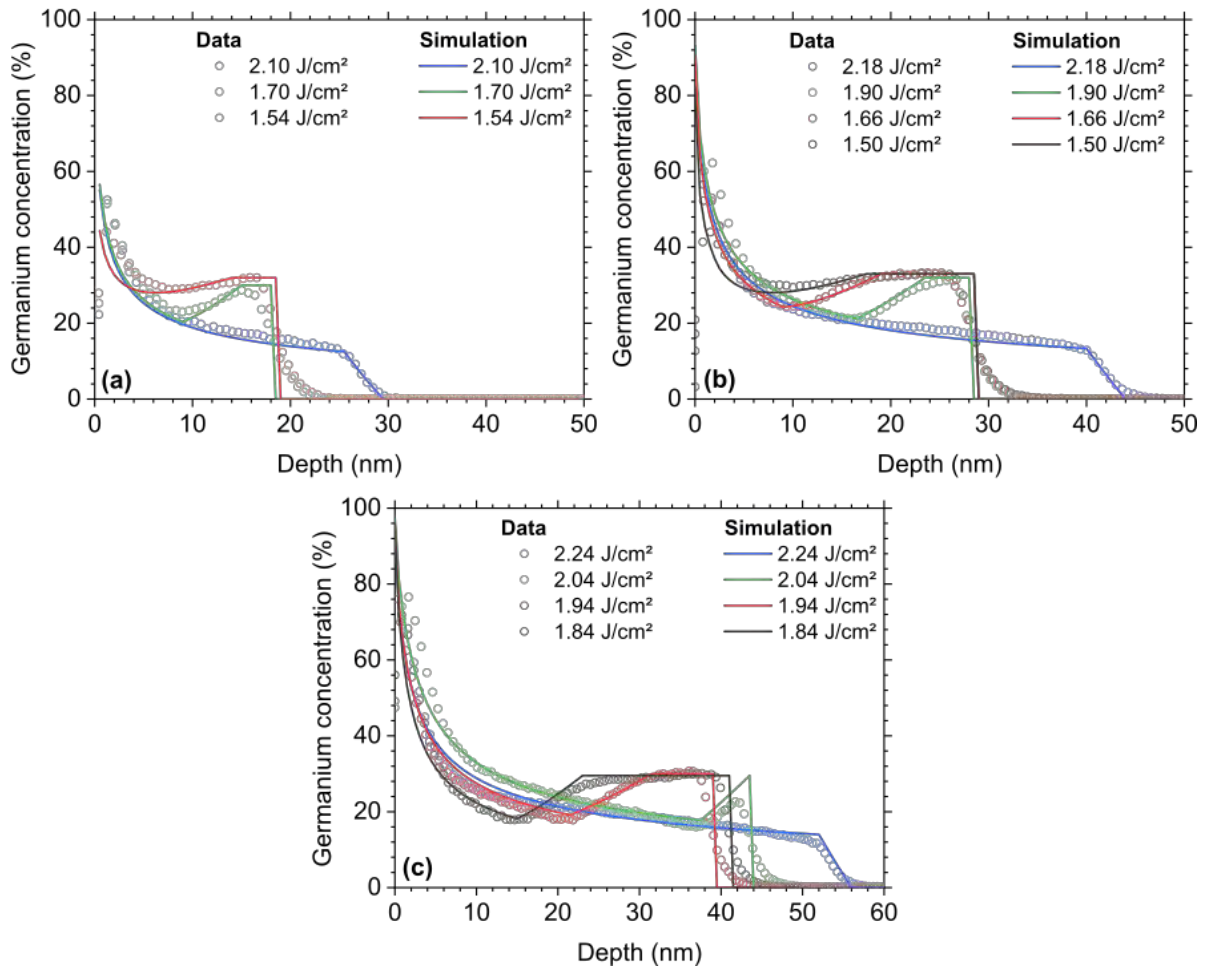


Figure III - 35. Simulated Ge concentration depth profiles (lines) for the Si<sub>0.7</sub>Ge<sub>0.3</sub> series compared with the experimental SIMS data (open symbols). Graphs (a), (b) and (c) respectively correspond to layers 20, 30 and 45 nm thick. Calculations for low energy densities were not able to perfectly reproduce the experimental profiles.

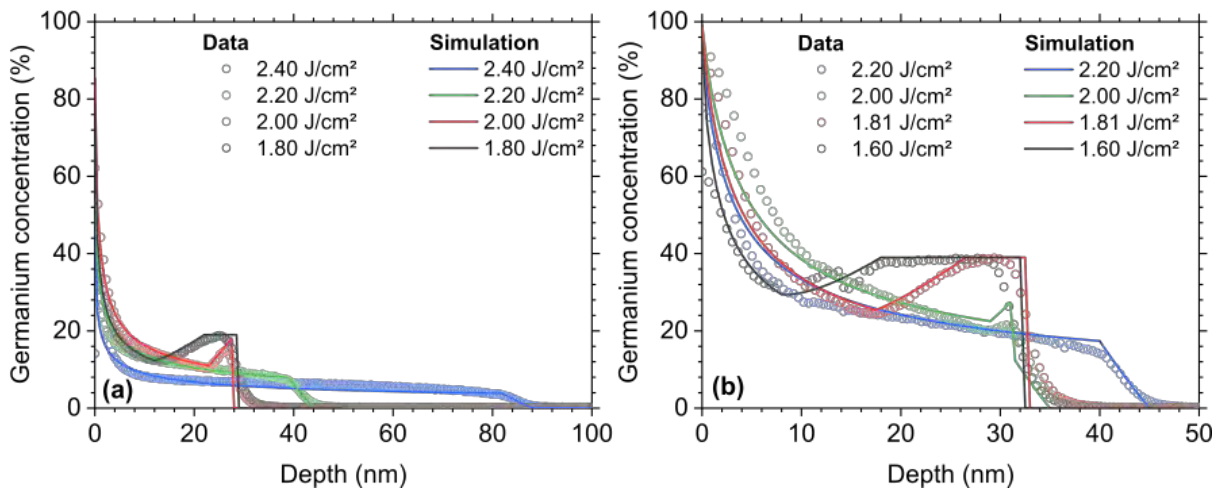


Figure III - 36. Simulated Ge profiles (lines) for the 30 nm series compared with the experimental SIMS data (open symbols). Graphs (a) and (b) respectively correspond to SiGe layers with 20 and 40% initial Ge content. Calculations for low energy densities were not able to perfectly reproduce the experimental profiles.

An average partition coefficient during solidification can be extracted from the best fit. This was done by excluding the 5 nm near the surface, as they tend to exhibit strong Ge

gradients. The final partition coefficients are presented in Figure III - 37 for both the 30 nm series (a) and the  $\text{Si}_{0.7}\text{Ge}_{0.3}$  series (b). All samples exhibit average  $k_i$  in the 0.5 to 0.6 range, with limited variations, with an overall average value near 0.57. This highlights that the partition coefficient, though it varies with the Ge content, remains in a stable range during most of the solidification, as the Ge content does not change much. As highlighted earlier, the solidification velocities did not exceed 1.2 nm/ns in these layers. No clear difference is observed with the pulse duration, as the average values for each series are respectively (a) 0.57 and (b) 0.58.

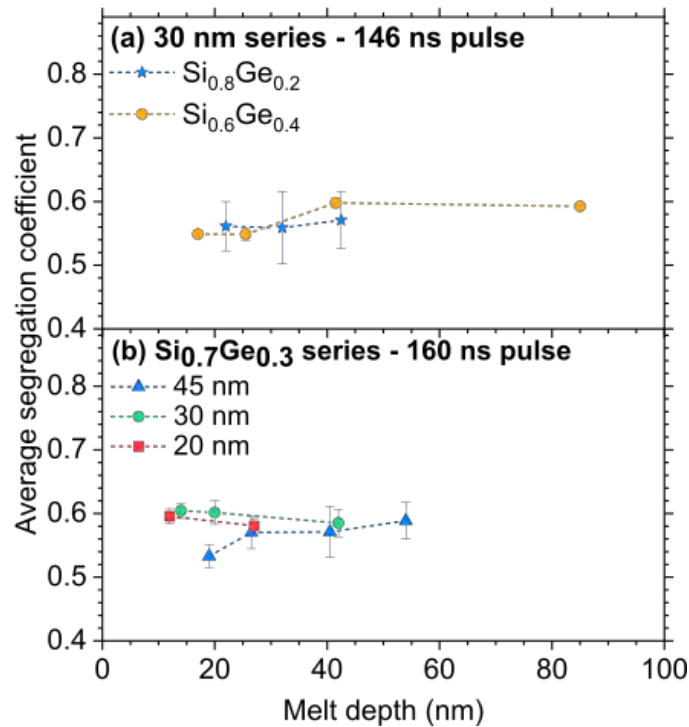


Figure III - 37. Average partition coefficient as a function of melt depth for the 30 nm series (a) and the  $\text{Si}_{0.7}\text{Ge}_{0.3}$  series (b). The error bars correspond to the maximum variation range observed for each sample.

This validates the use of a fixed  $k_i$  in all samples in the LIAB simulations, though the values found with both methods differ (0.57 versus 0.45). A variable partition coefficient is however more efficient to simulate the near surface gradient, as the Ge content may reach values above 50% and thus lead to higher  $k_i$ .

## V – MODIFICATIONS IN REFLECTIVITY SIGNALS

In-situ Time-Resolved Reflectometry (TRR) is a powerful tool for direct study of the melt properties, as the measurement occurs directly during the anneal and registers the complete heating, melting and solidification processes. It can therefore be used to extract several information on melt duration, melt velocity and sometimes melt depth.

### 1. TRR signals on SiGe

The characteristics of TRR signals on SiGe slightly differ from the signals on Si and are not as well known. This section focuses on the observed differences and their possible origins.

#### a) Evolution with energy density

##### i. At high energy densities

Figure III - 38 presents the TRR signal and laser intensity as a function of time after NLA at  $2.40 \text{ J/cm}^2$  on a 30 nm thick  $\text{Si}_{0.7}\text{Ge}_{0.3}$  layer (from the  $\text{Si}_{0.7}\text{Ge}_{0.3}$  series). This corresponds to the full melt regime, with an estimated melt depth above 60 nm. The obtained evolution is identical to the results on Si (see Chapter II) layers at high energy densities: TRR intensity remains stable until the laser pulse starts heating the surface near 190 ns. This causes a progressive increase in the TRR intensity. A stronger increase in TRR signal is observed when the layer reaches its melting point, near 215 ns. A plateau is reached at 260 ns and ends near 405 ns. This plateau is observed when the melt depth exceeds the depth probed by TRR laser beam in the liquid. It is expected for melt depths above 20 nm in Si and Ge layers, and therefore at similar depths in the SiGe alloys. A sharp decrease of the intensity is measured during solidification. A final very progressive decrease can be noticed after  $\sim 440$  ns, which corresponds to the cooling of the material.

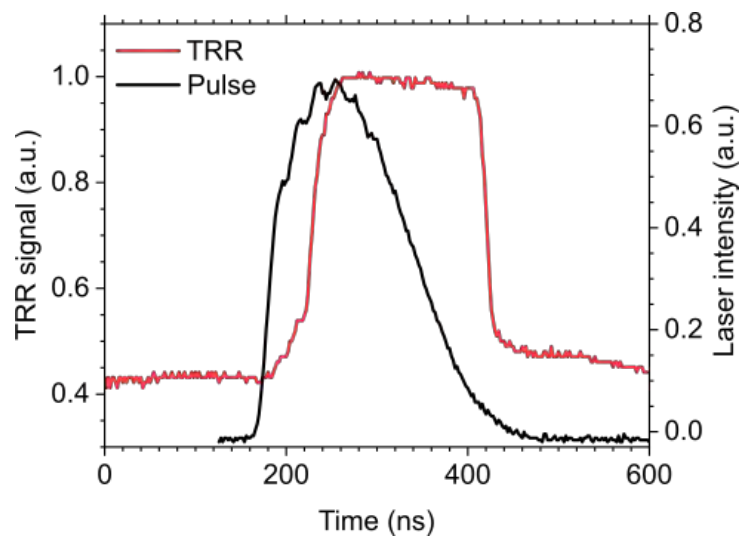


Figure III - 38. Time-Resolved Reflectivity signal and laser pulse intensity as a function of time during UV-NLA on a 30 nm-thick  $\text{Si}_{0.7}\text{Ge}_{0.3}$  layer at  $2.40 \text{ J/cm}^2$ . It is similar to profiles observed for pure Si at high energy densities.

#### ii. Evolution from sub-melt to full melt

There are however a few differences that can be noticed for lower energy densities. Several profiles are shown in Figure III - 39 for a 30 nm-thick  $\text{Si}_{0.7}\text{Ge}_{0.3}$  annealed at various energy densities. The first one (a) corresponds to the sub-melt regime and is similar to what can be observed on Si and Ge – see Figure III - 40 (a) and (e) for comparison. Differences however appear as soon as the melt threshold is reached (above  $1.45 \text{ J/cm}^2$  for the  $\text{Si}_{0.7}\text{Ge}_{0.3}$  sample): Figure III - 40 (b) corresponds to annealing in the surface melt, with a very progressive decrease of TRR intensity during the solidification. This slow solidification behaviour occurs neither in Si, nor in Ge. For these materials, the decrease appears much sharper even in the surface melt regime in Figure III - 40 (b) and (f). This behaviour seems to be specific to the  $\text{Si}_{1-x}\text{Ge}_x$  samples after NLA, and is not an evolution from “Si behaviour” to “Ge behaviour”.

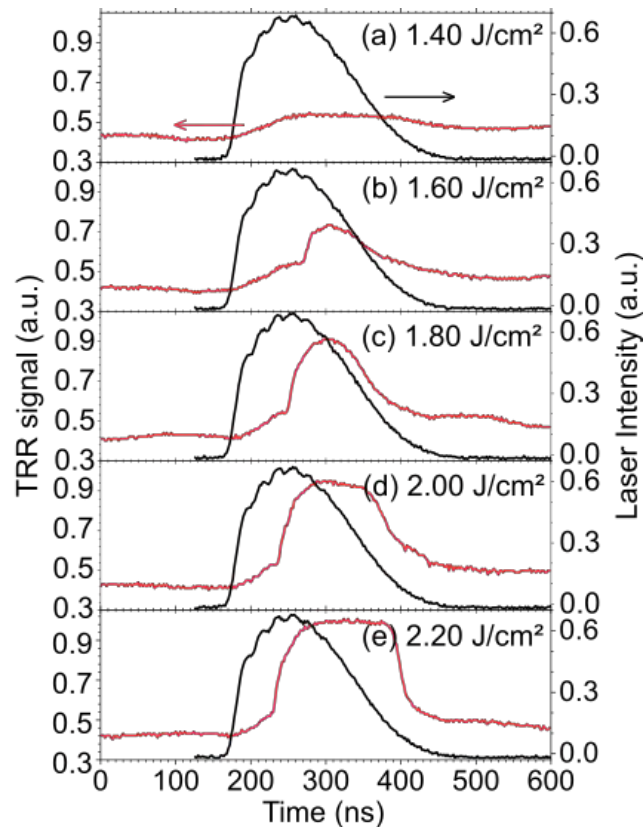


Figure III - 39. Time-Resolved Reflectivity profiles and laser pulse recorded during UV-NLA on a 30 nm-thick  $\text{Si}_{0.7}\text{Ge}_{0.3}$  layer at various energy densities. At  $1.40 \text{ J/cm}^2$  (a), there is no trace of melt, while it appears at  $1.60 \text{ J/cm}^2$  (b) and above. The intensity increases for higher energy densities (c-d) and finally reaches a plateau (d-e). A slope change during solidification can be observed in (c-d-e), respectively near 370 ns, 390 ns and 400 ns.

The solidification velocity slightly increased in pure Si and pure Ge at higher energy densities, as evidenced by the TRR profiles shown in Figure III - 40 (c-d) and (g-h) with a steeper intensity drop. A similar evolution can be noticed for  $\text{Si}_{0.7}\text{Ge}_{0.3}$  in Figure III - 39 (c-d-e) over a larger energy density range, though it remained much more progressive. In addition, a slope change can be noticed near 360 ns and 390 ns for the samples annealed at  $1.80 \text{ J/cm}^2$  and  $2.00 \text{ J/cm}^2$  respectively. Up to this point, the slope is relatively steep (though less than for Si or Ge) and adopts a more moderate value afterwards.

Compared to bulk Si and Ge, the TRR profiles collected for thin  $\text{Si}_{1-x}\text{Ge}_x$  epilayers thus exhibit mainly differences related to the solidification: a more progressive TRR signal decrease from the plateau in two steps, with a first slope already less steep than for pure Si or Ge, and a second more moderate slope, that is not detected for Si nor for Ge.

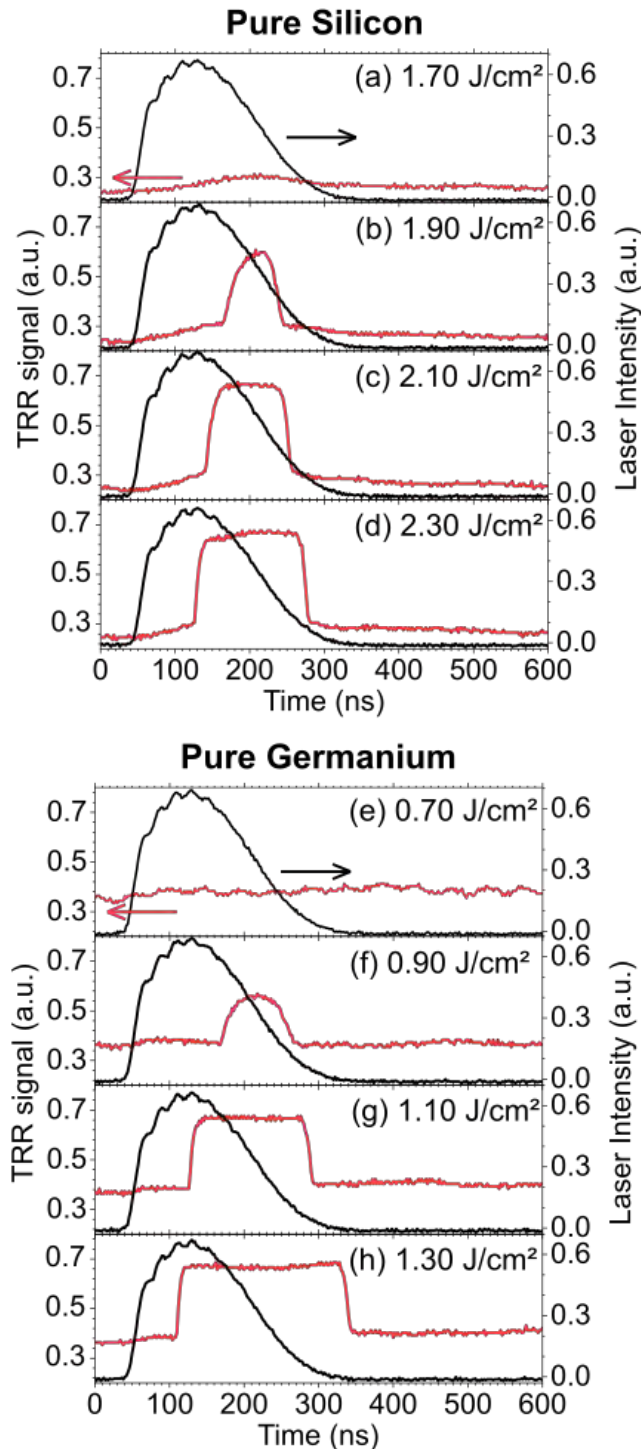


Figure III - 40. Time-Resolved Reflectivity signal and laser intensity as a function of time during UV-NLA on pure Si (a to d) and pure Ge (e to h) layers at various energy densities. The melt thresholds were reached at  $1.80 \text{ J/cm}^2$  and  $0.88 \text{ J/cm}^2$  respectively. Graphs (a, e) correspond to the sub-melt regime, while (b, f) are taken in the surface melt regime. Finally (c, d, g, h) are all part of the full melt regime.

### iii. Origin of second slope

As this behaviour could not be observed in either Si or Ge during solidification, it can be attributed to the specificities of the alloy itself. In addition, as the second slope appears at the end of the solidification, it is likely related to the high Ge content near the surface caused by the Ge segregation. Its exact origin however remains unsure, as it may correspond to either a solidifying superficial layer whose solidification velocity is slowed by the high Ge content, or to

the cooling of the Ge-rich surface. It may also be related to the I/s interface roughness that is observed until the full melt. At the onset of solidification, the I/s interface is known to be rough: if we consider that the solidification proceeds at the same velocity in the whole sample, the I/s interface does not reach the surface at the same time everywhere. This likely causes the formation of Ge-rich liquid pockets at the surface, which solidify at an even lower velocity than the rest. This cannot be observed in Si and Ge, even in the surface melt regime (in which the I/s interface is rough), as the liquid pockets would have the same solidification velocity as the rest of the sample and follow the same tendencies. Though it is the most consistent explanation, it has not been proven yet.

#### b) Impact of chuck temperature on signal

As samples from the doped series were laser annealed at both room temperature and at 450°C using the heating chuck, it is possible to explore the impact of initial sample temperature. TRR maps obtained for samples with medium boron doping levels are shown in Figure III - 41, for (a) laser annealing at room temperature and (b) at 450°C. As expected, the use of the heating chuck lowers the energy density required to reach the melt threshold from 1.45 J/cm<sup>2</sup> to 0.95 J/cm<sup>2</sup> (see white lines in Figure III - 41). In addition, the melt duration increases at a faster rate.

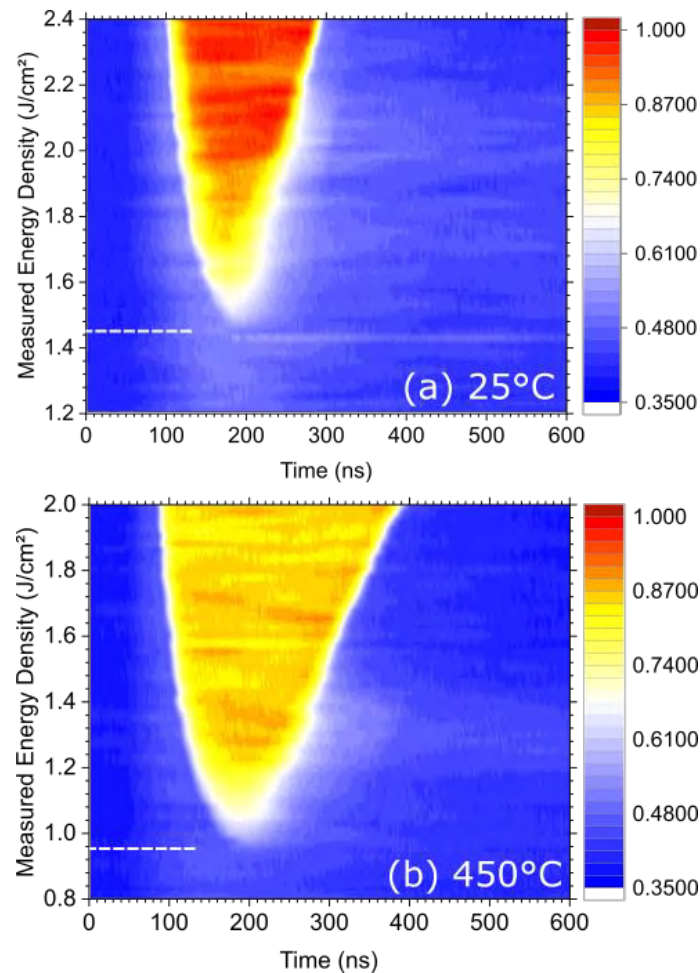


Figure III - 41. TRR maps corresponding to 30 nm-thick Si<sub>0.7</sub>Ge<sub>0.3</sub> layers (medium boron doping level), laser annealed while the sample was initially at room temperature (a) or at 450°C thanks to the heating chuck (b).

The TRR maximum intensity appears ~8% lower for the liquid phase at 450°C, though the initial values for cold layer are closer (4% difference). The photodiode parameters used for data

collection were identical in both cases. Its origin is not yet understood, though it might be due to changes in liquid reflectivity at high temperatures [16].

## 2. Kinetics evaluation

### a) Automatic extraction

In order to easily measure melt durations and velocities, the time and TRR intensity of key points were automatically extracted using a Matlab® program developed during this PhD. Its principle is to smooth the initial TRR signal at a given energy density and obtain its first and second derivatives, as illustrated in Figure III - 42. It corresponds to the raw data from Figure III - 39(d). This code was made to detect whether fusion, plateau and second slope appear in the TRR signal or not, and register several key points according to these information. It relied on the maxima and minima of the second derivative, and their respective positions.

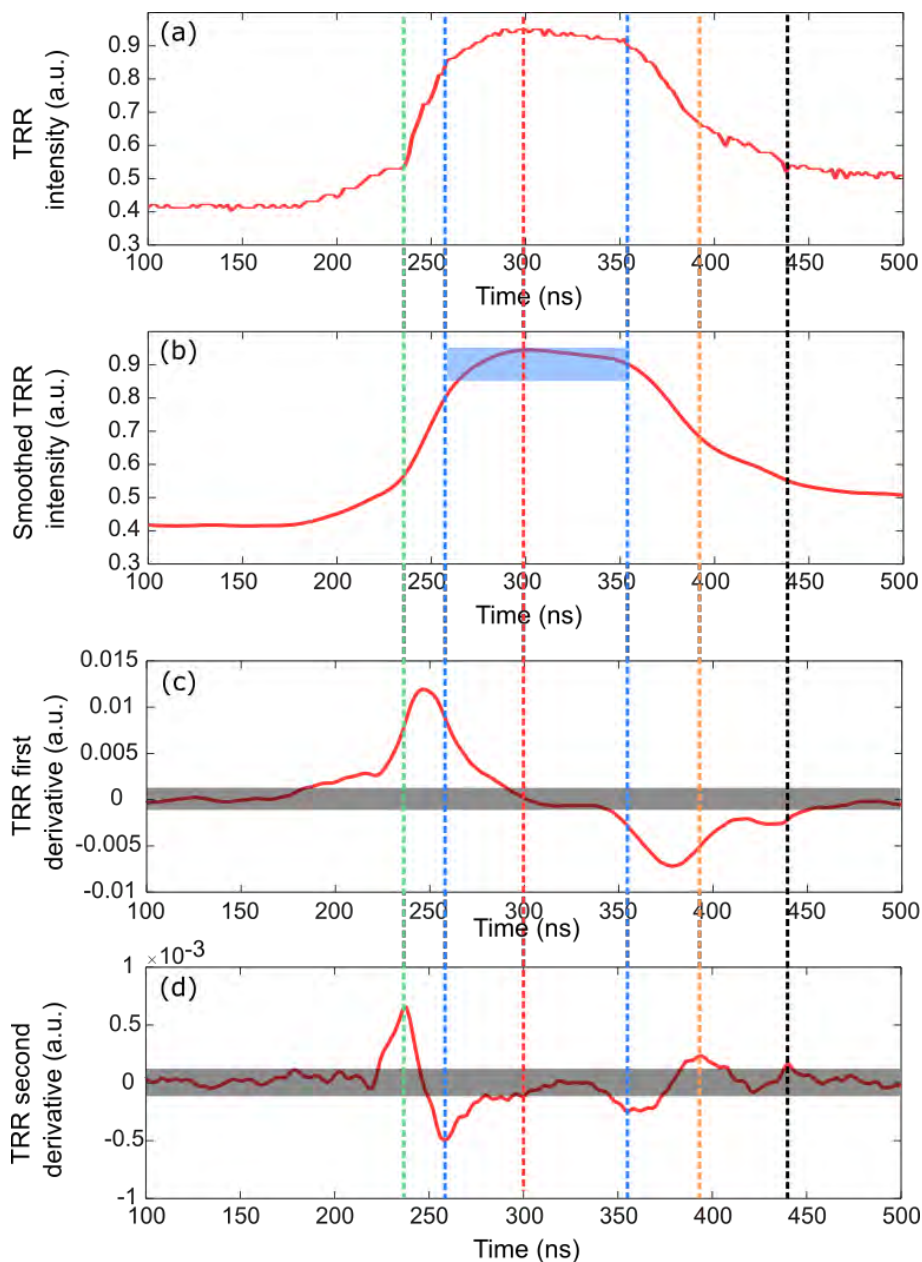


Figure III - 42. TRR signal as a function of time for a 30 nm thick  $\text{Si}_{0.7}\text{Ge}_{0.3}$  sample annealed at  $2.00 \text{ J/cm}^2$  before (a) and after smoothing (b), with the associated first (c) and second (d) derivatives. These data are used to determine the key points indicated by the coloured lines.

The measured points are the following:

- Start of melt It corresponds to the first maximum of the second derivative observed in Figure III - 42, indicated by a green dotted line.
- Plateau limits These key values, indicated by blue dotted lines in Figure III - 42, are searched for only if two clear minima exist on the second derivative, above the noise level. The plateau limits are taken for a TRR intensity equal to the maximum level minus 0.1.
- Slope change It corresponds to the second maximum of the second derivative, above the noise level observed in Figure III - 42 and indicated by the yellow dotted line.
- End of second slope It corresponds to the last maximum of the second derivative, above the noise level. Due to weak slope and proximity to the solidification time, it was often impossible to detect.

The program can take into account several hundreds of TRR signals simultaneously. It therefore allowed to study the complete range of energy densities for a given sample rapidly.

#### b) Melt duration evolution

The melt duration was measured between melting point and slope change during solidification. The results plotted as a function of the energy density, are presented in Figure III - 43.

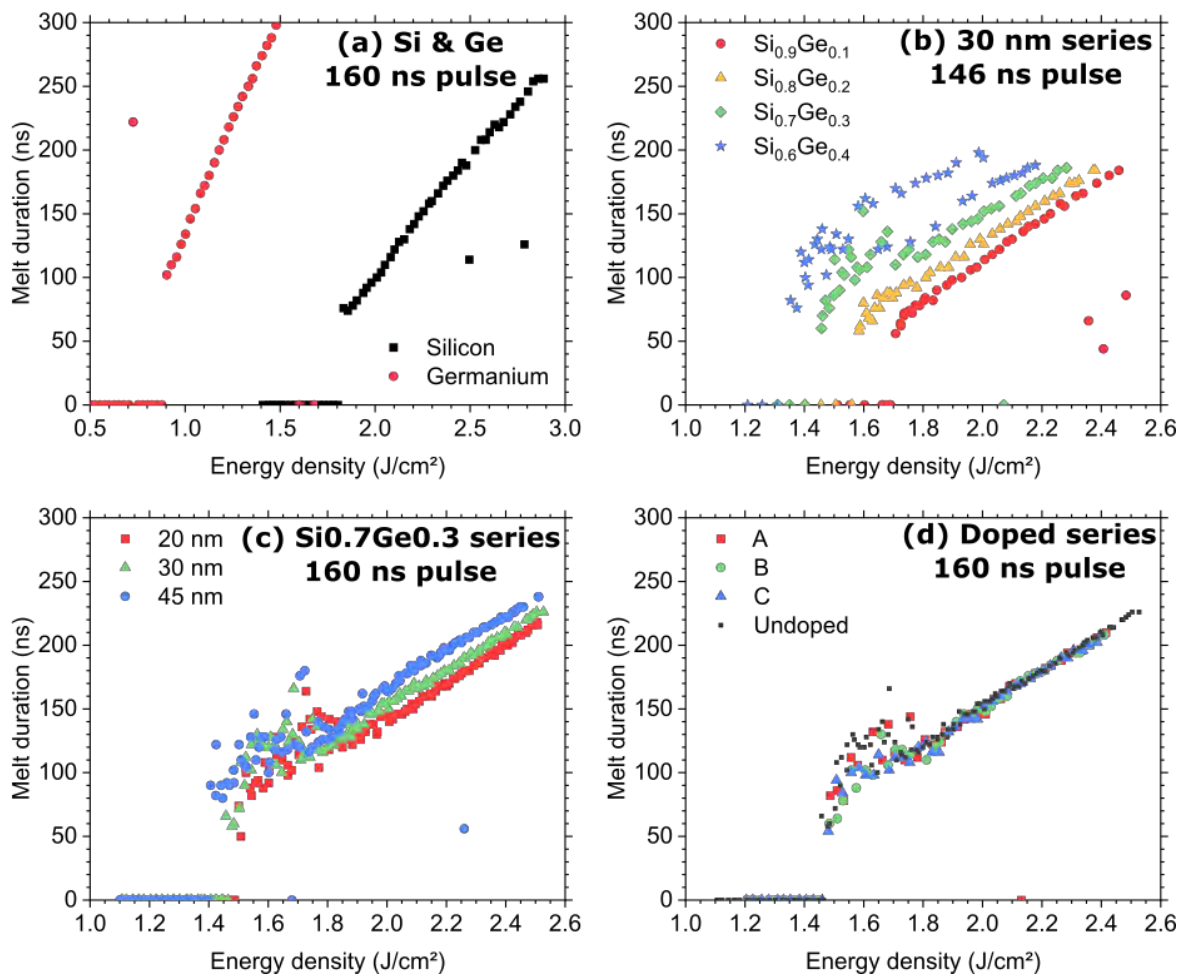


Figure III - 43. Melt duration as a function of the energy density as measured by TRR for pure Si and Ge (a), the 30 nm series (b), the Si<sub>0.7</sub>Ge<sub>0.3</sub> series (c) and the doped series (d). The variability for SiGe layers at low energy densities is caused by the weak slope during solidification, which interferes with detection of the solidification point.

For low energy densities, the TRR intensity variations for SiGe layers are not strong enough to offer reliable detection of the interest points. The detection generally improves once the plateau is observed, as transitions become more pronounced. This leads to inaccuracy in the melt duration in the first part of the curves, which will thus not be discussed in the following sections. Comparison between Si and Ge in Figure III - 43 (a) shows that the melt duration at a given energy density is longer for Ge than for Si, as expected, and that it increases at a faster rate for Ge. Similar conclusions can be made for the comparison of various Ge concentrations in  $\text{Si}_{1-x}\text{Ge}_x$  alloys in Figure III - 43 (b): the melt duration was longer at a given energy density for initially Ge-rich alloys. They however present similar increase rates, though the measurement was highly unstable for the  $\text{Si}_{0.6}\text{Ge}_{0.4}$  layer. The thickness comparison in Figure III - 43 (c) exhibited little difference between the three samples, with a slight increase of the melt duration for the thicker layers. For example, the melt duration evolves from 140 ns to 168 ns when the  $\text{Si}_{0.7}\text{Ge}_{0.3}$  thickness is increased from 20 to 45 nm, at  $2.0 \text{ J/cm}^2$ . Finally, the boron concentration has no impact on the melt duration as observed in Figure III - 43 (d). The differences in increase rate seem related to the differences in thermal conductivity between Si and Ge [17,18], as well as the difference in the melting point. As Ge has much lower thermal conductivity, it takes longer to evacuate a similar amount of accumulated heat than in Si, leading to longer melt duration. The slope for  $\text{Si}_{0.1-x}\text{Ge}_x$  layers does not change much, and is very similar to the Si slope. This highlights the impact of the Si substrate that acts as a heat sink.

#### c) Estimated liquid/solid interface velocities

Another use of the TRR signal is the estimation of the time taken to melt from the surface down to 20 nm depths (maximum depth probed by TRR in liquid Si and Ge). This is performed only for energy densities where the plateau was observed.

##### *i. Time required to melt the upper 20 nm*

The time required to melt the first 20 nm (see Chapter II, section III – 1),  $t_{M-20}$ , is measured between the melting point and the start of the plateau. Figure III - 44 presents the measured  $t_{M-20}$  values for Si and Ge (a), the 30 nm series (b), the  $\text{Si}_{0.7}\text{Ge}_{0.3}$  series (c) and the doped series (d). It was almost identical in all cases, whatever the Ge and B concentrations or thicknesses, with a value close to 20 ns. Variations up to 30 ns are observed for the  $\text{Si}_{0.6}\text{Ge}_{0.4}$  sample, but it is likely related to measurement inaccuracy. It therefore seems that these parameters have a limited impact on the melt velocity in the first 20 nm, and that the average melt velocity is close to 1 nm/ns. We can only extract an average velocity with these measurements, though the velocity may vary during the melt. This fits the values expected on Si for this type of lasers [19], between 1 nm/ns and 3 nm/ns. This however cannot account for what occurs beyond 20 nm.

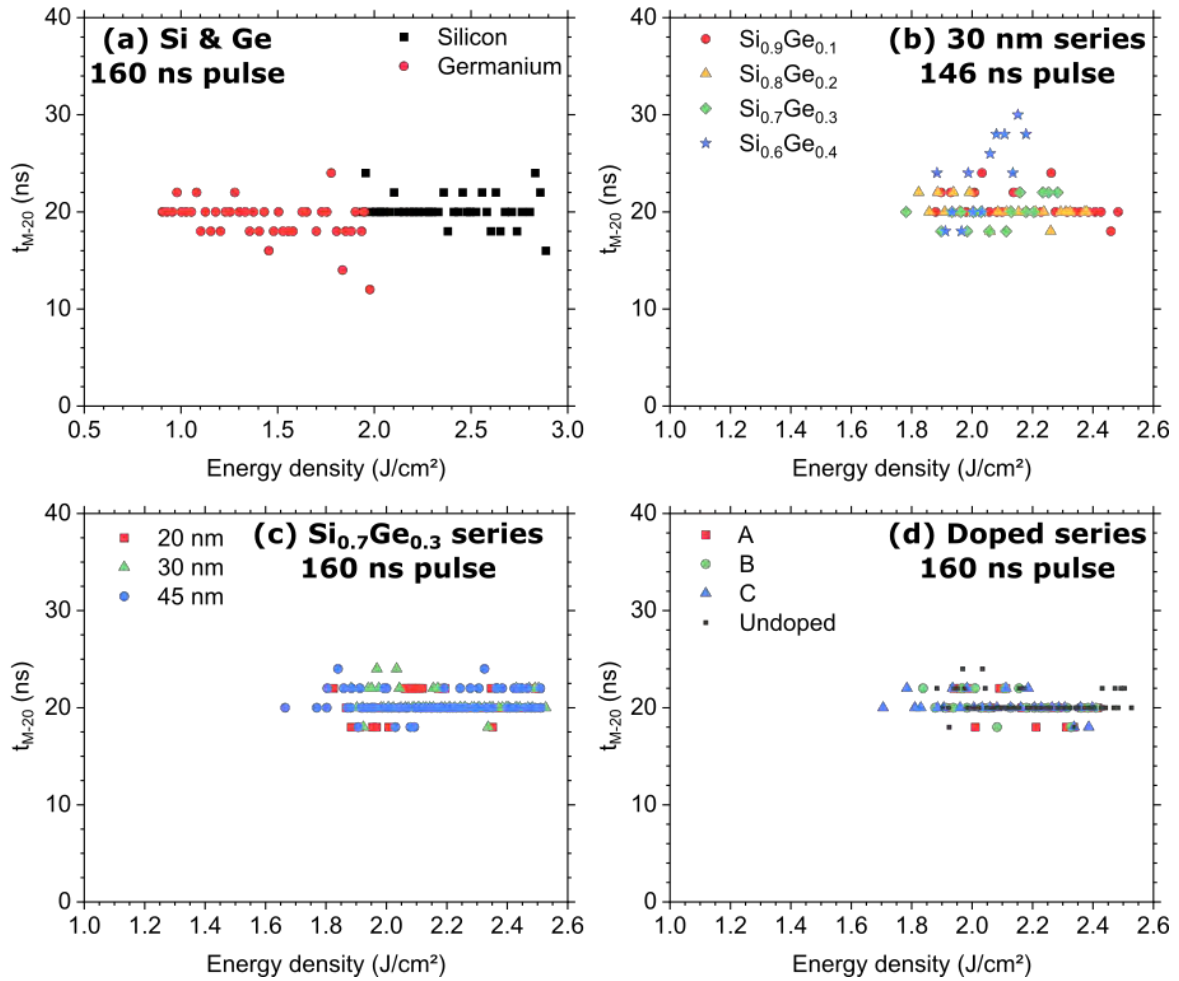


Figure III - 44. Time required to melt the first 20 nm,  $t_{M-20}$ , as a function of energy density as measured by TRR for pure Si and Ge (a), the 30 nm series (b), the  $\text{Si}_{0.7}\text{Ge}_{0.3}$  series (c) and the doped series (d). The measurement is only performed for samples with a melt depth equal or superior to 20 nm.

*ii. Time required for the solidification of the upper 20 nm*

A similar calculation is performed for the time required for the solidification of the last 20 nm,  $t_{S-20}$ : it is the time between the end of the plateau and the slope change. The  $t_{S-20}$  values as a function of energy density are shown in Figure III - 45.

Similarly to  $t_{M-20}$ ,  $t_{S-20}$  is identical for Si and Ge, with values close to 20 ns. This implies that these materials both melt and solidify at the same velocities with the applied process conditions, at least in the upper 20 nm thin region. However, this behaviour differed for  $\text{Si}_{1-x}\text{Ge}_x$  layers, with a visible gradient. The solidification of the last 20 nm appears longer at low energy densities and progressively decreases to stabilize at 20 ns, i.e. the reference value for Si and Ge. This likely reflects the “weak slopes” observed in Figure III - 39, and highlights the difference in solidification velocities for the alloys. This may be due to the Ge segregation, as the solidification temperature of the liquid decreases as it becomes Ge-rich, thus requiring a larger drop in temperature to solidify. The maximum solidification velocity was observed to decrease with the Ge content during explosive crystallization [20]: this may also be the case in other regimes.  $t_{S-20}$  values around 40 ns correspond to velocities near 0.5 nm/ns. When increasing the laser energy density (full melt regime), Ge is redistributed over a larger depth, the amount of Ge near the surface reduced and the behaviour becomes similar to that of silicon.

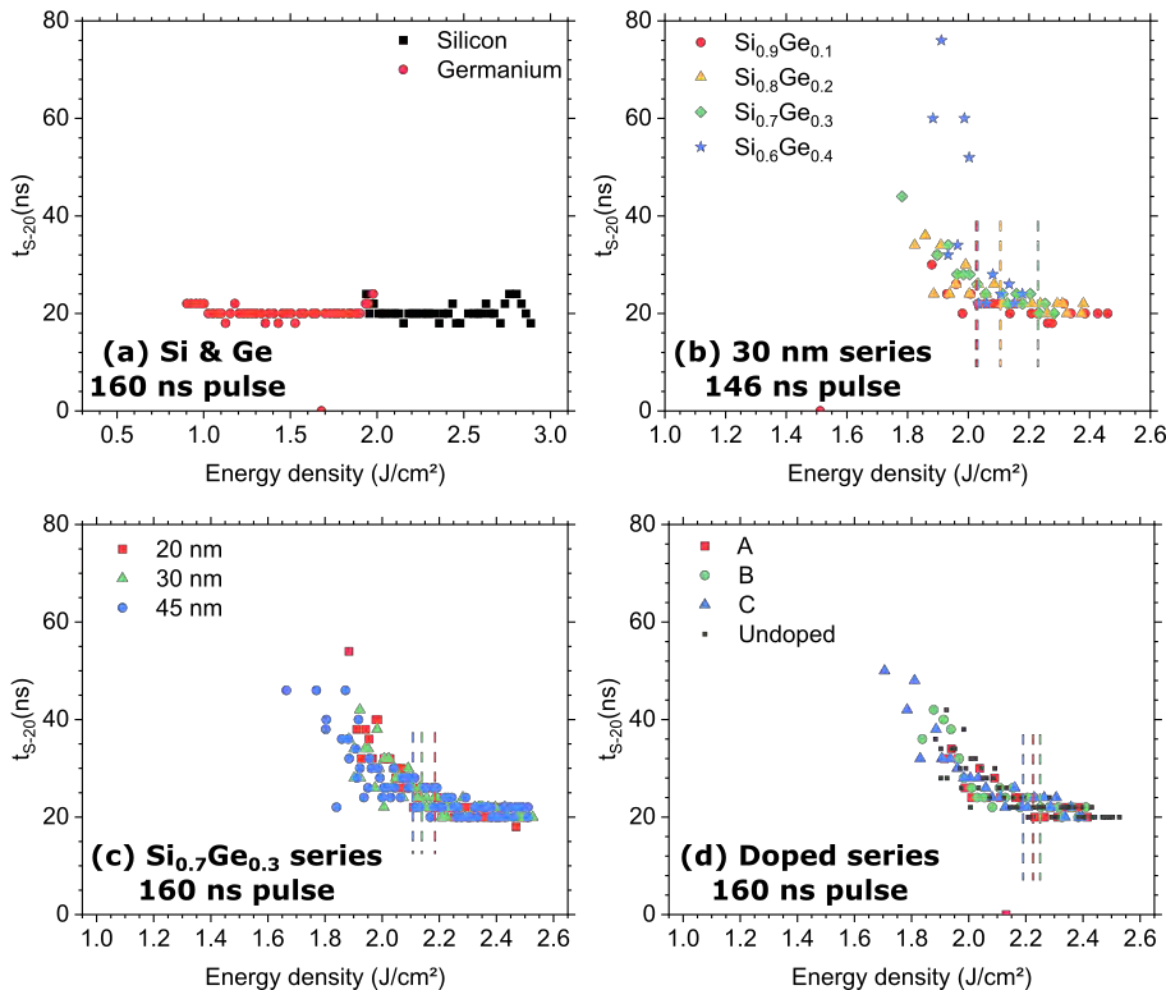


Figure III - 45. Time required for the solidification of the last 20 nm as a function of energy density as measured by TRR for pure Si and Ge (a), the 30 nm series (b), the  $Si_{0.7}Ge_{0.3}$  series (c) and the doped series (d). The measurement is only performed for samples with a melt depth equal or superior to 20 nm. The energy density for which each curve stabilizes is indicated by a dotted line.

The laser energy density at which the solidification velocity in the last 20 nm stabilizes can be used to have a first estimation of the full melt limit without SIMS measurements, as it occurs only when sufficient redistribution occurred. It is however not as reliable, as it seems linked to the amount of Ge in the layer. A comparison of the limits or SIMS and TRR is shown in Table III - 1. The measurements tend to be in the same range and confirm that the TRR can be used to estimate the onset of substrate melt.

Table III - 1. Comparison of the full melt start as detected by SIMS measurements or TRR observations. As the behaviour were identical for each doped sample, they are presented as one.

	Sample	SIMS measurement	TRR measurement
30 nm series	10% Ge	2.00 – 2.20 $J/cm^2$	$2.03 \pm 0.25 J/cm^2$
	20% Ge	2.00 – 2.20 $J/cm^2$	$2.11 \pm 0.25 J/cm^2$
	30% Ge	2.00 – 2.20 $J/cm^2$	$2.23 \pm 0.25 J/cm^2$
	40% Ge	2.00 – 2.20 $J/cm^2$	$2.03 \pm 0.25 J/cm^2$
$Si_{0.7}Ge_{0.3}$ series	20 nm	1.70 – 2.10 $J/cm^2$	$2.19 \pm 0.25 J/cm^2$
	30 nm	1.90 – 2.18 $J/cm^2$	$2.14 \pm 0.25 J/cm^2$
	45 nm	2.04 – 2.24 $J/cm^2$	$2.11 \pm 0.25 J/cm^2$
Doped series	A	~2.10 $J/cm^2$	$2.23 \pm 0.25 J/cm^2$
	B	~2.10 $J/cm^2$	$2.25 \pm 0.25 J/cm^2$
	C	19.5 – 2.10 $J/cm^2$	$2.19 \pm 0.25 J/cm^2$

Automatic extraction of key points enables the comparison of melt duration, as well as melt and solidification kinetics for a wide range of energy densities. This highlights how these values are impacted by the Ge or B content, as well as the layer thickness. The average melt velocity was observed to be close to 1 nm/ns, regardless of the layer properties. The solidification however seems impacted by the alloy, which may be caused by the segregation. This effect reduces as the layer reaches the full melt, as the Ge diffuses in depth.

## CONCLUSION

This chapter focused on the regimes encountered in  $\text{Si}_{1-x}\text{Ge}_x$  layers submitted to nanosecond laser annealing depending on their composition and thicknesses and their means of detection. The different phenomena observed were then detailed, and their properties were described for the different regimes. The regimes encountered were named the surface melt regime, the partial melt regime, and the full melt regime. The regimes limits detection relies on several characterization techniques, in particular Time-Resolved Reflectometry to deduce the melt threshold and observe the melt duration, SP2 Haze for surface evolution, which enables the detection of regimes with high surface roughness and ToF-SIMS measurements for Ge distribution.

The surface melt regime corresponds to an increase of the surface roughness, associated with the formation of isolated molten islands. These islands are visible by surface microscopy (AFM or SEM), and segregation within was observed thanks to TEM cross-sections, coupled to EDX analysis. These isolated molten regions progressively merge with increasing energy density, until the surface has fully melted and becomes smoother. This corresponds to the end of the surface melt regime. This regime was observed for every sample, even pure silicon layers, and is therefore not related to the Ge content. The shape and growth of the islands is however impacted by the Ge content within the layer: they appear smaller and star-shaped in Ge-rich alloys, rather than square-shaped. In addition, amorphous layers exhibit slightly different behaviours.

The partial melt regime is characterized by a continuous molten layer within the SiGe film. It exhibits strong Ge segregation, with the formation of a Ge-rich surface and a depleted region near the melt depth. Simulations of the Ge profiles were performed with two methods, taking into account a Ge concentration dependence or not. The partition coefficient was estimated in the 0.4-0.45 range for the approach with no Ge concentration dependence. In the other case, only the solidification velocity could be estimated. It was estimated in the range from 0.4 to 1.0 nm/ns, which is consistent with other observations. TEM observations, along with Ge depth profiles, showed that the liquid/solid interface remained rough until the full melt was reached.

The full melt is reached when the whole SiGe layer melts, and eventually part of the substrate. This leads to the Ge redistribution over a thicker layer, resulting in a decrease in the amount of Ge near the surface. In this regime, the properties of the layer progressively become closer to that of pure Si, as it mixes with the substrate.

In the case of amorphized layers, an additional regime exists at the onset of melt, namely the explosive regime. In this regime, only the amorphous layer melts and solidifies at very high velocities. It was shown experimentally that the complete amorphous layer melts even at low energy densities, confirming that explosive crystallization is a self-sustained process. In addition, there are hints of the crystallization going from the surface to the bottom of the layer.

Finally, TRR was presented as a powerful tool for in-situ analysis. Key point extraction gave access to velocities for both melt and solidification, and highlighted the differences between pure materials and alloys where segregation occurs. In particular, the solidification was much slower for layers with a Ge-rich surface. It may also be used to obtain an overview of the different annealing regimes encountered in  $\text{Si}_{1-x}\text{Ge}_x$  with increasing energy density, as the melt characteristics change with the regimes.

## KEY INFORMATION

REGIMES IDENTIFICATION	Various regimes are encountered with increasing energy density
1. Surface melt	<ul style="list-style-type: none"> <li>➔ Appearance of geometric nanostructures on the surface               <ul style="list-style-type: none"> <li>○ Detected by surface analysis : AFM, SEM, SP2 Haze</li> </ul> </li> </ul>
2. Partial melt	<ul style="list-style-type: none"> <li>➔ Melt depth within the SiGe layer               <ul style="list-style-type: none"> <li>○ Identified by chemical profiles</li> </ul> </li> </ul>
3. Full melt	<ul style="list-style-type: none"> <li>➔ Melt depth beyond the SiGe layer</li> </ul>
MELT THRESHOLD	Onset of melt
1. Concentration impact	<ul style="list-style-type: none"> <li>➔ Lower melt threshold for Ge-rich alloys               <ul style="list-style-type: none"> <li>○ Lower melt temperature</li> <li>○ Lower thermal conductivity</li> </ul> </li> </ul>
2. Thickness impact	<ul style="list-style-type: none"> <li>➔ Slight reduction of melt threshold for thicker layers</li> </ul>
SURFACE STRUCTURATIONS	Geometric nanostructures observed during the surface melt regime
1. Structures origin	<ul style="list-style-type: none"> <li>➔ Formation of isolated molten islands               <ul style="list-style-type: none"> <li>○ Segregation observed by TEM inside the structures</li> <li>○ Grow and merge - cover the surface at high EDs</li> </ul> </li> </ul>
2. Evolution with layer properties	<ul style="list-style-type: none"> <li>➔ Shape modifications               <ul style="list-style-type: none"> <li>○ Growth along the <math>\langle 100 \rangle</math> directions in Ge-rich alloys</li> <li>○ No impact of layer thickness</li> </ul> </li> </ul>
SEGREGATION	Formation of Ge gradients with a Ge-rich surface
1. Melt depth	<ul style="list-style-type: none"> <li>➔ Enables melt depth estimations               <ul style="list-style-type: none"> <li>○ Similar results at every concentration/thickness</li> </ul> </li> </ul>
2. Interface roughness	<ul style="list-style-type: none"> <li>➔ Ge redistribution highlights the liquid/solid interface shape               <ul style="list-style-type: none"> <li>○ Rough liquid/solid interface in surface and partial melt</li> <li>○ Smooth liquid/solid interface in full melt</li> </ul> </li> </ul>
3. Simulations	<ul style="list-style-type: none"> <li>➔ Partition coefficient estimated around 0.4-0.45</li> </ul>
SiGe REFLECTIVITY	Analysis of the reflectivity signals and comparison
1. Differences with Si and Ge	<ul style="list-style-type: none"> <li>➔ Signals on alloys differ from the results on pure materials               <ul style="list-style-type: none"> <li>○ Weak solidification slope</li> <li>○ Longer energy density range to reach the TRR plateau</li> </ul> </li> </ul>
2. Melt duration and velocities	<ul style="list-style-type: none"> <li>➔ Automatic extraction of key points               <ul style="list-style-type: none"> <li>○ Melt velocity is equivalent for all materials, near 1 nm/ns</li> <li>○ Solidification velocity is lower for SiGe alloys</li> <li>○ Increases to 1 nm/ns after intermixing with Si</li> </ul> </li> </ul>

## BIBLIOGRAPHY

- [1] A.S. Royet, Undoped SiGe material calibration for numerical laser annealing simulation, in: 2020.
- [2] K. Huet, J. Aubin, P.-E. Raynal, B. Curvers, A. Verstraete, B. Lespinasse, F. Mazzamuto, A. Sciuto, S.F. Lombardo, A. La Magna, P. Acosta-Alba, L. Dagault, C. Licitra, J.-M. Hartmann, S. Kerdilès, Pulsed laser annealing for advanced technology nodes: Modeling and calibration, *Applied Surface Science*. 505 (2020) 144470. <https://doi.org/10.1016/j.apsusc.2019.144470>.
- [3] G.E. Jellison, D.H. Lowndes, D.N. Mashburn, R.F. Wood, Time-resolved reflectivity measurements on silicon and germanium using a pulsed excimer KrF laser heating beam, *Phys. Rev. B*. 34 (1986) 2407–2415. <https://doi.org/10.1103/PhysRevB.34.2407>.
- [4] J.F. Young, J.E. Sipe, H.M. van Driel, Laser-induced periodic surface structure. III. Fluence regimes, the role of feedback, and details of the induced topography in germanium, *Phys. Rev. B*. 30 (1984) 2001–2015. <https://doi.org/10.1103/PhysRevB.30.2001>.
- [5] K.-H. Heinig, Effects of local melting on semiconductor surfaces, *Energy Pulse Modification of Semiconductors and Related Materials*. (1984) 265–279.
- [6] D. Skarlatos, V. Ioannou-Sougleridis, M. Barozzi, G. Pepponi, D. Velessiotis, M.C. Skoulikidou, N.Z. Vouroutzis, K. Papagelis, P. Dimitrakis, C. Thomidis, B. Colombeau, Phosphorous Diffusion in N<sub>2</sub><sup>+</sup>-Implanted Germanium during Flash Lamp Annealing: Influence of Nitrogen on Ge Substrate Damage and Capping Layer Engineering, *ECS J. Solid State Sci. Technol.* 6 (2017) P418–P428. <https://doi.org/10.1149/2.0201707jss>.
- [7] M. Smith, R. McMahan, M. Voelskow, W. Skorupa, J. Stoemenos, G. Ferro, Process control and melt depth homogenization for SiC-on-Si structures during flash lamp annealing by carbon implantation, *Journal of Applied Physics*. 100 (2006) 094909–094909. <https://doi.org/10.1063/1.2359684>.
- [8] Q.S. Mei, K. Lu, Melting and superheating of crystalline solids: From bulk to nanocrystals, *Progress in Materials Science*. 52 (2007) 1175–1262. <https://doi.org/10.1016/j.pmatsci.2007.01.001>.
- [9] H.A. Atwater, C.V. Thompson, H.I. Smith, Mechanisms for crystallographic orientation in the crystallization of thin silicon films from the melt, *Journal of Materials Research*. 3 (1988) 1232–1237. <https://doi.org/10.1557/JMR.1988.1232>.
- [10] J.C. Brice, P.A.C. Whiffin, The temperature distribution in pulled germanium crystals during growth, *Solid-State Electronics*. 7 (1964) 183–187. [https://doi.org/10.1016/0038-1101\(64\)90143-1](https://doi.org/10.1016/0038-1101(64)90143-1).
- [11] V.M. Glazov, O.D. Shchelikov, Volume changes during melting and heating of silicon and germanium melts, *High Temperature*. 38 (2000) 405–412.
- [12] W. Sinke, F.W. Saris, Evidence for a Self-Propagating Melt in Amorphous Silicon upon Pulsed-Laser Irradiation, *Phys. Rev. Lett.* 53 (1984) 2121–2124. <https://doi.org/10.1103/PhysRevLett.53.2121>.
- [13] S.F. Lombardo, S. Boninelli, F. Cristiano, I. Deretzis, M.G. Grimaldi, K. Huet, E. Napolitani, A. La Magna, Phase field model of the nanoscale evolution during the explosive crystallization phenomenon, *Journal of Applied Physics*. 123 (2018) 105105. <https://doi.org/10.1063/1.5008362>.

- [14] M.O. Thompson, G.J. Galvin, J.W. Mayer, P.S. Peercy, J.M. Poate, D.C. Jacobson, A.G. Cullis, N.G. Chew, Melting Temperature and Explosive Crystallization of Amorphous Silicon during Pulsed Laser Irradiation, *Phys. Rev. Lett.* 52 (1984) 2360–2363. <https://doi.org/10.1103/PhysRevLett.52.2360>.
- [15] D.P. Brunco, M.O. Thompson, D.E. Høglund, M.J. Aziz, H. -J. Gossmann, Germanium partitioning in silicon during rapid solidification, *Journal of Applied Physics.* 78 (1995) 1575–1582. <https://doi.org/10.1063/1.360251>.
- [16] M.O. Lampert, J.M. Koebel, P. Siffert, Temperature dependence of the reflectance of solid and liquid silicon, *Journal of Applied Physics.* 52 (1981) 4975–4976. <https://doi.org/10.1063/1.329436>.
- [17] P.I. Gaiduk, S.L. Prakopyeu, V.A. Zajkov, G.D. Ivlev, E.I. Gatskevich, Laser-induced melting and recrystallization of CVD grown polycrystalline Si/SiGe/Ge layers, *Physica B: Condensed Matter.* 404 (2009) 4708–4711. <https://doi.org/10.1016/j.physb.2009.08.127>.
- [18] C.J. Glassbrenner, G.A. Slack, Thermal Conductivity of Silicon and Germanium from 3\ifmmode^\circ\else\textdegree\fi{}K to the Melting Point, *Phys. Rev.* 134 (1964) A1058–A1069. <https://doi.org/10.1103/PhysRev.134.A1058>.
- [19] M. Hernandez, J. Venturini, D. Zahorski, J. Boulmer, D. Débarre, G. Kerrien, T. Sarnet, C. Laviron, M.N. Semeria, D. Camel, J.L. Santailier, Hernandez2003; Laser thermal processing for ultra shallow junction formation: numerical simulation and comparison with experiments, *Applied Surface Science.* 208–209 (2003) 345–351. [https://doi.org/10.1016/S0169-4332\(02\)01395-8](https://doi.org/10.1016/S0169-4332(02)01395-8).
- [20] Q. Yu, M.O. Thompson, P. Clancy, Solidification kinetics in SiGe alloys, *Phys. Rev. B.* 53 (1996) 8386–8397. <https://doi.org/10.1103/PhysRevB.53.8386>.



---

# CHAPTER IV

## STRAIN EVOLUTION UPON NANOSECOND LASER ANNEALING

I – EVOLUTION OF STRAIN STATE WITH THE ANNEALING REGIMES : $\text{Si}_{0.6}\text{Ge}_{0.4}$ EXAMPLE .....	138
1. Strain state observed for each regime .....	138
2. Origin of relaxation .....	142
a) Impact of the liquid/solid interface roughness .....	142
b) Elastic energy-driven relaxation .....	143
i. Bi-layer formation at high energy densities .....	143
ii. Elastic energy density calculations .....	144
II – IMPACT OF SiGe LAYER PROPERTIES ON STRAIN RELAXATION .....	145
1. Impact of Germanium concentration and layer thickness.....	146
a) Strain relaxation in 30 nm thick layers: impact of Ge content.....	146
b) Strain relaxation in $\text{Si}_{0.7}\text{Ge}_{0.3}$ layers : impact of thickness.....	149
c) Elastic energy density limit for strain relaxation .....	151
d) Predictive calculations for elastic energy-induced relaxation.....	152
e) Conclusion on pseudomorphic undoped layers.....	153
2. Amorphous SiGe layers: comparison with epi-layers.....	153
a) Initial state.....	153
b) Relaxation for 15 nm and 30 nm thick amorphized layers .....	154
i. In explosive regime .....	154
ii. In other regimes.....	156
III – BORON IMPACT ON THE RELAXATION OF 30 NM-THICK $\text{Si}_{0.7}\text{Ge}_{0.3}$ LAYERS.....	157
1. Relaxation in pseudomorphic doped layers .....	157
2. Relaxation in amorphized doped layers.....	159
CONCLUSION .....	161
KEY INFORMATION .....	162
BIBLIOGRAPHY .....	163

# CHAPTER IV

## STRAIN EVOLUTION UPON NANOSECOND LASER ANNEALING

The evolution of strain in  $\text{Si}_{1-x}\text{Ge}_x$  layers submitted to laser annealing with increasing energy density was studied by means of XRD and TEM observations. The evolution of macroscopic relaxation levels and defects nature is described for each of the previously detailed regimes (sub-melt, surface melt, partial melt and full melt), showing how the initial layer nature (i.e. its composition, thickness and crystalline quality) influences the strain. The potential origins of the strain relaxation are detailed, enabling to find conditions to avoid it.

Similarly to the approach followed in Chapter III, the experimental results and possible origins of the observed strain evolution are first discussed for a 30 nm-thick  $\text{Si}_{0.6}\text{Ge}_{0.4}$  sample, and then extended to all the investigated series.

### I – EVOLUTION OF STRAIN STATE WITH THE ANNEALING REGIMES : $\text{Si}_{0.6}\text{Ge}_{0.4}$ EXAMPLE

As detailed in Chapter III, submitting  $\text{Si}_{1-x}\text{Ge}_x$  layers to NLA changes their morphology, and various regimes can be distinguished depending on the surface state, Ge distribution and reflectivity during the anneal. The regimes observed for an initially pseudomorphic layer are the sub-melt, the surface melt, the partial melt and the full melt. The sub-melt does not lead to any morphological changes compared to non-annealed layers, while samples in surface melt present multiple isolated molten islands on the surface. The partial melt and full melt both show Ge redistribution, with Ge segregation towards the surface. They are distinguished by the melt depth, that extends beyond the initial SiGe/Si interface for the full melt. In addition, partial melt tends to exhibit a rough liquid/solid interface.

#### 1. Strain state observed for each regime

Reciprocal Space Maps (RSM) around the (224) diffraction order were used to obtain the degree of strain relaxation  $R$  for all annealing regimes in  $\text{Si}_{0.6}\text{Ge}_{0.4}$  samples. These measurements enable to identify the position of the SiGe spot in reciprocal space relatively to the Si spot, and measure its coordinates in reciprocal space. As this corresponds to an asymmetrical measurement, the position of the spot along the  $q_x$  is indicative of the relaxation: it is vertically aligned with the Si spot (same  $q_x$  value) for a strained layer. The peak position along the  $q_x$  and  $q_z$  axis of the reciprocal space depends on strain and on composition, as shown in Figure II – 17. For comparison, the examples of peak position and shapes in Reciprocal Space Maps for strained layers, relaxed layers and bilayers are shown in Chapter II (Figure II – 18).

The RSMs measured on  $\text{Si}_{0.6}\text{Ge}_{0.4}$  layers submitted to NLA are presented in Figure IV - 1 for the different regimes. For the layer in sub-melt (a), the RSM exhibits a SiGe spot vertically aligned with the Si spot, and exhibits thickness fringes. These fringes correspond to the less intense spots visible between the SiGe and Si spots, and are indicative of a uniform pseudomorphic layer. Higher energy densities (b,c) lead to a displacement of the SiGe peak towards the left (i.e. lower  $q_x$  values), with more diffuse spots. At 1.81 J/cm<sup>2</sup>, the SiGe spot is on the tilted line corresponding to full relaxation and is highly diffuse. Annealing at 2.00 and 2.20 J/cm<sup>2</sup> lead to the appearance of a double spot on the RSMs: one is vertically aligned with

the Si spot, while the other remains diffuse, with lower  $q_x$  values. This indicates the formation of a bilayer.

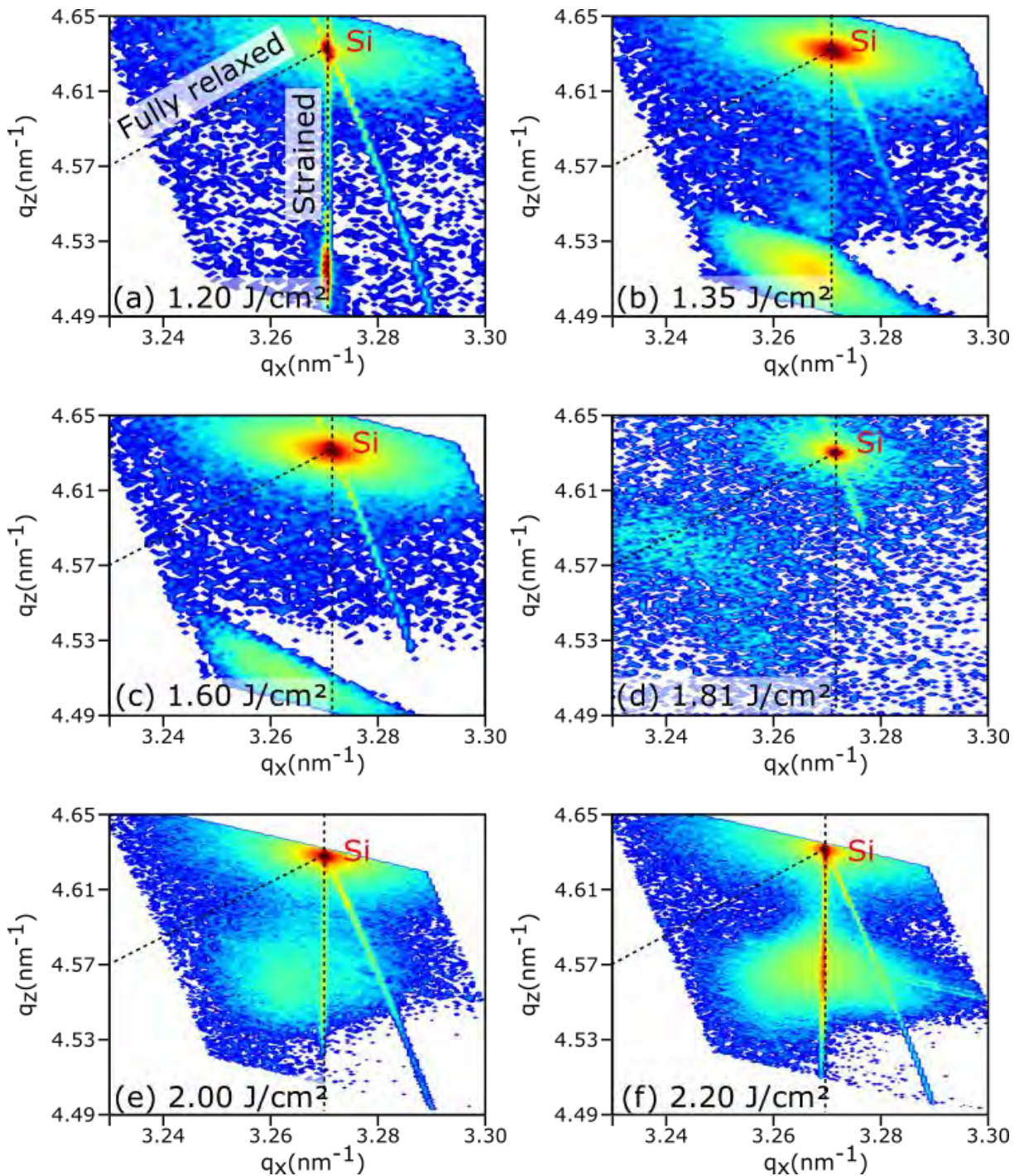


Figure IV - 1. Reciprocal Space Maps along the (224) direction on 30 nm-thick  $\text{Si}_{0.6}\text{Ge}_{0.4}$  layers laser annealed at (a) 1.20 J/cm<sup>2</sup>, (b) 1.35 J/cm<sup>2</sup>, (c) 1.60 J/cm<sup>2</sup>, (d) 1.81 J/cm<sup>2</sup>, (e) 2.00 J/cm<sup>2</sup> and (f) 2.20 J/cm<sup>2</sup>. The tilted and vertical dotted lines starting from the bulk silicon peak respectively indicate the theoretical position of the SiGe spot for a fully relaxed layer and a fully strained layer.

The macroscopic level of strain relaxation can be estimated by measuring the ( $q_x$ ,  $q_z$ ) position of the SiGe spot in the reciprocal space map and following the method described in Chapter II (Eq. II – [11-16]), with the relaxation  $R$  written as [1,2]:

$$R = \frac{a_{\text{SiGe}}^{\parallel} - a_{\text{Si}}}{a_{\text{SiGe}}^0 - a_{\text{Si}}} \quad \text{Eq. IV - [1]}$$

where  $a_{\text{SiGe}}^{\parallel}$  is the in-plane lattice parameter of the strained SiGe layer,  $a_{\text{SiGe}}^0$  is the lattice parameter of completely relaxed SiGe and  $a_{\text{Si}}$  the lattice parameter of relaxed Si ( $a_{\text{Si}} = 5.43105 \text{ \AA}$ ). The degree of macroscopic relaxation is plotted in Figure IV - 2 as a function of the laser energy density for the 30 nm-thick  $\text{Si}_{0.6}\text{Ge}_{0.4}$  layer.

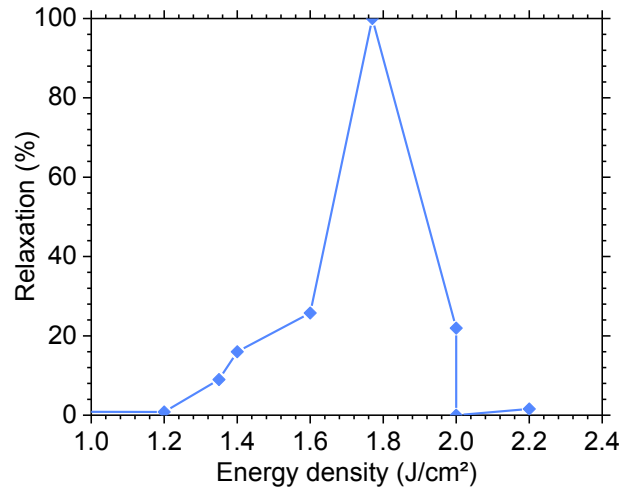


Figure IV - 2. Evolution of the macroscopic degree of relaxation as a function of the laser energy density for 30 nm-thick  $\text{Si}_{0.6}\text{Ge}_{0.4}$  layers. These data were extracted from (224) XRD RSM such as the ones shown in Figure IV - 1.

As expected, as-grown samples were pseudomorphic. Samples remained pseudomorphic in the sub-melt regime, as shown in Figure IV - 1(a) after annealing at  $1.20 \text{ J/cm}^2$ . Partial relaxation occurred for samples in the surface melt regime, with a degree of relaxation that increased with the laser energy density, i.e. from 10% at  $1.35 \text{ J/cm}^2$  up to 26% at  $1.60 \text{ J/cm}^2$  (RSM in Figure IV - 1(b-c)). As mentioned previously, these maps presented wide and diffuse spots, extending over a large  $q_x$  and  $q_z$  range: this is indicative of defects and mosaicity within the layer [3]. Diffuse spots may also be related to a strain gradient [4]. In Figure IV - 1 (b), some thickness fringes can still be observed between the SiGe and Si spots, revealing that a relatively large part of the material still remained strained and with a uniform Ge content. For the sample annealed at  $1.60 \text{ J/cm}^2$ , with about 60% of surface melted, no fringes were observed in the RSM (Figure IV - 1(c)). Samples annealed in the partial melt regime presented apparently disparate results. For a laser energy density of  $1.81 \text{ J/cm}^2$ , the layer was found to be fully relaxed, as shown in Figure IV - 1(d). The SiGe spot was very diffuse and extended, indicating the presence of numerous defects. At the end of the partial melt ( $2.00 \text{ J/cm}^2$ ), two relaxation values are indicated in the graph due to the double spot: part of the layer shows a relaxation level near 22% and the rest is fully strained. This is shown on Figure IV - 2 with two data points at  $2.00 \text{ J/cm}^2$ . A similar double contribution is observed on the RSM at  $2.20 \text{ J/cm}^2$  (f), but the relaxation value could not be measured for the relaxed spot as it is too diffuse. There is therefore only one data point at  $2.20 \text{ J/cm}^2$  on Figure IV - 2, though it is a bilayer.

Dark Field (DF) TEM micrographs from samples annealed at energies from  $1.60 \text{ J/cm}^2$  to  $2.20 \text{ J/cm}^2$  are presented in Figure IV - 3. Two diffracting vectors were used for each sample:  $g = [004]$  (Figure IV - 3(a-d)) and  $g = [220]$  (Figure IV - 3(e-h)). These images give insight on the defects position in the annealed layers. The micrographs for the sample annealed at  $1.60 \text{ J/cm}^2$  (i.e. surface melt regime, Figure IV - 3 (a,e)), show defects over the whole thickness, even below the maximum melt depth. The observed defects consisted mostly of (111) Stacking Faults (SFs) located beneath the melted islands. Some misfit dislocations (MDs) parallel to the SiGe

interface were also occasionally observed, with most of the defects underneath the hillocks. This suggests that the hillocks play a role in the defect formation, and could explain the progressive increase of the relaxation level in the surface melt regime as the density of molten areas increases. The remaining thickness fringes at 1.35 J/cm<sup>2</sup> (see Figure IV - 1(a)) are likely due to the large part of the material that does not present hillocks, and therefore are less prone to defect formation even in depth. RSM from the sample annealed at 1.81 J/cm<sup>2</sup> (i.e. first sample of partial melt) indicated complete relaxation, and hinted the presence of numerous defects. The corresponding TEM images (Figure IV - 3 (b,f)) confirm this result, by showing an increased density of defects over the whole layer thickness. Both Stacking faults (SFs) and Misfit Dislocations (MDs) can be observed, the latter being more effective in relieving elastic strain [5].

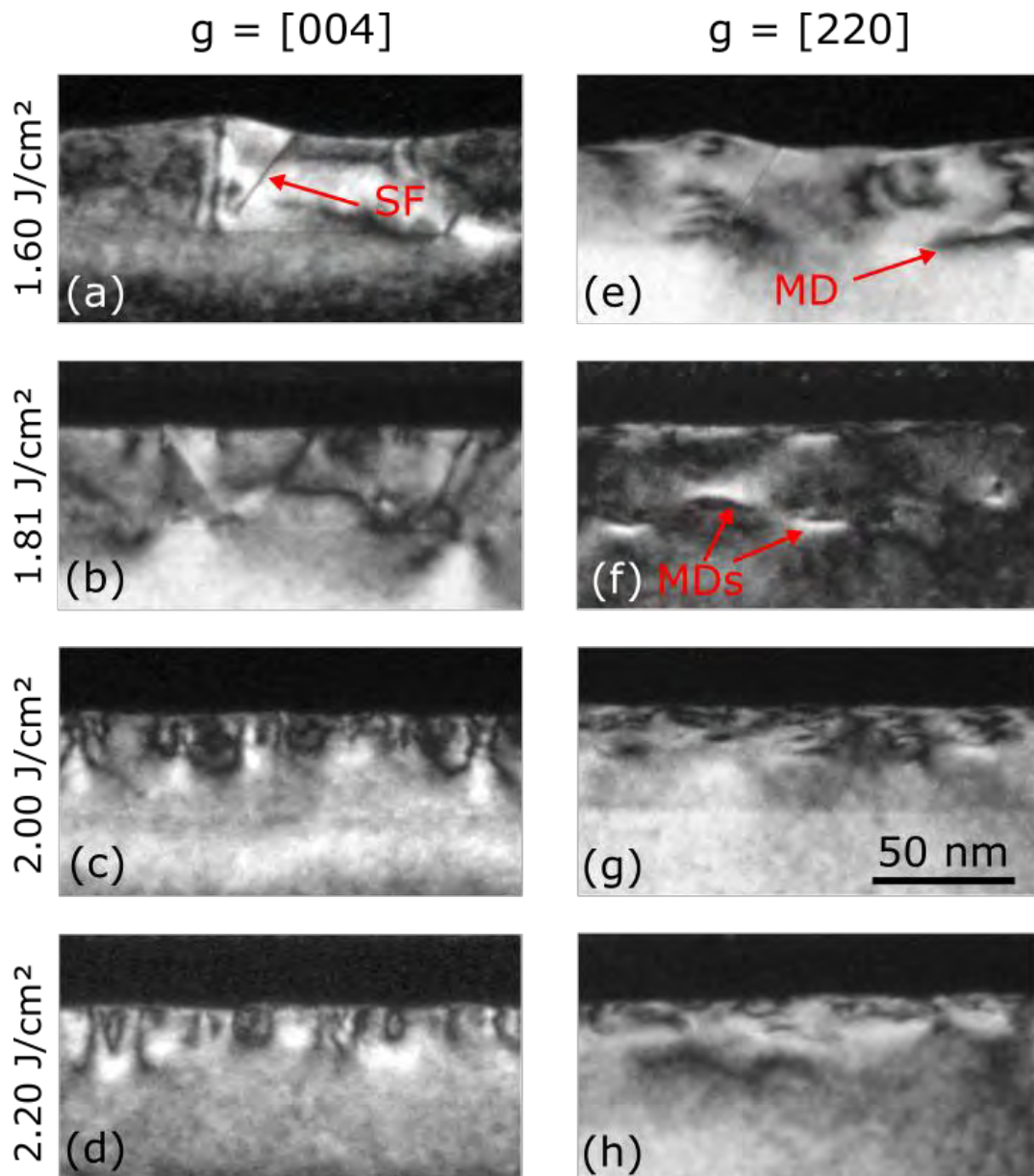


Figure IV - 3. Cross sectional TEM images in the Dark Field mode of 30 nm thick Si<sub>0.6</sub>Ge<sub>0.4</sub> layers annealed at laser energy densities ranging from 1.60 to 2.20 J/cm<sup>2</sup>. For each sample, two diffracting vectors were used:  $g = [004]$  and  $[220]$ . Some stacking faults (SF) and misfit dislocations (MD) are highlighted by red arrows.

In contrast, at the threshold between the partial and the full melt regime (2.00 J/cm<sup>2</sup>), the annealing process resulted in a bilayer. The DF-TEM in Figure IV - 3 (c,g) confirmed this

observation and showed that, in this case, the defect band related to relaxation was confined within a surface layer ~15 nm thick. The underlying layer, down to the SiGe/Si interface, was defect free and therefore corresponds to the fully strained region detected by XRD.

Finally, a similar result was obtained for the sample annealed in the full melt regime at 2.20 J/cm<sup>2</sup>. A bilayer was also observed by XRD in that case, even though the degree of relaxation of the partially relaxed layer could not be measured due to the low intensity of the XRD signal. Again, the dark-field TEM micrographs from this sample confirmed this result (cf. Figure IV - 3 (d,h)), by showing that the lower part of the SiGe layer exhibited no defects, while a defective region was confined within the first 15 nm below the surface.

## 2. Origin of relaxation

### a) Impact of the liquid/solid interface roughness

Several samples corresponding to surface or partial melt regimes resulted in the formation of strain relieving extended defects throughout the whole SiGe layer. Typical examples are the Si<sub>0.6</sub>Ge<sub>0.4</sub> samples annealed at 1.60 J/cm<sup>2</sup> shown in Figure IV - 3(a) and (e) or at 1.81 J/cm<sup>2</sup> shown in Figure IV - 3(b) and (f). These results can be explained considering the impact of the liquid/solid (l/s) interface roughness on the solidification mechanism.

Thanks to STEM-HAADF, where contrast is linked to chemical elements, the morphology of the liquid/solid (l/s) interface at maximum melt depth, i.e. at the beginning of solidification, was determined for surface melt and partial melt regimes. Corresponding images are shown in Figure IV - 4: due to Ge segregation, the unmelted area at the bottom remains uniform in contrast, while the lower Ge content near the maximum melt depth causes darker areas. In both cases, solidification started from a non-planar l/s interface. This was previously mentioned in Chapter III, where several images of non-planar interfaces were presented. In particular, the isolated molten islands present on the surface exhibited a curved liquid/solid interface for the sample annealed at 1.60 J/cm<sup>2</sup> (surface melt regime). They were thus likely to induce regrowth along different crystallographic directions, favouring the formation of strain relieving defects. It can be noticed on Figure IV - 3 (a,e) that most defects form directly underneath the melted areas.

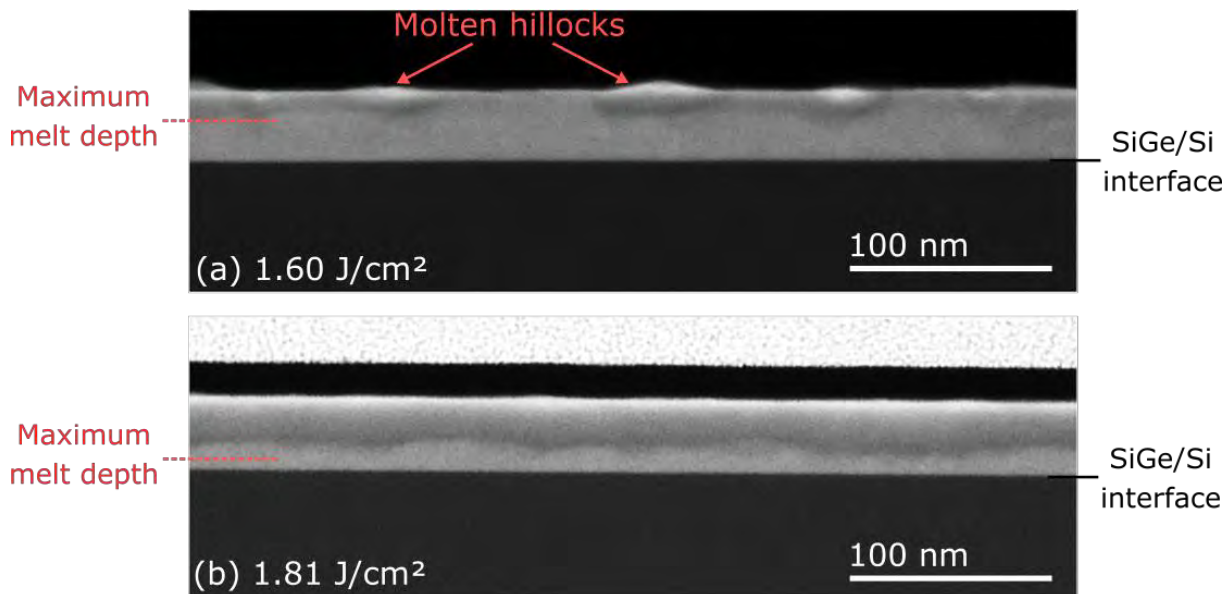


Figure IV - 4. STEM-HAADF micrographs of 30 nm Si<sub>0.6</sub>Ge<sub>0.4</sub> samples annealed at 1.60 J/cm<sup>2</sup> (a), and 1.81 J/cm<sup>2</sup> (b). The contrast is related to the chemical composition: Ge-rich areas are brighter. This enables to distinguish limits between un-melted areas and melted areas where segregation occurred.

STEM-HAADF observations clearly showed a rough I/s interface for the sample annealed at  $1.81 \text{ J/cm}^2$  (partial melt regime), with a variation of several nanometers in the interface depth. Finally, in both cases, the defects formed during annealing caused some strain relaxation. In particular, partial relaxation ( $\sim 26\%$ ) was found for the sample in the surface melt regime, when only half of the surface melted during the anneal. Meanwhile, a 100% relaxation was measured when a continuous liquid layer was obtained at  $1.81 \text{ J/cm}^2$ .

This is similar to what has been observed during the Low Temperature Solid Phase Epitaxial Regrowth (LT-SPER) of amorphized SiGe/Si epilayers. For instance, in [6,7], amorphous layers were obtained by Ion Implantation. These amorphous layers extended beyond the SiGe layer into the Si substrate. It was observed that during SPER, the initially flat amorphous/crystalline interface progressively transformed into a faceted one (along  $\{111\}$  planes) during recrystallization when it moved through the SiGe layer. The interface roughness increased proportionally to the Ge content. It favoured the formation of strain relieving defects (including SFs and MDs), provided that the elastic energy density stored in the layer exceeded a critical value [8]. For SiGe layers obtained by ion beam synthesis (i.e. high dose Ge<sup>+</sup> ion implantation), the critical elastic energy density value for strain relaxation was estimated at  $\sim 300 \text{ mJ/m}^2$  [9]. In contrast to such “elastic energy-driven” relaxation mechanism, when the regrowth started inside the SiGe layer, extended defects were formed in the whole regrown layer, regardless of the Ge content, eventually leading to some strain relaxation [10].

#### b) Elastic energy-driven relaxation

##### i. Bi-layer formation at high energy densities

In contrast to the behaviour described in previous section, samples annealed at  $2.00 \text{ J/cm}^2$  (end of the partial melt regime) or  $2.20 \text{ J/cm}^2$  (full melt regime) seemed to follow the “elastic energy-driven” relaxation mechanism discussed above for LT-SPER. In both cases, solidification started from a flat interface, as shown in Figure IV - 5.

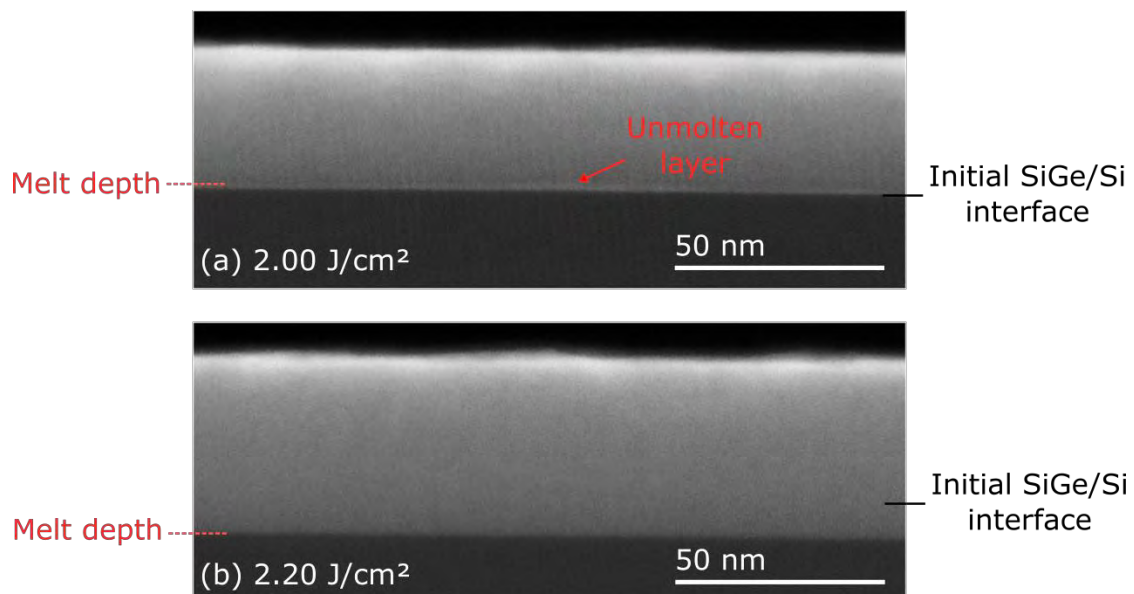


Figure IV - 5. STEM-HAADF micrographs of  $30 \text{ nm Si}_{0.6}\text{Ge}_{0.4}$  samples annealed at  $2.00 \text{ J/cm}^2$  (a), and  $2.20 \text{ J/cm}^2$  (b). The contrast is related to the chemical composition: Ge-rich areas are brighter. This enables to distinguish the thin unmelted layer at the bottom of the SiGe layer at  $2.00 \text{ J/cm}^2$ .

This resulted in defect-free bottom layers capped with layers containing stress relieving defects, as found by the DF-TEM analysis presented in Figure IV - 3(c, d, g, h). These observations are consistent with the presence of a “bilayer”, as deduced from XRD for the same samples (cf. Figure IV - 1(c)). In this case, it can therefore be inferred that the formation of a large

amount of defects occurs when the elastic energy density stored in the regrown layer exceeds a critical value  $E_{TH}$ .

ii. Elastic energy density calculations

The basic principle for elastic energy density  $E_{EL}$  ( $\text{mJ}/\text{m}^2$ ) calculation was presented at the end of Chapter II. The layer is divided into multiple sub-layers with a thickness  $t = 0.5$  nm. The elastic energy density is calculated for each sub-layer with the following formula [11]:

$$E_{EL} = \int_{z=0}^{z=z_{max}} B \cdot \varepsilon(z)^2 \cdot dz \quad \text{Eq. IV - [2]}$$

with

$$B = 2\mu(z) \cdot \frac{1 + \nu(z)}{1 - \nu(z)} \quad \text{Eq. IV - [3]}$$

Where  $z_{max}$  is the thickness of the SiGe layer,  $\varepsilon(z)$  is the strain,  $\mu(z)$  the shear modulus and  $\nu(z)$  the Poisson's ratio. These parameters depend on the Ge content and therefore on the depth. The Ge concentration in each sub-layer can be estimated by interpolation of the experimental data. To do so, the Ge concentration depth profile measured by SIMS is first slightly smoothed to limit the impact of noise on the result. The Ge concentration at a given depth is then obtained by interpolation between two neighbour experimental points. The elastic energy density calculated using this methodology are presented as red squares in Figure IV - 6.

As the result is highly dependent on the Ge content, any non-uniformities in the initial layer, either thickness or content, may impact the result. The normalized Ge content,  $Ge_n$ , was therefore estimated for each annealed layer by calculating the integral of Ge content over the whole layer, and normalizing with the value obtained for the reference (non-annealed) sample. The values are shown in black circles in Figure IV - 6, and it can be noticed that the content is indeed unstable, mainly due to thickness non-uniformities.

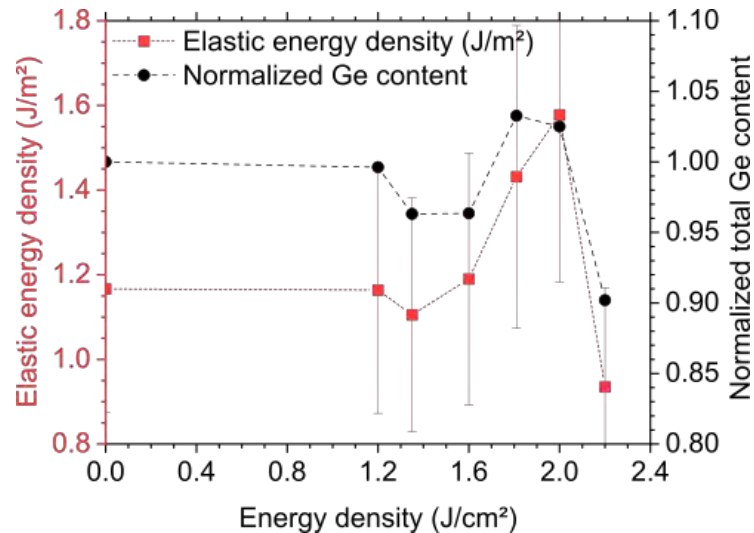


Figure IV - 6. Evolution of the elastic energy density (left axis, red squares) stored in a laser annealed 30 nm-thick  $\text{Si}_{0.6}\text{Ge}_{0.4}$  as a function of the energy density. The calculation is performed using interpolation of the SIMS Ge profile. The corresponding normalized total Ge content is also plotted (right axis, black symbols) as a function of the laser energy density for the same samples.

To avoid the artefact caused by these non-uniformities, a normalized elastic energy density  $E_n$  was calculated and plotted in Figure IV - 7. It is defined as:

$$E_n = \frac{E_{EL}}{Ge_n} \quad \text{Eq. IV – [4]}$$

The normalized elastic energy density was also plotted with another method (red triangles), in which the Ge content in each sub-layer is estimated by segregation simulation. The segregation calculation is identical to the one presented in Chapter III for variable k. Both exhibit similar results. It can be noticed that the elastic energy density variations for the interpolation method are reduced compared to Figure IV - 6, which confirms the impact of layer non-uniformities on the overall result. The elastic energy density remains stable up to 1.35 J/cm<sup>2</sup>, as no changes can be observed in the SIMS profiles at these laser energy densities. At values that lead to visible segregation (1.60 J/cm<sup>2</sup> and above), an increase of elastic energy density with laser energy density is observed. The maximum is reached for 2.00 J/cm<sup>2</sup>, and the higher energy density leads to a reduced elastic energy density.

The increase in elastic energy density is caused by the Ge gradient observed in the surface and partial melt regimes. The highest value is at the limit between partial and full melt, when all the Ge is redistributed and displaced toward the surface. The gradient and Ge content near surface are reduced when the full melt is reached, due to depth redistribution. This shows that the elastic energy density is expected to be maximal for the transition between partial and full melt regimes.

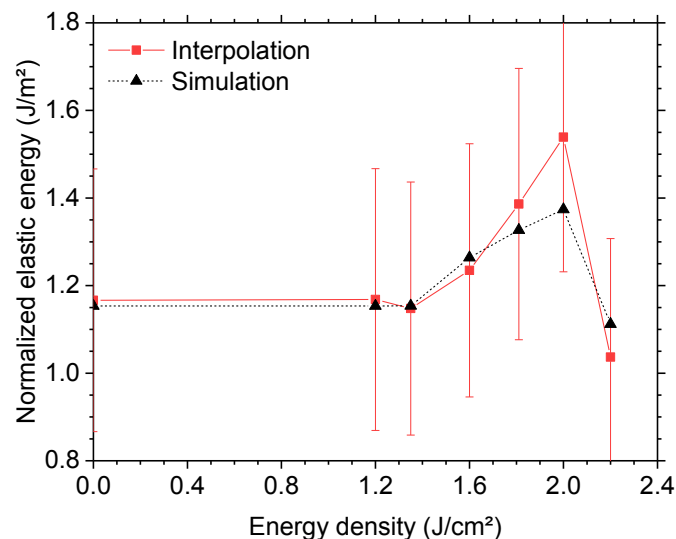


Figure IV - 7. Evolution of the normalized elastic energy density stored in a laser annealed 30 nm-thick Si<sub>0.6</sub>Ge<sub>0.4</sub> as a function of the laser energy density. The calculation is performed with the Ge profile, either by interpolation of SIMS data (red squares) or by simulation of the segregation (black triangles). Both present a maximum at laser energy densities corresponding to the end of the partial melt regime.

The study of strain relaxation on a 30 nm-thick Si<sub>0.6</sub>Ge<sub>0.4</sub> layer submitted to NLA at increasing energy densities showed that partial or full relaxation is expected if the liquid/solid interface is rough, while a bilayer is formed when the l/s interface is smooth. The bilayer formation, where the upper region is relaxed and the lower region strained, is consistent with an excess of elastic energy density stored in the layer. Due to the Ge redistribution during the anneal, the elastic energy density is maximal at the end of the partial melt regime, when the Ge gradients are the strongest.

## II – IMPACT OF SiGe LAYER PROPERTIES ON STRAIN RELAXATION

Strain relaxation measurements were performed in the same manner for all layers. The impact of Ge concentration and layer thickness are first detailed, along with a method to

accurately predict the strain relaxation. The modifications in the strain evolution caused by amorphization, or by the presence of boron in the initial SiGe layers are then developed.

For comparison, the limits of the various annealing regimes are indicated in Chapter III in Figure III – 8 for each presented sample.

### 1. Impact of Germanium concentration and layer thickness

#### a) Strain relaxation in 30 nm thick layers: impact of Ge content

Macroscopic relaxation levels measured by XRD are presented in Figure IV - 8 for the 30 nm-thick series. As expected, as-grown samples were found to be perfectly strained. It was also the case for all samples annealed in the sub-melt regime, independently of the initial Ge content. In addition, the  $\text{Si}_{0.9}\text{Ge}_{0.1}$  samples (red squares in Figure IV - 8) did not show any relaxation regardless of the annealing regime. This is in agreement with the low level of elastic energy density stored in such layers, as it never exceeded  $130 \text{ mJ/m}^2$  even in the “worst” case scenario (i.e. at the threshold between the partial and the full melt regime). At such low levels, even the presence of a rough I/s interface does not seem to be sufficient to cause defect formation.

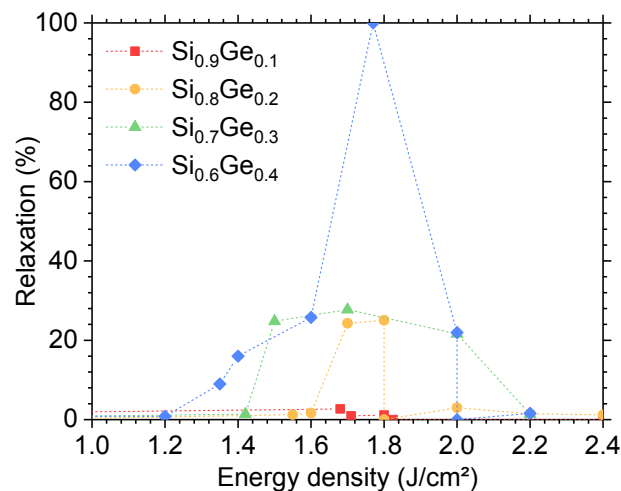


Figure IV - 8. Evolution of the macroscopic strain relaxation level as a function of laser energy density for 30 nm-thick layers with Ge contents ranging from 10% to 40%. Some plots exhibits two relaxation values for a given energy density: it corresponds to the appearance of two SiGe peaks in the RSM indicating a bilayer. An example of such a map can be found in Figure IV - 1(e-f).

Relaxation levels for  $\text{Si}_{0.8}\text{Ge}_{0.2}$  samples are represented by yellow circles in Figure IV - 8, along with BF-TEM observations in Figure IV - 10. In the beginning of surface melt regime (at  $1.55 \text{ J/cm}^2$  and  $1.59 \text{ J/cm}^2$ ), it was found that NLA did not cause any relaxation, although the surface had locally started to melt. For these samples, the surface coverage by molten islands remained under 20%, so only a small portion of the sample may have started to form strain relieving defects. At higher energy densities near the end of the surface melt regime ( $1.70 \text{ J/cm}^2$  and  $1.80 \text{ J/cm}^2$ ), most of the surface melted and recrystallization started from a non-planar I/s interface[12]. This led to the formation of defects in the whole regrown layer, accompanied by partial relaxation (~25% in this case). In the case of the sample annealed at  $1.80 \text{ J/cm}^2$ , the RSM indicated that a bilayer was formed, as shown in Figure IV - 9 : the main peak indicates that some of the SiGe layer is partially relaxed, while a faint peak indicates that another region remained strained.

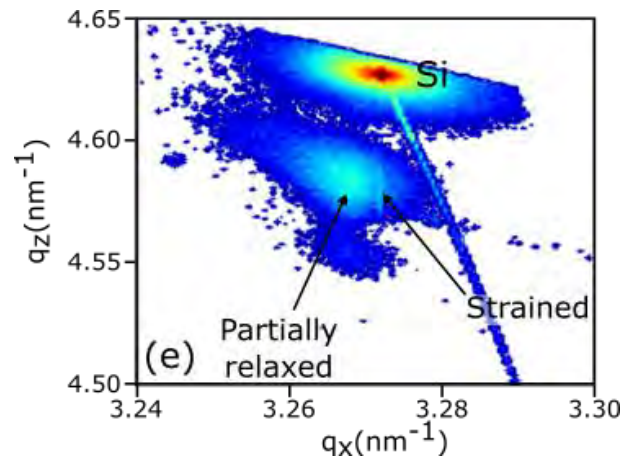


Figure IV - 9. Reciprocal Space Map along the (224) direction on 30 nm-thick  $\text{Si}_{0.8}\text{Ge}_{0.2}$  layers laser annealed at  $1.80 \text{ J/cm}^2$ .

BF-TEM images corresponding to the samples annealed at  $1.80$ ,  $2.00$  and  $2.40 \text{ J/cm}^2$  are shown in Figure IV - 10. The micrograph for the layer annealed at  $1.80 \text{ J/cm}^2$  (a) appears highly contrasted, while the contrast is much smoother for the other samples. This contrast is likely due to the presence of numerous defects in the layer. As presented in Chapter III (Figure III – 25), the I/s interface was rough at  $1.80 \text{ J/cm}^2$ , while it was smooth for the samples annealed at  $2.00 \text{ J/cm}^2$  and  $2.40 \text{ J/cm}^2$ , with layers that appear defect-free. XRD shows that samples annealed at  $2.00 \text{ J/cm}^2$  and above are fully strained, indicating that the elastic energy density stored was lower than the critical value for relaxation. The elastic energy density stored was estimated at  $\sim 330 \text{ mJ/m}^2$ ,  $\sim 280 \text{ mJ/m}^2$  and  $\sim 130 \text{ J/cm}^2$  after annealing at  $2.00 \text{ J/cm}^2$ ,  $2.20 \text{ J/cm}^2$  and  $2.40 \text{ J/cm}^2$ , respectively.

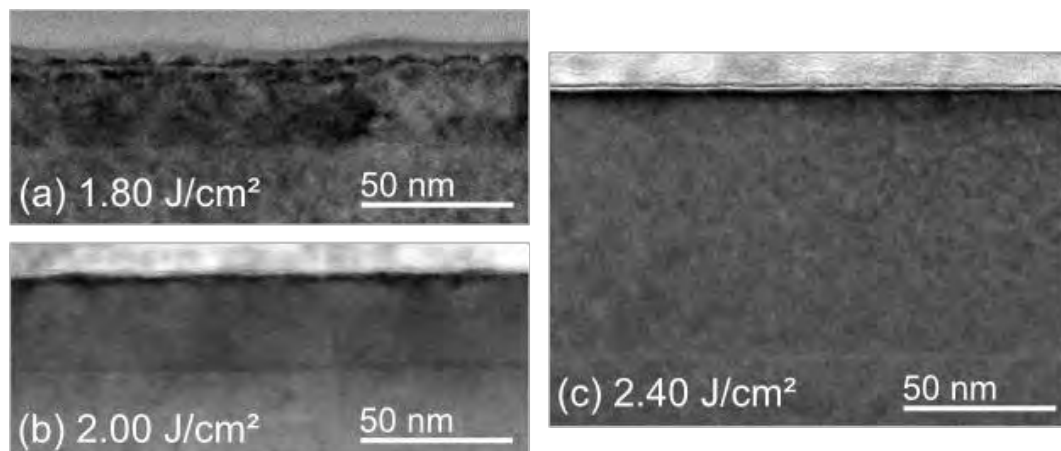


Figure IV - 10. Bright Field TEM images on a 30 nm-thick  $\text{Si}_{0.8}\text{Ge}_{0.2}$  annealed at (a)  $1.80 \text{ J/cm}^2$ , (b)  $2.00 \text{ J/cm}^2$  and (c)  $2.40 \text{ J/cm}^2$ . Image (b) is a concatenation of two images taken next to each other.

Relaxation results for the  $\text{Si}_{0.7}\text{Ge}_{0.3}$  samples correspond to the green triangles in Figure IV - 8. They are once again consistent with the scenario described above. BF-TEM images corresponding to the surface melt regime are shown in Figure IV - 11, while DF-TEM images are shown for all regimes in Figure IV - 12. For samples in the surface melt regime, the observed defect density remains lower than in the partial melt (cf. Figure IV - 12), with defects mainly located underneath the surface hillocks as shown in Figure IV - 11(a,b). Several stacking faults can be observed, crossing through the whole layer.

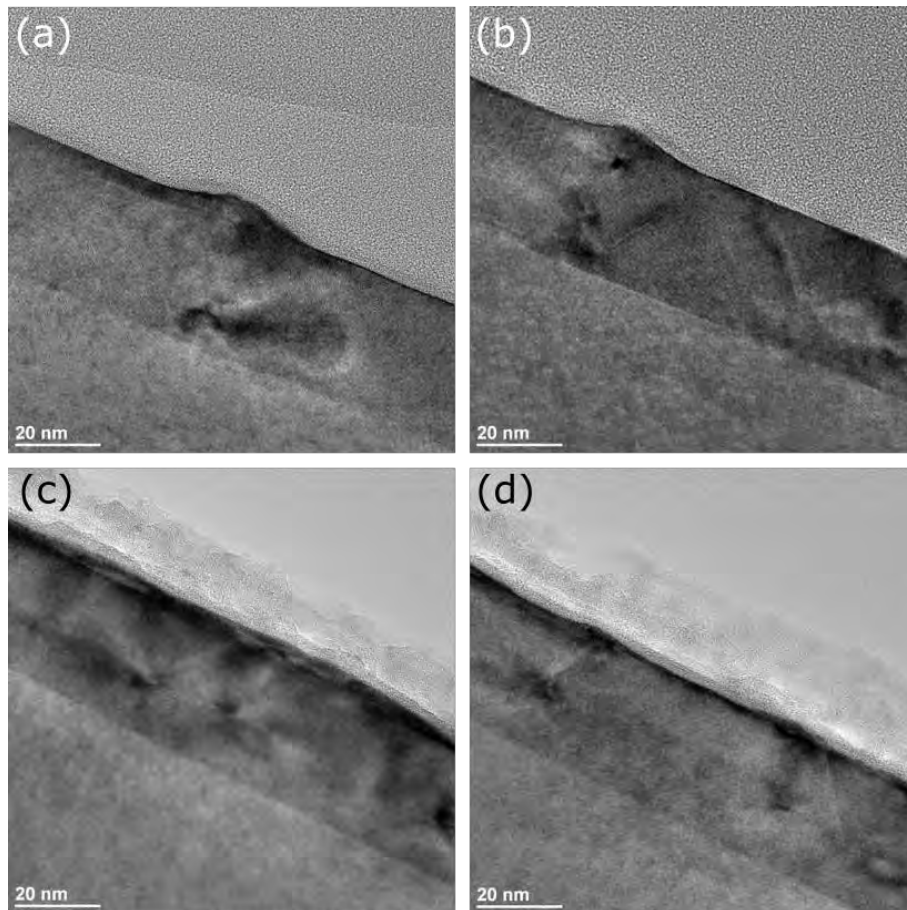


Figure IV - 11. BF TEM images on a 30 nm-thick Si<sub>0.7</sub>Ge<sub>0.3</sub> layer annealed at 1.50 J/cm<sup>2</sup> (a,b) and 1.70 J/cm<sup>2</sup> (c,d).

Partial melt regime (at 1.70 J/cm<sup>2</sup> and 2.00 J/cm<sup>2</sup>) leads to partial relaxation, with strain relieving defects located near the maximum melt depth, as seen in Figure IV - 11(c,d) and Figure IV - 12(c,d) near the middle of the layer (for a 1.70 J/cm<sup>2</sup> anneal) or in Figure IV - 12(e,f) at the bottom of the layer (2.00 J/cm<sup>2</sup> anneal). This confirms the idea that the rough I/s interface facilitates defects formation. A fully strained layer was obtained after annealing at 2.20 J/cm<sup>2</sup>, corresponding to an elastic energy density of ~640 mJ/m<sup>2</sup>. TEM images, either in Bright Field (cf. Figure IV - 11) or Dark Field modes (cf. Figure IV - 12(g,h)) show that remaining defects are observed near the surface though the layer was fully strained according to XRD.

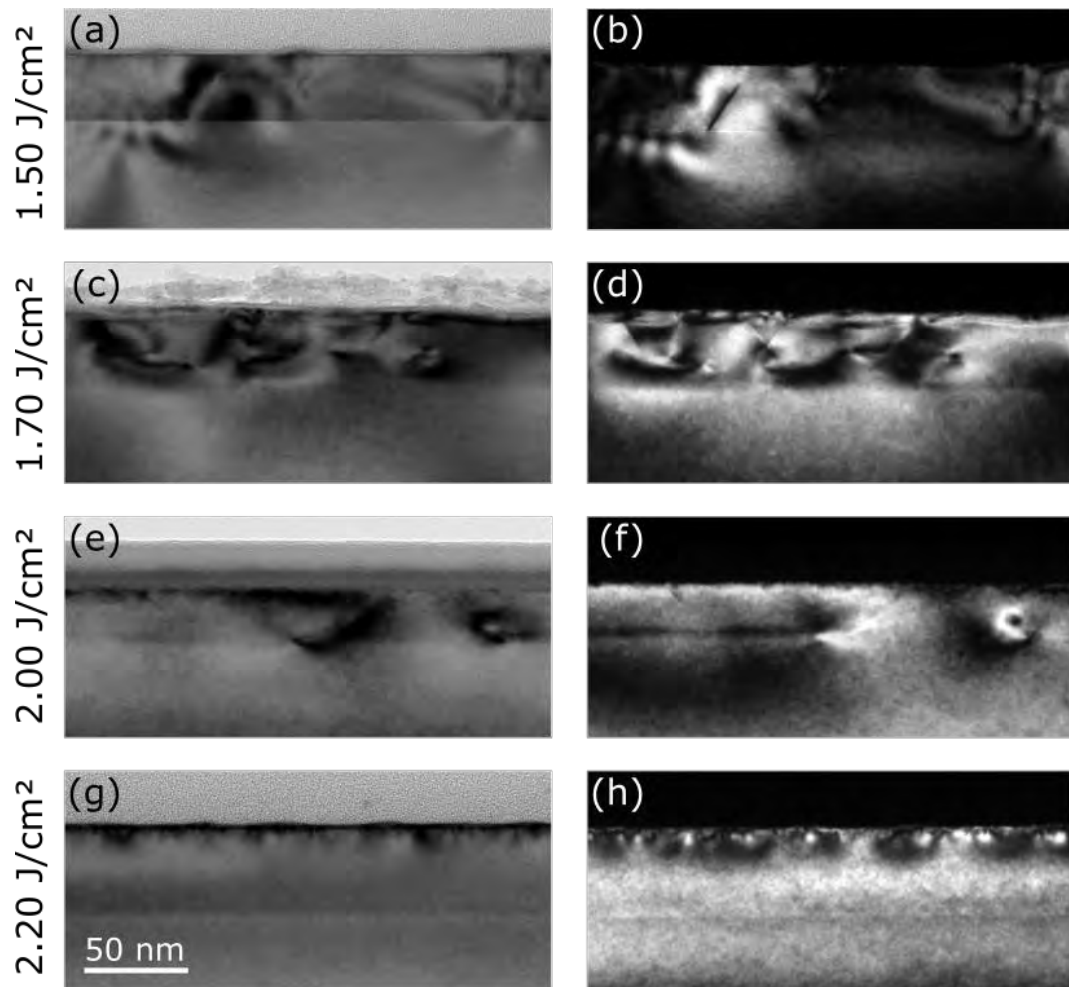


Figure IV - 12. BF-TEM (left column) and DF-TEM (right column) images on a 30 nm-thick  $\text{Si}_{0.7}\text{Ge}_{0.3}$  layer annealed at (a,b) 1.50 J/cm<sup>2</sup>, (c,d) 1.70 J/cm<sup>2</sup>, (e,f) 2.00 J/cm<sup>2</sup> and (g,h) 2.20 J/cm<sup>2</sup>. The BF and DF images for each sample are taken in the same area. The diffracting vector used for the DF-TEM is  $g=[004]$ .

#### b) Strain relaxation in $\text{Si}_{0.7}\text{Ge}_{0.3}$ layers : impact of thickness

The relaxation evolution as a function of the energy density for various thicknesses ( $\text{Si}_{0.7}\text{Ge}_{0.3}$  series) is presented in Figure IV - 13. The 20 nm-thick sample remains strained in the sub-melt, while it is partially relaxed ( $R \sim 30\%$ ) in the surface melt regime. There is no measurement in the partial melt regime. A fully strained sample is obtained in the full melt regime, at 2.10 J/cm<sup>2</sup>. The 30 nm-thick sample presents almost-identical results, with partial relaxation close to 30% in the surface melt regime. The relaxation level is slightly higher, near 40%, in the partial melt regime (1.90 J/cm<sup>2</sup>). The SIMS profile of this sample (see Appendix I – 3(b)) suggests that the I/s interface was still rough. Once a smooth I/s interface is obtained in full melt, the layer is fully strained (2.18 J/cm<sup>2</sup>). For the 45 nm-thick layer, the surface melt regime still leads to partial relaxation (near 25%), as well as the onset of partial melt regime (1.80 J/cm<sup>2</sup>). At 1.84 J/cm<sup>2</sup>, an unusual bilayer is formed (see the RSM in Figure IV - 14): the main peak indicates that part of the layer is relaxed near 20%, while a more faint peak indicates that the rest of the layer has started to fully relax, likely the Ge-rich surface. Annealing at 1.94 J/cm<sup>2</sup>, still in the partial melt regime, leads to complete relaxation. It is likely due to a combination of the rough I/s interface and high elastic energy density stored caused by the Ge gradient. Energy densities corresponding to the transition between partial and full melt, or to the full melt, lead to bilayers similar to the result on a 30 nm-thick  $\text{Si}_{0.6}\text{Ge}_{0.4}$  layer. At 2.04 J/cm<sup>2</sup> (transition from partial to full melt), part of the layer shows relaxation near 17%, while the rest is fully strained. At

2.24 J/cm<sup>2</sup>, the relaxation value for the partially relaxed could not be measured due to its low intensity, while the strained peak was clearly visible.

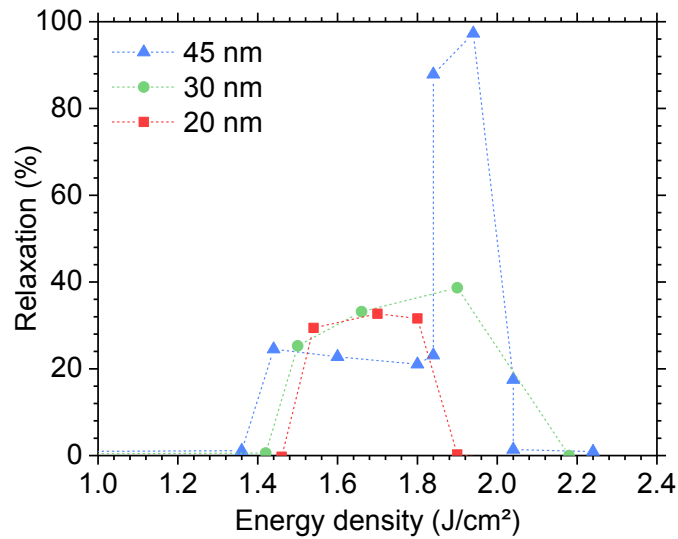


Figure IV - 13. Evolution of the macroscopic strain relaxation level as a function of laser energy density for 20, 30 and 45 nm-thick Si<sub>0.7</sub>Ge<sub>0.3</sub> layers. Some plots exhibits two relaxation values for a given energy density: it is caused by the appearance of two SiGe peaks in the RSM.

This suggests that the previous hypothesis on the origin of relaxation are still valid for various thicknesses: a rough interface in surface or partial melt causes the formation of defects and therefore partial relaxation. In cases with high elastic energy density (thick layer, high Ge content) and rough interface, this can lead to full relaxation. When a smooth interface is obtained at the end of partial melt or in full melt, the regrown layer is pseudomorphic unless excessive elastic energy density is stored in the layer.

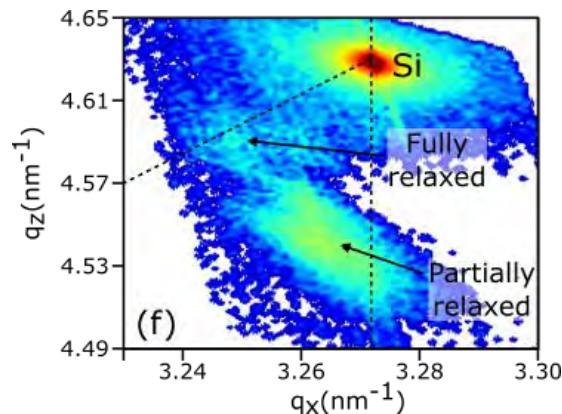


Figure IV - 14. Reciprocal Space Map along the (224) direction on 45 nm-thick Si<sub>0.7</sub>Ge<sub>0.3</sub> layers laser annealed at 1.84 J/cm<sup>2</sup>.

Results obtained here are in agreement with some studies from the literature where strained layers were also obtained when the final Ge content was low [13–15] and the I/s interface at maximum melt was deeper than the original SiGe/Si interface [16–19]. For example, bilayers obtained by Kociniewski et al. [19] were likely related to the high Ge content in the final layers. They disappeared when the Ge was diluted at higher energy densities, which reduced the stored elastic energy density. Ong [16] observations of a fully strained layer in partial melt (Si<sub>0.78</sub>Ge<sub>0.22</sub> at 0.7 J/cm<sup>2</sup>) still matches with the previous observations, as the sample exhibited a smooth I/s interface. In contrast, the bilayer observed by Frangis [20] does not seem consistent with our observations, as the layer thickness (~35 nm) and Ge concentration (below 30%) measured were low. Their Ge profile however does not seem realistic, and was not

obtained by SIMS: considering a 10 nm a-Ge layer mixed with ~25 nm of Si, the final concentration is likely higher than 30%. If that was indeed the case, the elastic energy density stored can be well above the 750 mJ/m<sup>2</sup> threshold.

### c) Elastic energy density limit for strain relaxation

These results clearly indicated that, when solidification starts from a flat l/s interface, the relaxation mechanism is driven by the amount of elastic energy density stored in the regrown layers. For all samples with such a relaxation mechanism, the corresponding elastic energy density values were plotted in Figure IV - 15, with the interpolation method previously presented. In this figure, solid symbols correspond to fully strained samples, whereas empty symbols indicate samples with a “bilayer” stack, i.e. a defect-free region in the lower part of the regrown layer and a defective layer at the surface, which forms when the critical elastic energy density is exceeded. The estimated elastic energy density for Ong sample annealed at 0.70 J/cm<sup>2</sup> is added (in black) for comparison [16].

As all samples showing a bilayer are visibly in the upper part of the graph, while the strained ones are below, it is possible to estimate the upper limit for pseudomorphic regrowth. The threshold for strain relaxation is therefore at ~750 mJ/m<sup>2</sup>. Fully pseudomorphic regrowth will therefore be obtained for SiGe/Si epilayers subjected to melt NLA only if the built-in elastic energy density is lower than this threshold. The value from literature [16] for a fully strained layer is below this threshold, and therefore is in agreement with the 750 mJ/cm<sup>2</sup> value.

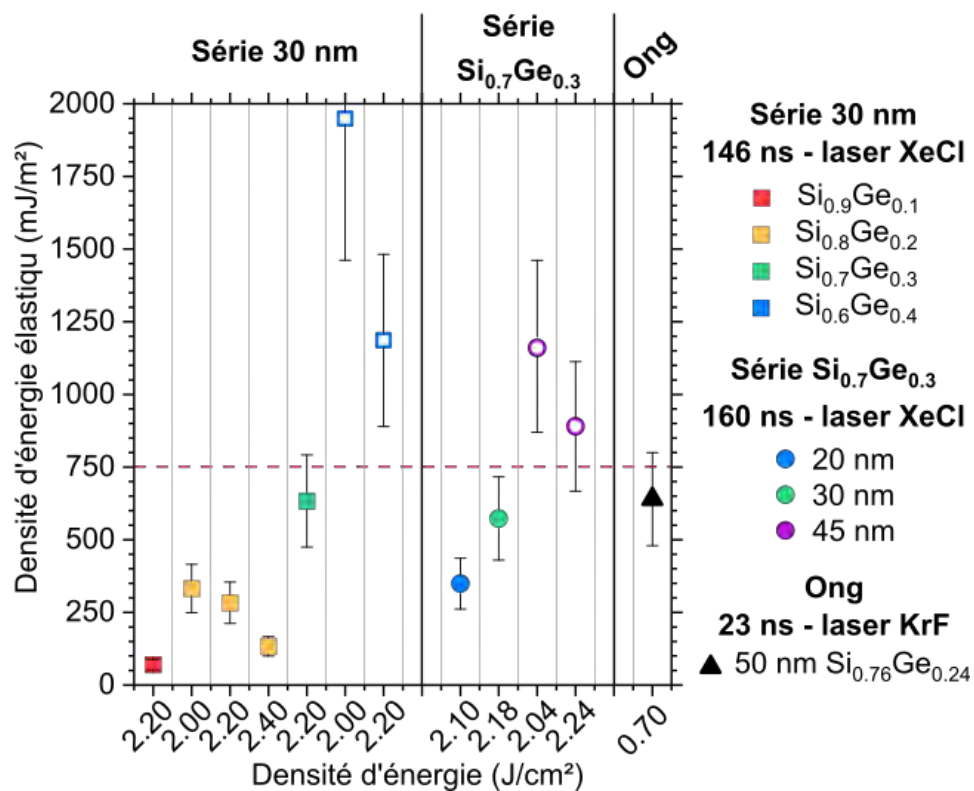


Figure IV - 15. Total elastic energy density in SiGe layers after laser anneal, calculated using an interpolation of the experimental Ge concentration profiles. Results are shown only for layers with a smooth l/s interface. Initial samples 30 nm thick with various Ge contents are on the left, and the Si<sub>0.7</sub>Ge<sub>0.3</sub> samples with various initial thicknesses are plotted on the right. Layers that were perfectly strained are represented by full squares, while the ones with a bilayer are represented by open symbols. The estimated elastic energy density for Ong sample annealed at 0.70 J/cm<sup>2</sup> is added (in black) for comparison [16].

While being well above the value previously determined for Ion Beam Synthesised SiGe layers (~300 mJ/m<sup>2</sup>), the critical elastic energy density for NLA SiGe layers is lower than the one

achieved for CVD grown SiGe layer with constant Ge concentrations (near 1400 mJ/m<sup>2</sup> for a 30 nm-thick Si<sub>0.6</sub>Ge<sub>0.4</sub> layer)[2,8]. However, NLA offers some versatility by enabling the formation of steep Ge gradients with concentration levels at the surface as high as 80% at.Ge.

d) Predictive calculations for elastic energy-induced relaxation

As calculation tools were developed to reproduce Ge profiles for annealed layers and calculate the stored elastic energy density corresponding to a given profile, it becomes possible to simulate the elastic energy density stored in any given layer. This was done in the form of colour maps presented in Figure IV - 16.

These simulations aim to evaluate the evolution of elastic energy density for a set of given layers, at various melt depths. This can be used to estimate the melt depth required to reach elastic energy densities below the strain relaxation threshold at 750 mJ/m<sup>2</sup> for a given initial content and thickness. Two types of plots (abacus) were created:

- Constant layer thickness: the elastic energy density is calculated for a set of Ge concentrations (user-chosen), with the same initial thickness for each layer. The elastic energy density is calculated for melt depths up to twice the initial layer thickness. Examples are shown in Figure IV - 16 for initial layer thicknesses of 30 nm (a) and 45 nm (b).
- Constant Ge content: the elastic energy density is calculated for a set of layer thicknesses (user-chosen), with the same initial Ge content for each layer. The maximum melt depth calculated is chosen by the user. An example is shown in Figure IV - 17.

The precision is chosen by the user, that can select the "step" in between two tested thicknesses or two tested contents. Variations of the solidification velocity during regrowth are not taken into account. Also, the same interface roughness is used for all profiles. This may induce some discrepancies with experimental profiles and corresponding amounts of elastic energy density stored. All the color maps presented here were obtained with a solidification velocity at 0.6 nm/ns and a l/s interface thickness of 5 nm.

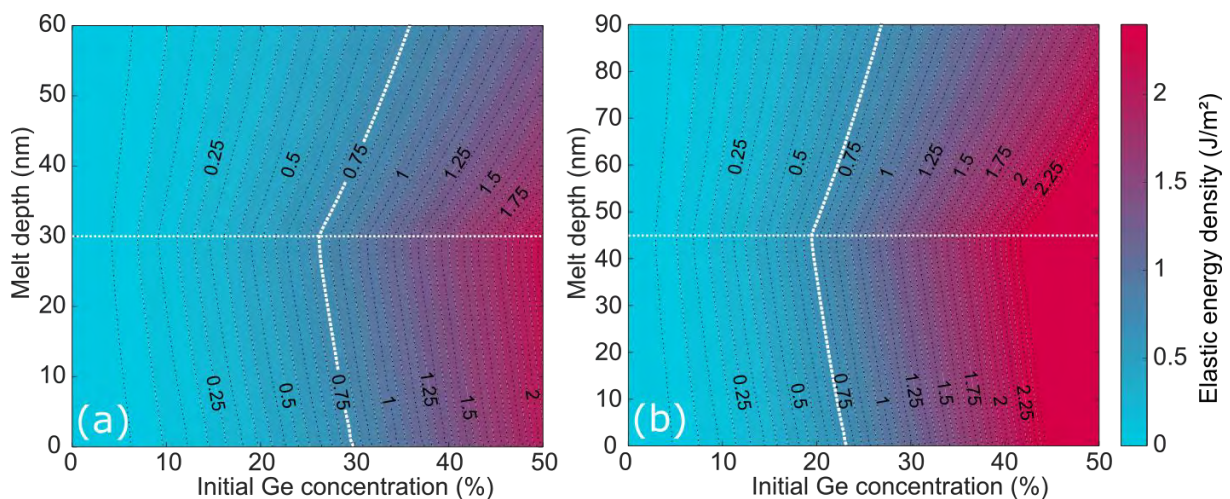


Figure IV - 16. Colour maps of the calculated elastic energy density for regrown SiGe layers of different initial Ge contents after laser-induced melt at different depths. A constant solidification velocity at 0.6 m/s has been considered for all calculations. Calculations are shown for an initial layer thickness of 30 nm (a) and 45 nm (b). The strain relaxation threshold at 750 mJ/m<sup>2</sup> is highlighted with a white dotted line.

A clear bend in contour lines is observed on every graph, and corresponds to the point where the melt depth is equivalent to the initial layer thickness. For melt depths below the layer

thickness, Ge redistribution leads to an intense Ge gradient near the surface and therefore an increase in elastic energy density. For melt depths beyond the layer thickness, the elastic energy density increase due to the Ge surface gradient is counter-balanced by the Ge redistribution over thicker regions, leading to an overall decrease of the stored elastic energy density.

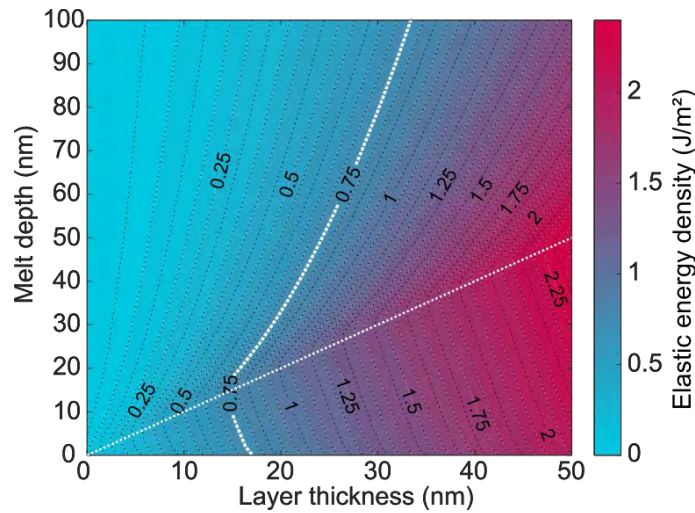


Figure IV - 17. Colour map of the calculated elastic energy density for regrown  $\text{Si}_{0.6}\text{Ge}_{0.4}$  layers of different initial thicknesses after laser-induced melt at different depths. A constant solidification velocity at 0.6 m/s has been considered for all calculations. The strain relaxation threshold at  $750 \text{ mJ/m}^2$  is highlighted with a white dotted line.

These tools can be useful to predict the final relaxation state in undoped  $\text{Si}_{1-x}\text{Ge}_x$  layers at different melt depths. It should be kept in mind that samples in surface or partial melt will likely present a rough I/s interface, and therefore be partially or fully relaxed.

#### e) Conclusion on pseudomorphic undoped layers

The evolution of the strain in laser annealed  $\text{Si}_{1-x}\text{Ge}_x$  layers was studied with increasing energy density for multiple layers with either varying Ge content or varying thickness. In all cases, the observations are consistent with the results on 30 nm-thick  $\text{Si}_{0.6}\text{Ge}_{0.4}$  layers, and show that the relaxation is related to the liquid/solid interface quality and to the stored elastic energy density. The rough I/s interfaces obtained in surface or partial melt regimes facilitate defect formations and thus lead to partial relaxation. In layers with high elastic energy density (Ge-rich or thicker), full relaxation can be reached. Pseudomorphic layers with a graded Ge content can however be obtained for a smooth I/s interface (i.e. at the end of partial melt or in the full melt regime), if the stored elastic energy density is below  $750 \text{ mJ/m}^2$ . The elastic energy density is highly dependent on the Ge content and distribution, and it is maximum at the end of the partial melt regime is due to the Ge gradients.

## 2. Amorphous SiGe layers: comparison with epi-layers

#### a) Initial state

30 nm-thick  $\text{Si}_{0.7}\text{Ge}_{0.3}$  layers were amorphized to two different depths by Ge implantation (see Chapter II for details). XRD Rocking-curves from the amorphized layers are shown in Figure IV - 18, together with a scan recorded from a fully crystalline  $\text{Si}_{0.7}\text{Ge}_{0.3}$  as-grown layer for comparison. The SiGe peaks are visible for the as-epi layer (black curve) and for the 15 nm amorphization (red curve). Simulations on these XRD profiles (not shown) indicate that the initial layer before amorphization was indeed 30 nm-thick, and that only 15 nm of crystal can be observed after the amorphization. This confirms that 15 nm were amorphized. There is

no SiGe peak observed for the 30 nm amorphization as there is no contribution from the amorphous layer. It is therefore not possible to evaluate the real thickness of the amorphous layer, though we consider it must be close to 30 nm.

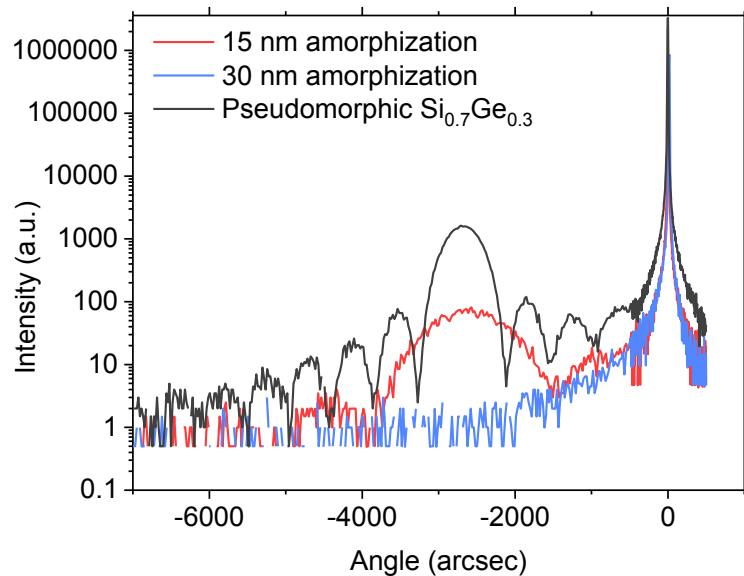


Figure IV - 18. XRD scans along the (004) direction on 30 nm-thick  $\text{Si}_{0.7}\text{Ge}_{0.3}$  samples that were fully strained (black curve), or amorphized by Ge implantation over 15 nm (red curve) or 30 nm (blue curve). These scans confirmed that the entire SiGe layer was amorphised in the latter case.

#### b) Relaxation for 15 nm and 30 nm thick amorphized layers

##### i. In explosive regime

The explosive regime corresponds to the 1.05 - 1.35 J/cm<sup>2</sup> and 0.98 – 1.26 J/cm<sup>2</sup> ranges for the 15 nm amorphization and the 30 nm amorphization respectively (see Figure III – 8), as indicated by the TRR measurements. As shown by the SIMS profiles in Figure III – 28, the complete amorphous layer melts as soon as the explosive threshold is reached, as Ge redistribution is observed down to the bottom of the SiGe layer. There was however no change in the RSMs for samples in the explosive regime compared to the sub-melt. For the 15 nm amorphization, the SiGe peak observed is associated with the 15 nm-thick monocrystalline layer underneath the amorphized layer, and does not change in the explosive regime. There is no observable SiGe peak in the 30 nm amorphization sample.

TEM images, shown in Figure IV - 20, highlight the morphological changes in the explosive regime for the 15 nm amorphization sample after laser annealing at 1.10 J/cm<sup>2</sup> (b) and 1.25 J/cm<sup>2</sup> (c). The as-implanted sample is shown in (a), and indeed presents a 15 nm amorphous layer on top of a 15 nm monocrystalline SiGe layer. In the explosive regime, at both 1.10 J/cm<sup>2</sup> and 1.25 J/cm<sup>2</sup>, the formation of monocrystalline areas separated from each other is observed, while the rest of the upper layer becomes polycrystalline. The underlying SiGe, that was not amorphized, remains monocrystalline. It can be inferred that the monocrystalline areas are caused by the melt depth non-uniformities. In these regions, the melt front may reach the a/c interface, and the upper layer then regrows from the monocrystalline seed, from the bottom to the top. The polycrystalline regions are however formed by the melt and explosive solidification that propagates from the top to the bottom of the amorphous layer, as well as laterally. Due to misorientation and small sizes, the grains do not contribute to the SiGe peak in the RSM.

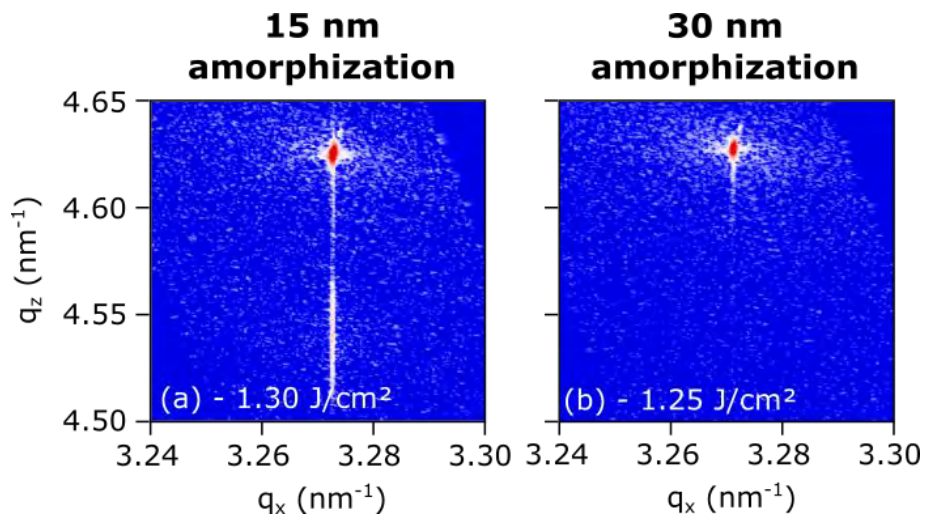


Figure IV - 19. Reciprocal Space Maps along the (224) direction on 30 nm-thick  $\text{Si}_{0.7}\text{Ge}_{0.3}$  layers initially amorphized over 15 nm (a) or 30 nm (b) and subsequently submitted to NLA at respectively  $1.30 \text{ J/cm}^2$  and  $1.25 \text{ J/cm}^2$ . This corresponds to the end of the explosive regime.

The same phenomena may have occurred for the 30 nm amorphization sample, though there are no TEM observations to confirm. In any case, it seems that the density of these regrown areas is too low to have an impact on the RSM shown in Figure IV - 19.

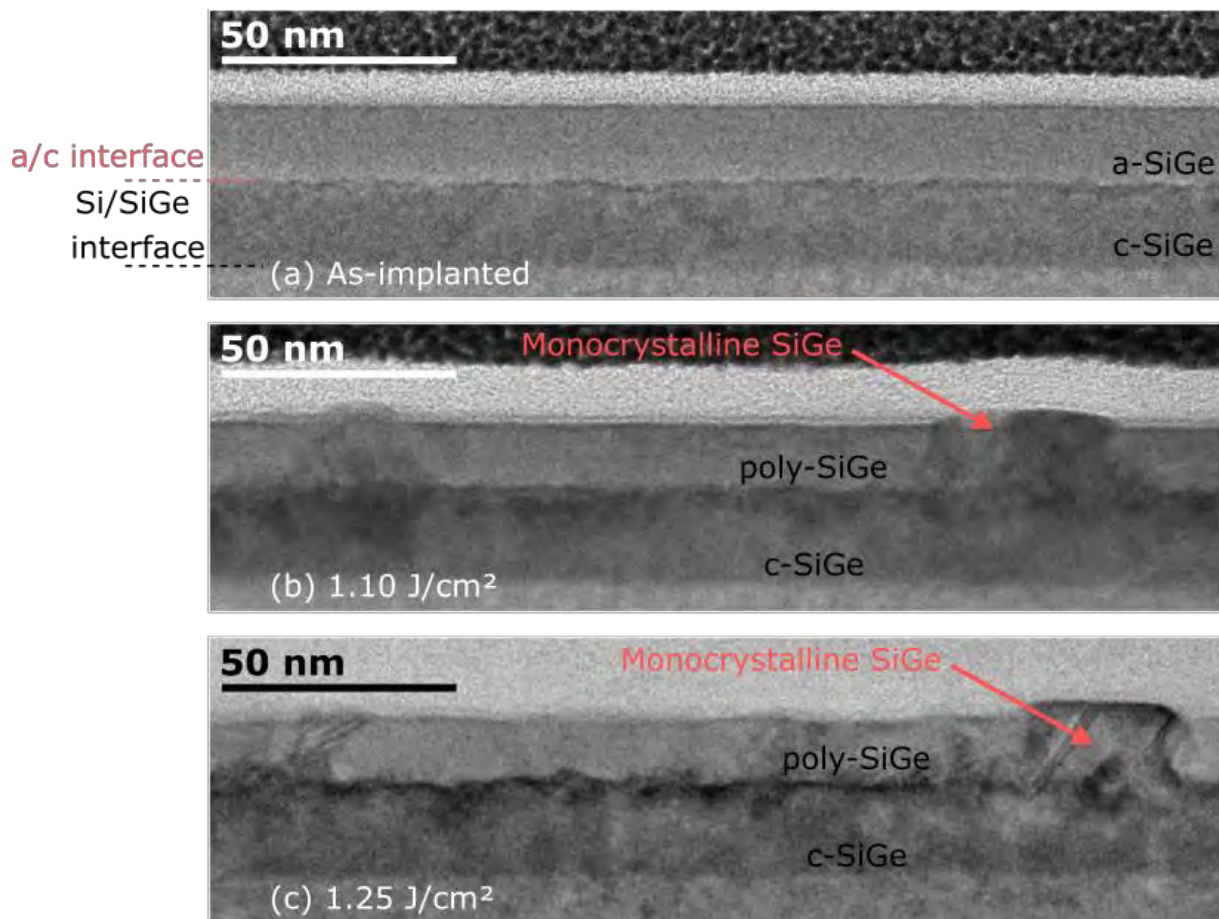


Figure IV - 20. Cross-section TEM observations of the 30 nm-thick  $\text{Si}_{0.7}\text{Ge}_{0.3}$  layers initially amorphized over 15 nm (a) and subsequently submitted to NLA at respectively (b)  $1.10 \text{ J/cm}^2$  and (c)  $1.25 \text{ J/cm}^2$ . This corresponds to the explosive regime

## ii. In other regimes

Once the second melt is reached, the regimes are similar to the ones on a pseudomorphic layer, with surface melt, partial melt and full melt regimes. It is however likely that the onset of surface melt regime only impacts the nanocrystalline part in the upper region. Reciprocal Space Maps are shown in Figure IV - 21 for the surface melt (a,b) partial melt (c,d) and full melt (e,f) regimes while the relaxation levels estimated are presented in Figure IV - 22. For the 15 nm amorphization, the RSM at 1.60 J/cm<sup>2</sup> (a), in the surface melt regime, shows changes compared to the explosive regime. The SiGe peak is now diffuse, though it remains near the vertical line, and the relaxation is estimated close to 5%. A faint SiGe peak associated with a fully strained layer can still be observed. At 1.90 J/cm<sup>2</sup> (c), a diffuse peak is observed, caused by a partially relaxed layer with R~30%. Finally, RSMs at 2.10 (e) and 2.30 J/cm<sup>2</sup> show a peak vertically aligned with the Si peak, indicating a fully strained graded layer.

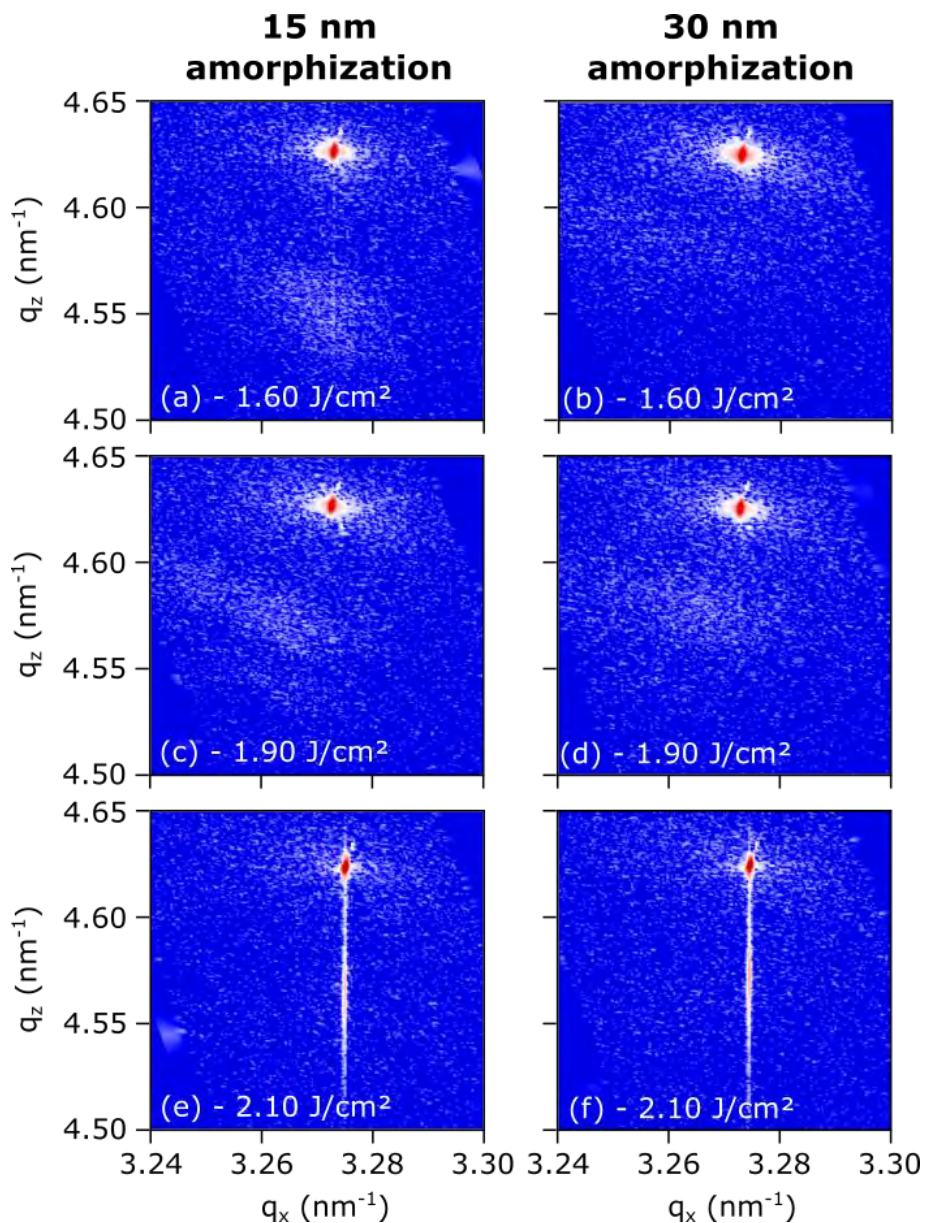


Figure IV - 21. Reciprocal Space Maps along the (224) direction on 30 nm-thick Si<sub>0.7</sub>Ge<sub>0.3</sub> layers amorphized over 15 nm (left column) or 30 nm (right column). Each line respectively corresponds to the surface melt regime (1.60 J/cm<sup>2</sup>), the partial melt regime (1.90 J/cm<sup>2</sup>) and the full melt regime (2.10 J/cm<sup>2</sup>).

In the surface melt regime, the relaxation level is much lower for amorphized samples than in pseudomorphic samples. Due to the melt front roughness, the melt depth may have reached the monocrystalline layers in some areas while it did not elsewhere. The relaxation is caused by defects extending through the monocrystalline layers, in regions where it was impacted by the melt. At higher energy densities, the behaviour is identical to pseudomorphic samples, as the polycrystalline layer has fully melted. The layer quality then only depends on I/s interface quality and elastic energy density.

The observations for the 30 nm amorphization are similar: a faint peak associated to relaxed SiGe is observed in the surface melt regime (its relaxation level cannot be measured). The layer is relaxed near 30% in the partial melt (1.90 J/cm<sup>2</sup>, (d)) and fully strained in full melt (2.10 J/cm<sup>2</sup> (f)). The faint peak in surface melt regime may be due to growth on some of the monocrystalline areas formed by the explosive melt (shown in Figure IV - 20). At 1.90 J/cm<sup>2</sup>, we suggest that the Si/SiGe interface was reached in some areas, while others regrow from the isolated monocrystalline regions. The overall results is similar to the pseudomorphic samples. Finally, the full melt is identical for every sample, as the melt depth extends beyond the initial a/c interface. Due to the combination of a smooth interface with low elastic energy density, the final layer at 2.10 and 2.30 J/cm<sup>2</sup> is pseudomorphic.

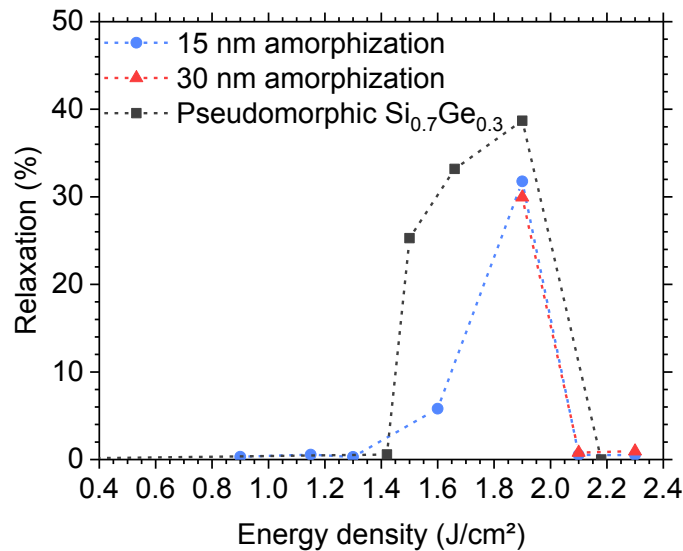


Figure IV - 22. Evolution of the macroscopic degree of strain relaxation as a function of laser energy density for 30 nm-thick Si<sub>0.7</sub>Ge<sub>0.3</sub> layers initially amorphized over 15 nm (blue curve) or 30 nm (red curve). A reference on a 30 nm-thick pseudomorphic Si<sub>0.7</sub>Ge<sub>0.3</sub> layer (grey curve) is also shown, taken from the Si<sub>0.7</sub>Ge<sub>0.3</sub> series.

The origins of relaxation are similar in all Si<sub>1-x</sub>Ge<sub>x</sub> layers, at all thicknesses and Ge concentrations. It is caused either by the rough I/s interface observed during the surface and partial melt regimes, or by excessive elastic energy density. The same mechanisms are observed in amorphized layers.

### III – BORON IMPACT ON THE RELAXATION OF 30 NM-THICK Si<sub>0.7</sub>Ge<sub>0.3</sub> LAYERS

#### 1. Relaxation in pseudomorphic doped layers

Macroscopic relaxation levels for laser annealed boron-doped samples was assessed by XRD, with RSMs around the (224) direction. The results are presented in Figure IV - 23 and compared with the relaxation levels obtained for a 30 nm undoped layer from the Si<sub>0.7</sub>Ge<sub>0.3</sub> series. As a reminder, the corresponding annealing regimes are shown in Figure IV - 8. The transition from one regime to the other occurred at similar energy densities values for each of the three doping levels, and are close to the transitions observed in the undoped layer.

The undoped sample (30 nm-thick undoped layer from the  $\text{Si}_{0.7}\text{Ge}_{0.3}$  series) shows relaxation near 30% in the surface and partial melt regimes due to the rough I/s interface. Pseudomorphic layers are obtained in the full melt regime, once the interface is smooth and the stored elastic energy density is below  $750 \text{ mJ/m}^2$ . Strain relaxation in sample A is similar to the relaxation in the reference sample, with partial relaxation near 30% in both surface and partial melt regimes. A return to full strain is observed in the full melt regime at  $2.10$  and  $2.30 \text{ J/cm}^2$ . For these samples, the elastic energy density is likely below the  $750 \text{ mJ/m}^2$  threshold. Samples B and C also exhibit partial relaxation in the surface melt regime ( $1.60 \text{ J/cm}^2$ ) and at the beginning of partial melt regime ( $1.80 \text{ J/cm}^2$ ). They however show a return to fully strained state at  $1.95 \text{ J/cm}^2$ , even though the SiGe layer did not fully melt. In the full melt, the layer is pseudomorphic as expected.

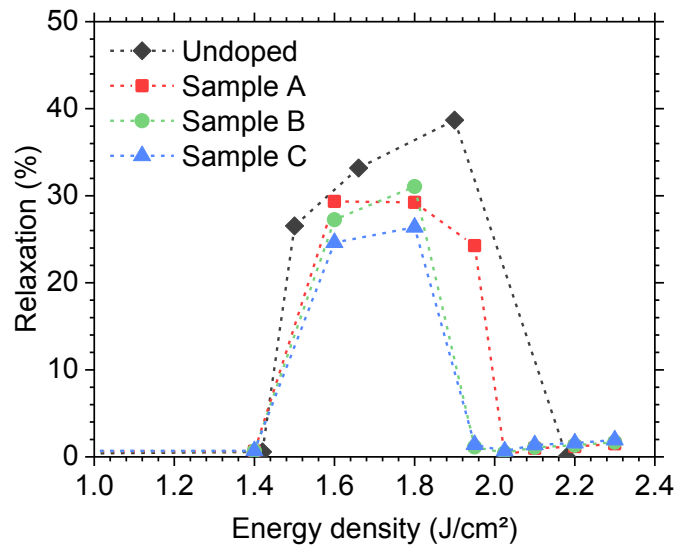


Figure IV - 23. Macroscopic relaxation levels for boron doped  $\text{Si}_{0.7}\text{Ge}_{0.3}$  samples annealed at various laser energy densities. The data is compared with relaxation results from an undoped  $\text{Si}_{0.7}\text{Ge}_{0.3}$  layer, already presented in Figure IV - 8.

All doped layers consistently presented lower relaxation levels than the undoped layer, with minimum relaxation values for the sample C. This can be explained by the inclusion of boron atoms in the lattice. Indeed, thanks to its lower covalent radius (compared to both silicon and germanium), the presence of boron results in a reduction of the SiGe:B lattice parameter (with respect to the undoped case). It causes strain compensation and therefore reduces the stored elastic energy density even though the Ge content is stable. This may limit the strain relaxation during regrowth as it was observed during SPER [1], where the boron doped samples exhibited lower strain relaxation compared to the undoped layers.

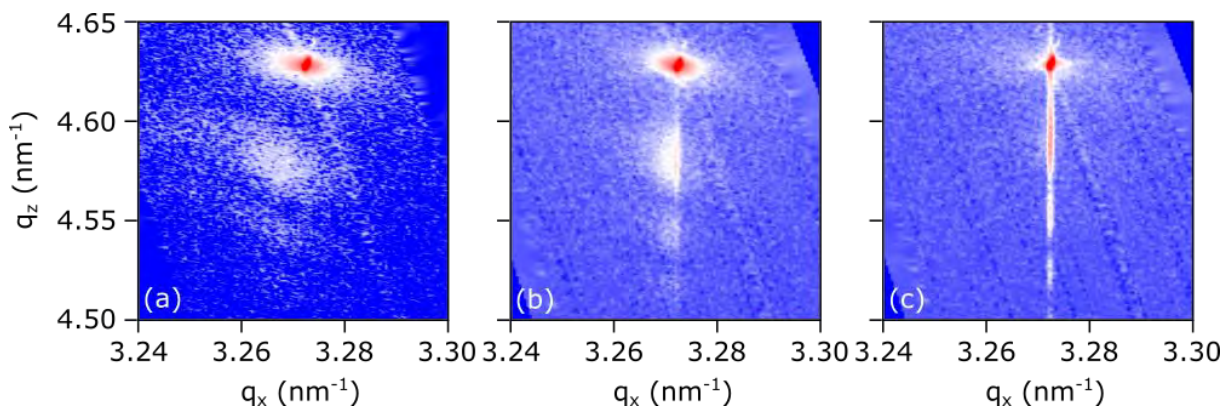


Figure IV - 24. Reciprocal Space Maps along the (224) direction for boron-doped  $\text{Si}_{0.7}\text{Ge}_{0.3}$  layers on Si and annealed at  $1.95 \text{ J/cm}^2$ , for low (a), medium (b) and high (c) incorporated boron levels. The alignment of the SiGe under the Si peaks indicates its strain level.

The gap in strain observed at  $1.95 \text{ J/cm}^2$  can be further studied by XRD and TEM observations. It should be noted that these three layers have a similar melt depth, in the 20-24 nm range. RSMs for samples A, B and C are shown in Figure IV - 24, and present a progressive evolution in layer quality. The sample A, with the lowest boron concentration, is associated with a diffuse spot, not aligned with the Si peak, indicating the presence of partial relaxation. For the sample B, this SiGe peak is vertically aligned with the Si peak, but exhibits a tail towards the low  $q_x$  values: this shows that numerous defects can still be found in the layer, with slight relaxation. Finally, the SiGe peak for sample C indicates a pseudomorphic, defect-free layer.

A STEM-HAADF is shown in Figure IV - 25 (a) for sample A. The presence of a rough I/s interface confirms that the behavior of this sample is similar to the undoped SiGe layers, and that a rough I/s interface remains until the layer is fully melted, which facilitates the formation of strain relieving defects. The STEM-HAADF image for sample C shown in Figure IV - 25(b) however presents a smooth I/s interface, though the melt depth was similar to sample A. This suggests that the return to strain was this time determined only by the elastic energy density stored. Though it could not be calculated for this sample, the large concentration of boron likely reduces the elastic energy density compared to an undoped sample with a similar Ge profile.

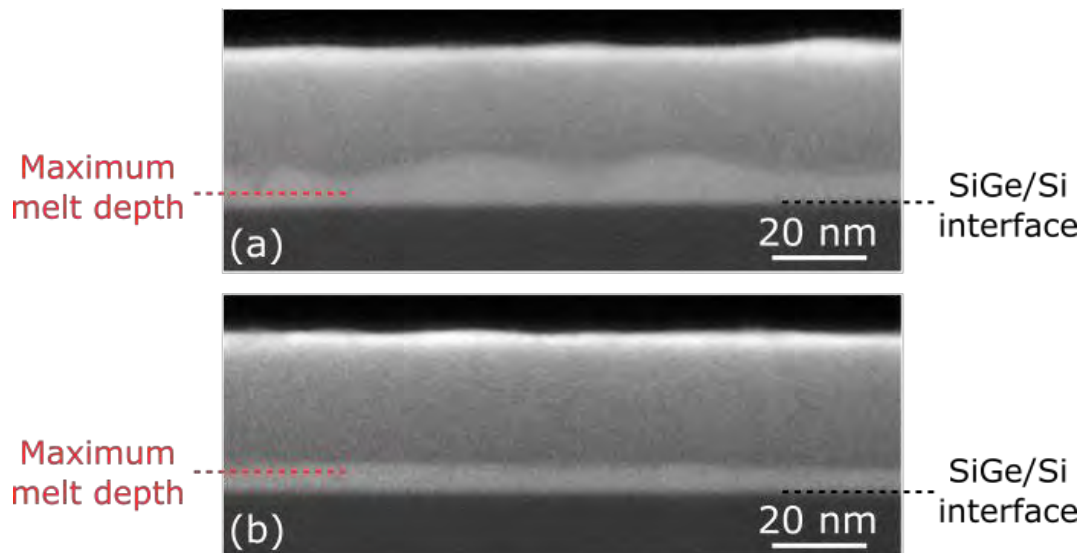


Figure IV - 25. STEM-HAADF images on  $\text{Si}_{0.7}\text{Ge}_{0.3}$  samples annealed at  $1.95 \text{ J/cm}^2$  for sample A (a) and sample C (b).

The relaxation in doped layers therefore seems to originate from the same phenomena as the undoped layers, with a facilitated return to smooth I/s interfaces for the highest boron contents. This effect is not fully understood yet, and will require additional investigations. It may allow to form pseudomorphic layers with high Ge content, and a graded profile, under conditions that would lead to relaxation in undoped layers.

## 2. Relaxation in amorphized doped layers

A 15 nm amorphization was performed on a 30 nm-thick  $\text{Si}_{0.7}\text{Ge}_{0.3}$  layer with boron doping identical to sample C. The amorphization was performed with Ge implantation, under the same conditions as the layer presented in section II – 2. The detected regimes are almost identical for the doped layer compared to the undoped 15 nm amorphization (see Figure IV - 8). We therefore assume that the melt depths and Ge profiles are similar in both samples. The macroscopic level of relaxation measured is plotted in Figure IV - 26 as a function of the laser

energy density. The relaxation levels after UV-NLA for undoped samples with a 15 nm amorphization and no amorphization are shown along for comparison purposes.

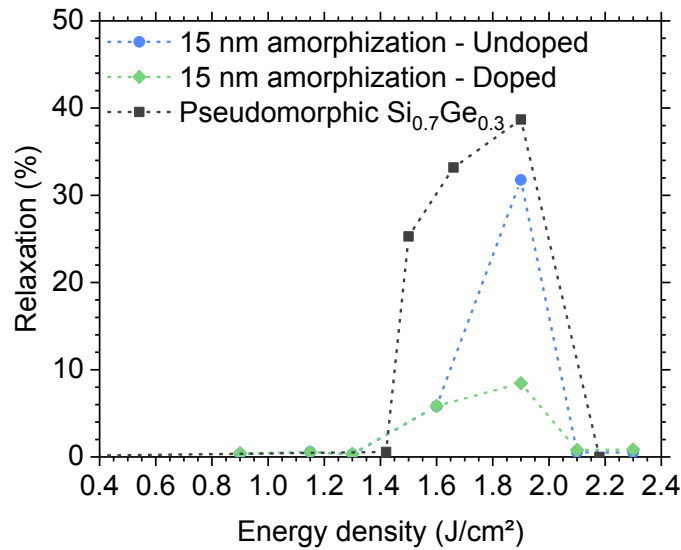


Figure IV - 26. Evolution of the macroscopic degree of strain relaxation as a function of laser energy density for a 30 nm-thick  $\text{Si}_{0.7}\text{Ge}_{0.3}$  layer with medium boron doping initially amorphized over 15 nm. A comparison is made with a 30 nm-thick pseudomorphic  $\text{Si}_{0.7}\text{Ge}_{0.3}$  layer (black) taken from the  $\text{Si}_{0.7}\text{Ge}_{0.3}$  series, as well as with a 30 nm-thick undoped  $\text{Si}_{0.7}\text{Ge}_{0.3}$  layer initially amorphized over 15 nm.

As it was the case for undoped layers, there is no change in the RSMs and thus in the macroscopic relaxation during the explosive melt regime (1.08 – 1.36 J/cm<sup>2</sup>). The contribution of the nanocrystals is likely negligible due to their misorientation and size, and the bottom crystalline layer does not relax. Once the second melt threshold is reached, partial relaxation is once again noticed for the surface and partial melt regimes. These values are however much lower than for the other amorphized or undoped samples, near 6% and 8%. Finally, the full melt, with a smooth interface and low elastic energy density, leads to pseudomorphic layers as expected.

The low relaxation level in surface melt can be explained by the fact that the nanocrystalline layer may not have fully melted yet and therefore limited the formation of defects in the underlying crystalline layer. The low value in partial melt, at 1.90 J/cm<sup>2</sup>, may be due to the smoothening of the interface facilitated by the boron concentration that was already observed on doped pseudomorphic layers in the previous section.

The relaxation levels observed in doped layers, with or without amorphization, were consistently lower than in the undoped layers. It appears that the boron presence offers a strain compensation in the concentration range studied, which leads to a relaxation decrease and an apparent earlier return to smooth I/s interfaces in the partial melt regime. These results are promising for future doped junctions.

## CONCLUSION

The crystalline quality of  $\text{Si}_{1-x}\text{Ge}_x$  layers submitted to UV-NLA was studied in depth by using Reciprocal Space Maps along the (224) direction in order to evaluate the macroscopic level of relaxation. These assessments were completed with TEM observations, both in bright and dark field modes, as well as STEM-HAADF, to locate the defects and understand the origins of the relaxation.

Measurements on initially pseudomorphic and undoped  $\text{Si}_{1-x}\text{Ge}_x$  layers at various compositions and thicknesses have shown that the relaxation highly depends on the liquid/solid interface quality. As the layer starts to melt, the formation of isolated molten islands causes the formation of a rough l/s interface, that is still observed in the partial melt regime. This rough interface facilitates the formation of strain relieving defects in samples with sufficient elastic energy density stored, leading to partial relaxation near 30% or complete relaxation for layers with the highest Ge content or thickest. The defect formation and level of relaxation is impacted by the elastic energy density within the layer: at low levels (below 10% at.Ge), no relaxation is observed, as the energy is too low for defects formation. On the contrary, thicker or Ge rich layers (i.e. with high elastic energy density levels) present a complete relaxation, with numerous defects visible in TEM images. It has been shown that the elastic energy density, related to the Ge content, increases for layers that show a Ge gradient, and is maximum at the end of the partial melt regime, when the content is fully redistributed towards the surface.

At the end of partial melt or in full melt regimes, the smooth l/s interface obtained enables the pseudomorphic regrowth of samples that have elastic energy density levels below  $750 \text{ mJ/m}^2$ , even with high Ge-content near the surface. The samples with elastic energy density above this threshold present a bilayer, confirmed by both XRD and TEM. In this case, the lower part of the layer then appears fully strained, but the near surface layer is partially relaxed. UV-NLA at higher energy densities on these samples allow to further dilute the Ge, and therefore to reduce the elastic energy density below the  $750 \text{ mJ/m}^2$  threshold.

The relaxation in amorphized undoped layers can be explained with the same phenomena. It appears that the smooth l/s interface is only obtained in the full melt regime, and that these layers show the same behaviour once the melt depth extends beyond the initial a/c interface.

Boron-doped layers were also found to follow similar rules, with partial relaxation for rough l/s interfaces, and strain for smooth l/s interfaces. The presence of boron however leads to a strain compensation and thus lower relaxation values. It was noticed that smooth l/s solid interfaces can be obtained in the partial melt regime for high substitutional B concentrations (above  $1 \times 10^{20} \text{ B}\cdot\text{cm}^{-3}$ ). It is therefore possible to eliminate relaxation in the partial regime for highly doped boron layers, though the origin of the smoothing is not yet understood.

## KEY INFORMATION

 $\text{Si}_{0.6}\text{Ge}_{0.4}$  EXAMPLE

1. Evolution with laser energy density

The relaxation levels evolve with the annealing regimes

- All regimes present various elastic energy levels :
- Surface melt leads to increasing relaxation levels
  - Partial melt causes full relaxation
  - Full melt leads to the formation of a bilayer with strained lower part and relaxed upper part

2. Rough I/s interface

→ Surface and partial melt regimes present a rough liquid/solid interface

- Facilitates the formation of strain-relieving defects
- May originate from the local surface melt

3. Excessive elastic energy

→ End of partial melt and full melt present a smooth liquid/solid interface and a bilayer

- Defects are formed only when a threshold in elastic energy is reached
- Elastic energy increases with the formation of Ge gradients with a maximum at the end of partial melt

## UNDOPED LAYER PROPERTIES

1. Evolution with Ge content or thickness

→ The evolution with various content and various thickness nuance the observations on  $\text{Si}_{0.6}\text{Ge}_{0.4}$

- Partial relaxation in surface melt and partial melt
- Fully strained layers in full melt unless the Ge content is high or the layer is thicker.

2. Elastic energy threshold

→ Relaxation in full melt regime is controlled by elastic energy

- The layer is fully strained below  $750 \text{ mJ/m}^2$
- A bilayer is observed above  $750 \text{ mJ/m}^2$

3. Amorphized layers

→ Phenomena are similar, with full strain only in the full melt regime

## BORON-DOPED LAYERS

1. Pseudomorphic layers

Facilitated return to smooth I/s interfaces and lower relaxation in highly doped layers.

→ Same origins of relaxation

- Relaxation levels are reduced for higher boron contents
- The I/s interface is smooth for lower energy densities for higher Ge content → To be further studied

2. Amorphized layers

→ Low relaxation levels in both surface and partial melt

## BIBLIOGRAPHY

- [1] A. Rodríguez, T. Rodríguez, A. Kling, J.C. Soares, M.F. da Silva, C. Ballesteros, Strain and defects depth distributions in undoped and boron-doped Si<sub>1-x</sub>Ge<sub>x</sub> layers grown by solid phase epitaxy, *J. Appl. Phys.* 82 (1997) 2887–2895. <https://doi.org/10.1063/1.366121>.
- [2] J.M. Hartmann, A. Abbadie, S. Favier, Critical thickness for plastic relaxation of SiGe on Si(001) revisited, *J. Appl. Phys.* 110 (2011) 083529. <https://doi.org/10.1063/1.3656989>.
- [3] W.-X. Ni, K. Lyutovich, J. Alami, C. Tengstedt, M. Bauer, E. Kasper, X-ray reciprocal space mapping studies of strain relaxation in thin SiGe layers ( $\leq 100$ nm) using a low temperature growth step, *J. Cryst. Growth.* 227–228 (2001) 756–760. [https://doi.org/10.1016/S0022-0248\(01\)00821-1](https://doi.org/10.1016/S0022-0248(01)00821-1).
- [4] S.A. Speakman, Introduction to High Resolution X-Ray Diffraction of Epitaxial Thin Films, (n.d.). <http://prism.mit.edu/xray/oldsite/Introduction%20to%20HRXRD.pdf>.
- [5] P.M. Mooney, Strain relaxation and dislocations in SiGe/Si structures, *Mater. Sci. Eng. R Rep.* 17 (1996) 105–146. [https://doi.org/10.1016/S0927-796X\(96\)00192-1](https://doi.org/10.1016/S0927-796X(96)00192-1).
- [6] R.G. Elliman, W.C. Wong, The fabrication of epitaxial GeSi<sub>1-x</sub> layers by ion implantation, *Nucl. Instrum. Methods Phys. Res. Sect. B Beam Interact. Mater. At.* 80–81 (1993) 768–772. [https://doi.org/10.1016/0168-583X\(93\)90678-Y](https://doi.org/10.1016/0168-583X(93)90678-Y).
- [7] D.C. Paine, D.J. Howard, N.G. Stoffel, J.A. Horton, The growth of strained Si<sub>1-x</sub>Ge<sub>x</sub> alloys on  $\langle 001 \rangle$  silicon using solid phase epitaxy, *J. Mater. Res.* (1990) 1023–1031.
- [8] R. People, J.C. Bean, Calculation of critical layer thickness versus lattice mismatch for GeSi<sub>1-x</sub>/Si strained-layer heterostructures, *Appl. Phys. Lett.* 47 (1985) 322–324. <https://doi.org/10.1063/1.96206>.
- [9] F. Cristiano, A. Nejim, Y. Suprun-Belevich, A. Claverie, P.L.F. Hemment, Formation of extended defects and strain relaxation in ion beam synthesised SiGe alloys, *Nucl. Instrum. Methods Phys. Res. Sect. B Beam Interact. Mater. At.* 147 (1999) 35–42. [https://doi.org/10.1016/S0168-583X\(98\)00589-8](https://doi.org/10.1016/S0168-583X(98)00589-8).
- [10] D.C. Paine, D.J. Howard, N.G. Stoffel, Strain relief in compositionally graded SiGe formed by high dose Ion implantation, *J. Electron. Mater.* 20 (1991) 735–746. <https://doi.org/10.1007/BF02665959>.
- [11] S.C. Jain, W. Hayes, Structure, properties and applications of GeSi<sub>1-x</sub>strained layers and superlattices, *Semicond. Sci. Technol.* 6 (1991) 547–576. <https://doi.org/10.1088/0268-1242/6/7/001>.
- [12] L. Dagault, P. Acosta-Alba, S. Kerdilès, J.P. Barnes, J.M. Hartmann, P. Gergaud, T.T. Nguyen, A. Grenier, A.M. Papon, N. Bernier, V. Delaye, J. Aubin, F. Cristiano, Impact of UV Nanosecond Laser Annealing on Composition and Strain of Undoped Si<sub>0.8</sub>Ge<sub>0.2</sub> Epitaxial Layers, *ECS J. Solid State Sci. Technol.* 8 (2019) P202–P208. <https://doi.org/10.1149/2.0191903jss>.
- [13] R. Larciprete, M.G. Grimaldi, E. Borsella, S. Cozzi, S. Martelli, S. Pieretti, I. Vianey, Larciprete1998; KrF laser epitaxy of silicon germanium alloy layers by irradiation of Si(1-x)Ge<sub>x</sub>/Si (100) structures, *J. Vac. Sci. Technol. B Microelectron. Nanometer Struct. Process. Meas. Phenom.* 16 (1998) 1589–1594. <https://doi.org/10.1116/1.589944>.

- [14] K. -Josef Kramer, S. Talwar, T.W. Sigmon, K.H. Weiner, Crystallinity, strain, and thermal stability of heteroepitaxial Si<sub>1-x</sub>Ge<sub>x</sub>/Si (100) layers created using pulsed laser induced epitaxy, *Appl. Phys. Lett.* 61 (1992) 769–771. <https://doi.org/10.1063/1.107793>.
- [15] L. Vincent, F. Fossard, T. Kociniewski, L. Largeau, N. Cherkashin, M.J. Hÿtch, D. Debarre, T. Sauvage, A. Claverie, J. Boulmer, D. Bouchier, Nanoscale concentration and strain distribution in pseudomorphic films Si<sub>1-x</sub>Ge<sub>x</sub>/Si processed by pulsed laser induced epitaxy, *Appl. Surf. Sci.* 258 (2012) 9208–9212. <https://doi.org/10.1016/j.apsusc.2011.07.074>.
- [16] C.Y. Ong, K.L. Pey, K.K. Ong, D.X.M. Tan, X.C. Wang, H.Y. Zheng, C.M. Ng, L. Chan, A low-cost method of forming epitaxy SiGe on Si substrate by laser annealing, *Appl. Phys. Lett.* 94 (2009) 082104. <https://doi.org/10.1063/1.3086881>.
- [17] J.R. Abelson, T.W. Sigmon, K.B. Kim, K.H. Weiner, Epitaxial GeSi/Si (100) structures produced by pulsed laser mixing of evaporated Ge on Si (100) substrates, *Appl. Phys. Lett.* 52 (1988) 230–232. <https://doi.org/10.1063/1.99528>.
- [18] S. Lombardo, K. Kramer, M.O. Thompson, D.R. Smith, Pulsed laser assisted epitaxy of Ge<sub>x</sub>Si<sub>1-x</sub> alloys on Si <100>, *Appl. Phys. Lett.* 59 (1991) 3455–3457. <https://doi.org/10.1063/1.105676>.
- [19] T. Kociniewski, F. Fossard, J. Boulmer, D. Bouchier, Synthesis of strained SiGe on Si(100) by pulsed laser induced epitaxy, *Thin Solid Films.* 518 (2010) 2542–2545. <https://doi.org/10.1016/j.tsf.2009.09.154>.
- [20] N. Frangis, J. Van Landuyt, R. Larciprete, S. Martelli, E. Borsella, S. Chiussi, J. Castro, B. León, High resolution electron microscopy and x-ray photoelectron spectroscopy studies of heteroepitaxial Si<sub>x</sub>Ge<sub>(1-x)</sub> alloys produced through laser induced processing, *Appl. Phys. Lett.* 72 (1998) 2877–2879. <https://doi.org/10.1063/1.121487>.





# CHAPTER V

## ELECTRICAL PROPERTIES OF BORON DOPED $\text{Si}_{0.7}\text{Ge}_{0.3}$ LASER ANNEALED LAYERS

I – DOPANT ACTIVATION IN $\text{Si}_{0.7}\text{Ge}_{0.3}$ LAYERS.....	168
1. Dopant activation in pseudomorphic layers .....	168
a) Metrology .....	168
b) Initial state after epitaxy .....	168
c) Electrical properties of SiGe:B laser annealed with a single pulse .....	170
i. Boron redistribution .....	170
ii. Impact of layer quality and doping level .....	171
c) Electrical properties with single pulse at 450°C .....	174
d) Electrical properties with multiple pulses at room temperature .....	175
2. Dopant activation in initially amorphous layers.....	176
II – THERMAL STABILITY OF BORON ACTIVATION FOLLOWING A SUBSEQUENT ANNEALING STEP .....	177
1. Samples and annealing conditions.....	177
a) Selected samples .....	177
b) Furnace annealing conditions.....	178
c) Modifications assessment .....	179
2. Morphological and electrical evolutions with anneal temperature .....	180
a) Samples without laser anneal.....	180
i. Structural modifications.....	180
ii. $R_s$ evolution upon subsequent furnace anneal.....	183
b) Laser annealed samples.....	184
i. Structural modifications.....	184
ii. $R_s$ evolution upon subsequent furnace anneal.....	187
CONCLUSION .....	189
KEY INFORMATION .....	190
BIBLIOGRAPHY .....	191

# CHAPTER V

## ELECTRICAL PROPERTIES OF BORON DOPED Si<sub>0.7</sub>Ge<sub>0.3</sub> LASER ANNEALED LAYERS

### I – DOPANT ACTIVATION IN Si<sub>0.7</sub>Ge<sub>0.3</sub> LAYERS

Most of the interest for SiGe layers is focused on forming p-type layers, by either gallium or boron doping. This work is focused on boron in situ-doping of SiGe layers. Boron is introduced during the epitaxial growth as presented in Chapter II. Three boron concentration levels are used, and named samples A, B and C from the lowest to the highest concentration. Growth conditions are detailed in Chapter II, and led to the formation of pseudomorphic layers in each case.

#### 1. Dopant activation in pseudomorphic layers

##### a) Metrology

The evolution of the electrical properties was followed primarily with four-point probe measurements to obtain the sheet resistance, and completed with Hall effect measurements. Due to the thin doped SiGe layers used, this method is highly sensitive to probe depth penetration and therefore on the probe characteristics [1]. Clear reductions of the measured sheet resistance can be observed when the probe curvature radius is reduced, as the probe penetrates down to the substrate. We have therefore tried to consistently use the largest probes available, and an indication will be given for samples for which this was not doable. This implies that in some cases quantitative comparison between different experiments is not possible. In such cases, only the sheet resistance trends will be qualitatively discussed.

In addition to electrical characterizations, the boron chemical concentration depth profiles were obtained via ToF-SIMS measurements. These aim to evaluate the boron amount in the layers and to study the boron distribution after NLA, as well as to estimate the active boron percentage (when combined to Hall measurements). Ideally, SIMS boron profiles should be obtained with O ions as they enable better depth resolution. The Ge gradients in molten samples are however measured with Cs<sup>+</sup> protocols, and are essential to correct the sputtering rate. To avoid multiplying measurements on the numerous samples, the boron profiles were also collected with Cs<sup>+</sup>. The signal tail extending beyond the SiGe/Si interface is a consequence of this protocol: this artefact should be ignored in the following discussions. The Relative Sensitivity Factor (RSF, see Chapter II) was estimated on a boron-implanted Si (001) wafer, as it appears that it is independent of the Ge content [2].

##### b) Initial state after epitaxy

In our experimental conditions (thin layers), the most adapted measurement conditions should correspond to large probes. From the sheet resistance values, we can easily calculate the resistivity of the layers and then estimate the carrier concentration for each sample, if we consider that there is no mobility degradation caused by any residual defects in the as-grown samples [3,4]. Figure V - 1 shows the resistivity values obtained for samples A, B and C after epitaxy. This leads to initially active concentrations of  $7.23 \times 10^{19}$ ,  $1.13 \times 10^{20}$  and  $1.31 \times 10^{20}$  cm<sup>-3</sup> for samples A, B and C respectively.

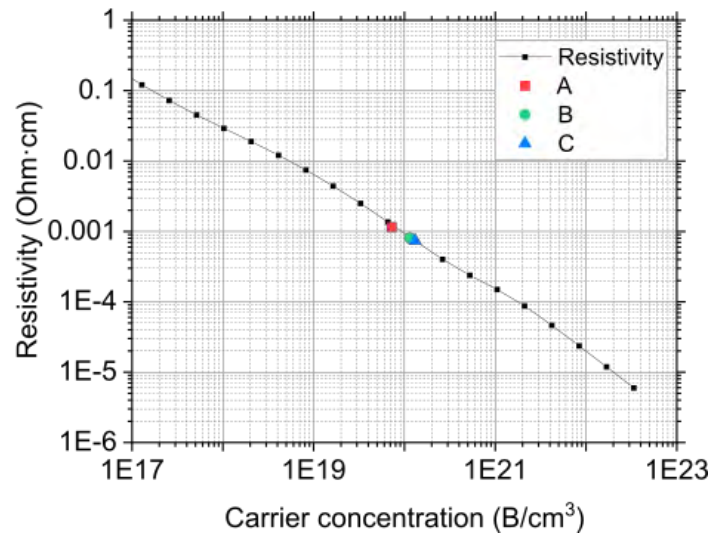


Figure V - 1. Evolution of resistivity in a boron doped  $\text{Si}_{0.7}\text{Ge}_{0.3}$  layer as a function of the carrier concentration [3,4].

In addition to four-point probe, multiple SIMS analysis were performed. The reference profiles are shown in Figure V - 2 for the three doping levels. Dotted lines indicate for each sample the  $\text{SiGe/Si}$  interface measured from the Ge SIMS profiles. As mentioned previously, the tail after the end of the layer is due to a measurement artefact and will be ignored in the following discussions. It is however believed that the pile-up observed before the interface (in the 25-30 nm range) is real, as it has been observed in multiple samples and can disappear depending on the layer growth conditions [5,6]. A decrease of the B concentration is observed near the surface in each sample, which is likely due to a measurement artefact.

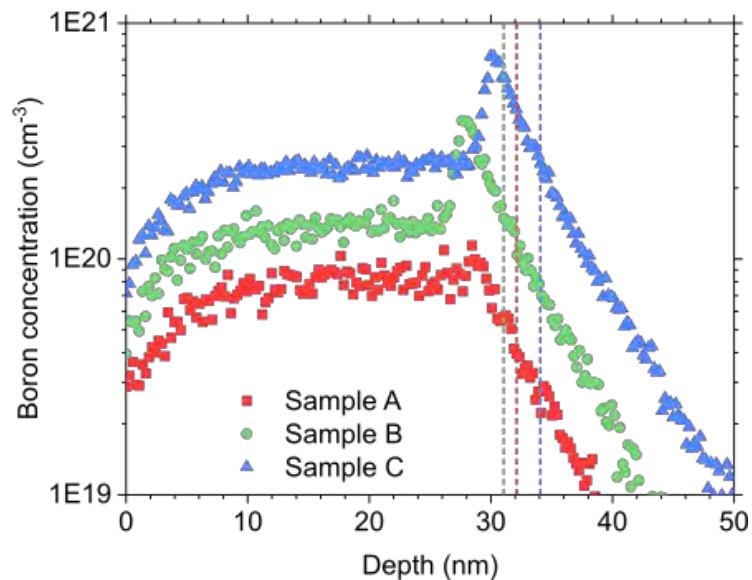


Figure V - 2. Boron concentration depth profiles after epitaxy, obtained by ToF-SIMS, for samples A (red), B (green) and C (blue). For each sample, a vertical line (same colour) indicates the bottom of the  $\text{SiGe}$  layer. The progressive decrease of the signal after the layer is an artefact caused by the use of Cs ions for the analysis.

The obtained curves show a plateau (from 5 nm to 25 nm) with atomic concentrations of  $7.79 \times 10^{19}$ ,  $1.38 \times 10^{20}$  and  $2.46 \times 10^{20} \text{ cm}^{-3}$ . These values correspond to the boron atomic concentration in the samples: this content corresponds to what was introduced during epitaxy and may not be fully activated. It should be compared with the active concentration estimated from sheet resistance, i.e.  $7.23 \times 10^{19}$ ,  $1.13 \times 10^{20}$  and  $1.31 \times 10^{20} \text{ cm}^{-3}$ . This shows that B

atoms in sample A are almost all electrically activated after epitaxy (93%), while part of the boron concentration remains inactive in samples B (82%) and C (53%) after epitaxy.

c) Electrical properties of  $\text{SiGe:B}$  laser annealed with a single pulse

*i. Boron redistribution*

SIMS analysis were performed on samples from levels A, B and C at energy densities corresponding to the surface melt ( $1.60 \text{ J/cm}^2$ ), partial melt ( $1.95 \text{ J/cm}^2$ ) and full melt ( $2.10 \text{ J/cm}^2$ ). An additional point at  $2.30 \text{ J/cm}^2$  was also assessed for the sample B. The obtained profiles are shown in Figure V - 3, along with the references before laser anneal.

Laser annealing at  $1.60 \text{ J/cm}^2$ , corresponding to the surface melt, causes only a slight reduction of the boron concentration in the near surface region, where the layer is known to melt. Higher energy densities, in the partial or full melt regimes, however modified the boron concentration profiles: a pile-up is observed near the maximum melt depth (shown by arrows in Figure V - 3), while a depletion occurred near the surface. A box-like profile is obtained at the highest studied energy density ( $2.30 \text{ J/cm}^2$ ), with almost uniform concentration through the layer. A boron depletion is observed near the surface, and appears more pronounced than in the reference samples. Part of this may be caused by a measurement artefact, but also to a boron out-diffusion.

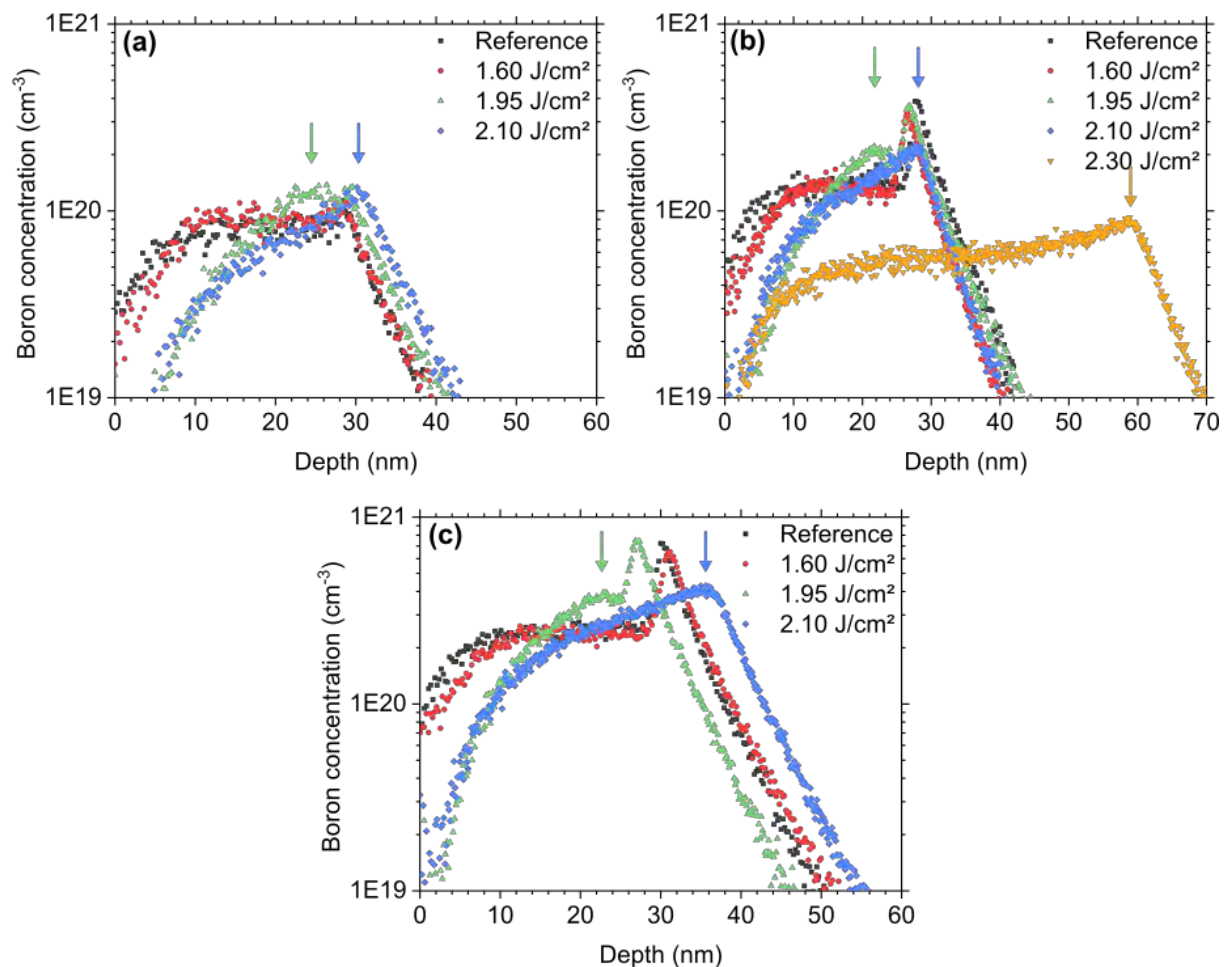


Figure V - 3. Boron concentration profiles as a function of depth, measured by ToF-SIMS for 30 nm-thick  $\text{Si}_{0.7}\text{Ge}_{0.3}$  samples annealed at various laser energy densities. The graphs (a), (b) and (c) respectively correspond to samples A, B and C. Arrows indicate the position of the boron pile-up, near the maximum melt depth.

This type of profiles was already observed in boron-doped Si and Ge layers [7–10], and seems related to the boron diffusivity properties within the liquid phase [11]. Especially, the pile-up close to the maximum melt depth cannot be explained by a standard diffusion model taking into account the partition at the l/s interface with a partition coefficient  $k < 1$ . Fiscaro et al. [11] rather explain such anomalous impurity redistribution by the co-existence of two different states for B atoms in the liquid phase : a highly mobile metallic local bond state and a slow-diffusing covalent bond state. The balance between both states as a function of the temperature in the liquid phase would be responsible for an adsorption behavior of the l/s boundary, acting as an impurity sink. Our results suggest that boron atoms behave in a similar way during laser annealing of SiGe, compared to pure Si or pure Ge.

Figure V - 4 presents the evolution of the boron total dose (integral over the SiGe layer depth) for each doping level. The total boron content generally tends to decrease with the energy density for each sample, though the variation remains within the measurement error. The maximum boron loss is 12%, 25% and 18% respectively for samples A, B and C. The measurement in sample C at 2.10  $\text{J}/\text{cm}^2$  is likely related to a thickness measurement error, and should not be compared with the other data points. The slight reduction observed may be due to out-diffusion, as it was observed in several occurrences for boron-doped Ge layers [10,12]. These studies have shown that near 10% of the initial boron dose out-diffuses during NLA in Ge layers. This effect becomes more pronounced with multiple pulses, up to 35%. Capping layers may allow to reduce this out-diffusion and contain the B within the layer.

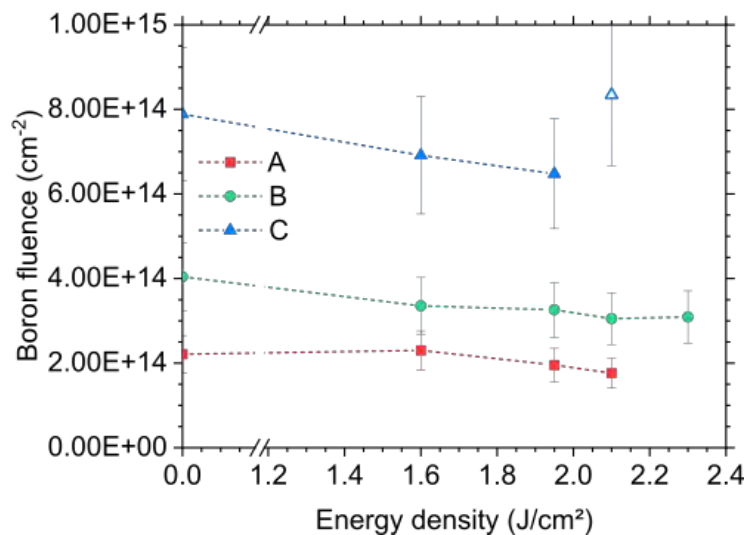


Figure V - 4. Boron fluence measured within the SiGe layer for various energy densities.

### ii. Impact of layer quality and doping level

The sheet resistance variations (measured by four-point probes) with increasing laser energy density are shown for samples A, B and C in Figure V - 5, along with the average  $R_s$  level before laser annealing, represented by horizontal lines. Sheet resistance values extracted from Hall measurements are added on the graphs. It can be noticed that both Hall and four point probe measurements match well, which supports the use of probes with large curvature radius for our measurements. As a reminder, the energy density range corresponding to different regimes are almost identical for the three samples (see chapter III): the melt threshold is reached near 1.45  $\text{J}/\text{cm}^2$ , the end of the surface melt at 1.78  $\text{J}/\text{cm}^2$ , while the full melt is observed at 2.10  $\text{J}/\text{cm}^2$  for samples A and B. It is reached between 1.95 and 2.10  $\text{J}/\text{cm}^2$  for sample C.

There is no change in sheet resistance up to the melt threshold, indicating that the sub-melt regime did not cause any modification in the layer for any of the samples. Tendencies

differ between the samples once the melt threshold is reached. For samples A and B, a sheet resistance degradation occurs as soon as the melt threshold is reached and continues until the end of the partial melt regime near 2.03-2.04  $\text{J}/\text{cm}^2$ . This degradation in surface and partial melt regimes is not observed for the sample C, with the highest boron concentration: on the contrary, the sheet resistance steadily decreases. All samples exhibit an abrupt improvement in sheet resistance near the transition to full melt, at respectively 2.04  $\text{J}/\text{cm}^2$ , 2.01  $\text{J}/\text{cm}^2$  and 1.98  $\text{J}/\text{cm}^2$  for samples A, B and C. Final sheet resistance values in the full melt regime are below the as-epi level for samples B and C, but remain higher for sample A.

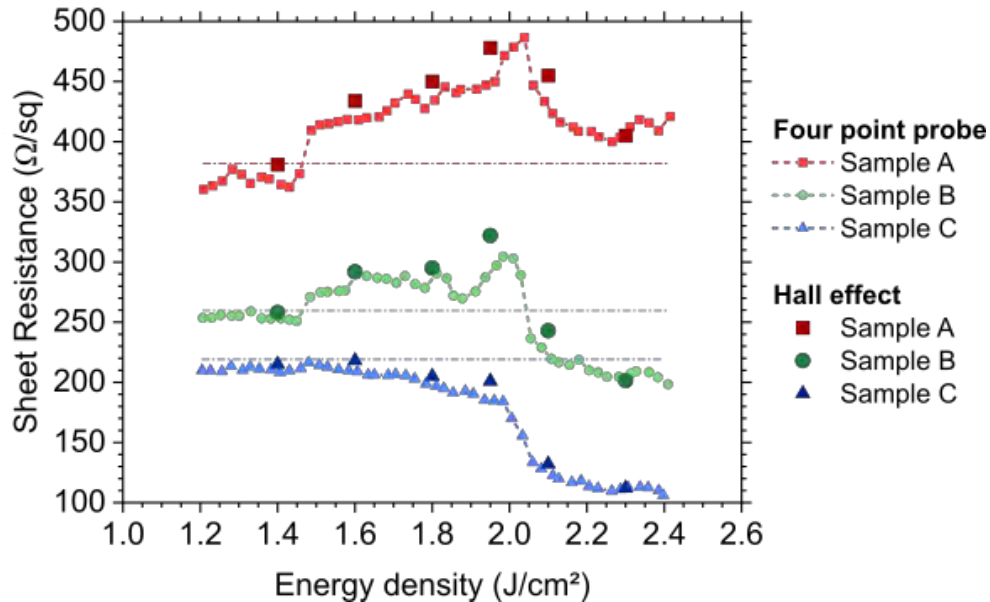


Figure V - 5. Evolution of sheet resistance with increasing energy density for samples A, B and C, by both four-point probe and Hall measurements. Horizontal lines indicate the average sheet resistance measured after epitaxy.

The Hall mobility and Hall dose measured are presented in Figure V - 6 for a set of selected samples, with at least one in each regime. These results highlight the changes in active dose and mobility caused by NLA. We first focus on the evolutions observed for the Hall dose. For sample A, the active dose decreases once the melt threshold is reached, and remains below the initial value even in the full melt regime. Sample B presents a lower active dose in both surface and partial melt regimes, and a slightly higher active dose in the full melt regime. Finally, the active dose was almost stable in sample C during surface and partial melt regimes, and showed a strong increase once the full melt is reached. These three samples showed partial relaxation in surface and partial melt regimes, as discussed in Chapter IV, at levels near 30%. The presence of crystalline defects linked to relaxation causes an apparent decrease in the active boron dose [13]. This is confirmed by multiple studies, showing that the presence of dislocations (either misfit or threading) in relaxed SiGe layers leads to the formation of traps or recombination centers for holes [14]. Additionally, the reduction in active dose might also be a direct consequence of the slight boron loss, observed in Figure V - 4. The same phenomena likely occur in sample C, with part of the carriers trapped by crystalline defects. However, the stability of the measured active dose suggests that additional boron atoms (initially electrically inactive) are activated during the laser anneal and compensate the trapped carriers. It is likely that the results in sample B are a combination of both phenomena, though the additional activation does not seem sufficient to replace the trapped boron. The drop at the end of partial melt is likely due to defect healing, leading to higher active doses. Finally, the strong increase in carrier mobility observed at 2.30  $\text{J}/\text{cm}^2$  in all samples is related to the redistribution of boron in depth (~60 nm SiGe layer) that leads to a lower average active concentration.

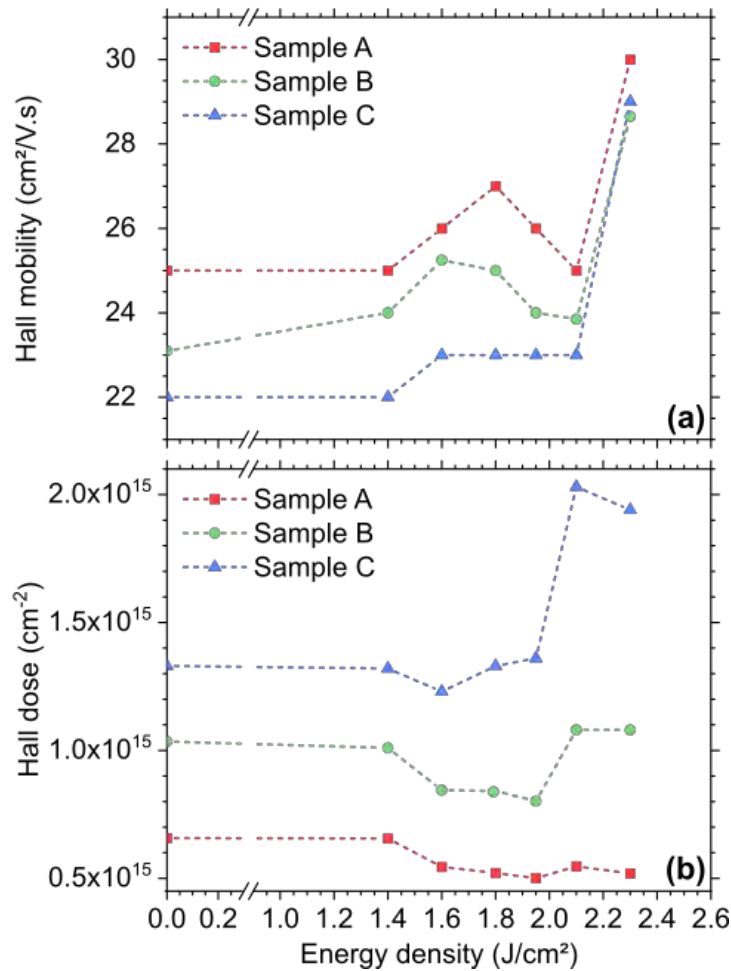


Figure V - 6. Hall mobility (a) and Hall dose (b) values obtained after laser annealing for samples A (red), B (green) and C (blue).

Calculations were performed to estimate the maximum active concentration by taking into account the Hall measurement and SIMS profiles for given energy densities [15], considering a Hall scattering coefficient  $r_H$  of 0.33 [4]. From these calculations, it is possible to deduce the evolution of the activation rate as well as a possible degradation of the carrier mobility caused by any residual defects. As shown in Figure V - 7, before laser anneal, the activation rate is near 95%, 80% and 50% for samples A, B and C respectively. For sample A, the active percentage is indeed lower in surface and partial melt regimes (75% and 90%) and finally reaches 100% in full melt regime. This is consistent with the observed boron loss and lower active dose in full melt: the boron is fully activated, but the total content is slightly lower than in the as-epi sample due to out-diffusion. In sample B, the active percentage is stable in surface and partial melt regimes, while full activation of the remaining B is observed in full melt regime. In sample C, a continuous increase of the active percentage is found, up to 80% in the full melt regime. No carrier mobility degradations were deduced from the analysis of the results, even in the case of surface or partial melt regimes (where strain relaxation is observed). Mobility degradation has been observed in Si samples doped with Boron by ion implantation, and associated to the presence of boron-interstitial clusters (BICs) [15] formed by the interactions between Boron atoms and Si self-interstitials generated during the ion implantation [16]. In the case investigated here, doping occurs *in situ* during low temperature CVD growth, a process during which Si self-interstitials are less likely to form in agreement with our results. In addition, it appears that even the extended defects formed upon strain relaxation do not induce any detectable mobility degradation in the annealed samples, despite previous reports had shown such an effect [14].

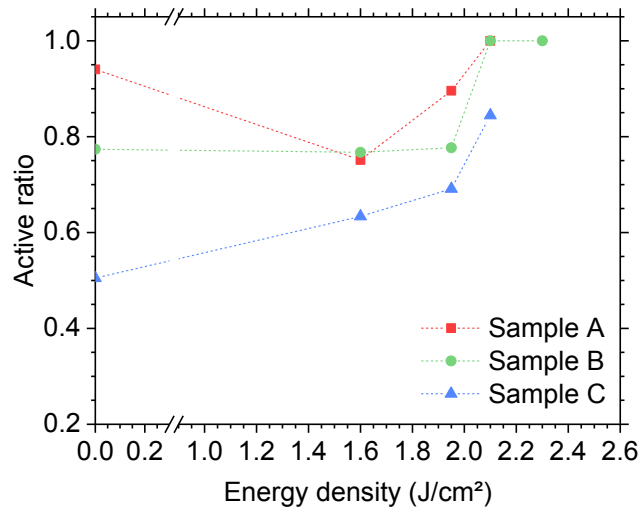


Figure V - 7. Evolution of the active percentage of dopants as a function of energy density for samples A, B and C. These values are extracted from a joint analysis of Ge and B SIMS profiles with the Hall effect measurements.

NLA therefore enables activation levels in highly doped layers above their initial post-epi levels, with no mobility degradation. The ideal case for this type of layers is a laser anneal with energy densities just beyond the partial-full melt transition, as it leads to pseudomorphic SiGe, with high activated doses and a high Ge content near the surface. This type of boron doped layers are particularly interesting for the formation of S/D regions, as the high-Ge content near the surface appears to improve the contact resistivity [17–19].

#### c) Electrical properties with single pulse at 450°C

Nanosecond laser annealing was performed on a heating chuck, at 450°C, to understand its impact on dopant activation and on the various regimes. The sheet resistance measurements had to be performed with sharper probes, and the values cannot be compared with those obtained on samples annealed at room temperature. The results are presented in Figure V - 8, with horizontal lines indicating the average sheet resistance measured before laser anneal with the same set of probes.

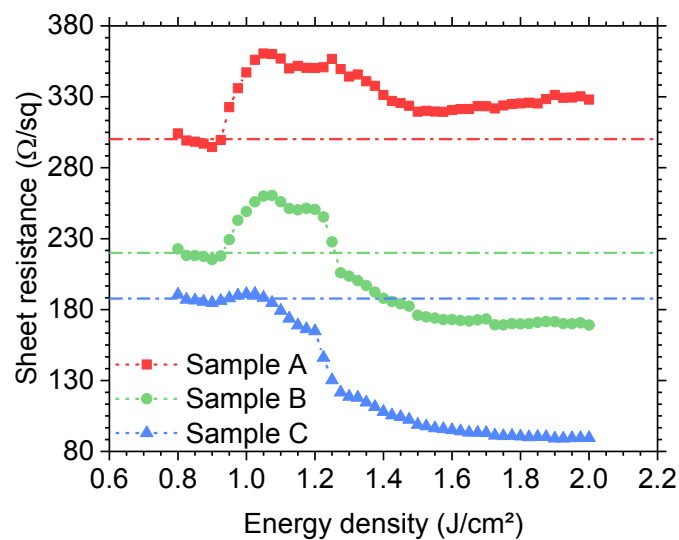


Figure V - 8. Evolution of the sheet resistance as a function of laser energy density for samples A, B and C after NLA on a heating chuck at 450°C. The four-point probe measurement could not be performed with the same probe as in Figure V - 5, therefore causing a shift in the measured values. A horizontal line indicates the average sheet resistance of the sample before laser anneal for each sample, with the probes used in this case.

As mentioned in Chapter III, the regimes are shifted towards lower energy densities when the chuck is maintained at  $450^\circ\text{C}$ , with a melt threshold at  $0.95 \text{ J/cm}^2$  instead of  $1.45 \text{ J/cm}^2$  at room temperature. The sheet resistance evolutions with energy density are similar to those observed on samples annealed at room temperature for each doping level, with a sheet resistance increase in the surface and partial melt regimes for samples A and B. Lower sheet resistances are obtained in the full melt regime for all samples, though, for sample A, the sheet resistance remains above the initial value. It can therefore be considered that activation on a heating chuck did not bring any clear advantage compared to activation at room temperature, and that it did not modify the phenomena occurring during the laser anneal. Using the TRR extraction method presented in Chapter III section V, it is possible to compare the solidification time  $t_{s-20}$  for both heating chuck settings, i.e. room temperature and  $450^\circ\text{C}$ . Both are presented for sample B in Figure V - 9: they exhibit an identical evolution, with  $t_{s-20}$  approaching 20 ns. This suggests that the solidification is similar at both temperatures, even though the total melt duration increased at  $450^\circ\text{C}$ .

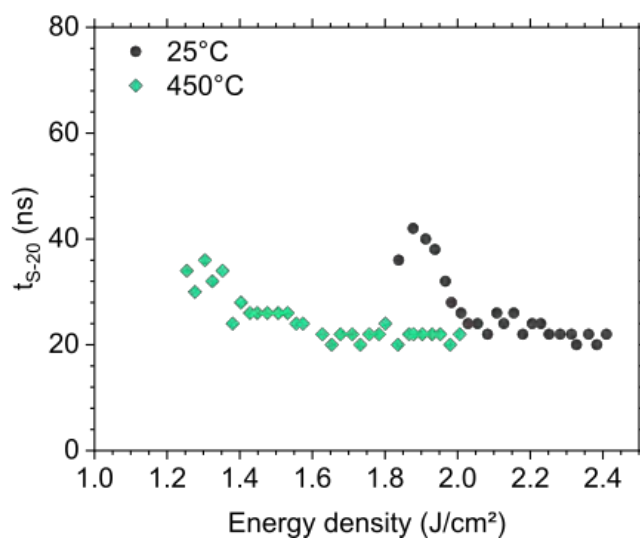


Figure V - 9. Time for solidification of the last 20 nm for sample B during laser annealing with a chuck at room temperature (black dots) or at  $450^\circ\text{C}$  (green diamond).

#### d) Electrical properties with multiple pulses at room temperature

Four energy densities were selected to evaluate the impact of a multi-pulse irradiation cumulating 3, 10 and 30 pulses on boron-doped  $\text{Si}_{0.7}\text{Ge}_{0.3}$  layers. These correspond to the sub-melt at  $1.40 \text{ J/cm}^2$ , the surface melt at  $1.70 \text{ J/cm}^2$ , the limit between partial and full melt at  $2.10 \text{ J/cm}^2$ , and the full melt at  $2.30 \text{ J/cm}^2$ . Tests with 100, 300 and 1000 pulses were also performed for the sub-melt regime, at  $1.40 \text{ J/cm}^2$ .

The resulting sheet resistance values are shown in Figure V - 10, along with the measurement for previously presented single pulse anneals. In almost every case, the sheet resistance remains higher than the value obtained for a single pulse, showing no improvement of dopant activation. This is observed even for sample C, in which a large part of the dopants is inactive in the sub-melt regime. Results from samples A and B show strong variability of the sheet resistance after multi-pulse annealing at  $1.40 \text{ J/cm}^2$  and  $1.70 \text{ J/cm}^2$ . For the samples annealed at  $\sim 1.40 \text{ J/cm}^2$ , the energy density variation (up to 3%) may cause the sample to reach the melting threshold during some pulse, thus leading to an abrupt increase in sheet resistance. The variations observed near  $1.70 \text{ J/cm}^2$  may however be related to cumulative effects on the surface and on the Ge segregation. Further investigations necessitate AFM and SIMS observations. It therefore seems that multi-pulse is not an efficient method for boron activation in pseudomorphic SiGe layers.

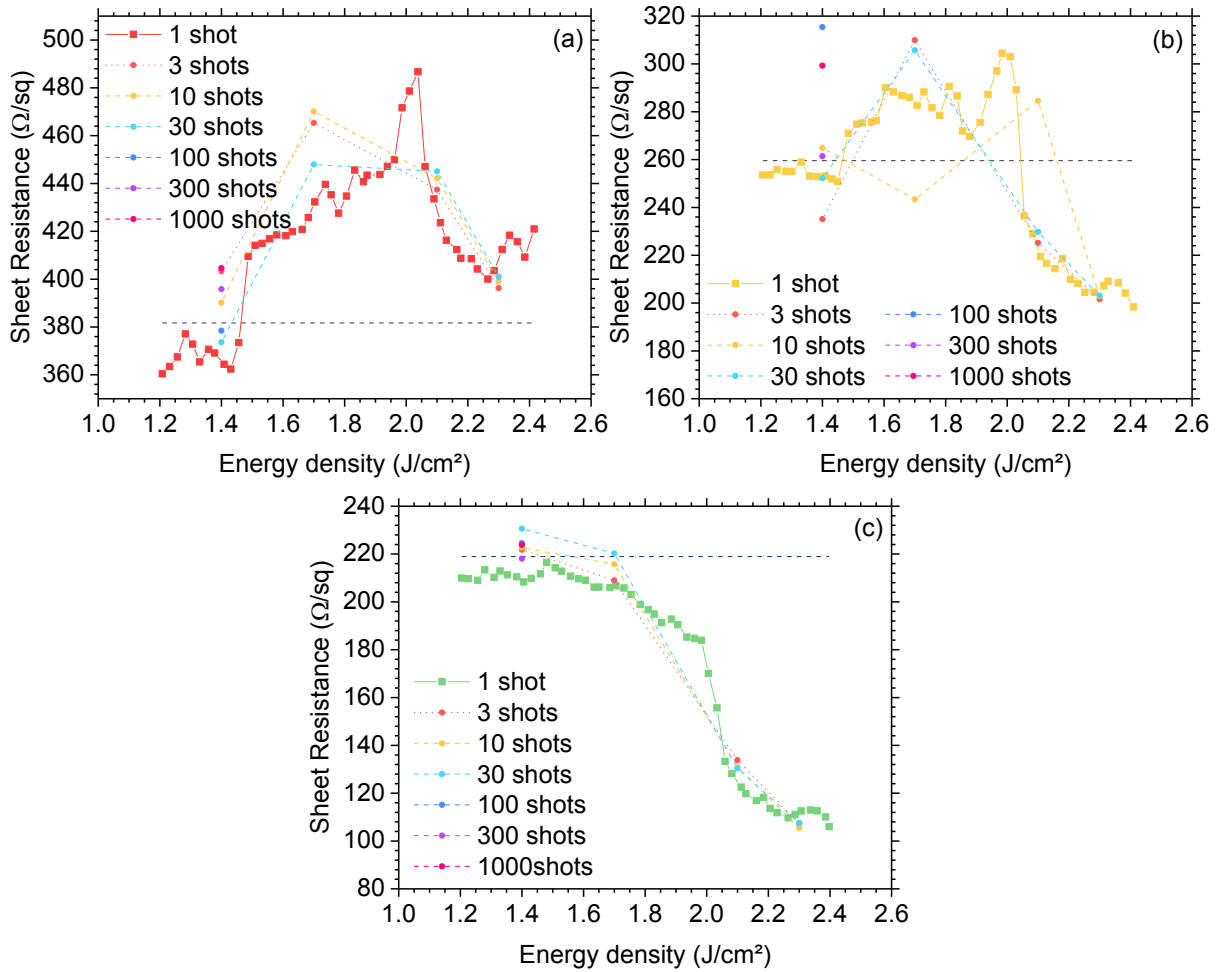


Figure V - 10. Sheet resistance as a function of energy density for multi-pulse annealing at room temperature for samples A (a), B (b) and C (c). Data were recorded for 3, 10, 30, 100, 300 and 1000 pulses. The measurements are presented along the sheet resistance obtained for a single pulse irradiation, already shown in Figure V - 5.

## 2. Dopant activation in initially amorphous layers

For comparison with results obtained on pseudomorphic SiGe layers, one of the doped wafers (sample B) was amorphized over 15 nm by  $\text{Ge}^+$  implantation with a  $1.50 \times 10^{15} \text{ cm}^{-3}$  dose at 6 keV. The regimes observed during the laser annealing are presented in Chapter III. In this section, we focus on the evolution of the sheet resistance. Note that in this case the four-point probe measurements could not be performed with the ideal set of probes.

The sheet resistance evolution with increasing energy density is presented in Figure V - 11. Vertical lines delimitate the sub-melt regime, explosive melt regime, surface melt and partial melt regimes. The average value on areas that were not laser annealed was  $1790 \Omega/\text{sq}$ , a high value caused by the partial amorphization of the SiGe layer. A decrease in sheet resistance is already observed in the sub-melt regime, supporting the idea that the sub-melt regime is efficient for dopant activation in amorphous layers. Solid Phase Epitaxial Regrowth (SPER) may occur over 2-3 nm for energy densities just below the melt threshold, as it was observed on amorphous Si layers [20]. The sheet resistance decrease extends into the explosive regime until a plateau is reached. A second drop in sheet resistance is observed at the onset of the surface melt regime: as the second melt occurs, larger crystals may be formed, until the polycrystalline layer obtained after explosive recrystallization is fully melted. The value remains relatively stable within surface and partial melt regimes. A final drop is observed near  $2.00 \text{ J}/\text{cm}^2$ , which likely

corresponds to the full melt: the formation of a monocrystalline layer improves dopant activation, as previously observed.

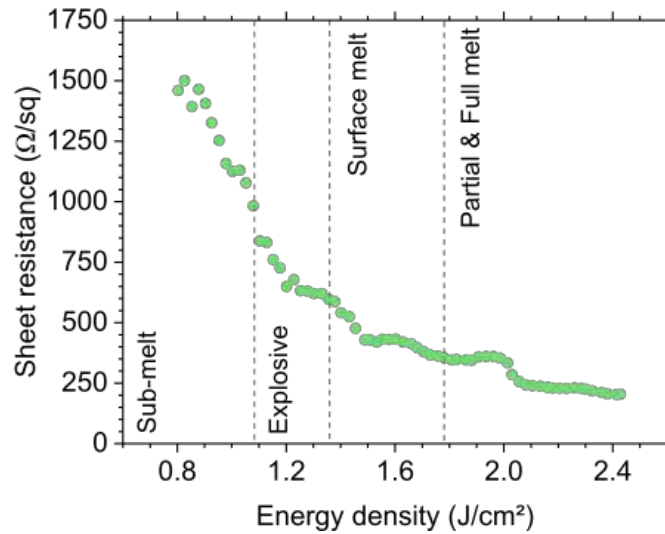


Figure V - 11. Sheet resistance as a function of laser energy density for a boron doped (sample B) 30 nm-thick layer, amorphized over 15 nm by Ge implantation.

Surface, partial and full melt regimes present tendencies similar to what is observed in pseudomorphic layers. The main difference is the improvement observed even within the sub-melt regime, and should be further explored. The expected Solid Phase Epitaxial Regrowth after one or several laser pulses in the submelt regime is at the heart of a new thesis just starting in the laboratory.

## II – THERMAL STABILITY OF BORON ACTIVATION FOLLOWING A SUBSEQUENT ANNEALING STEP

Additional annealing may cause multiple modifications in boron doped SiGe layers, including relaxation, germanium or boron diffusion, as well as boron deactivation. The effect may depend on the initial boron concentrations, as it was observed in boron-doped silicon layers [21,22].

### 1. Samples and annealing conditions

#### a) Selected samples

Samples from the three doping levels (A, B, C) were submitted to additional anneals in furnaces. In addition to a reference sample without any laser anneal, two energy densities were chosen: 2.10 J/cm<sup>2</sup> and 2.30 J/cm<sup>2</sup>. These samples are pseudomorphic, as presented in Chapter IV, and respectively correspond to the end of the partial melt and to the full melt regime. The samples annealed at 2.10 J/cm<sup>2</sup> presented Ge content near 75% at the surface (see Chapter III), while the ones annealed at 2.30 J/cm<sup>2</sup> should present ~25% Ge near the surface. Several samples were cleaved from one single wafer for each doping level. In that way, we can apply different thermal budgets to each sample without cumulating the effects on one single sample. The mapping is shown in Figure V - 12: multiple strips of three samples (such as the one shown in the white rectangle) were prepared, each containing identical conditions. This includes a reference area without laser anneal in the middle, a shot at 2.10 J/cm<sup>2</sup> (in blue) and a shot at 2.30 J/cm<sup>2</sup> (in red). The strips were then separated and submitted to different furnace anneal conditions.

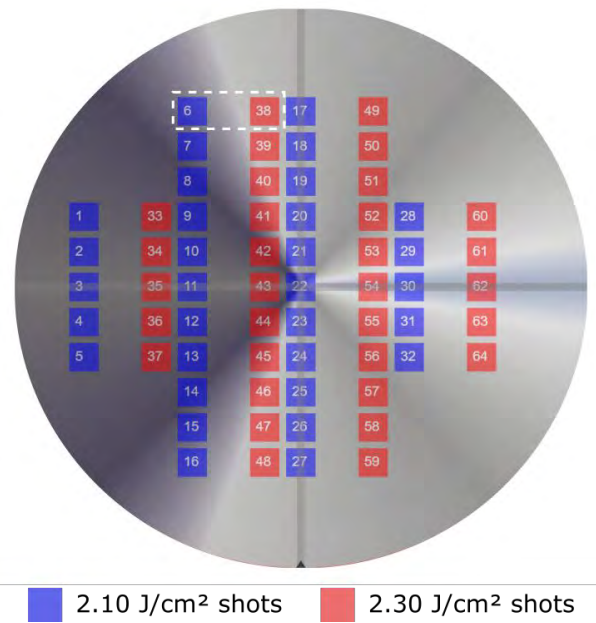


Figure V - 12. Mapping for deactivation experiments, with the  $2.10 \text{ J/cm}^2$  and the  $2.30 \text{ J/cm}^2$  shots shown in blue and red respectively. The furnace anneals are subsequently performed on individual strips (obtained by cleavage) such as the one shown in white, which contain a reference area (in the middle), a  $2.10 \text{ J/cm}^2$  shot and a  $2.30 \text{ J/cm}^2$  shot.

#### b) Furnace annealing conditions

The furnace anneals were performed at temperatures ranging from  $400^\circ\text{C}$  to  $950^\circ\text{C}$ . This range enables to study low temperatures, where thermally activated phenomena are limited, as well as temperatures close to the melting point. It was not possible to test temperatures above  $950^\circ\text{C}$ , as the samples with strong Ge segregation might have molten. The anneals were performed in a TEMPRESS horizontal tube in  $\text{N}_2$  at atmospheric pressure, and lasted near 20 minutes at the chosen temperature ( $\pm 5^\circ\text{C}$ ). The entrance in the furnace was done at  $700^\circ\text{C}$  for anneals with set temperature above  $700^\circ\text{C}$ . In other cases, the entrance was performed at the same temperature as the soak. An example of a temperature profile is shown in Figure V - 13, for an anneal at  $700^\circ\text{C}$ , starting from the point where the samples are introduced in the furnace. The chosen plateau temperature at  $700 \pm 5^\circ\text{C}$  is shown by two red lines, and lasted for 18 minutes in that case.

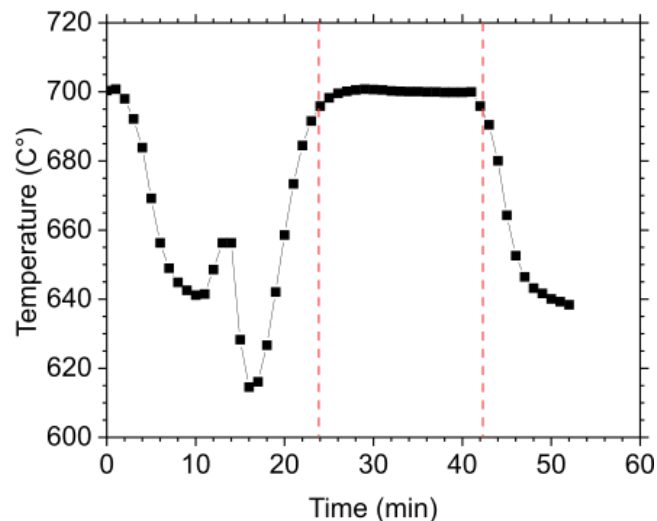


Figure V - 13. Temperature profile as a function of time during a furnace anneal at  $700^\circ\text{C}$ . The red lines indicate the plateau region, calibrated to last near 20 minutes at  $700 \pm 5^\circ\text{C}$ .

## c) Modifications assessment

The evolution of the samples with additional furnace anneals is assessed through sheet resistance. For this experiment, a different four-point probe tool was used compared to that used for all previously shown results, thus causing a shift in the measured sheet resistance due to differences in probe weight and curvature radius [1]. The  $R_s$  values measured by the second four-point probe measurement are ~15% lower than the previous measurements (see Figure V - 5, with the large curvature radius). As a consequence, the following results will not be compared with the sheet resistance values presented previously. The sheet resistance after furnace anneal will instead be qualitatively compared with the sheet resistance expected after laser anneal. To do so, five samples of each energy density, from each doping level, were selected and measured after laser annealing, to serve as reference. The minimum, average and maximum measured values are shown in Table V - 1 for each studied sample: any change within this range will be considered as negligible.

Table V - 1. Sheet resistance average, maximum and minimum values for each sample and each energy density used, before the furnace anneals. These measurements were performed by taking five strips of each wafer, in different areas.

Initial sheet resistance	Sample A			Sample B			Sample C		
	0	2.10	2.30	0	2.10	2.30	0	2.10	2.30
Minimum	308.6	342.7	330.6	222.7	199.8	181.6	189.4	115.5	99.5
Average	315.9	348.5	339.7	228.5	201.92	186.6	194.0	116.5	103.5
Maximum	326.1	354.8	354.1	235.8	204.9	194.0	199.5	118.4	109.3

As multiple phenomena may occur during these furnace anneals, including dopant or Ge diffusion and relaxation of the SiGe layer, X-ray diffraction measurements were performed. As it was not possible to obtain RSM on each individual sample after the furnace anneals, a strip (with a reference, 2.10 and 2.30 J/cm<sup>2</sup> shots) of each boron level was selected to undergo in-situ XRD measurements during a temperature ramp up to 950°C under an N<sub>2</sub> atmosphere, with  $\omega$ -2 $\theta$  scans collected at regular temperature intervals. The temperature ramp is shown in Figure V - 14. The whole duration of the procedure was about three hours long, while an individual scan lasted less than seven minutes, during which the temperature increased by 50°C for temperatures below 600°C and by 20°C for temperatures above 600°C. The aim is to follow any changes in intensity or peak position that may be due to diffusion or relaxation. Separate sample strips are used for the XRD measurements and the furnace anneals.

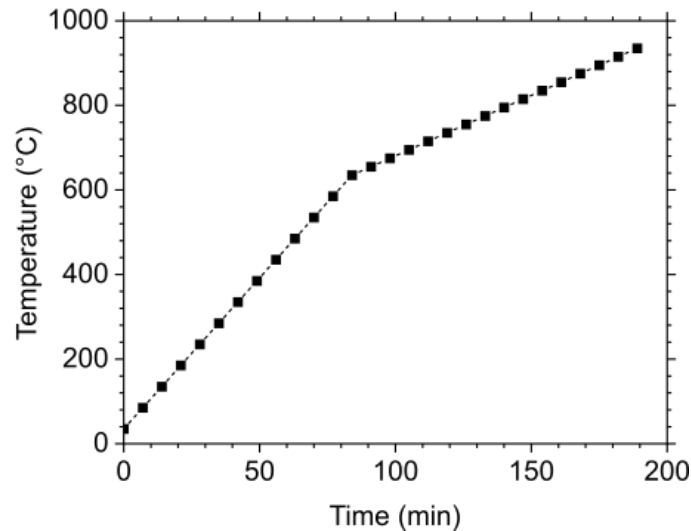


Figure V - 14. Temperature ramp used for the in-situ XRD measurements. The total duration is near three hours.

## 2. Morphological and electrical evolutions with anneal temperature

### a) Samples without laser anneal

The structural evolution or modification due to the furnace anneals are first described for samples without nanosecond laser annealing, in order to better identify the effects coming from the subsequent furnace annealing and those coming from NLA.

#### *i. Structural modifications*

The XRD measurements are presented as maps in Figure V - 15 for the reference samples (without NLA). The  $x$  and  $y$  axes respectively correspond to the scan angle  $\omega$  and the temperature and each horizontal line corresponds to an  $\omega$ - $2\theta$  scan, with the intensity as the color scale. Two peaks can be observed on each map: the more intense, near  $34.56^\circ$  at low temperature, corresponds to the Si substrate, while the less intense one on the left is associated with the SiGe layer. Measurements for samples A and C were performed with a shorter range of intensity due to an added slit. The slit was removed for the measurements on sample B, offering a wider intensity scale. In that case, thickness fringes can be observed around the SiGe peak.

Both Si and SiGe peaks are observed to move toward smaller angles with increasing temperature. The layer quality can be estimated with the observation of thickness fringes on the maps, particularly well-defined for sample B. Their appearance up to  $700$ - $750^\circ\text{C}$  indicates high strain and crystallinity in the SiGe layers. The SiGe peak intensity drops for all samples near  $850^\circ\text{C}$ , while an additional peak is observed at small angles ( $\sim 33.2^\circ$ ) in the  $900$ - $950^\circ\text{C}$  range. This new peak indicates the formation of a relaxed Ge layer, likely caused by the "Ge condensation" phenomenon occurring during thermal oxidation of the SiGe surface layer [23–25]. This phenomenon is due to the presence of oxygen traces in the heating cell used for in-situ XRD measurements, and should not occur if samples are annealed in a pure  $\text{N}_2$  atmosphere.

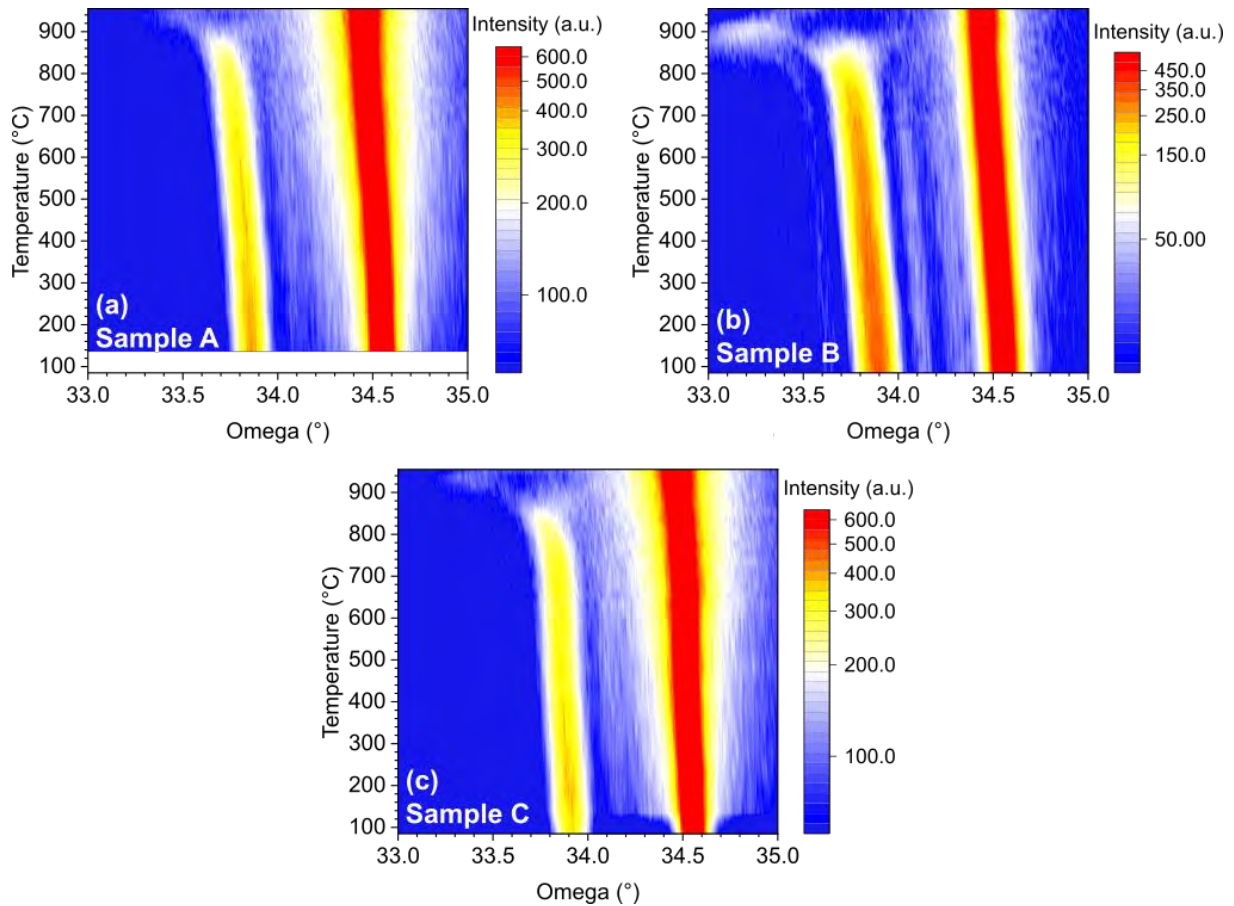


Figure V - 15.  $\omega$ - $2\theta$  maps, as a function of both the  $\omega$  angle and the temperature for samples A, B and C without nanosecond laser annealing. The more intense peak on the right is caused by the Si substrate, while the less intense peak on the left corresponds to the SiGe layer.

Figure V - 16 presents the evolution of the peak position in sample B for both Si and SiGe, as a function of the temperature. As observed in the maps, both peaks shift toward smaller angles with increasing temperature, which indicates that the perpendicular lattice parameter increases in both layers. For Si, this displacement is almost linear, and is likely caused by the thermal expansion of the lattice. For better visualization, the angular gap between the two peaks is plotted in Figure V - 17. In these graphs, a dotted line indicates for each sample the theoretical gap if the peak positions of both Si and SiGe are solely determined by the thermal expansion. As the thermal expansion coefficient  $\alpha_{TH}$  is higher in SiGe [26,27] than in Si, its lattice parameter increases at a higher rate and the expected peaks become more distant. The measured gap matches this evolution up to 700°C-750°C, indicating that the peak displacement is likely not related to any other phenomena below these temperatures.

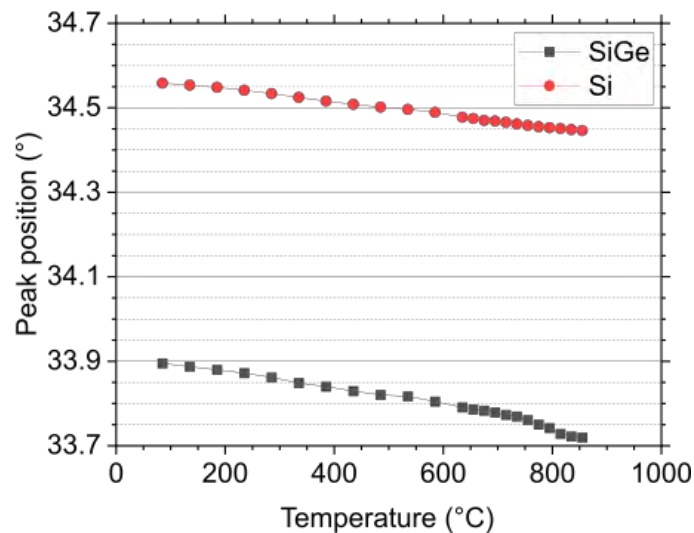


Figure V - 16. Evolution of the peak position as a function of temperature for Si and SiGe in sample B during furnace annealing only.

Above 700-750°C, the SiGe peak displacement toward low angles becomes more pronounced and cannot be explained by thermal expansion alone. It therefore corresponds to an additional increase in lattice parameter, which is tentatively associated with the onset of boron deactivation. Indeed, Boron-induced strain compensation in pseudomorphic SiGe layers is strongly reduced as boron atoms move out of substitutional sites. It can be noticed that the displacement toward shorter angles occurs at slightly lower temperatures for samples with a higher boron concentration, respectively at 700°C, 735°C and 750°C for samples C, B and A. This is consistent with Takamura observations, showing that the samples with higher B content are prone to deactivation at lower temperatures [21], due the higher Boron concentration excess with respect to the solid solubility limit. Besides, the peak displacement toward shorter angles and its disappearance near 900°C may also be caused by the progressive Ge-enrichment during thermal oxidation, which can occur as the XRD analysis is performed under atmospheric pressure with some remaining oxygen in the cell. As both boron deactivation and SiGe thermal oxidation lead to displacement of the SiGe toward small angles, they cannot be distinguished with these measurements. Finally, strain relaxation in the SiGe layer might also occur at these temperatures but it would have an opposite effect, with a peak displacement toward larger angles. Though relaxation cannot be excluded, its effect appears to be compensated by boron deactivation and/or the non-intentional oxidation.

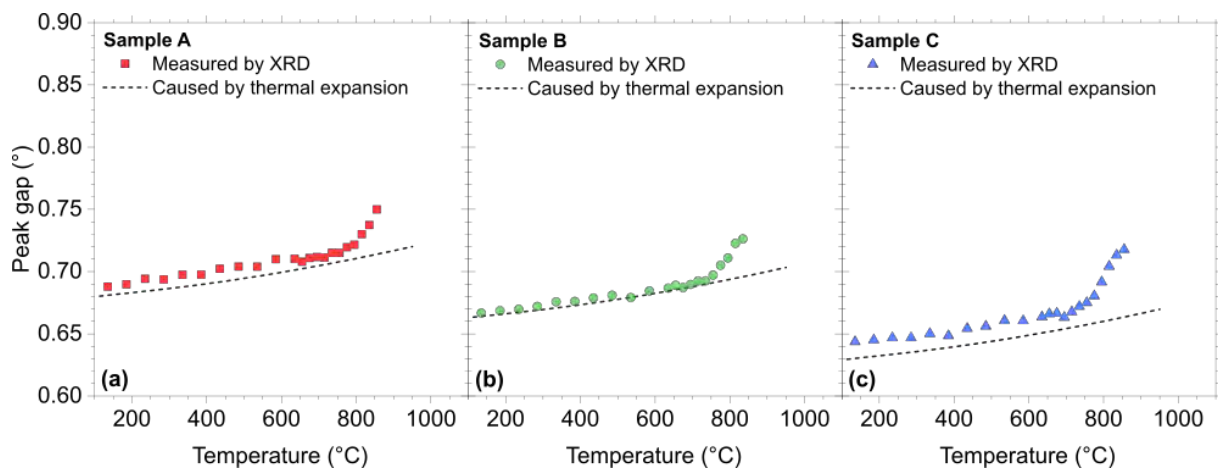


Figure V - 17. Angular gap observed between the Si peak and SiGe peak as a function of temperature for samples A (a), B (b) and C (c) without laser annealing. A grey line presents the expected evolution of the gap when only thermal expansion is taken into account.

*ii.  $R_s$  evolution upon subsequent furnace anneal*

The structural changes, caused by boron deactivation and thermal oxidation, are likely to modify the electrical results. This section presents the electrical results obtained on samples submitted to furnace anneals for 20 minutes. The thermal oxidation observed during the high temperature XRD should not occur during the furnace anneals. The evolution of the sheet resistance as a function of furnace anneal temperature is shown in Figure V - 18 for samples without NLA. For all of them, the measured sheet resistance remains almost constant up to 600°C. A slight increase is observed after 600°C for the three samples, up to 800°C. At higher temperatures, the tendencies are highly dependent on boron concentration: sample A keeps deteriorating and reaches 350  $\Omega/\text{sq}$ , while both samples B and C exhibit a decrease in the measured sheet resistance, at a stronger rate for sample C.

It can therefore be considered that the furnace anneals do not cause any substantial changes up to 600°C for 20 minutes anneals, as no changes in sheet resistance can be noticed. The in-situ XRD measurements presented previously also concluded that the layers are stable up to 600°C, though the thermal budget differs. The sheet resistance degradation observed at 700-800°C for all samples is likely related to the boron deactivation already suggested from the XRD observations, as the boron above the solid solubility limit can deactivate to reach the equilibrium [21,28]. An onset of relaxation may also have a detrimental impact on the sheet resistance (as seen in the first section of this chapter), but this could not be directly observed. The change in behavior after 800°C can however be associated to the competition between deactivation in SiGe and activation of boron atoms diffusing into the Si substrate [29,30]. In sample A, the boron is fully activated from the start: the boron atoms can diffuse but the active dose cannot increase, and the sheet resistance keeps deteriorating up to 950°C. This deactivation likely occurs in samples B and C as well, but appears to be compensated by diffusion and additional activation of boron [29,30]. As the temperature increases, the boron atoms diffuse over larger depths and can activate in the Si substrate, leading to the drop in sheet resistance.

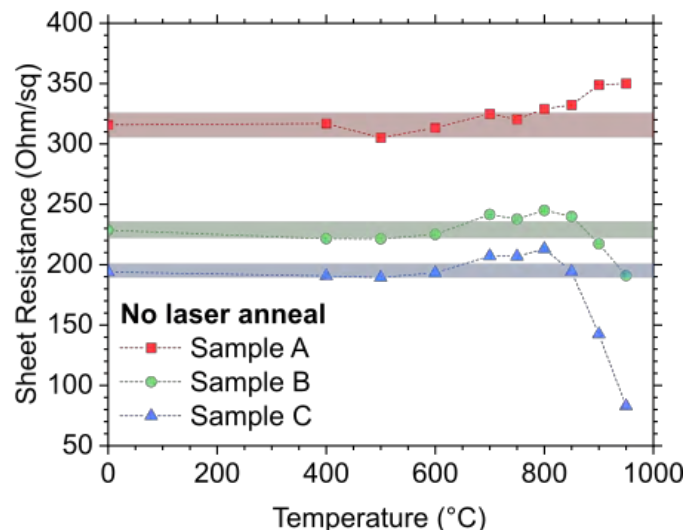


Figure V - 18. Sheet resistance as a function of furnace anneal (20 minutes in pure  $\text{N}_2$ ) temperature for samples without NLA. The color stripes respectively indicate the variations observed on the initial samples for the three doping levels (see Table V-1).

There are numerous phenomena observed during the furnace anneal of boron-doped SiGe layers. They appear stable up to 600°C, and the first signs of deactivation occur near 700°C, causing a sheet resistance increase. At high temperatures, the boron diffusion and activation into the Si substrate cause a sheet resistance reduction in samples B and C.

## b) Laser annealed samples

An identical procedure was applied to the laser annealed samples (2.10 and 2.30 J/cm<sup>2</sup>). Both samples correspond to the full melt regime, with melt depth close to 30-35 nm for 2.10 J/cm<sup>2</sup> and close to 60 nm for 2.30 J/cm<sup>2</sup>. In-situ XRD measurements during annealing were also performed on the laser annealed samples, following the same procedure as the one presented for reference samples.

*i. Structural modifications*

In-situ XRD measurements were performed on these samples during the same temperature ramp-up (see Figure V - 14): the corresponding XRD maps are shown in Figure V - 19 for all samples at 2.10 and 2.30 J/cm<sup>2</sup>. There is again a difference in the intensity scale between the various samples, with a larger intensity range observed for sample B. Due to the Ge gradients (hence strain gradients) in these laser annealed layers, no thickness fringes are observed on these XRD measurements. In addition, the presence of a Ge concentration gradient complicates the thermal expansion calculation.

At 2.10 J/cm<sup>2</sup>, the SiGe peak presents a low intensity for all samples and it is difficult to clearly distinguish it from the Si peak. As they seem to follow similar evolution whatever the doping level, we use the map obtained from sample B in order to describe the evolution. Both the Si and SiGe peaks progressively shift toward small angles for temperatures below 500°C, which can be associated with the impact of thermal expansion. Near 600-800°C, the SiGe peak appears shifted toward higher angles, indicating a reduction in the lattice parameter. This can be caused by either relaxation or boron activation, as the boron in substitution leads to a strain compensation. Above 850°C, the SiGe peak disappears and a new peak is observed at low angles. This is again associated with the formation of a Ge-rich layer due to thermal oxidation.

At 2.30 J/cm<sup>2</sup>, the SiGe peak is clearly visible and is close to the Si peak: due to the Ge redistribution over ~60 nm corresponding to the melt depth, the Ge concentration is much lower than in the as-epi samples. The SiGe peak position at low temperatures roughly correspond to the expected position for layers with ~20% and ~10% Ge, matching the plateau concentrations observed by SIMS for these samples after NLA. It can also be noticed that the peak are even closer for boron-rich layers, which is due to the strain compensation by the boron atoms. Once again, the SiGe and Si peaks progressively shift toward lower angles. There is no strong fluctuation observed in the maps. The peak intensity appears to decrease near 900°C, and a peak with very low intensity is observed in (e) at low angles. This indicates that a slight thermal oxidation can still occur in this sample, though it appears to be limited. The lower Ge concentration at the surface after laser annealing at 2.30 J/cm<sup>2</sup>, compared to 2.10 J/cm<sup>2</sup>, is expected to reduce the oxidation rate [31].

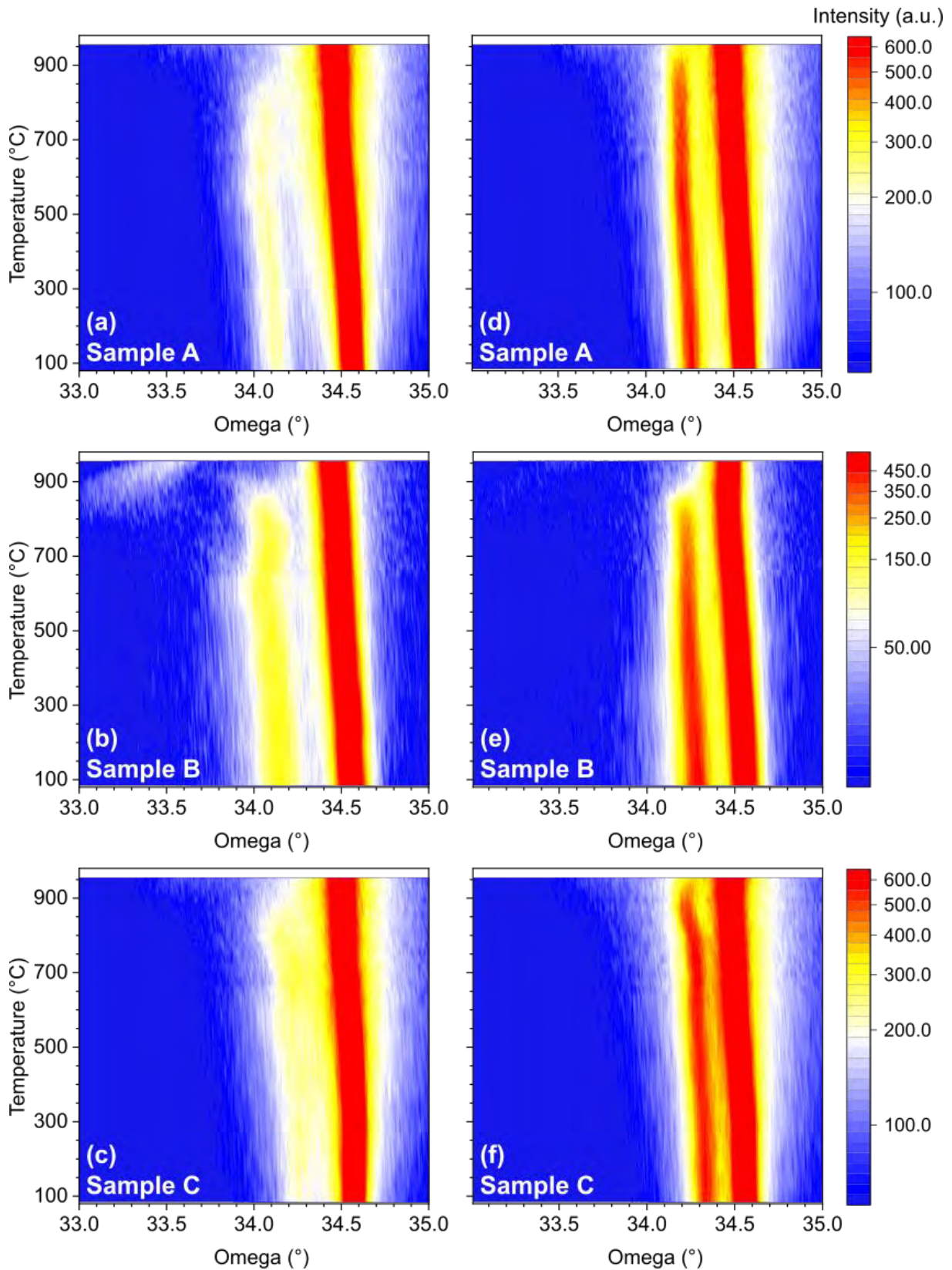


Figure V - 19.  $\omega$ - $2\theta$  maps, as a function of both the  $\omega$  angle and the temperature for samples A (a,d), B(b,e) and C (c,f) after nanosecond laser annealing at  $2.10 \text{ J/cm}^2$  (a,b,c) and  $2.30 \text{ J/cm}^2$  (d,e,f). The more intense peak on the right of each map is caused by the Si substrate, while the less intense peak on the left corresponds to the SiGe layer.

The gaps between Si and SiGe peaks are plotted as a function of the furnace anneal temperature for all samples annealed at 2.10 and 2.30  $\text{J}/\text{cm}^2$  in Figure V - 20. Dotted lines indicate the expected gap caused by the thermal expansion, assuming that most of the layer is near 20% Ge for 2.10  $\text{J}/\text{cm}^2$  and near 10% for 2.30  $\text{J}/\text{cm}^2$ . As this cannot take into account the Ge gradients, the calculation is not as reliable as it is for uniform layers. Below 500°C, the gap follows an evolution similar to the expected one with expansion at both energy densities. The layer is therefore considered stable. Gap variations can be noticed at higher temperatures, with a sharp increase for 2.10  $\text{J}/\text{cm}^2$  between 500°C and 600°C, followed by a drop above 600°C. The evolution is less contrasted at 2.30  $\text{J}/\text{cm}^2$ , with a continuous gap decrease above 500°C. For sample C, the gap increases at both energy densities above 700°C. As mentioned previously, a gap increase can be associated with a boron deactivation or Ge-enrichment via thermal oxidation. These effects are however unexpected at low temperature: the increase near 500-600°C cannot be explained yet. The decrease observed in all samples highlights a reduction of the SiGe lattice parameter. This is unlikely to be related to additional boron incorporation, as samples A and B already presented full activation after NLA at 2.10 and 2.30  $\text{J}/\text{cm}^2$ . It can however be caused by relaxation in the layers. In contrast, the gap increase in sample C above 700°C may be related to the onset of thermal oxidation, or boron deactivation and diffusion in depth.

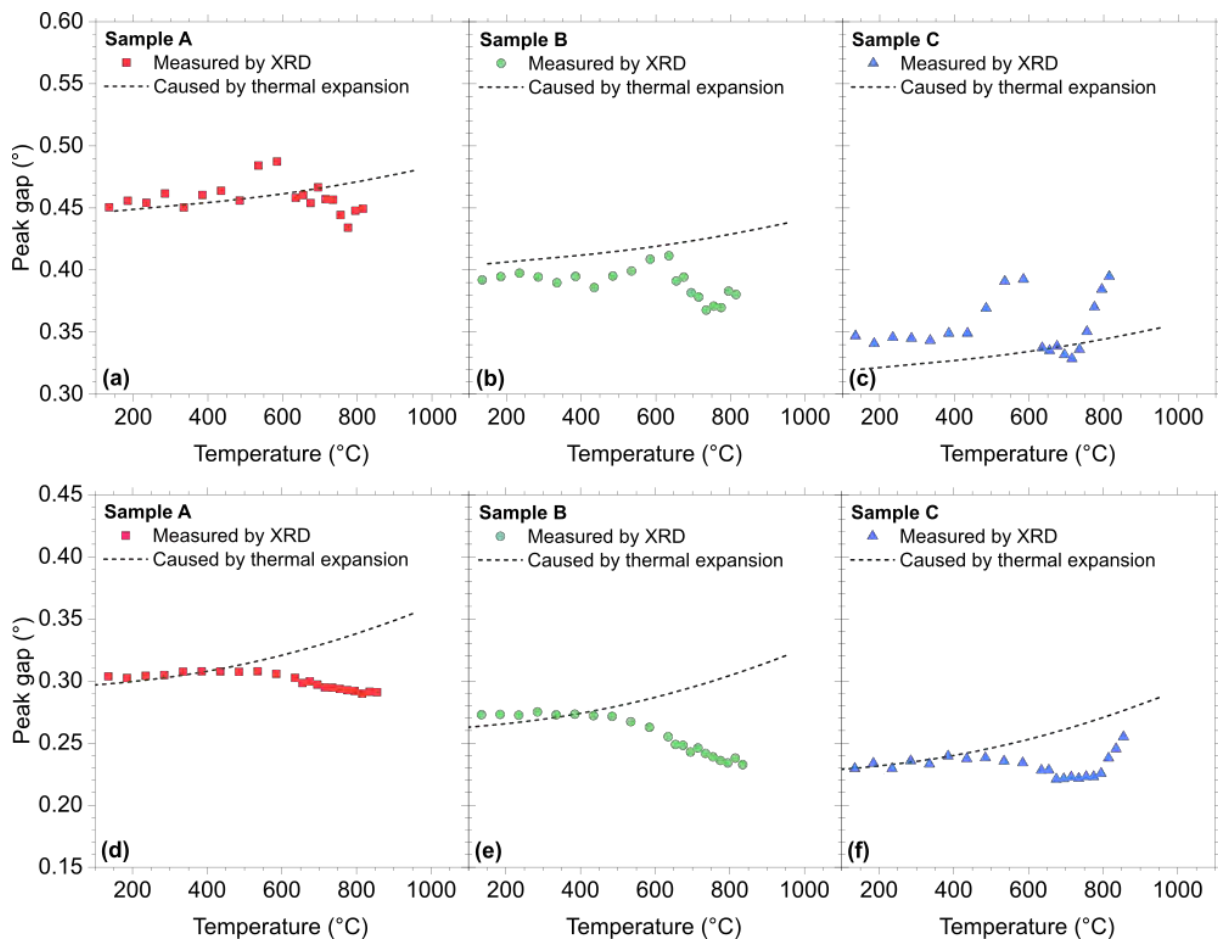


Figure V - 20. Angular gap observed between the Si peak and SiGe peak as a function of temperature for samples A (a,d), B (b,e) and (c,f) after laser annealing at 2.10  $\text{J}/\text{cm}^2$  and 2.30  $\text{J}/\text{cm}^2$ . A grey line presents the expected evolution of the gap when only thermal expansion is taken into account.

In summary, samples submitted to laser annealing at 2.10 and 2.30  $\text{J}/\text{cm}^2$  and subsequently submitted to in-situ XRD measurements up to 950°C exhibit similar structural evolutions for a given boron level, though they widely differ from the observations on samples

without laser annealing. It is therefore believed that the physical phenomena leading to these results are identical for both energy densities.

ii.  $R_s$  evolution upon subsequent furnace anneal

Furnace anneals were performed on samples strips after laser annealing, to measure the sheet resistance. Figure V-22 displays  $R_s$  as a function of the anneal temperature for the three initial doping levels (A, B and C) and the two laser treatment conditions. The evolution of the sheet resistance with increasing furnace anneal temperature will be described simultaneously for samples annealed at 2.10 and 2.30  $\text{J}/\text{cm}^2$ , as they appear to follow similar tendencies. Up to 600°C, the sheet resistance variations can be considered as negligible for all samples, as they fall in the range indicated in Table V - 1 for each sample. From 600°C to 850°C, a clear decrease in sheet resistance is observed, with a more pronounced change in layers with less incorporated boron (sample A). Divergences depending on the boron concentration can be noticed once again above 900°C: sample A presents an increase in sheet resistance, while it decreases or remains stable in samples B and C.

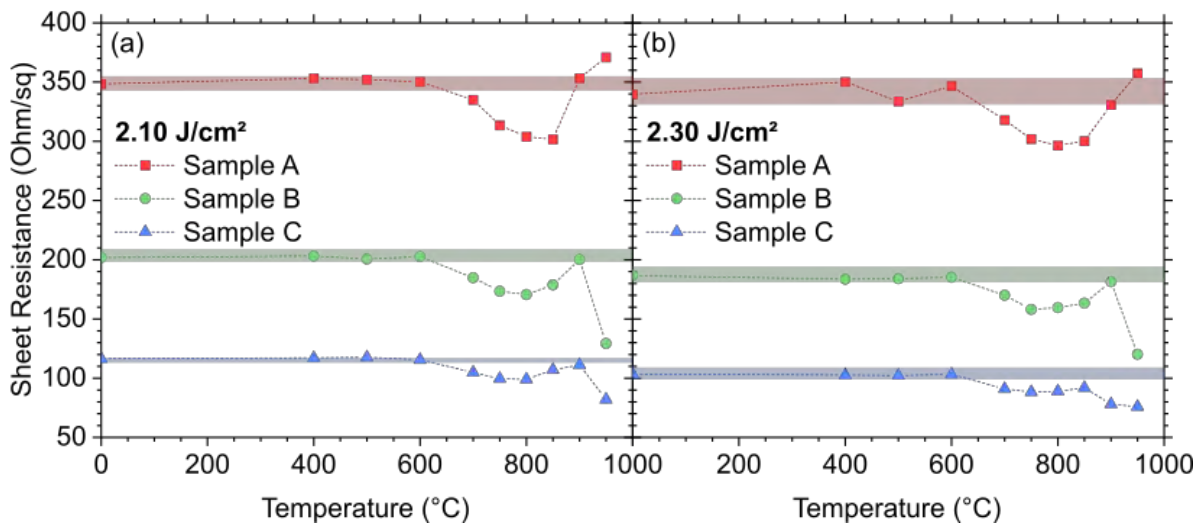


Figure V - 21. Sheet resistance as a function of furnace anneal temperature for samples previously laser annealed at 2.10  $\text{J}/\text{cm}^2$  (a) and 2.30  $\text{J}/\text{cm}^2$  (b). The color bands respectively indicate the variations observed on the initial samples for the three doping levels (see Table V-1).

The laser annealed samples are considered electrically stable up to 600°C. The sudden drop in sheet resistance in the 700-800°C range remains unexplained, as boron diffusion is unlikely to occur over large distances at these temperatures. It could either be due to healing of remaining crystalline defects, or to additional boron activation. This would suggest that the total boron dose observed by SIMS measurement is incomplete for the samples annealed at 2.10 and 2.30  $\text{J}/\text{cm}^2$ , and requires further investigation. In the 900-950°C temperature range, the behavior seems to be similar to the as-epi samples, and to result from a trade-off between deactivation to reach the solid solubility limit and dopant diffusion/activation in depth.

Complete understanding of the deactivation phenomena in laser annealed boron-doped layers will require more extended studies. In particular, it seems necessary to obtain the chemical distribution of boron and Ge at various temperatures, to evaluate the impact of possible thermal oxidation during in-situ XRD experiments (not furnace anneals) and boron diffusion. This may allow distinguishing these effects for temperatures above 700°C, as they both reduce the perpendicular lattice parameter and could not be separated with the use of  $\omega$ -2 $\theta$  scans. The assessment of the layer quality should be performed with Reciprocal Space Maps for a set of selected samples, while XRR may enable to evaluate the oxide thickness in case of

thermal oxidation. Additional anneals may be performed with longer and shorter durations, to evaluate the stability.

The laser annealed samples are considered electrically stable up to  $600^{\circ}\text{C}$ , which is already technologically very interesting in view of 3D sequential integration in which the maximum acceptable temperature is about  $500^{\circ}\text{C}$  with classical thermal treatments (duration  $> 1$  second). Both laser-annealed samples followed a similar evolution with increasing temperature: though the exact origins of modifications remain unclear, they seem to be caused by competition between deactivation, relaxation and boron diffusion.

## CONCLUSION

Boron activation in  $\text{Si}_{0.7}\text{Ge}_{0.3}$  layers with nanosecond laser annealing was studied under various conditions. Three in-situ doping boron concentrations were assessed, named A, B and C, with total dopants concentrations near  $7.8 \times 10^{19}$ ,  $1.4 \times 10^{20}$  and  $2.4 \times 10^{20}$  B/cm<sup>3</sup>, respectively.

A laser annealing study, performed with a chuck at room temperature has shown that the electrical properties (sheet resistance and activation levels) are highly dependent on the layer quality, and that part of the dopants are deactivated in regimes leading to poor crystalline quality. This can be compensated by additional activation in layers with very high boron concentration. The highest active doses were obtained for layers with chemical boron concentration above  $10^{20}$  cm<sup>-3</sup>, that were annealed in the full melt regime. In these cases, the active dose was superior to what was obtained by the epitaxy. In terms of dopant activation, the best case is a layer with high boron concentration, annealed at the limit between partial and full melt: this forms a fully strained layer, with high Ge content near the surface and high active boron levels.

It was found that the heating chuck or anneals with multi-pulse did not offer any advantages for dopant activation in pseudomorphic SiGe layers. It however appears that annealing in the sub-melt regime improves the sheet resistance for amorphized layers.

Furnace anneals up to 950°C were performed to study the stability of these layers when submitted to additional thermal budget. This was done with samples that showed good crystalline quality after laser annealing at 2.10 and 2.30 J/cm<sup>2</sup>, as well as samples without laser anneal for comparison. The furnace anneals lasted for 20 minutes at the chosen temperature. It was shown that the SiGe layers are electrically stable up to 600°C, though morphological changes may occur at temperatures as low as 500°C in laser annealed samples. At higher temperatures, multiple variations in sheet resistance are observed. These variations are likely due to competition between several effects, including dopant deactivation, relaxation, thermal oxidation and dopant diffusion into the Si substrate and reactivation. A clear understanding will however require additional studies based on the crystalline quality and dopant diffusion.

KEY INFORMATION

<p><b>BORON ACTIVATION</b></p> <p>1. Boron redistribution</p> <p>2. Activation in each regime</p> <p>3. Amorphous layers</p>	<p>Evolution with the annealing regimes and layer quality</p> <ul style="list-style-type: none"> <li>➔ Boron concentration in the <math>7.8 \times 10^{19}</math> - <math>2.4 \times 10^{20}</math> B/cm<sup>3</sup> range</li> <li>➔ Modified boron distribution after laser annealing             <ul style="list-style-type: none"> <li>○ Pile-up near the melt depth</li> <li>○ Depletion near the surface with possible out-diffusion</li> <li>○ Similar to the results on Si and Ge</li> </ul> </li> <li>➔ Depends on the crystalline quality and boron concentration             <ul style="list-style-type: none"> <li>○ Active dose reduces in layers with crystalline defects</li> <li>○ Can be compensated by additional activation in layers where part of the boron was initially inactive</li> </ul> </li> <li>➔ Lower sheet resistance are obtained in the full melt regime</li> <li>➔ Multi-pulse annealing does not offer any advantages</li> <li>➔ Sheet resistance value reduces in the submelt regime and explosive melt regime</li> <li>➔ Similar to the pseudomorphic samples in other regimes</li> </ul>
<p><b>DEACTIVATION IN FURNACE</b></p> <p>1. As-epi samples</p> <p>2. Laser annealed samples</p>	<p>Sheet resistance evolution during 20 minutes anneals up to 950°C</p> <ul style="list-style-type: none"> <li>➔ Stable up to 600°C</li> <li>➔ Sheet resistance variations above 600°C             <ul style="list-style-type: none"> <li>○ Deactivation of boron above the solid solubility limit</li> <li>○ Additional activation and diffusion</li> </ul> </li> <li>➔ Electrically stable up to 600°C</li> <li>➔ Origin of variations at higher temperatures still unclear</li> </ul>

## BIBLIOGRAPHY

- [1] T. Clarysse, D. Vanhaeren, W. Vandervorst, Impact of probe penetration on the electrical characterization of sub-50 nm profiles, *J. Vac. Sci. Technol. B Microelectron. Nanometer Struct. Process. Meas. Phenom.* 20 (2002) 459–466. <https://doi.org/10.1116/1.1432965>.
- [2] H.-U. Ehrke, H. Maul, Quantification of Ge and B in SiGe using secondary ion mass spectrometry, *Mater. Sci. Semicond. Process.* 8 (2005) 111–114. <https://doi.org/10.1016/j.mssp.2004.09.059>.
- [3] G. Masetti, Relationship between carrier mobility and electron concentration in silicon heavily doped with phosphorus, 3 (n.d.) 4.
- [4] R. Daubriac, Characterization of alternative ion implantation techniques for the optimization of the source-drain module of FDSOI 28 nm technology, Theses, INSA de Toulouse, 2018. <https://hal.laas.fr/tel-02087031> (accessed June 29, 2020).
- [5] M. Labrot, F. Cheynis, D. Barge, M. Juhel, P. Müller, Improvement of Boron Doping in SiGe Raised Sources and Drains for FD-SOI Technology by Carbon Incorporation, *ECS Trans.* 75 (2016) 29. <https://doi.org/10.1149/07508.0029ecst>.
- [6] J.M. Hartmann, M. Veillerot, HCl  $\text{GeH}_4$  etching for the low temperature cyclic deposition/etch of Si, Si:P, tensile-Si:P and SiGe(:B), *Semicond. Sci. Technol.* 35 (2019) 015015. <https://doi.org/10.1088/1361-6641/ab52ec>.
- [7] M. Shayesteh, D.O. Connell, F. Gity, P. Murphy-Armando, R. Yu, K. Huet, I. Toqué-Tresonne, F. Cristiano, S. Boninelli, H.H. Henrichsen, P.F. Nielsen, D.H. Petersen, R. Duffy, Optimized Laser Thermal Annealing on Germanium for High Dopant Activation and Low Leakage Current, *IEEE Trans. Electron Devices.* 61 (2014) 4047–4055. <https://doi.org/10.1109/TED.2014.2364957>.
- [8] M. Hackenberg, K. Huet, R. Negru, J. Venturini, G. Fisicaro, A. La Magna, P. Pichler, Modeling boron profiles in silicon after pulsed excimer laser annealing, *AIP Conf. Proc.* 1496 (2012) 241–244. <https://doi.org/10.1063/1.4766533>.
- [9] F. Cristiano, M. Shayesteh, R. Duffy, K. Huet, F. Mazzamuto, Y. Qiu, M. Quillec, H.H. Henrichsen, P.F. Nielsen, D.H. Petersen, A. La Magna, G. Caruso, S. Boninelli, Defect evolution and dopant activation in laser annealed Si and Ge, *Mater. Sci. Semicond. Process.* 42 (2016) 188–195. <https://doi.org/10.1016/j.mssp.2015.09.011>.
- [10] R. Milazzo, G. Impellizzeri, D. Piccinotti, A. La Magna, G. Fortunato, D. De Salvador, A. Carnera, A. Portavoce, D. Mangelinck, V. Privitera, E. Napolitani, Impurity and defect interactions during laser thermal annealing in Ge, *J. Appl. Phys.* 119 (2016) 045702. <https://doi.org/10.1063/1.4940737>.
- [11] G. Fisicaro, K. Huet, R. Negru, M. Hackenberg, P. Pichler, N. Taleb, A. La Magna, Anomalous Impurity Segregation and Local Bonding Fluctuation in I-Si, *Phys. Rev. Lett.* 110 (2013) 117801. <https://doi.org/10.1103/PhysRevLett.110.117801>.
- [12] G. Impellizzeri, E. Napolitani, R. Milazzo, S. Boninelli, M. Cuscunà, G. Fisicaro, A. La Magna, G. Fortunato, F. Priolo, V. Privitera, Role of oxygen on the electrical activation of B in Ge by excimer laser annealing, *Phys. Status Solidi A.* 211 (2014) 122–125. <https://doi.org/10.1002/pssa.201300308>.
- [13] G. Rengo, C. Porret, A.Y. Hikavy, E. Rosseel, N. Nakazaki, G. Pourtois, A. Vantomme, R. Loo, (Invited) Highly Doped Si<sub>1-x</sub>Ge<sub>x</sub> Epitaxy in View of S/D Applications, *ECS Trans.* 98 (2020) 27. <https://doi.org/10.1149/09805.0027ecst>.

- [14] P.M. Mooney, Strain relaxation and dislocations in SiGe/Si structures, *Mater. Sci. Eng. R Rep.* 17 (1996) 105–146. [https://doi.org/10.1016/S0927-796X\(96\)00192-1](https://doi.org/10.1016/S0927-796X(96)00192-1).
- [15] F. Severac, F. Cristiano, E. Bedel-Pereira, P.F. Fazzini, J. Boucher, W. Lerch, S. Hamm, Influence of boron-interstitials clusters on hole mobility degradation in high dose boron-implanted ultrashallow junctions, *J. Appl. Phys.* 107 (2010) 123711. <https://doi.org/10.1063/1.3446844>.
- [16] S.C. Jain, W. Schoenmaker, R. Lindsay, P.A. Stolk, S. Decoutere, M. Willander, H.E. Maes, Transient enhanced diffusion of boron in Si, *J. Appl. Phys.* 91 (2002) 8919–8941. <https://doi.org/10.1063/1.1471941>.
- [17] C.Y. Chang, F.A. Khaja, K.E. Hollar, K.V. Rao, C. Lazik, M. Jin, H. Zhou, R. Hung, Y.C. Huang, H. Chung, A. Mayur, N. Kim, Ultra-low (1.2E-9 ohmcm<sup>2</sup>) p-Si<sub>0.55</sub>Ge<sub>0.45</sub> contact resistivity using nanosecond laser anneal for 7nm nodes and beyond, in: 2017 17th Int. Workshop Junction Technol. IWJT, 2017: pp. 23–26. <https://doi.org/10.23919/IWJT.2017.7966504>.
- [18] K.C. Saraswat, G. Shine, (Invited) Low Resistance Contacts to Nanoscale Semiconductor Devices, *ECS Trans.* 75 (2016) 513. <https://doi.org/10.1149/07508.0513ecst>.
- [19] C.N. Ni, Y.C. Huang, S. Jun, S. Sun, A. Vyas, F. Khaja, K.V. Rao, S. Sharma, N. Breil, M. Jin, C. Lazik, A. Mayur, J. Gelatos, H. Chung, R. Hung, M. Chudzik, N. Yoshida, N. Kim, PMOS contact resistance solution compatible to CMOS integration for 7 nm node and beyond, in: 2016 Int. Symp. VLSI Technol. Syst. Appl. VLSI-TSA, 2016: pp. 1–2. <https://doi.org/10.1109/VLSI-TSA.2016.7480531>.
- [20] P. Acosta Alba, J. Aubin, S. Perrot, F. Mazzamuto, A. Grenier, S. Kerdilès, Solid phase recrystallization induced by multi-pulse nanosecond laser annealing, *Appl. Surf. Sci. Adv.* 3 (2021) 100053. <https://doi.org/10.1016/j.apsadv.2020.100053>.
- [21] Y. Takamura, S.H. Jain, P.B. Griffin, J.D. Plummer, Thermal stability of dopants in laser annealed silicon, *J. Appl. Phys.* 92 (2002) 230–234. <https://doi.org/10.1063/1.1481975>.
- [22] W. Luo, S. Yang, P. Clancy, M.O. Thompson, Deactivation kinetics of supersaturated boron:silicon alloys, *J. Appl. Phys.* 90 (2001) 2262–2268. <https://doi.org/10.1063/1.1385360>.
- [23] T. Tezuka, N. Sugiyama, T. Mizuno, M. Suzuki, S. Takagi, A Novel Fabrication Technique of Ultrathin and Relaxed SiGe Buffer Layers with High Ge Fraction for Sub-100 nm Strained Silicon-on-Insulator MOSFETs, *Jpn. J. Appl. Phys.* 40 (2001) 2866. <https://doi.org/10.1143/JJAP.40.2866>.
- [24] F. Rozé, O. Gourhant, E. Blanquet, F. Bertin, M. Juhel, F. Abbate, C. Pribat, R. Duru, Oxidation kinetics of Si and SiGe by dry rapid thermal oxidation, in-situ steam generation oxidation and dry furnace oxidation, *J. Appl. Phys.* 121 (2017) 245308. <https://doi.org/10.1063/1.4987040>.
- [25] B.E. Deal, A.S. Grove, General Relationship for the Thermal Oxidation of Silicon, *J. Appl. Phys.* 36 (1965) 3770–3778. <https://doi.org/10.1063/1.1713945>.
- [26] Y. Okada, Y. Tokumaru, Precise determination of lattice parameter and thermal expansion coefficient of silicon between 300 and 1500 K, *J. Appl. Phys.* 56 (1984) 314–320. <https://doi.org/10.1063/1.333965>.
- [27] M.E. Levinshteĭn, S.L. Romyantsev, M. Shur, *Properties of advanced semiconductor materials: GaN, AlN, InN, BN, SiC, SiGe*, Wiley, New York, 2001.

- [28] Y. Takamura, P.B. Griffin, J.D. Plummer, Physical processes associated with the deactivation of dopants in laser annealed silicon, *J. Appl. Phys.* 92 (2002) 235–244. <https://doi.org/10.1063/1.1481974>.
- [29] F. Cristiano, N. Cherkashin, P. Calvo, Y. Lamrani, X. Hebras, A. Claverie, W. Lerch, S. Paul, Thermal stability of boron electrical activation in preamorphised ultra-shallow junctions, *Mater. Sci. Eng. B.* 114–115 (2004) 174–179. <https://doi.org/10.1016/j.mseb.2004.07.049>.
- [30] F. Cristiano, Y. Lamrani, F. Severac, M. Gavelle, S. Boninelli, N. Cherkashin, O. Marcelot, A. Claverie, W. Lerch, S. Paul, N. Cowern, Defects evolution and dopant activation anomalies in ion implanted silicon, *Nucl. Instrum. Methods Phys. Res. Sect. B Beam Interact. Mater. At.* 253 (2006) 68–79. <https://doi.org/10.1016/j.nimb.2006.10.046>.
- [31] M. Spadafora, G. Privitera, A. Terrasi, S. Scalese, C. Bongiorno, A. Carnera, M. Di Marino, E. Napolitani, Oxidation rate enhancement of SiGe epitaxial films oxidized in dry ambient, *Appl. Phys. Lett.* 83 (2003) 3713–3715. <https://doi.org/10.1063/1.1622439>.

---

## CONCLUSION

This work aimed to unify and complete the knowledge on the impact of UltraViolet Nanosecond Laser Annealing (UV-NLA) of  $\text{Si}_{1-x}\text{Ge}_x$  layers, by detailing the various phenomena caused by the annealing and their dependence on the layer properties. Systematic characterizations were used to establish the annealing regimes and how they affect the surface roughness, the crystalline structure, the chemical distribution and the strain state, on  $\text{Si}_{1-x}\text{Ge}_x$  layers with content up to 40% and thicknesses up to 45 nm.

The first chapter described the context of this study, starting with the MOSFET transistor and how its shrinking has influenced the materials, processes and architectures used. The formation of smaller devices requires the formation of highly doped shallow junctions: annealing processes evolved toward shorter duration and higher temperatures. In addition, source and drain regions formed with SiGe were introduced to add strain into the Si channel, improving the electrical properties. UV-NLA is a promising method which enables annealing at very high temperature near the surface while keeping the bulk material at low temperature. As the anneal duration is in the nanosecond time-scale, diffusion is almost suppressed in the solid regions and can notably occur in liquid layers. Numerous studies of NLA Si and Ge materials were performed in the previous years, showing that monocrystalline layers with high dopant activation rates, above the solid solubility limits, can be obtained. The results on SiGe layers were also presented, and highlighted the lack of understanding on the origin of relaxation and on the dopant activation.

The second chapter presented the samples and characterization methods. Four series of samples were defined, each with distinct varying parameters, either Ge composition, thickness, boron concentration or the presence of amorphous materials. Most of these layers were initially pseudomorphic, to limit the impact of pre-existing defects. These samples were submitted to UV-NLA with an LT3100 tool from SCREEN-LASSE, with a 160 ns pulse duration and a 308 nm wavelength. A wide range of energy densities was used for each sample, in order to study multiple annealing regimes, from sub-melt to full melt. These samples were then studied by multiple characterizations methods, to gain insight on their surface quality, chemical composition, strain state and electrical properties. An in-situ characterization method, Time-Resolved Reflectometry, enables the recording of a signal proportional to the reflectivity during the anneal. The surface roughness study relies on Haze, Atomic Force Microscopy and occasionally Scanning Electron Microscopy, as the laser in melt conditions is known to modify the surface roughness. Secondary Ion Mass Spectrometry and Energy-Dispersive X-Ray were used to detect the chemical distribution within the samples, highlighting the changes brought by the liquid phase. The strain relaxation study was performed primarily with X-Ray diffraction, and completed with Transmission Electron Microscopy (TEM). Finally, boron doped samples were studied by means of Four Point Probe and Hall effect measurements.

The third chapter first focused on the various annealing regimes, and how they can be distinguished. Several regimes were defined in initially pseudomorphic layers thanks to changes in surface quality, Ge distribution and layer reflectivity: the sub-melt, the surface melt, the partial melt and the full melt regimes. In amorphous layers, the explosive regime, observed before the surface melt, was reached due to the lower melt temperature of the amorphous phase. The sub-melt regime did not show any change compared to as-epi samples, though the layers reached high temperatures. The surface melt regime was distinguished by a sudden increase in surface roughness, caused by the formation of isolated molten islands. These islands grew and merged by increasing the laser energy density, to finally cover the complete surface at the end of this regime. This behavior was observed even in pure Si or Ge, but the shape and size were influenced by the Ge content and might be related to strain effects. In SiGe, these isolated structures were clearly identified as molten islands, as the Ge segregation enabled to

distinguished melted and unmelted areas with STEM-HAADF. Afterwards, the partial melt regime was characterized by a smooth surface, a continuous liquid layer and a melt depth within the initial SiGe layer. This regime exhibited strong Ge segregation, with the formation of a Ge-rich layer near the surface, well above 50 at.% Ge in some cases. The presence of a rough liquid/solid interface in these regimes was inferred from both EDX and SIMS measurements, and was attributed to a lingering effect of the isolated molten islands formation at the onset of melt. Additionally, the interface was observed to smoothen as the melt depth reached the SiGe/Si interface. Finally, the full melt was defined as the regime where the liquid/solid interface reaches the initial SiGe/Si interface. In that case, the Ge was observed to redistribute in depth, forming thicker SiGe layers with an overall lower Ge content. The effect of the Ge segregation were however still observed, with much higher Ge levels near the surface. This regime also exhibited smooth liquid/solid interfaces. The regimes transitions and durations were shown to be modified by the Ge content or the layer thicknesses, as the melt temperature and thermal properties of the stack are modified. Time-Resolved reflectometry was proven to be a powerful tool for the in-situ study of these layers, giving insight on the regime transitions as well as on the kinetics of melt and solidification processes.

The fourth chapter was dedicated to the strain relaxation observed in laser annealed SiGe layers, and aimed to offer a unified understanding. It relied mainly on X-Ray diffraction and TEM observations. It was shown that the formation of strain relieving defects in SiGe layers was caused by either the presence of a rough liquid/solid interface or excessive stored elastic energy. In regimes where a rough liquid/solid interface was observed (i.e. surface and partial melt regimes), most samples exhibited partial relaxation near 30%, as the rough interface facilitated the formation of defects. In layers with high elastic energy (thicker layers or with higher Ge content), full relaxation could be observed. On the contrary, pseudomorphic layers were observed when layers presented a smooth liquid/solid interface (i.e. at the end of partial melt or in full melt regimes) and elastic energy below 750 mJ/m<sup>2</sup>. Layers with smooth interface and elastic energy above this 750 mJ/m<sup>2</sup> were found to form bilayers, with a relaxed upper region and strained lower region. Elastic energy calculations, based on the chemical profiles, indicated that the elastic energy increased due to the formation of a Ge gradient by the segregation, and the highest value is reached at the end of the partial melt regime. The relaxation behavior in amorphized or boron-doped layers was consistent with these results, though the boron presence was shown to reduce the relaxation. This enabled the formation of boron doped pseudomorphic layers at lower laser energy densities.

The final chapter focused on boron-doped Si<sub>0.7</sub>Ge<sub>0.3</sub> layers, to highlight the activation evolution with the regimes, and evaluate the stability of these layers when submitted to subsequent furnaces anneals. The boron was introduced during the layer growth, with three chemical boron concentration in the  $7.3 \times 10^{19}$  to  $2.4 \times 10^{20}$  cm<sup>-3</sup> range. The layer with the lowest concentration was fully activated in the as-epi sample. NLA caused a redistribution of both the Ge and the B in the layer: the Ge segregated toward the surface as expected, while the boron formed a pile-up near the maximum depth of the liquid/solid interface and a depletion near the surface, which is consistent with the known profiles in Si and Ge. The active dose after laser annealing was shown to highly depend on the crystalline quality, as the strain relieving defects are responsible for boron deactivation. In highly doped layers, this effect can be compensated by activation of initially inactive dopants. The highest activation and lowest sheet resistance were observed in the full melt regime, when a pseudomorphic layer was formed. When submitted to additional 20 minutes-long furnace anneals, the sheet resistance of samples in the full melt regime was stable up to 600°C for all dopant concentrations. These samples can therefore be used in devices and remain stable if the processes performed afterwards remain under 600°C. At higher temperatures, many changes in sheet resistance are observed, and can be attributed to a competition between various phenomena, including relaxation, dopant deactivation and additional activation due to diffusion and cluster dissolution. As these effects

are not fully understood yet in laser-annealed SiGe layers and may have a critical impact on devices, they should be further documented. In-depth studies of the crystalline quality and of boron and Ge diffusion at high temperature will be necessary for a complete understanding.

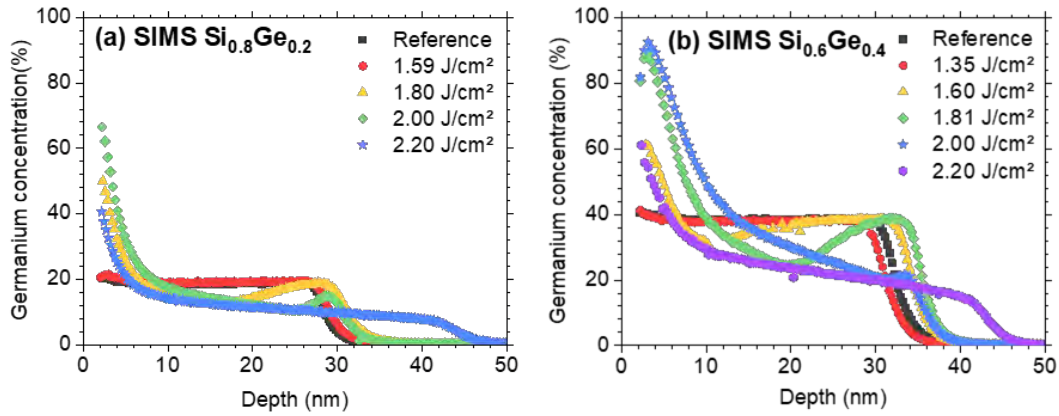
This work has highlighted many of the morphological and electrical changes brought by NLA in SiGe layers. There is however numerous additional studies that can be performed to gain a complete understanding of these phenomena. In particular, the origin of the surface structures during the surface melt regime can be studied at higher Ge contents, and at other wavelengths. Regarding the strain relaxation, we suggest further studying of the I/s interface smoothing, in particular in the presence of boron. It might also be worth to study the relaxation of Ge-rich SiGe layers grown on Ge virtual substrates, to compare the relaxation mechanisms, as well as the kinetics during melt and solidification. The investigation of dopant activation by NLA must also be completed and include activation of ion implanted dopants, in particular boron and gallium, as well as their deactivation. Finally, the transfer and adaptation of these concepts to patterned wafers is a key-step to produce future devices.

---

# APPENDICES

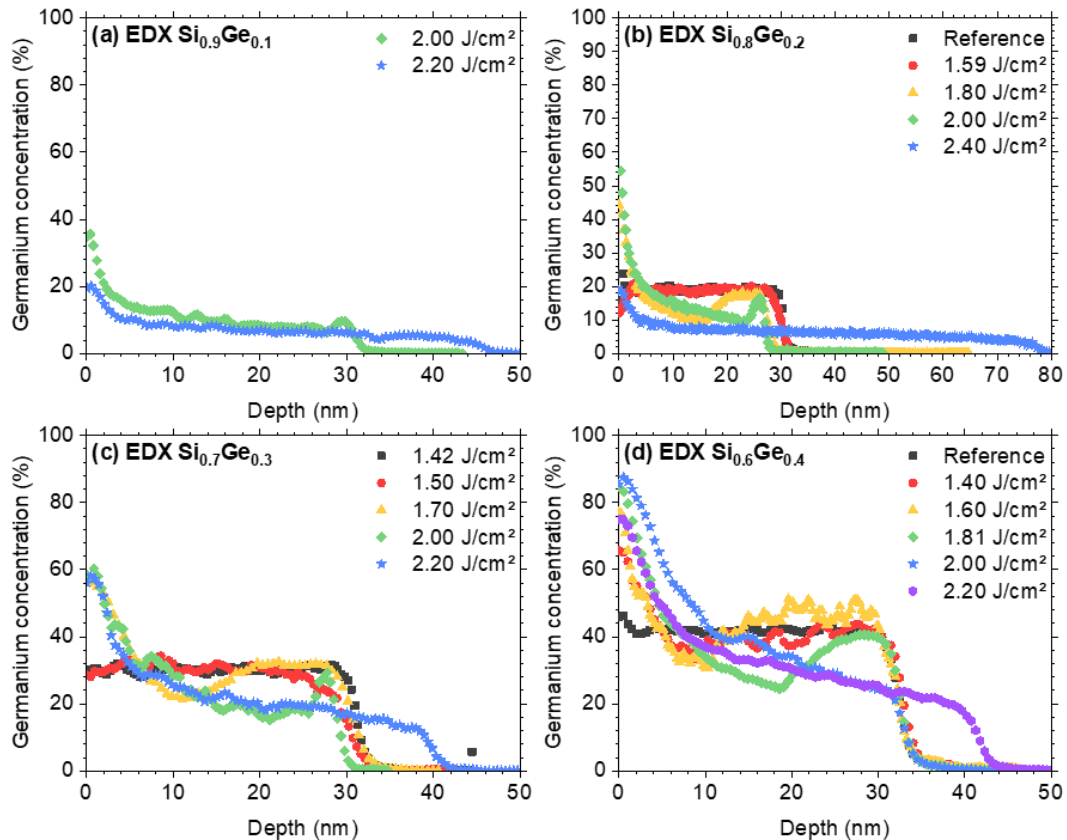
APPENDIX I – GERMANIUM PROFILES

This document presents every Ge depth profile obtained and used for the study of UV-NLA on crystalline SiGe layers. The various annealed samples have shown similar characteristic with increasing energy density, whether the measurements are performed with ToF-SIMS or EDX. SIMS and EDX profiles on 30 nm-thick samples are shown in Appendix I - 1 and Appendix I - 2.



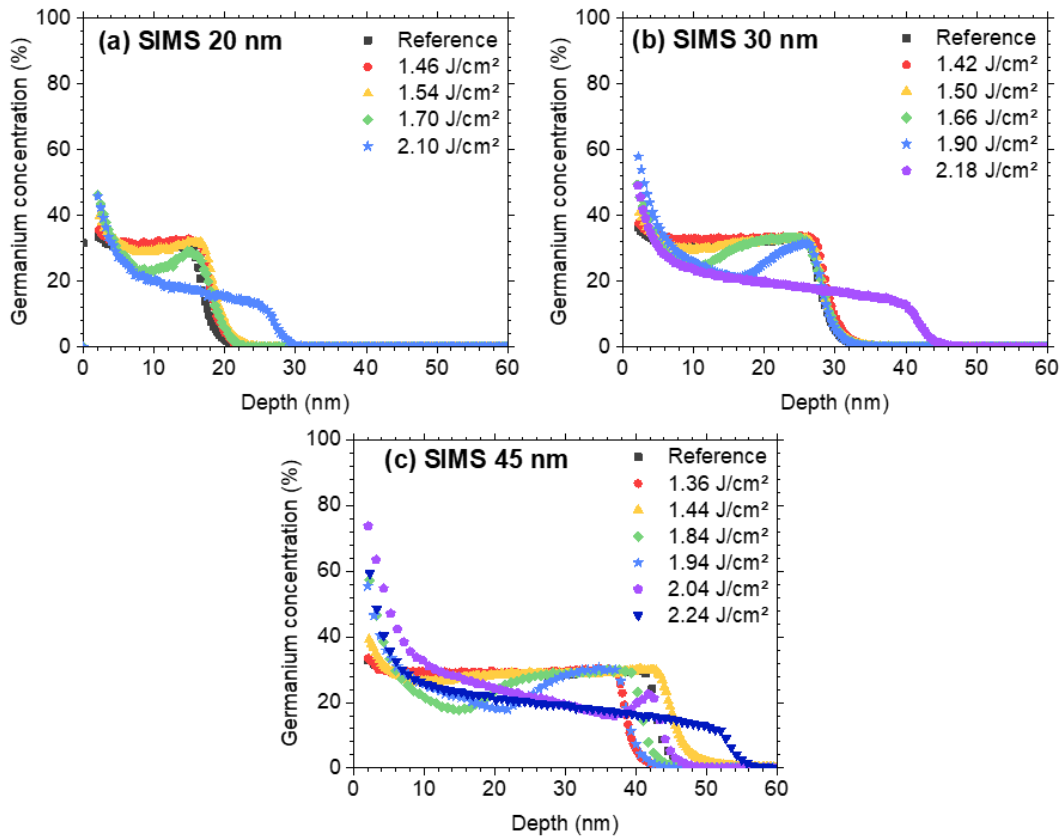
Appendix I - 1. SIMS germanium profiles after UV-NLA on 30 nm-thick Si<sub>0.8</sub>Ge<sub>0.2</sub> (a) and Si<sub>0.6</sub>Ge<sub>0.4</sub> (b) layers.

The observed melt depths are close for both methods, though the interfaces appear sharper for EDX profiles. It can also be noticed that the EDX profiles present more noise due to smaller studied areas. This is especially true for the Si<sub>0.6</sub>Ge<sub>0.4</sub> annealed at 1.40 and 1.60 J/cm<sup>2</sup>, as the profiles were taken on isolated molten islands.



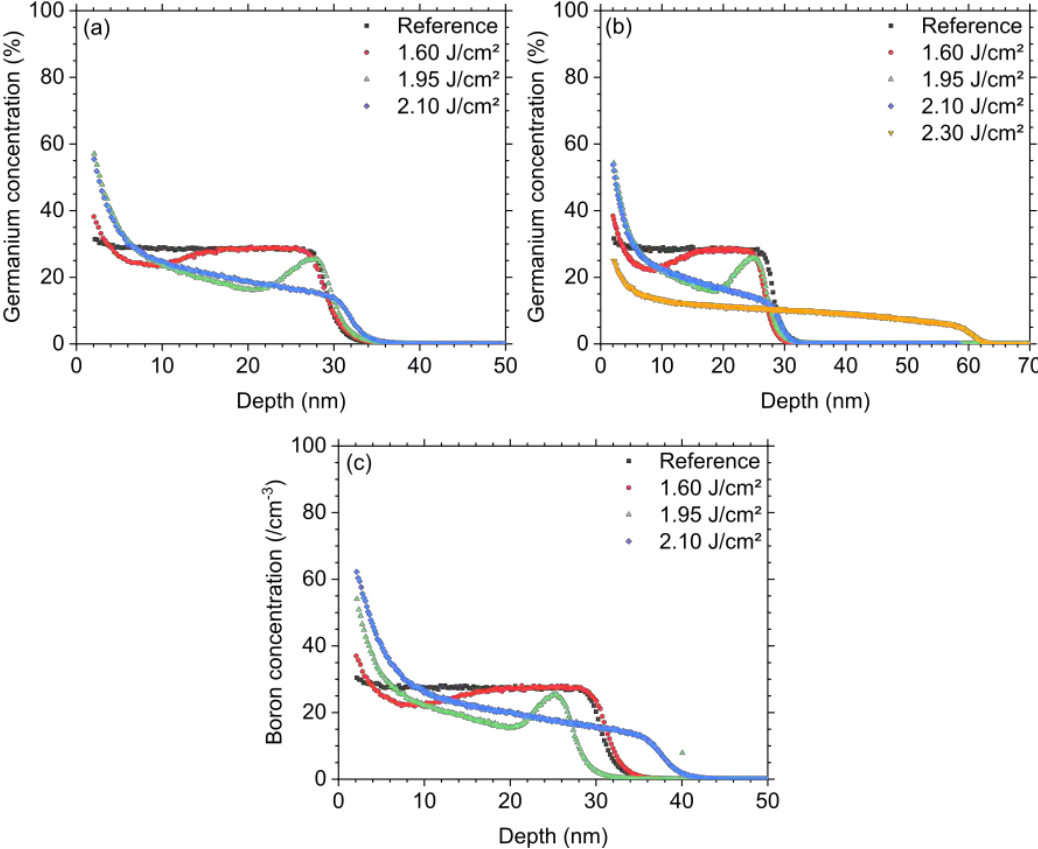
Appendix I - 2. EDX germanium profiles after UV-NLA on 30 nm-thick Si<sub>0.9</sub>Ge<sub>0.1</sub> (a), Si<sub>0.8</sub>Ge<sub>0.2</sub> (b), Si<sub>0.7</sub>Ge<sub>0.3</sub> (c) and Si<sub>0.6</sub>Ge<sub>0.4</sub> (d) layers.

SIMS profiles for layers with various thicknesses are shown in Appendix I - 3, and present a similar behavior: segregation occurs as soon as the layer reaches its melt threshold. Higher energy densities lead to deeper melt depths and cause a more pronounced Ge redistribution, with a Ge-Rich surface. Finally, the full melt leads to a redistribution of Ge in depth. The full melt regime was reached slightly earlier for thinner layers, even though the thickest layer had a lower melt threshold. Variations in layer thickness are observed for the 45 nm-thick layer, and may be due to the thickness non-uniformities in the as-epi layer.



Appendix I - 3. SIMS germanium profiles after UV-NLA on 20 nm (a), 30 nm (b) and 45 nm (c) thick Si<sub>0.7</sub>Ge<sub>0.3</sub> layers.

Finally, germanium profiles for doped layers are presented in Appendix I - 4 for three boron-doping levels. All three have almost identical profiles up to 1.95 J/cm<sup>2</sup>, with melt depth near the bottom of the SiGe layer. There are a few differences observed at 2.10 J/cm<sup>2</sup>: the full melt seems to be reached for all samples, with a deeper melt depth for the highest boron-doping level (c). This may be due to differences in thermal properties.



Appendix I - 4. SIMS germanium profiles after UV-NLA on boron-doped 30 nm-thick Si<sub>0.7</sub>Ge<sub>0.3</sub> layers with low (a), medium (b) or high (c) boron content.

---



# COMPORTEMENT DE COUCHES $Si_{1-x}Ge_x$ SOUMISES AU RECUIIT LASER NANOSECONDE

## INTRODUCTION

La miniaturisation des composants électroniques complexifie leur fabrication, et oblige à faire évoluer leur architecture, ainsi que les matériaux utilisés, pour conserver un bon contrôle sur les propriétés électroniques. Cela a conduit à de multiples changements, en particulier concernant le canal de conduction et la grille des transistors. L'une des évolutions utilisées aujourd'hui pour améliorer la mobilité des porteurs dans un canal Si est l'introduction d'une contrainte uniaxiale. Celle-ci est obtenue avec la croissance de zones source et drain en SiGe contraint, autour du canal. Il est en revanche nécessaire que ces jonctions soient ultra-fines et fortement dopées, ce qui est rendu possible par l'utilisation de recuits thermiques à très haute température pour des durées limitées. Cela permet d'activer les dopants présents dans la couche tout en limitant leur diffusion en profondeur. Les méthodes actuelles utilisent des recuits de l'ordre de la milliseconde, et évoluent vers des recuits proches de la nanoseconde. Le recuit laser nanoseconde est une technique prometteuse, car elle permet d'atteindre des températures extrêmement élevées, uniquement à la surface du matériau. Des études sur Si et Ge ont montré que cette méthode peut faire fondre une fine couche de matériau à la surface, qui peut ensuite recroître en formant une couche monocristalline, selon les conditions. Grâce à la très faible durée de recuit, les dopants n'ont pas le temps de diffuser dans la phase solide, alors qu'ils peuvent diffuser en phase liquide. Cela permet d'incorporer de très grandes concentrations de dopants dans le matériau, au-delà des limites de solubilité solide. Cette méthode reste en revanche trop peu connue pour le SiGe, et de nombreuses interrogations persistent sur l'évolution de la contrainte et sur l'activation des dopants.

Ce travail se consacre donc à l'étude de l'impact du recuit laser nanoseconde sur des couches de SiGe, et s'attache tout d'abord à distinguer les caractéristiques des différents régimes de recuit. Dans un second temps, il détaille l'évolution de la contrainte dans les différents régimes, et explique à quoi elle est due. Enfin, l'activation du bore dans le SiGe est étudiée, ainsi que sa stabilité lors de recuits postérieurs.

## I – LE RECUIIT LASER NANOSECONDE EN MICROELECTRONIQUE

### 1. Evolutions des dispositifs et adaptation des procédés

#### a) Miniaturisation du MOSFET

Les dispositifs MOSFET, inventés en 1925, sont composés principalement d'un substrat, de régions source et drain dopées et d'une grille qui contrôle le passage du courant dans le canal. Afin d'améliorer leur performance et de réduire les coûts, leurs dimensions ont été continuellement réduites, en suivant la loi de Moore. Cette réduction de taille cause l'apparition de multiples effets parasites et nécessite une évolution des procédés et des architectures utilisés. L'une des modifications possibles consiste à utiliser des régions source et drain en SiGe pour contraindre un canal en Si. Cela cause une contrainte uniaxiale dans le canal et améliore la mobilité des porteurs. Cette méthode est déjà couramment employée, mais est constamment améliorée pour former des jonctions plus fines et plus fortement dopées.

#### **b) Alliages SiGe pour l'ingénierie de contrainte**

Le silicium et le germanium sont tous deux des semiconducteurs qui cristallisent dans une structure diamant (CFC) et sont miscibles sur toute la gamme de concentration. Il est donc

possible de former des alliages de  $\text{Si}_{1-x}\text{Ge}_x$ , qui auront un paramètre de maille  $a_{\text{SiGe}}^0$  variable avec la concentration en Ge,  $x$ :

$$a_{\text{SiGe}}^0 = a_{\text{Si}} + 0.1988 \cdot x + 0.028 \cdot x^2 \quad \text{Eq. [1]}$$

Il est donc possible de faire croître du SiGe monocristallin par-dessus du Si ou du Ge, puisque la maille va se déformer pour s'adapter à celle du substrat tant que l'énergie élastique reste limitée. Au-delà d'une certaine épaisseur, qui dépend de la concentration  $x$ , il devient énergétiquement favorable de former des défauts et la couche de SiGe relaxe. Ceci se manifeste par la formation de dislocations misfits à l'interface entre le substrat et la couche de SiGe. Les propriétés électriques du SiGe évoluent avec la concentration en Ge, et avec la contrainte. Le Ge ayant une meilleure mobilité des trous que le Si, celle-ci s'améliore lorsque que la concentration augmente. La contrainte permet aussi d'augmenter la mobilité des porteurs.

### c) Procédés de recuit

Les procédés de recuits sont couramment utilisés pour activer les dopants dans les régions sources et drains. A cause de la réduction des dimensions, il est devenu nécessaire de limiter la diffusion en profondeur des dopants, qui agrandit la jonction, tout en conservant une forte concentration de dopants actifs. Ces deux phénomènes sont thermiquement activés, et sont donc déclenchés en chauffant les couches à haute température. Il est en revanche possible d'activer les dopants sans les faire diffuser en profondeur, car les deux effets n'ont pas lieu sur les mêmes échelles de temps. Les méthodes de recuit ont donc progressivement évolué pour passer de recuits de plusieurs heures à des recuits de quelques secondes ou microsecondes. A l'heure actuelle, le recuit laser nanoseconde explore des durées de quelques nanosecondes, permettant de former de forts gradients de température dans les matériaux.

## 2. Le recuit laser nanoseconde, une méthode de recuit en surface

### a) Absorption de la pulsation laser

Le principe du recuit laser nanoseconde (NLA) repose sur l'absorption d'une impulsion laser par un matériau. Cette impulsion dure typiquement moins de 200 ns. La zone et durée du recuit dépendent à la fois des propriétés du laser (longueur d'onde et durée de l'impulsion) et des propriétés du matériau (absorption et diffusion de chaleur). De multiples phénomènes électroniques ont lieu dans le matériau pour transformer l'énergie incidente en chaleur, mais cet effet peut être considéré instantané à l'échelle de la nanoseconde. Cette absorption et diffusion de la chaleur en surface permet d'atteindre des températures supérieures au point de fusion en surface, tout en conservant le substrat sous-jacent froid. Cela conduit à la fusion d'une fine couche en surface. Une impulsion courte, ou une longueur d'onde plus courte conduisent typiquement à des gradients de température plus marqués et des vitesses de solidification plus élevées, de l'ordre de plusieurs mètres par seconde. Un recuit laser est défini principalement par sa durée d'impulsion, sa longueur d'onde, son mode de couverture et sa densité d'énergie.

### b) Structure et qualité des matériaux après recuit

Comme mentionné, le recuit laser permet éventuellement la transition en phase liquide sur des couches allant jusqu'à quelques centaines de nanomètres dans le Si et le Ge. Ces couches vont ensuite solidifier à grande vitesse. La qualité de la couche finale est essentiellement dépendante de la qualité du substrat sur lequel elle solidifie, et de sa vitesse de solidification. La couche sera généralement d'excellente qualité si elle croît à partir d'un germe monocristallin, mais poly-cristalline si le substrat est amorphe ou poly-cristallin. En outre, des vitesses de solidification excessives (typiquement supérieures à 15 m/s) empêchent la cristallisation et causent la formation d'une couche amorphe. La vitesse et la formation de

défauts dépendent aussi de l'orientation du substrat : les couches monocristallines, sans défauts, sont plus faciles à obtenir à partir d'un substrat (001).

### c) Activation des dopants dans le Si et le Ge

Grâce à la très faible durée de recuit, aucune diffusion des dopants n'a lieu en phase solide. Elle peut en revanche avoir lieu dans la phase liquide, puisque les coefficients de diffusion sont largement plus élevés. Ils vont alors se redistribuer, et former un profil « boîte » dans le cas idéal, comme observé pour le phosphore. Des phénomènes de ségrégation sont observés au cours de la solidification pour certains dopants comme le gallium, et causent une accumulation de l'espèce en surface.

Grâce au passage en phase liquide et au piégeage des dopants, le recuit laser permet d'atteindre des concentrations de dopants actifs supérieures aux limites de solubilité en phase solide, ce qui n'est pas possible avec les méthodes de recuit classique. Un exemple est montré en Figure 1 pour le bore, comparant les valeurs relevées dans la littérature pour le recuit laser nanoseconde avec les limites de solubilité connues dans le Si. Ce dopage à très forte dose est en revanche métastable et risque la désactivation s'il est exposé à des recuits supplémentaires.

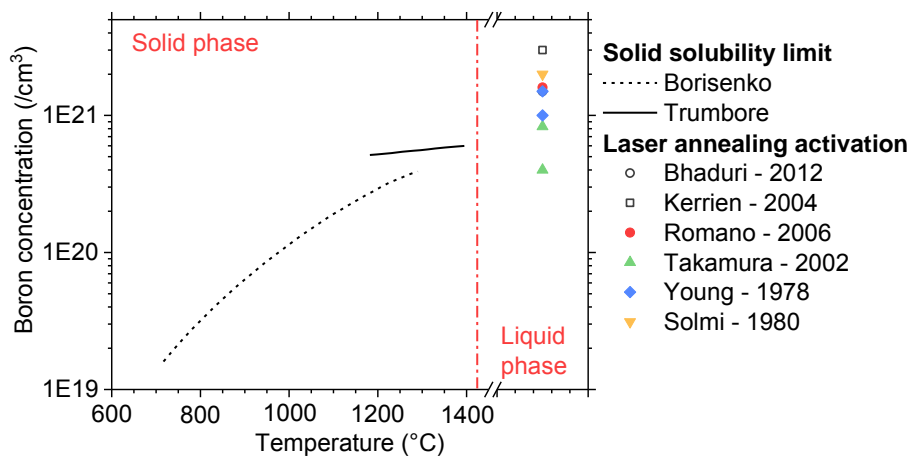


Figure 1. Dose active de bore obtenue après recuit laser, comparée avec la solubilité limite en phase solide dans le silicium.

### 3. Application aux alliages SiGe

Le recuit laser est donc prometteur pour la formation de jonctions ultra-fines et fortement dopées en SiGe. En outre, le phénomène de ségrégation du Ge lors de la solidification cause la formation d'un gradient et d'une zone riche en Ge à la surface, qui peut être bénéfique pour la formation de contacts. Les résultats sur la formation de défauts et la relaxation dans les couches sont en revanche incomplets : de nombreuses publications sont contradictoires, et l'origine de la relaxation reste inconnue. L'activation des dopants et leur répartition commence à être étudiée, mais elle est encore incomplète. D'une manière générale, il semble que l'activation s'améliore lorsqu'une bonne qualité cristalline est obtenue. L'objectif de ce travail est donc d'étudier en profondeur l'impact du recuit laser nanoseconde sur du SiGe, en commençant par des couches cristallines. Cela permet tout d'abord d'identifier les différents régimes de recuit, puis d'étudier l'évolution de la contrainte dans chaque régime et de proposer une explication unifiée pour la formation des défauts. Enfin, l'activation et la désactivation du bore est étudiée.

## II – ECHANTILLONS DE SiGe ET CARACTERISATIONS

### 1. Equipement de recuit laser

Les recuits sont réalisés avec un équipement LT-3100 fabriqué par SCREEN-LASSE. C'est un équipement basé sur une source XeCl ( $\lambda=308$  nm), avec une impulsion régulée à 160 ns. Il recuit une zone de  $15 \times 15$  mm<sup>2</sup> à la surface de l'échantillon, en formant un profil « Top-hat » à la surface. L'uniformité de l'énergie déposée à la surface est assurée par un système d'atténuation et un système d'homogénéisation. Les recuits peuvent être réalisés à température ambiante, ou jusqu'à 450°C grâce à un support chauffant. Enfin, une grande variation de densités d'énergie peut être étudiée sur une même plaque, puisque que la zone recuite est de  $15 \times 15$  mm<sup>2</sup>.

### 2. Echantillons

Plusieurs séries d'échantillons ont été réalisées, pour étudier l'impact du recuit laser sous différentes conditions. La formation de la couche de SiGe est faite par RP-CVD (Reduced Pressure Chemical Vapor Deposition), dans un réacteur ASM Epsilon 3200, après un nettoyage de surface. Trois séries ont ainsi été réalisées :

- Série 30 nm : couches de 30 nm de  $\text{Si}_{1-x}\text{Ge}_x$  ( $x=\{0, 0.1, 0.2, 0.3, 0.4\}$ ) déposées à 650°C
- Série  $\text{Si}_{0.7}\text{Ge}_{0.3}$  : Couches de  $\text{Si}_{0.7}\text{Ge}_{0.3}$  avec des épaisseurs de 20 nm, 30 nm et 45 nm
- Série dopée : Couches de 30 nm de  $\text{Si}_{0.7}\text{Ge}_{0.3}$  dopées à l'aide de bore au cours de l'épitaxie. Trois concentrations en bore, supérieures à  $7 \times 10^{19}$  cm<sup>-3</sup> sont utilisées.

Une série de couches amorphisées a aussi été étudiée (Série amorphe), comprenant deux couches de 30 nm de  $\text{Si}_{0.7}\text{Ge}_{0.3}$  non dopé amorphisées sur 15 nm et 30 nm respectivement, ainsi qu'une couche de  $\text{Si}_{0.7}\text{Ge}_{0.3}$  dopée au bore et amorphisée sur 15 nm. Les amorphisations sont faites par implantation de Ge. Ces couches sont recuites sur une large gamme de densité d'énergie (typiquement entre 1.20 J/cm<sup>2</sup> et 2.60 J/cm<sup>2</sup>), permettant d'observer tous les régimes de recuit.

### 3. Méthodes de caractérisation

#### a) Time Resolved Reflectivity (TRR)

La réflectivité des empilements de matériaux évolue avec leur température et leur phase. Il est donc possible d'estimer en temps réel l'état de la couche en monitorant sa réflectivité avec un laser ( $\lambda=638$  nm) concentré sur la zone de recuit. Un exemple de la variation de réflectivité enregistré sur du Si lors d'un pulse de 300 ns, avec  $\lambda=532$  nm, est présenté en Figure 2. On peut distinguer plusieurs étapes :

- ① : avant l'impulsion laser, la réflectivité du matériau froid est stable
- ② : la réflectivité de la couche augmente lorsque qu'elle chauffe
- ③ : la réflectivité augmente fortement lorsque la couche commence à fondre
- ④ : un plateau de réflectivité est atteint lorsque plus de 20 nm sont fondus
- ⑤ : la réflectivité diminue lorsque la couche se solidifie
- ⑥ : le signal décroît faiblement lorsque la couche refroidit

On peut ainsi détecter la densité d'énergie laser à partir de laquelle la couche fond, ainsi que la durée de fusion pour chaque densité d'énergie.

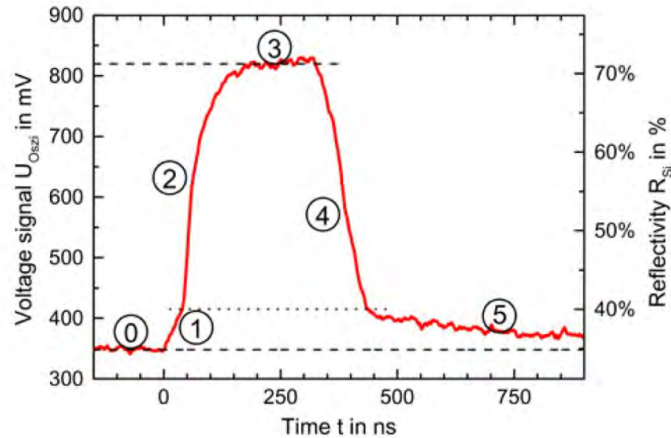


Figure 2. Profil TRR typique obtenu lors d'un recuit laser sur du silicium.

#### b) Etat de surface

Plusieurs techniques sont employées pour évaluer l'état de la surface après le recuit laser : la diffusivité de surface, l'AFM (Atomic Force Microscopy) et le MEB (Microscopie Electronique à Balayage). La mesure de diffusivité consiste à scanner la surface de l'échantillon avec un faisceau laser et à récupérer la lumière diffusée. Dans notre cas, on s'intéresse au bruit de fond de la mesure, associé à la qualité de la surface. L'AFM et le MEB permettent en revanche d'obtenir des images à petite échelle (entre 1  $\mu\text{m}$  et 10  $\mu\text{m}$  dans notre cas) de la surface et d'étudier sa morphologie. L'AFM permet de mesurer la rugosité RMS, sur les images de 10 $\times$ 10  $\mu\text{m}^2$ .

#### c) Qualité cristalline

La qualité cristalline des couches de SiGe avant et après le recuit est essentiellement étudiée par diffraction des rayons X (DRX), ce qui permet d'évaluer le niveau de relaxation de la couche. Une partie des mesures est complétée par des observations de microscopie électronique en transmission (MET), qui permettent de localiser les défauts cristallins dans la couche.

La diffraction des rayons X est due à l'interaction d'un faisceau de rayons X avec une structure périodique comme un cristal : les ondes diffusées peuvent former des interférences, qui sont constructives lorsque la condition de Bragg est respectée, avec  $n\lambda = 2d_{hkl}\sin(\theta_B)$ .  $\lambda$ ,  $d_{hkl}$  et  $\theta_B$  sont respectivement la longueur d'onde de la source de rayons X, la distance réticulaire entre deux plans  $\{hkl\}$  du cristal et l'angle de Bragg. On peut définir  $\vec{k}_i$  et  $\vec{k}_d$ , qui sont respectivement les vecteurs incidents et réfléchis, et le vecteur de diffraction  $\vec{q} = \vec{k}_d - \vec{k}_i$ . Une mesure XRD est considérée symétrique si  $\vec{q}$  est normal à la surface de l'échantillon : dans ce cas, seuls les plans parallèles à la surface sont étudiés. Dans le cas d'une mesure asymétrique, il devient possible d'étudier les plans cristallins inclinés par rapport à la surface. Afin d'évaluer le niveau de relaxation dans les couches de SiGe, il est nécessaire de connaître les paramètres de maille dans le plan et normal au plan, donc de réaliser une mesure asymétrique. On effectue donc des cartographies de l'espace réciproque (Reciprocal Space Maps, RSM), qui permettent de mesurer les paramètres de maille du SiGe et du Si. Le positionnement du pic de SiGe sur ces cartographies asymétriques est indicatif du niveau de contrainte de la maille, comme détaillé dans la Figure 3. Si la couche de SiGe est relaxée, le pic associé est décalé vers les plus petites valeurs de  $q_x$  par rapport au pic du silicium (a). Plus la couche est contrainte, et plus le pic va être aligné verticalement avec celui du Si (b), jusqu'à être parfaitement aligné pour une couche contrainte (c) : cela correspond à un paramètre de maille dans le plan égal à celui du Si.

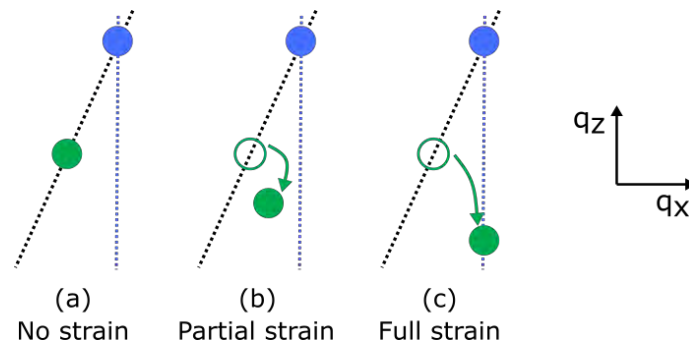


Figure 3. Schéma du déplacement du pic de SiGe par rapport au pic de Si sur une cartographie de l'espace réciproque avec la variation de contrainte.

Les paramètres de maille calculés grâce à ces cartographies permettent d'obtenir le niveau de relaxation macroscopique  $R$ , avec  $a_{SiGe}^0$  le paramètre de maille relaxé pour une couche avec la même concentration  $x$  en Ge.

$$R = \frac{a^{\prime\prime} - a_{Si}}{a_{SiGe}^0 - a_{Si}} \quad \text{Eq. [2]}$$

$$a_{SiGe}^0 = a_{Si} + 0.1988 \cdot x + 0.028 \cdot x^2 \quad \text{Eq. [3]}$$

La MET est utilisée pour observer la microstructure des échantillons. Pour ce faire, une lame mince est fabriquée, suffisamment fine pour être traversée par un faisceau électronique. Les électrons qui traversent la lame peuvent interagir de multiples façons avec le matériau, et peuvent être déviés de leur trajectoire initiale ou perdre de l'énergie. Les images en champ clair sont formées grâce aux électrons transmis directement, sans être déviés : les zones sombres de l'image vont alors correspondre aux endroits où des défauts ont empêché la transmission. À l'inverse, une image en champ sombre est réalisée à partir d'un faisceau d'électrons déviés : elle apparaît sombre, sauf dans les zones correspondant aux défauts causant la déviation. Il est aussi possible d'obtenir des images STEM-HAADF, où le contraste dépend des éléments chimiques présents.

#### d) Composition

La composition et distribution des éléments dans la couche est modifiée par le recuit laser. Il est donc nécessaire de mesurer les profils des différentes espèces attendues, pour connaître leur répartition finale. On suit principalement le Si, le Ge ainsi que le bore dans le cas de couches dopées. Les mesures sont faites soit par SIMS (Secondary Ion Mass Spectrometry) soit par EDX (Energy Dispersive X-Ray). La mesure SIMS consiste à pulvériser progressivement les atomes de l'échantillon à l'aide d'un faisceau d'ions incidents, généralement césium ou oxygène. Cela permet de graver progressivement l'échantillon et d'étudier la répartition des espèces en fonction de la profondeur. Une partie des particules arrachées est ionisée et peut être attirée vers un détecteur, qui permet de retrouver l'espèce chimique en triant avec la masse et l'énergie du composé. Cette mesure pour chaque espèce chimique d'intérêt permet initialement d'obtenir une variation d'intensité en fonction du temps de mesure. Grâce à plusieurs corrections, il est possible d'obtenir la concentration chimique en fonction de la profondeur. La mesure EDX est réalisée sur une lame mince de MET. Lors de l'interaction avec le faisceau électronique, les atomes de l'échantillon peuvent être excités et émettre des rayons X caractéristiques lors de la désexcitation. Ces rayons X sont collectés et triés, ce qui permet de connaître l'espèce atomique dans une zone donnée, et ainsi de tracer des profils chimiques en fonction de la profondeur.

## e) Mesures électriques

Les mesures électriques sont effectuées pour évaluer l'activation des dopants dans les couches contenant du bore. Des mesures de résistance carrée sont effectuées sur tous les échantillons par la méthode des quatre pointes, tandis que seuls quelques échantillons sont sélectionnés pour des mesures d'effet Hall. Les mesure de résistance carrée par quatre pointes (4PP) sont effectuées en appliquant quatre pointes à la surface de l'échantillon à mesurer. La résistance carrée  $R_s$  peut alors se calculer à partir du courant injecté  $I_{inj}$  et de la tension mesurée  $V_{mes}$  :

$$R_s = \frac{\rho}{t} = \Gamma \cdot \frac{V_{mes}}{I_{inj}} \quad \text{Eq. [4]}$$

Cette mesure permet d'éliminer l'effet de la résistance de contact. Elle peut en revanche être impactée par la taille et la forme des pointes, car ces paramètres modifient la profondeur de pénétration dans le matériau.

Les mesures d'effet Hall permettent d'estimer la dose de charges actives dans le matériau, ainsi que leur mobilité. Elles sont réalisées en appliquant un courant  $I_x$  au matériau qui est soumis à un champ magnétique  $B_z$ . Cela provoque une accumulation de charges de chaque côté du matériau, dans une direction orthogonale à la fois au courant et au champ magnétique. A l'équilibre, on peut mesurer la tension de Hall  $V_H$ , puis le coefficient de Hall  $R_H = 1/qn$ , la mobilité de Hall  $\mu_H = R_H/\rho$  et la concentration de Hall  $n_H = 1/(q \cdot R_H)$ , pour un échantillon idéal. Dans le cas d'un échantillon réel, il faut prendre en compte la diffusion grâce au facteur de diffusion  $r_H$ , ainsi que la répartition des dopants dans l'échantillon.

#### 4. Simulations numériques

## a) Avec le logiciel LIAB

Le logiciel LIAB conçu par SCREEN-LASSE est dédié à la simulation de recuit laser nanoseconde par éléments finis. Il est basé sur un couplage entre les solutions des équations de Maxwell (pour la source de chaleur) et les équations de diffusion de la chaleur dans le matériau. Après calibration des paramètres matériaux en fonction de la température et de la concentration en Ge, il permet de prédire les durées de fusion et profondeur de fusion, ainsi que les profils de composition. Les simulations sont réalisées en mode « Phase Field », ce qui signifie que la phase du matériau n'est pas seulement dépendante de la température, mais aussi des autres paramètres.

b) Ségrégation et **densité d'énergie élastique**

En connaissant les profondeurs de fusion, ainsi qu'une vitesse de solidification approximée, il est possible de reproduire les profils de Ge après recuit laser. La couche de SiGe est virtuellement divisée en de multiple sous-couches (d'épaisseur 0.5 nm), et une concentration en Ge est attribuée à chaque sous-couche en partant de la profondeur maximale. La concentration dépend de la concentration en Ge dans le liquide restant et du coefficient de ségrégation, qui lui-même dépend de la concentration en Ge du côté solide de l'interface et de la vitesse de solidification. A partir de ce profil de Ge, il est aussi possible de calculer la densité d'énergie élastique  $E_{EL}$  stockée dans la couche, exprimée par :

$$E_{EL} = \int_{z=0}^{z=z_{max}} B \cdot \varepsilon(x)^2 \cdot dz \quad \text{Eq. [5]}$$

$$B = 2\mu(z) \cdot \frac{1 + \nu(z)}{1 - \nu(z)} \quad \text{Eq. [6]}$$

$$\varepsilon(z) = \frac{a_{SiGe} - a_{Si}}{a_{Si}} \quad \text{Eq. [7]}$$

Avec  $z_{max}$  l'épaisseur de la couche de SiGe,  $\varepsilon(x)$  la déformation,  $\mu(z)$  le module de cisaillement et  $\nu(z)$  le coefficient de Poisson.

### III – REGIMES DE RECUIT DANS LE SiGe

#### 1. Identification des régimes

Les différents régimes de recuits et leurs caractéristiques sont d'abord décrits pour des couches de  $Si_{0.6}Ge_{0.4}$  de 30 nm, puis pour chacune des séries d'échantillons utilisés au cours de ce travail.

##### a) Régimes typiques

Le premier régime observé correspond à la sous-fusion, lors duquel la densité d'énergie n'est pas suffisante pour faire fondre la couche de SiGe, bien que celle-ci chauffe. En augmentant la densité d'énergie, on attend le seuil de fusion. Celui-ci peut être détecté grâce à une augmentation nette de la réflectivité de la couche enregistrée par la TRR, comme visible sur la cartographie TRR en Figure 4. Sur cette cartographie, on peut observer l'évolution de la TRR en fonction du temps et de la densité d'énergie laser : chaque ligne correspond à un signal TRR enregistré au cours d'un tir. Cela permet de constater l'apparition d'un pic lié à la fusion à partir de  $1.35 \text{ J/cm}^2$ , qui est donc le début de la fusion.

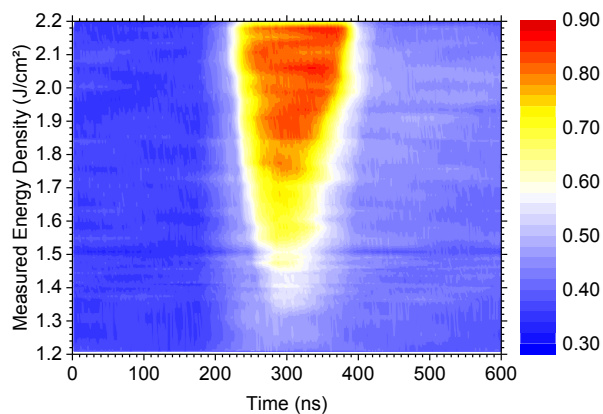


Figure 4. Cartographie TRR obtenue pour une couche de  $Si_{0.6}Ge_{0.4}$ .

Le début de la fusion est aussi détectable par AFM ou SP2 Haze, car il cause une augmentation de la rugosité en surface, comme montré en Figure 5(a). Un pic de l'intensité de Haze est observé de  $1.31 \text{ J/cm}^2$  jusqu'à  $1.72 \text{ J/cm}^2$ , accompagné par une augmentation de la rugosité RMS. Cela définit les limites du régime de fusion en surface, le premier après la fusion. La surface redevient bien plus lisse à la fin de ce régime. En continuant d'augmenter la densité d'énergie, on atteint le régime de fusion partielle, puis de fusion totale. Dans les deux cas, la surface apparaît lisse, et ils sont distingués grâce à la profondeur de fusion. En fusion partielle, l'interface liquide/solide ne dépasse pas l'interface initiale SiGe/Si, alors que c'est le cas pour la fusion totale. Les courbes SIMS de la Figure 5(b) montrent les profils de Ge en fonction de la profondeur pour plusieurs densités d'énergie, ce qui permet d'estimer la profondeur fondue. Le profil de Ge initial est plat, avec une concentration proche de 40%, et cela reste vrai au tout début de la fusion à  $1.35 \text{ J/cm}^2$ . A plus forte densité d'énergie, le Ge est redistribué à cause de la ségrégation : il est repoussé vers la surface au cours de la solidification, formant un gradient avec une très forte concentration en surface. On constate que le Ge ne se redistribue pas au-delà de l'interface initiale jusqu'à  $2.00 \text{ J/cm}^2$ . La fusion ne

dépasse la couche initiale que pour le profil mesuré à 2.20 J/cm<sup>2</sup>. On peut donc estimer que la transition de fusion partielle à fusion totale est entre 2.00 J/cm<sup>2</sup> et 2.20 J/cm<sup>2</sup>.

On a donc quatre régimes observés avec l'augmentation de la densité d'énergie : (i) la sous-fusion ; (ii) la fusion en surface, caractérisé par une surface rugueuse ; (iii) la fusion partielle, avec une surface lisse et une profondeur de fusion dans la couche initiale de SiGe ; et (iv) la fusion totale, avec une surface lisse et une profondeur de fusion supérieure à la couche initiale de SiGe.

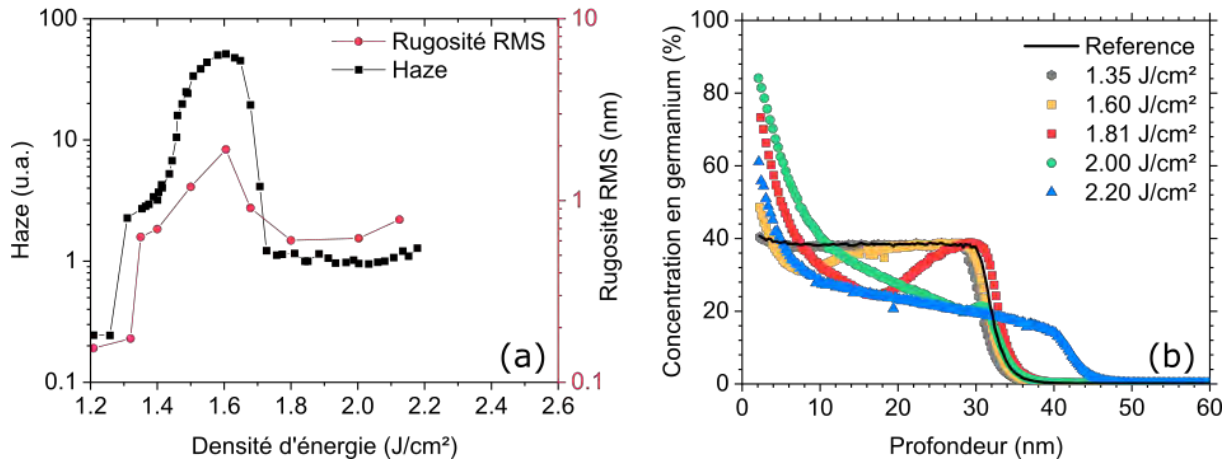


Figure 5. Evolution de la rugosité de surface et du signal de haze en fonction de la densité d'énergie (a), et profils de Ge mesurés à différentes densités d'énergie pour du Si<sub>0.6</sub>Ge<sub>0.4</sub>(b).

b) Extension à la totalité des échantillons

Ces régimes observés pour le Si<sub>0.6</sub>Ge<sub>0.4</sub> peuvent être observés pour tous les échantillons initialement pseudomorphes avec les mêmes méthodes. Les différents seuils de transition varient en fonction de l'épaisseur et de la composition de la couche, et sont indiqués dans le Tableau 1. Pour rappel, la série « 30 nm » a été réalisée avec un tir laser d'une durée de 146 ns, alors que les deux autres ont été réalisées avec un tir d'une durée de 160 ns : cela peut expliquer l'écart entre les seuils observés pour les deux échantillons de 30 nm de Si<sub>0.7</sub>Ge<sub>0.3</sub> dans les séries « 30 nm » et « Si<sub>0.7</sub>Ge<sub>0.3</sub> ».

Tableau 1. Limites de régimes observées pour les différentes séries d'échantillons étudiés.

Série	Echantillon	Seuil de fusion	Fusion partielle	Fusion totale
30 nm	Si	1.76	-	2.13
	Si <sub>0.9</sub> Ge <sub>0.1</sub>	1.66	1.94	2.00 – 2.20
	Si <sub>0.8</sub> Ge <sub>0.2</sub>	1.55	1.86	2.00 – 2.20
	Si <sub>0.7</sub> Ge <sub>0.3</sub>	1.40	1.75	2.00 – 2.20
	Si <sub>0.6</sub> Ge <sub>0.43</sub>	1.31	1.72	2.00 – 2.20
Si <sub>0.7</sub> Ge <sub>0.3</sub>	20 nm	1.49	1.80	2.00 – 2.19
	30 nm	1.45	1.78	2.08 – 2.14
	45 nm	1.39	1.75	2.10 – 2.11
Dopage (Si <sub>0.7</sub> Ge <sub>0.3</sub> )	A	1.46	1.78	2.04 – 2.23
	B	1.45	1.78	2.03 – 2.25
	C	1.49	1.78	2.03 – 2.19

## 2. Evolution du seuil de fusion avec la nature des couches

### a) Propriétés optiques et thermiques

L'évolution des propriétés optiques des couches avec la concentration en Ge ou en bore a pu être mesurée par ellipsométrie en température jusqu'à 600°C pour plusieurs longueurs d'onde. A la longueur d'onde utilisée pour le recuit laser ( $\lambda=308$  nm) et à température ambiante, on constate que le coefficient de réfraction  $n_{308}$  et le coefficient d'extinction  $k_{308}$  diminuent lorsque la couche s'enrichit en Ge. En augmentant la température,  $n_{308}(T)$  diminue pour toutes les concentrations, alors que  $k_{308}(T)$  augmente. A la longueur d'onde de 635 nm, utilisée pour les mesures de TRR,  $n_{635}$  et  $k_{635}$  augmentent avec la concentration en Ge. On constate en revanche assez peu de différence pour les différentes concentrations en bore (A, B, C) que ce soit à 635 nm ou 308 nm.

### b) Seuil de fusion

Comme indiqué dans le Tableau 1, les seuils de fusion varient en fonction de l'épaisseur et de la composition de la couche. La Figure 6 résume l'évolution de ce seuil pour les séries « 30 nm » (a) et «  $\text{Si}_{0.7}\text{Ge}_{0.3}$  » (b), en prenant les valeurs mesurées par TRR et par Haze. Dans les deux cas, les valeurs suivent des tendances identiques et sont très proches. En (a), on constate que le seuil de fusion diminue lorsque la concentration en Ge augmente, ce qui est compatible avec la diminution de la température de fusion des alliages riches en Ge. L'augmentation de l'épaisseur de la couche conduit aussi à une diminution du seuil de fusion (b) : puisqu'il n'y a aucun changement de température de fusion, cela peut être dû à la plus faible conductivité thermique du  $\text{Si}_{0.7}\text{Ge}_{0.3}$  comparé au silicium, ou à un changement dans la réflectivité de l'empilement. On peut aussi observer que la plus faible durée d'impulsion conduit à un seuil de fusion légèrement plus bas entre les deux couches de 30 nm de  $\text{Si}_{0.7}\text{Ge}_{0.3}$ .

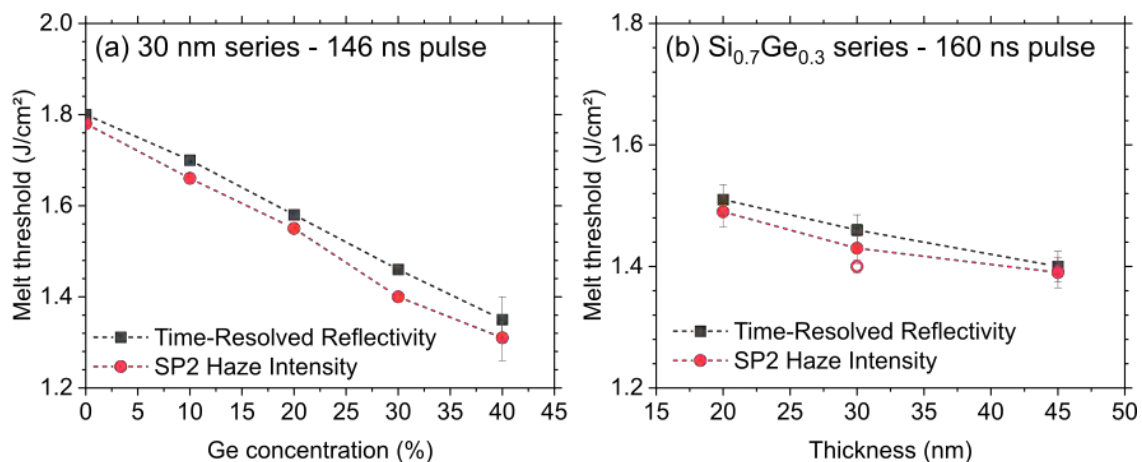


Figure 6. Evolution du seuil de fusion pour la série « 30 nm » (a) et la série «  $\text{Si}_{0.7}\text{Ge}_{0.3}$  » (b).

## 3. Structuration de surface

### a) Origine de la rugosité

Les mesures de Haze et par AFM indiquent une forte augmentation de la rugosité lors du régime de fusion en surface. Celle-ci est liée à l'apparition de structures géométriques en surface, comme celles visibles en Figure 7 pour une couche de 30 nm de  $\text{Si}_{0.6}\text{Ge}_{0.4}$ . La surface est parfaitement lisse sous la fusion (a), et des structures apparaissent dès le seuil de fusion (b). En augmentant la densité d'énergie, les structures se multiplient et fusionnent (c-f), recouvrant progressivement la surface. A la fin de ce régime, elles ont complètement recouvert la surface qui redevient alors plus lisse (g-h).

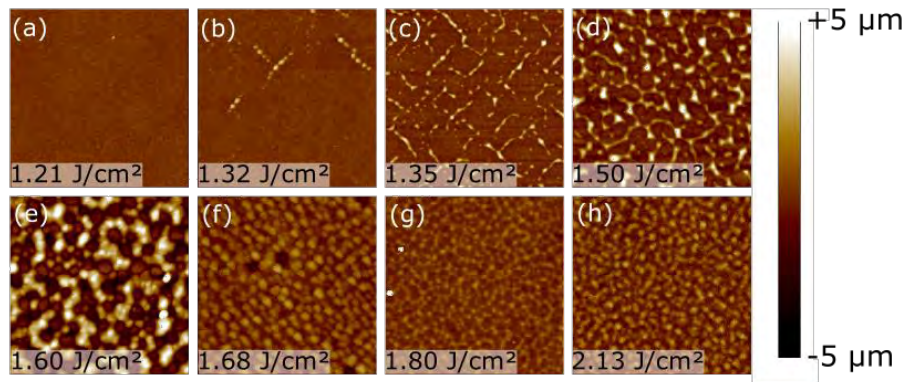


Figure 7. Images AFM ( $1 \times 1 \mu\text{m}^2$ ) sur du  $\text{Si}_{0.6}\text{Ge}_{0.4}$ , présentant l'évolution de la surface en fonction de la densité d'énergie.

Les mesures STEM-HAADF et les profils EDX associés permettent d'identifier la nature de ces structures géométriques. En Figure 8(a), une image STEM-HAADF obtenue sur un échantillon de  $\text{Si}_{0.6}\text{Ge}_{0.4}$  recuit à  $1.60 \text{ J/cm}^2$  est présentée, et correspond à l'image (e) de la Figure 7. Sur ces images, le contraste est lié aux éléments chimiques, avec des zones plus claires pour les éléments chimiques plus lourds. Les zones riches en Ge apparaissent donc plus claires. On y observe la formation de dômes en surface de chaque côté de l'image, alors que la surface reste lisse au centre : les dômes correspondent aux structures observées par AFM. Dans chacun de ces dômes, on constate que la surface est plus riche en Ge, alors que la région sous-jacente s'est appauvrie, ce qui est confirmé par le profil EDX rouge de la Figure 8(b). En revanche, la zone lisse au centre ne présente aucune variation de contraste, et le profil vert en (b) montre une concentration en Ge uniforme. Cela indique que la ségrégation du Ge a eu lieu uniquement dans les dômes, et que ce sont des îlots fondus, séparés les uns des autres. On comprend alors que le début de la fusion entraîne la formation de multiples zones fondues isolées les unes des autres, plutôt que d'une couche fondue uniforme. En augmentant la densité d'énergie, ces zones fondues se multiplient et se rejoignent, jusqu'à former une couche liquide continue à la fin du régime de fusion en surface.

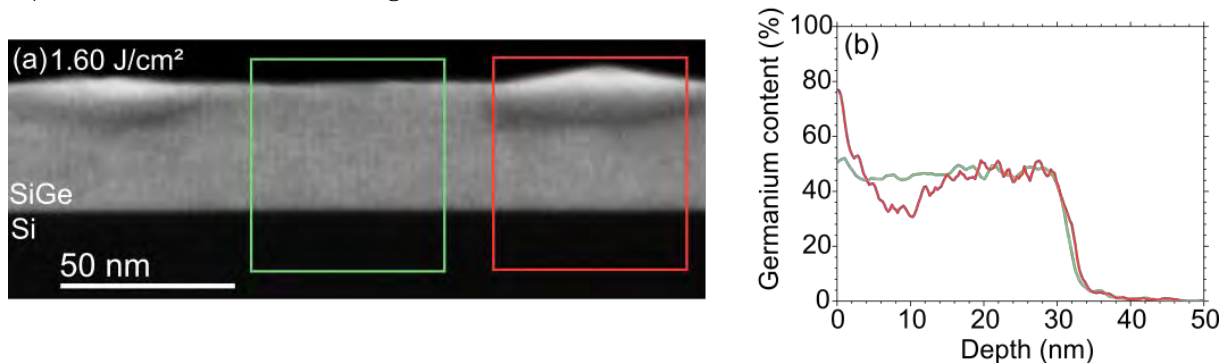


Figure 8. Image STEM-HAADF présentant les structures en surface de  $\text{Si}_{0.6}\text{Ge}_{0.4}$  recuit par laser à  $1.60 \text{ J/cm}^2$  (a), avec les profils EDX associés (b).

#### b) Impact de la nature de la couche

L'apparition de zones fondues en surface et l'augmentation de rugosité associée sont observées pour tous les échantillons, y compris pour les substrats de silicium. Ce n'est donc pas un effet de l'alliage SiGe. On constate en revanche que la forme des structures évolue avec la concentration en Ge, comme le montrent les images AFM en Figure 9. Pour du Si (a), les structures isolées apparaissent carrées en vue de dessus, avec des côtés parallèles aux directions cristallographiques  $\langle 110 \rangle$ . En augmentant la concentration en Ge, les structures deviennent moins larges et moins hautes, et se développent plutôt selon les directions  $\langle 010 \rangle$ . Les mesures AFM permettent aussi d'estimer le pourcentage de la surface recouvert par les

structures en fonction de la densité d'énergie : il apparaît qu'une concentration plus élevée en Ge semble « ralentir » le recouvrement de la surface. Il n'y a en revanche pas d'effet marqué de l'épaisseur ou de la concentration en bore.

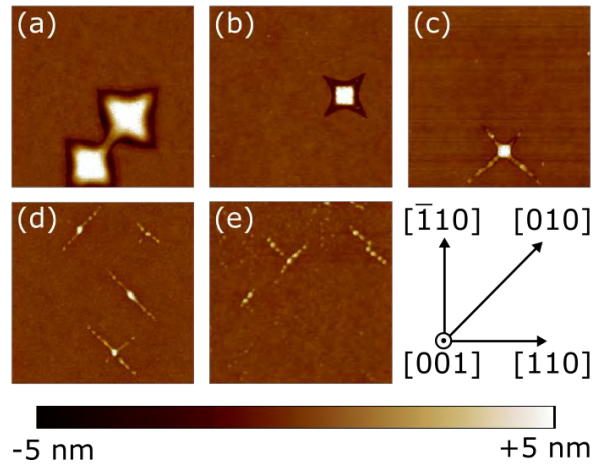


Figure 9. Images AFM sur des échantillons de Si (a),  $\text{Si}_{0.9}\text{Ge}_{0.1}$  (b),  $\text{Si}_{0.8}\text{Ge}_{0.2}$  (c),  $\text{Si}_{0.6}\text{Ge}_{0.4}$  (d) et de  $\text{Si}_{0.6}\text{Ge}_{0.4}$  (e), à des densités d'énergie correspondant au début de la fusion.

#### 4. Ségrégation et diffusion lors de la solidification

##### a) Ségrégation du Ge comme indicateur de fusion

La ségrégation du Ge a lieu lors de la solidification de la couche : à l'interface liquide/solide, seule une portion de Ge présent dans le liquide est incorporée dans la zone solide, ce qui cause un enrichissement en Ge progressif de la phase liquide. Le profil de Ge final est donc un gradient, avec une forte concentration à la surface, comme dans les profils SIMS présentés en Figure 5 pour du  $\text{Si}_{0.6}\text{Ge}_{0.4}$ . Des profils très similaires sont obtenus lors des mesures EDX, ce qui confirme l'existence de la ségrégation. Celle-ci a lieu pour toutes les couches de SiGe, quelle que soit la concentration en Ge et l'épaisseur. Les images STEM-HAADF permettent d'observer l'interface liquide/solide (l/s) dans la couche. Des exemples sont présentés en Figure 10 pour des échantillons de la série « 30 nm ».

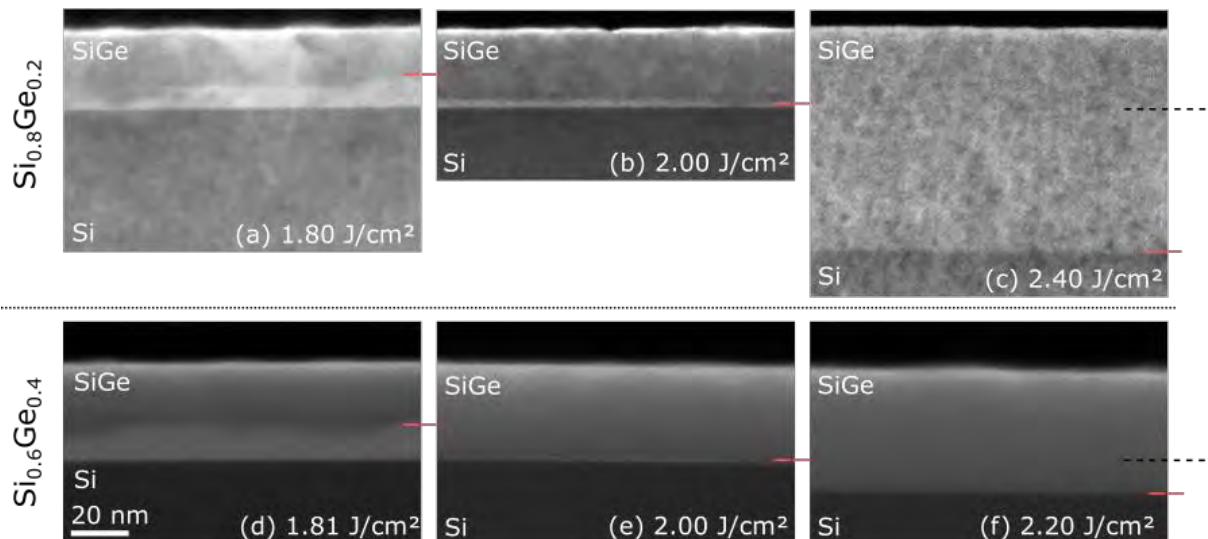


Figure 10. Images STEM d'échantillons de  $\text{Si}_{0.8}\text{Ge}_{0.2}$  (a-c) et de  $\text{Si}_{0.6}\text{Ge}_{0.4}$  (d-f) après recuit laser nanoseconde dans différents régimes, montrant la répartition du Ge dans la couche et l'interface l/s.

Tant que la fusion totale n'est pas atteinte, il reste une couche de SiGe en profondeur qui apparaît assez claire, ce qui correspond à la couche restée solide. Au-dessus, dans la couche fondue, on observe une zone plus sombre liée à la déplétion en Ge, et une surface

très claire liée à la forte concentration de Ge. Sur les images (a) et (d), pour des densités d'énergie faibles, on constate que l'interface l/s n'est pas lisse, et que sa profondeur varie de plusieurs nanomètres selon les endroits. Cet effet est réduit à 2.00 J/cm<sup>2</sup> (b,e) lorsque l'interface l/s est proche du fond de la couche de SiGe, et elle apparaît plus lisse. Enfin, en fusion totale (c,f), elle apparaît parfaitement lisse. Cette rugosité de l'interface est probablement liée à la fusion locale lors du début de la fusion. Elle est lissée lors du passage du front de fusion du SiGe au Si grâce à la différence de température de fusion : il est nécessaire d'atteindre des températures plus élevées pour fondre le Si, et le SiGe fond donc entièrement avant le Si.

#### b) Simulations de la ségrégation

Les profils de Ge peuvent servir d'indicateur de fiabilité lors des simulations, puisqu'ils permettent de comparer les profondeurs de fusion. Les paramètres thermiques utilisés pour les simulations proviennent essentiellement de la littérature, tandis que les paramètres optiques du SiGe sont tirés des mesures d'ellipsométrie en température présentées précédemment. Comme montré en Figure 11, ces paramètres conduisent à des profils simulés très proches de ceux obtenus par SIMS pour le Si<sub>0.8</sub>Ge<sub>0.2</sub> et le Si<sub>0.6</sub>Ge<sub>0.4</sub> en utilisant un coefficient de ségrégation constant et égal à 0.45. Cela souligne que le coefficient de ségrégation varie assez peu, quelle que soit la concentration en Ge.

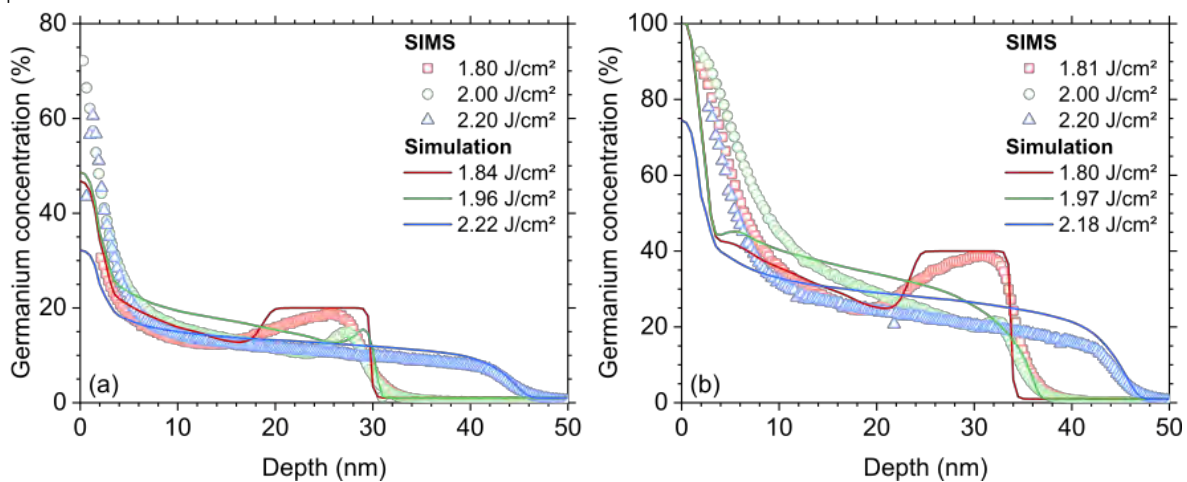


Figure 11. Simulations des profils de Ge après recuit laser nanoseconde sur des couches de Si<sub>0.8</sub>Ge<sub>0.2</sub> (a) et de Si<sub>0.6</sub>Ge<sub>0.4</sub> (b), comparées aux profils SIMS.

### 5. Mesures de réflectivité

La TRR permet d'enregistrer directement les évolutions du matériau au cours du recuit laser, et de comparer les signaux lors des différents régimes. La Figure 12 présente les signaux TRR pour un substrat Si et une couche épitaxiée de Si<sub>0.7</sub>Ge<sub>0.3</sub>. Pour le substrat Si, les courbes correspondent à la sous-fusion (a), la fusion en surface (b) et la fusion totale (c,d). Pour le SiGe, les courbes correspondent à la sous-fusion (e), la fusion en surface (f), la fusion partielle (g) et la fusion totale (h). Dans les deux cas, il n'y a pas de pic de TRR tant que le seuil de fusion n'a pas été atteint. Pour le Si, les courbes de TRR sont très proches de celle présentées en Figure 2, avec des montées (fusion) et descente (solidification) très abruptes, y compris lors de la fusion en surface. Pour rappel, le plateau de TRR indique que la fusion a dépassé la profondeur maximale sondée par la TRR dans le liquide, soit environ 20 nm. Pour le SiGe, la pente correspondant à la fusion apparaît assez abrupte, mais elle est beaucoup plus progressive lors de la solidification en (f,g), ce qui indique une vitesse de solidification réduite par rapport au Si. A forte densité d'énergie, en fusion totale (h), elle apparaît similaire à celle du Si. Ce n'est pas un effet direct de la concentration en Ge, car les courbes de TRR sur Ge sont proches de celles sur Si, avec une solidification abrupte. Cette solidification lente dans les régimes de fusion en surface et de fusion partielle n'est pas encore totalement comprise : il peut s'agir d'un effet

combiné de la rugosité de l'interface l/s et de la ségrégation. En effet, la solidification démarre à des profondeurs différentes du fait de la rugosité d'interface l/s et la surface va donc se solidifier plus tôt dans certaines régions. On forme donc des poches de liquide très riches en Ge à la surface, qui peuvent mettre plus longtemps à se solidifier du fait de leur plus faible température de solidification par rapport au reste du matériau.

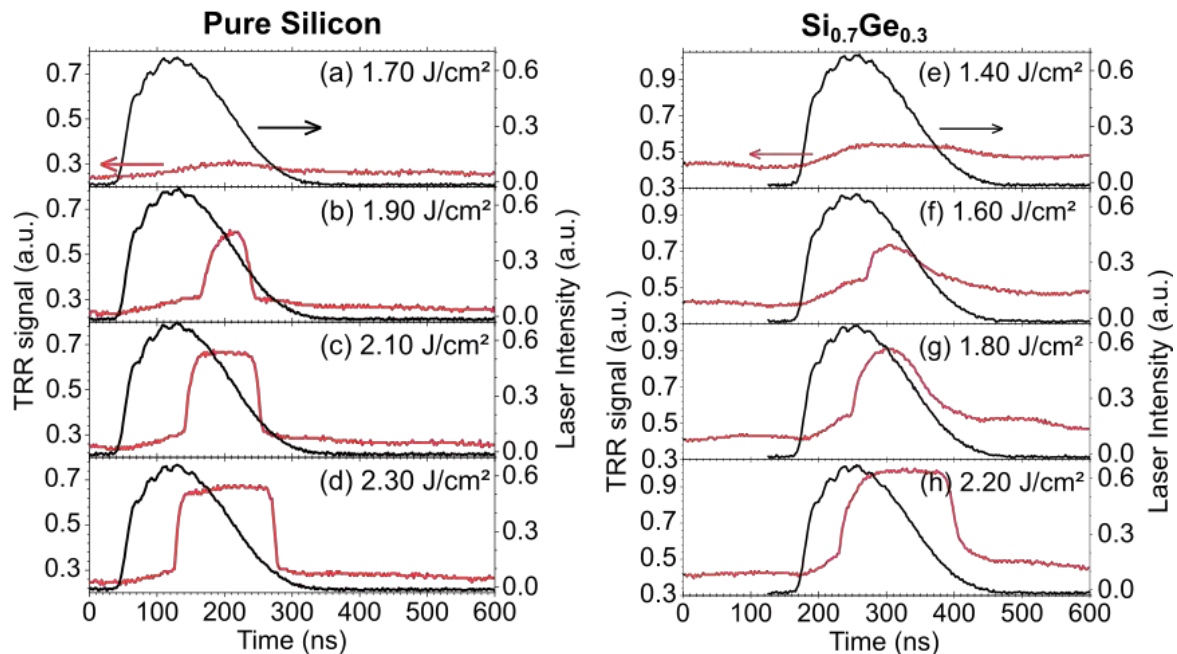


Figure 12. Profils TRR obtenus au cours des différents régimes de recuit pour un substrat Si (a-d) et une couche de Si<sub>0.7</sub>Ge<sub>0.3</sub> (e-h).

En extrayant les points majeurs de ces courbes, il est possible d'estimer des durées de fusion et de solidification sur les 20 nm proches de la surface (profondeur de liquide maximale observée). Pour le Si et le Ge, les durées de fusion et de solidification sont stables à 20 ns. Pour le Si<sub>1-x</sub>Ge<sub>x</sub>, la durée de fusion sur les 20 nm est elle aussi stable proche de 20 ns, quelle que soit l'épaisseur et la nature de la couche étudiée. A la solidification, on remarque en revanche bien l'effet de la pente douce : à faible densité d'énergie, les durées de solidification sont beaucoup plus élevées, et se réduisent progressivement pour atteindre 20 ns lors de la fusion totale. La TRR peut donc servir à facilement délimiter ces régimes sans avoir besoin de mesures SIMS.

#### IV – RELAXATION ET FORMATION DE DEFANTS

##### 1. Evolution de la contrainte : exemple du Si<sub>0.6</sub>Ge<sub>0.4</sub>

Les mesures de contrainte sont effectuées par XRD, grâce à des RSMs autour du pic de diffraction (224). Comme pour le détail des différents régimes, les résultats sont d'abord décrits pour une couche de Si<sub>0.6</sub>Ge<sub>0.4</sub> puis étendus à l'intégralité des échantillons étudiés. La Figure 13 présente quelques RSMs typiques des différents régimes. En sous-fusion (a), la RSM montre que le pic de SiGe (tâche rouge en bas) est verticalement aligné avec le pic du Si : cela correspond à une couche parfaitement contrainte. Dans le régime de fusion en surface (b), le pic de SiGe est décalé vers la gauche, et apparaît beaucoup plus diffus : cela dénote la formation de défauts cristallins et d'un relaxation partielle. Cette relaxation s'amplifie et devient totale dans le régime de fusion partielle (c). A la fin de la fusion partielle (d), on peut observer deux pics associés au SiGe sur la RSM : l'un est aligné verticalement avec le pic du Si et l'autre est légèrement décalé vers la gauche. Cela indique la formation d'une bicouche, dans laquelle une partie du SiGe est contraint tandis que le reste est partiellement relaxé. Une

RSM similaire est obtenue à 2.20 J/cm<sup>2</sup> en fusion totale (non montrée), bien que la valeur de relaxation associée soit trop faible pour être mesurée. Les images TEM présentées en Figure 14 permettent de localiser les défauts présents dans ces couches. Lors des régimes de fusion en surface (a,e) et de fusion partielle (b,f), on peut observer des défauts qui traversent l'intégralité de la couche, jusqu'en profondeur, avec plusieurs dislocations « misfit » qui conduisent à une relaxation partielle ou totale de la couche. Dans le cas des échantillons à la fin de la fusion partielle (c,g) ou en fusion totale (d,h), on constate que la partie inférieure de la couche ne présente aucun défaut, alors que la zone proche de la surface en contient. Cela indique que la zone contrainte est en profondeur, et la zone partiellement relaxée correspond à la surface.

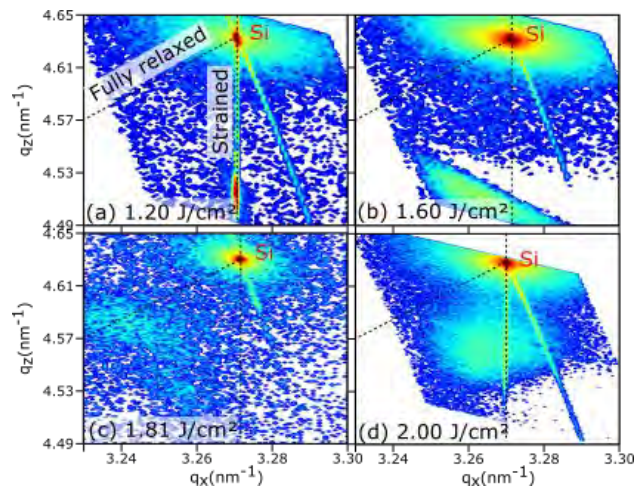


Figure 13. Cartographies de l'espace réciproque, RSMs, obtenues sur du Si<sub>0.6</sub>Ge<sub>0.4</sub> après recuit laser à 1.20 J/cm<sup>2</sup> (a), 1.60 J/cm<sup>2</sup> (b), 1.81 J/cm<sup>2</sup> (c) and 2.00 J/cm<sup>2</sup> (d).

Cette évolution de la contrainte avec les régimes peut être liée à l'état de l'interface l/s. Dans les régimes de fusion en surface et de fusion partielle (cf. Figure 8 et Figure 10, on a pu noter que l'interface était rugueuse, ce qui facilite la formation de défauts qui vont traverser la couche et donc la relaxation. A la fin du régime de fusion partielle, l'interface l/s devient plus lisse, comme expliqué précédemment. La solidification peut donc commencer sans défauts, et on obtient une zone en profondeur parfaitement contrainte. La présence d'une couche relaxée en surface est due à un excès d'énergie élastique stockée : similairement à l'épaisseur critique lors d'une croissance épitaxiale, la densité d'énergie élastique dans la couche en cours de solidification devient trop élevée et la formation de défauts est alors énergétiquement favorable. Le gradient de Ge causé par la ségrégation influence fortement sur la densité d'énergie élastique, et les valeurs maximales de densité d'énergie élastique correspondent à la fin du régime de fusion partielle. L'énergie élastique est plus élevée pour des couches plus épaisses ou plus riches en Ge.

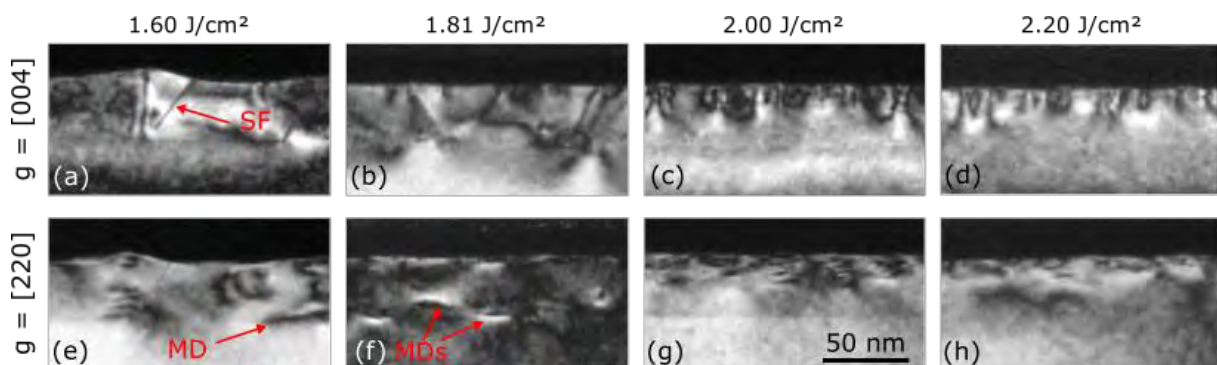


Figure 14. Images TEM d'un échantillon de Si<sub>0.6</sub>Ge<sub>0.4</sub> recuit à 1.60 J/cm<sup>2</sup> (a,e), 1.81 J/cm<sup>2</sup> (b,f), 2.00 J/cm<sup>2</sup> (c,g) and 2.20 J/cm<sup>2</sup> (d,h).

## 2. Impact de la nature des couches

Ces observations peuvent être étendues à l'intégralité des couches de SiGe pseudomorphes étudiées, en suivant l'évolution de la relaxation en fonction de la densité d'énergie laser, en Figure 15. Pour la série « 30 nm » (a), on peut constater que les tendances varient avec la concentration en Ge. Le  $\text{Si}_{0.9}\text{Ge}_{0.1}$  ne présente jamais de relaxation, même lors de la fusion en surface, ce qui est probablement lié à ses très faibles niveaux de densité d'énergie élastique. Pour le  $\text{Si}_{0.8}\text{Ge}_{0.2}$ , on constate que la couche relaxe partiellement lors de la fusion en surface et revient en contrainte durant le régime de fusion partielle, puis reste parfaitement contrainte à plus forte densité d'énergie. Dans le cas du  $\text{Si}_{0.7}\text{Ge}_{0.3}$ , on constate aussi une relaxation partielle lors de la fusion en surface, qui perdure dans le régime de fusion partielle et ne disparaît qu'à la fusion totale. Enfin, pour le  $\text{Si}_{0.6}\text{Ge}_{0.4}$ , les valeurs de relaxation sont en accord avec les observations de la section précédente : une relaxation partielle lors de la fusion en surface, totale lors de la fusion partielle et apparition d'une bicouche à la fin de la fusion partielle. Cela montre que lorsque l'interface I/s est lisse, les échantillons de  $\text{Si}_{0.8}\text{Ge}_{0.2}$  et de  $\text{Si}_{0.7}\text{Ge}_{0.3}$  ne dépassent pas la limite de densité d'énergie élastique et ne relaxent pas.

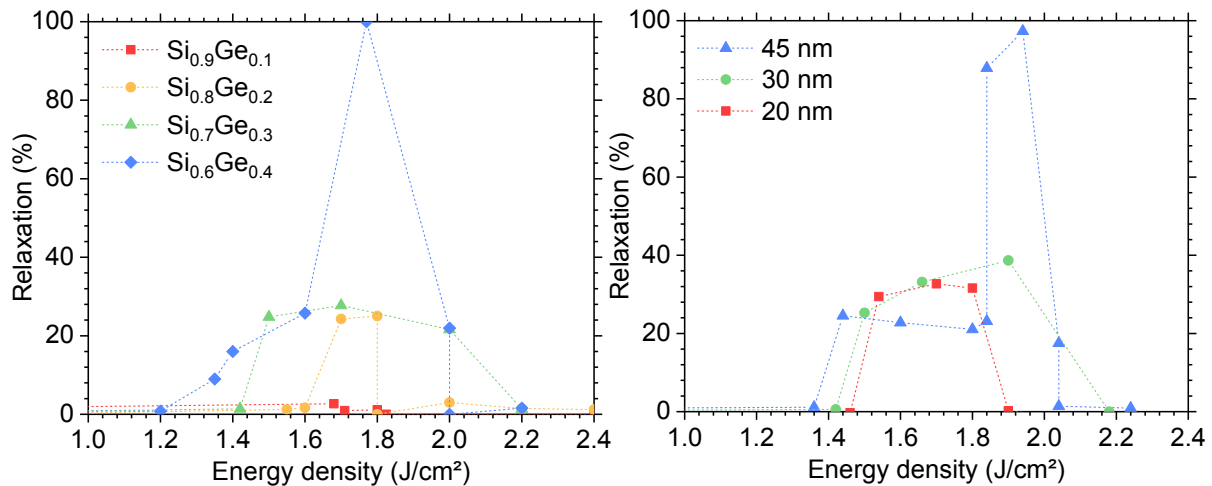


Figure 15. Evolution de la relaxation en fonction de la densité d'énergie pour la série « 30 nm » (a) et la série «  $\text{Si}_{0.7}\text{Ge}_{0.3}$  » (b).

La Figure 15 (b) présente l'évolution de la relaxation pour la série «  $\text{Si}_{0.7}\text{Ge}_{0.3}$  » en fonction de la densité d'énergie. Les échantillons de 20 et 30 nm sont partiellement relaxés durant les régimes de fusion en surface et de fusion partielle, tandis qu'ils sont contraints en fusion totale. La couche d'épaisseur 45 nm conduit à des résultats plus complexes. La relaxation est à nouveau partielle lors de la fusion en surface, mais approche des 100% pendant le régime de fusion partielle. C'est probablement dû à un effet combiné de la rugosité d'interface et de la forte densité d'énergie élastique. Enfin, on obtient des bicouches à la fin du régime de fusion partielle et en fusion totale, similaires à celles observées pour le  $\text{Si}_{0.6}\text{Ge}_{0.4}$ . Cela indique qu'on a dépassé le seuil maximal d'énergie élastique.

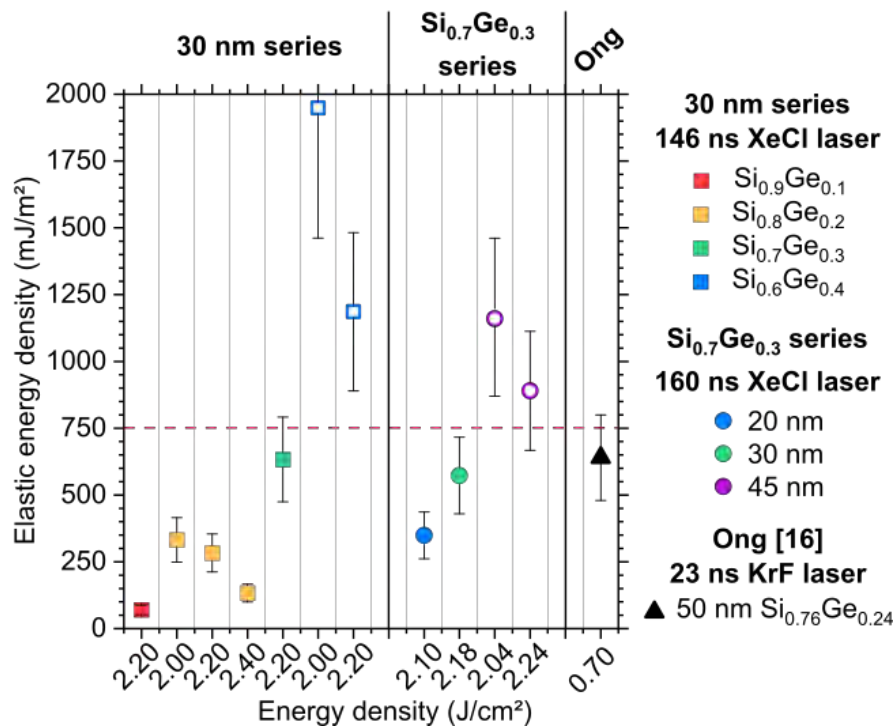


Figure 16. Comparaison de la densité d'énergie élastique maximale dans des couches de SiGe recuites par laser, dans des conditions conduisant à une interface liquide/solide lisse.

Grâce aux profils SIMS ou EDX des différents échantillons, il est possible de calculer la densité d'énergie élastique de chacun des échantillons. Les valeurs obtenues pour l'intégralité des échantillons ayant une interface l/s lisse sont présentées en Figure 16, avec une distinction entre les échantillons présentant une bicouche et ceux parfaitement contraints. On peut constater que les échantillons pseudomorphes ont des densités d'énergie élastique plus faible que ceux avec une bicouche, comme suggéré précédemment. D'après ces observations, il semble que le seuil de densité d'énergie élastique soit proche de 750 mJ/m<sup>2</sup> : au-delà, la partie supérieure de la couche sera relaxée.

### 3. Relaxation en présence de bore

L'évolution de la relaxation avec la densité d'énergie est présentée en Figure 17 pour les trois échantillons dopés, et une référence non dopée qui correspond à la couche de 30 nm de la série « Si<sub>0.7</sub>Ge<sub>0.3</sub> ». Pour l'échantillon A, la relaxation évolue de manière similaire à celle de la référence : elle est proche de 30% dans les régimes de fusion en surface et partielle, puis nulle en fusion totale. Les échantillons B et C présentent aussi une relaxation partielle durant le régime de fusion en surface (1.60 J/cm<sup>2</sup>) et au début de la fusion partielle (1.80 J/cm<sup>2</sup>), mais montrent un retour à la contrainte avant la fusion totale, à 1.95 J/cm<sup>2</sup>. On peut aussi constater que les niveaux de relaxation sont généralement plus faibles pour les couches plus riches en bore. Ce retour à la contrainte durant le régime de fusion partielle est probablement dû aussi à une compensation des contraintes en présence d'une large concentration de bore.

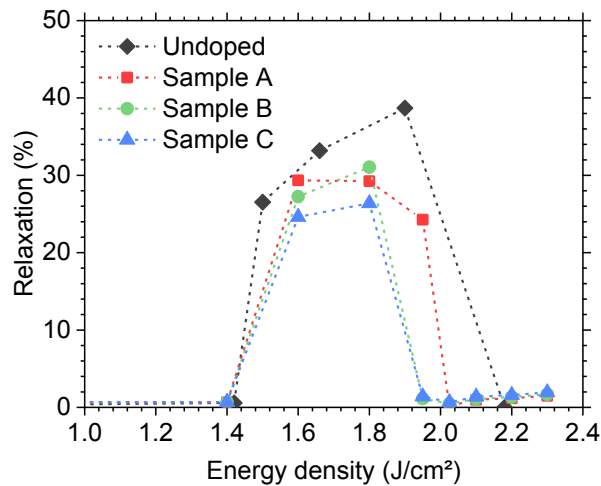


Figure 17. Evolution de la relaxation en fonction de la densité d'énergie pour des échantillons de  $\text{Si}_{0.7}\text{Ge}_{0.3}$  dopés à l'aide de bore, comparés avec un échantillon sans dopage.

## V – Evolution des propriétés électriques de couches dopées à l'aide de bore

### 1. Activation dans le $\text{Si}_{0.7}\text{Ge}_{0.3}$

Comme mentionné précédemment, trois types d'échantillons de  $\text{Si}_{0.7}\text{Ge}_{0.3}$  dopés sont étudiés, correspondant à trois concentrations en bore. La concentration de bore présente dans le matériau peut être mesurée par SIMS, et indique que les concentrations chimiques sont proches de  $7.79 \times 10^{19}$ ,  $1.38 \times 10^{20}$  and  $2.46 \times 10^{20} \text{ cm}^{-3}$  pour les échantillons A, B et C respectivement, pour des échantillons après épitaxie. Ces valeurs peuvent être comparées aux doses actives extraites des mesures Rs, soit  $7.23 \times 10^{19}$ ,  $1.13 \times 10^{20}$  and  $1.31 \times 10^{20} \text{ cm}^{-3}$ , ce qui indique une activation presque totale dès l'épitaxie pour l'échantillon A. Le recuit laser (avec fusion) est connu pour causer une redistribution des dopants à l'intérieur des couches : la Figure 18 présente les profils de bore obtenus pour l'échantillon B recuit à différentes densités d'énergie. Ces profils montrent une nette déplétion en bore près de la surface, ainsi qu'une accumulation en profondeur, marquée par des flèches de couleur. Ce type de profil est couramment observé dans du Si et du Ge.

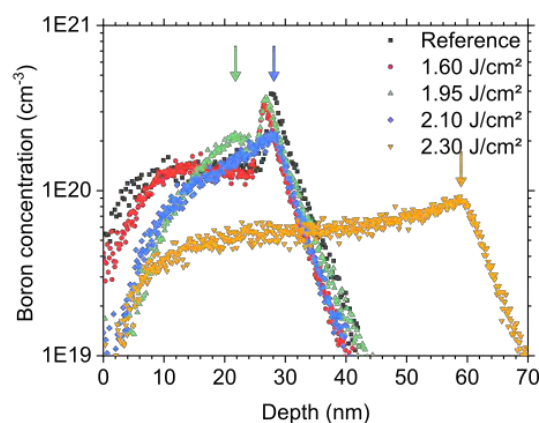


Figure 18. Profils de concentration de bore en fonction de la profondeur à différentes densités d'énergie pour l'échantillon B.

L'évolution de la résistance carrée avec la densité d'énergie est présentée en Figure 19(a) pour les trois échantillons, avec les valeurs extraites des mesures quatre points et des mesures d'effet Hall. Les deux méthodes donnent des valeurs proches. Pour les échantillons A et B, on observe une dégradation de la résistance carrée dès que la couche commence à

fondre. Elle ne diminue que lorsque la fusion totale est atteinte, près de 2.03-2.04 J/cm<sup>2</sup>. Pour l'échantillon B, cette amélioration permet de diminuer la  $R_s$  au-dessous de son niveau initial, ce qui n'est pas le cas pour le A. Aucune dégradation n'est observée pour l'échantillon C durant les régimes de fusion en surface et de fusion partielle : la résistance carrée diminue au contraire, bien que faiblement. On constate aussi une nette amélioration de la  $R_s$  à 1.98 J/cm<sup>2</sup>. Ces évolutions peuvent être comprises grâce aux mesures de dose de Hall, présentées en Figure 19(b). Les doses actives restent stables tant que le seuil de fusion n'est pas atteint. Pour l'échantillon A, le passage du seuil de fusion cause une diminution de la dose active, probablement à l'origine de la dégradation de  $R_s$ . La dose active reste inférieure à la dose initiale même en fusion totale. On constate aussi une diminution de la dose active pour l'échantillon B durant les régimes de fusion en surface et de fusion partielle, mais celle-ci augmente en fusion totale. La valeur finale est légèrement plus élevée qu'après épitaxie. Enfin, l'échantillon C ne présente presque pas de dégradation de la dose active lors des premiers régimes, et une dose active bien plus élevée à forte densité d'énergie.

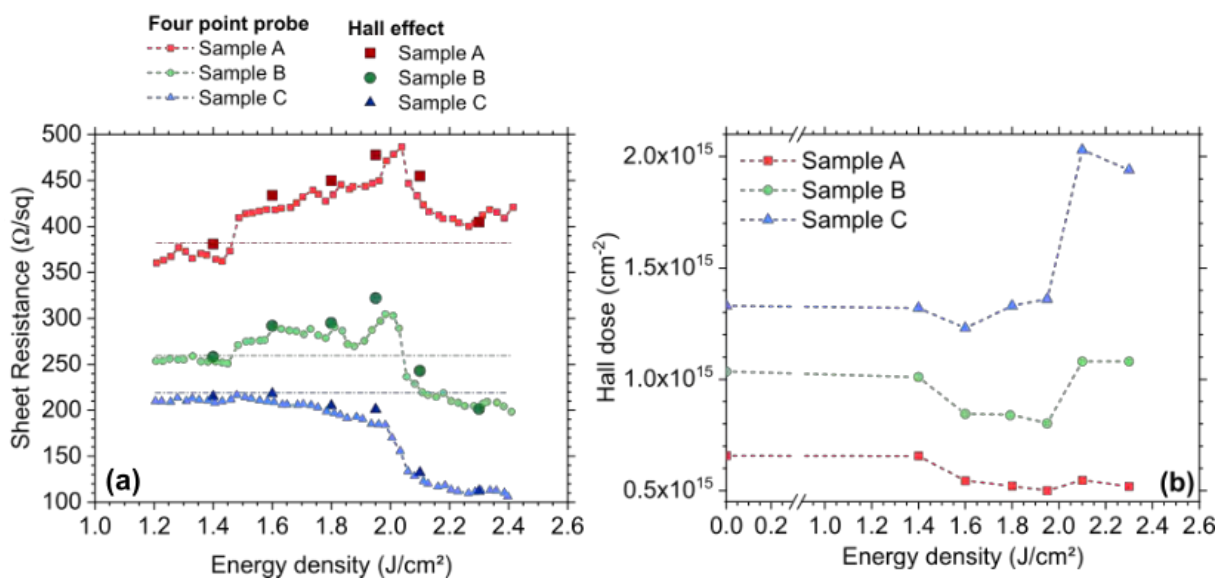


Figure 19. Evolution de la résistance carrée (a) et de la dose de Hall (b) en fonction de la densité d'énergie pour les échantillons A, B et C.

Ces variations de dose active et de résistance carrée semblent liées d'une part à la présence de défauts cristallins dans les couches. Durant les régimes de fusion en surface et de fusion partielle, de multiples défauts cristallins sont présents et sont susceptibles de piéger des charges, conduisant à une réduction de la dose active totale comme observé pour les échantillons A et B. Cet effet a probablement lieu aussi dans l'échantillon C. Cependant, la stabilité de la dose active indique qu'une activation supplémentaire a probablement lieu, à partir du bore initialement inactif dans la couche.

Le recuit laser permet donc d'obtenir des doses actives de bore élevées dans le SiGe pour des couches très riches en bore, à condition d'avoir une bonne qualité cristalline. Il est en revanche possible que ce dopage soit métastable, et soit sujet à des variations si les échantillons sont soumis à un budget thermique supplémentaire.

## II – Désactivation

Pour évaluer la désactivation éventuelle du bore, plusieurs échantillons de bonne qualité cristalline ont été soumis à des recuits en four de 20 minutes à des températures allant de 400°C à 950°C. Pour chaque niveau de dopage (A, B, C), on étudie l'évolution de la résistance carrée pour une référence sans recuit laser, ainsi que deux échantillons recuits à 2.10 J/cm<sup>2</sup> et 2.30 J/cm<sup>2</sup>. Chaque recuit est effectué sur un échantillon physique différent afin

de ne pas accumuler le budget thermique sur un même échantillon. L'évolution de la résistance carrée pour chaque échantillon est présentée en Figure 20, pour les échantillons sans recuit laser (a), les échantillons avec un recuit laser à 2.10 J/cm<sup>2</sup> (b) et à 2.30 J/cm<sup>2</sup> (c). Des barres de couleurs indiquent pour chaque couple dopage-densité d'énergie la variation de résistance carrée attendue sur la plaque, avant le recuit en four. Dans tous les cas, on observe que la résistance carrée reste dans cette gamme jusqu'à 600°C, indiquant que tous les échantillons sont électriquement stables jusqu'à cette température. Au-delà, les tendances divergent entre les échantillons avec et sans recuit laser.

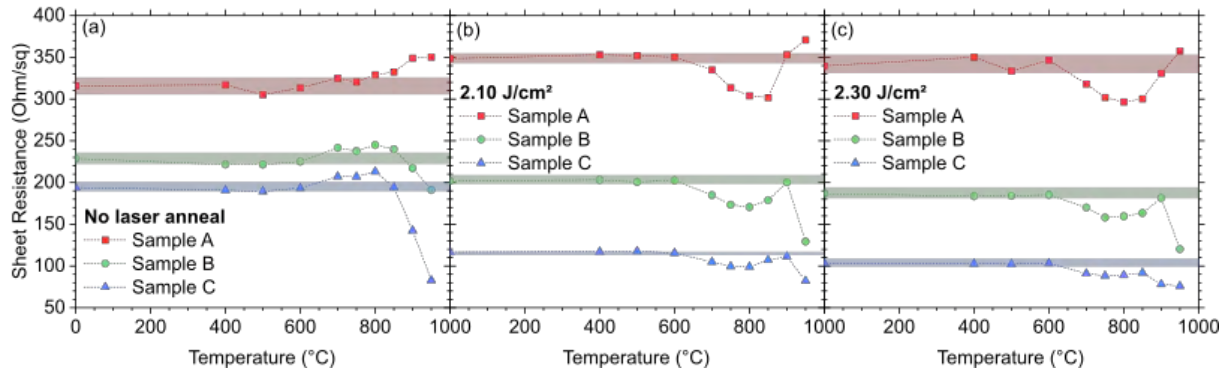


Figure 20. Evolution de la résistance carrée en fonction de la température de recuit en four pour des échantillons sans recuit laser (a) ou avec un recuit laser nanoseconde à 2.10 J/cm<sup>2</sup> (b) et 2.30 J/cm<sup>2</sup> (c).

Pour les échantillons sans recuit laser (a), on constate une augmentation de la résistance carrée entre 700°C et 800°C, qui est probablement lié à une désactivation du bore initialement en substitution. Cette tendance se poursuit à plus fortes températures pour l'échantillon A, tandis que la  $R_s$  diminue pour les échantillons B et C. Cela indique qu'une activation supplémentaire a lieu dans ces échantillons, qui compensent la désactivation initialement observée. Pour les échantillons avec recuit laser (b,c), on constate une diminution de  $R_s$  entre 700°C et 850°C, d'autant plus marquée que l'échantillon est faiblement dopé. On constate ensuite une augmentation de  $R_s$  pour l'échantillon A, tandis que la valeur diminue pour les échantillons B et C. L'origine de la réduction de  $R_s$  entre 700°C et 850°C reste encore inconnue, et peut être lié à une guérison de défauts encore présents, ou à une activation supplémentaire. La tendance aux températures les plus élevées semble en revanche lié à une activation supplémentaire dans les échantillons B et C, ce qui n'est pas possible pour le A.

Ces recuits permettent de confirmer que les couches de SiGe dopées bore et activées par recuit laser nanoseconde sont électriquement stables jusqu'à 600°C, tout comme celles sans recuit laser.

## CONCLUSION

Ce travail a permis dans un premier temps de distinguer les différents régimes de recuit pouvant être observés sur des couches de SiGe soumises à un recuit laser nanoseconde : le régime sous la fusion, la fusion en surface, la fusion partielle et la fusion totale. Cela a permis de mettre en lumière l'initiation localisée de la fusion, avec la formation de zones fondues isolées en surface à faible densité d'énergie. Le phénomène de ségrégation du Ge permet d'observer la profondeur fondue, ainsi que la rugosité de l'interface liquide/solide. Il apparaît que celle-ci reste rugueuse jusqu'à la fin du régime de fusion partielle, et est lisse par la suite.

La suite de ce travail est consacrée à l'évolution de la contrainte dans les couches pour les différents régimes de recuit. Celle-ci apparaît liée à la fois à la rugosité de l'interface l/s et à la densité d'énergie élastique stockée dans la couche. Une interface rugueuse facilite la formation de défauts lors de la solidification : cela cause une relaxation partielle ou totale

dans les régimes de fusion en surface et de fusion partielle. En revanche, la présence d'une interface l/s lisse permet une croissance sans défauts, tant que la densité d'énergie élastique reste inférieure à  $750 \text{ mJ/m}^2$ . Si ce seuil est dépassé, on forme une bicouche avec une zone contrainte en profondeur et une zone relaxée en surface.

Enfin, l'activation du bore semble fortement liée à la qualité cristalline de la couche : on observe une dégradation dans les régimes de fusion en surface et de fusion partielle, qui peut être compensée par une activation supplémentaire dans les couches très fortement dopées. Les meilleurs résultats électriques sont obtenus pour les couches les plus fortement dopées, dans le régime de fusion totale. Ces couches activées par recuit laser nanoseconde sont électriquement stables lors de recuit additionnels jusqu'à  $600^\circ\text{C}$ .





---

## Abstract

---

Nanosecond Laser Annealing is a promising method for dopant activation in thin junctions, enabling activation levels above the solid solubility limits in Si and Ge. Due to its short pulse duration, only the surface of the irradiated material is heated, which is particularly appropriate for 3D sequential integration. Materials such as Si and Ge can reach their melting point near the surface, causing the formation of a molten layer that solidifies at high velocities. This annealing technique can be applied to  $\text{Si}_{1-x}\text{Ge}_x$  junctions, but strain behavior and dopant activation are not fully understood yet. This work focuses on the detection of the various annealing regimes encountered when submitting  $\text{Si}_{1-x}\text{Ge}_x$  ( $x \leq 0.4$ ) layers to nanosecond laser annealing, the evolution of the strain and on the dopant activation as a function of the laser energy density. A first part is dedicated to the detection of the annealing regimes, and the corresponding SiGe layer characteristics. A particular focus is given to the surface melt regime, in which we observed the appearance of isolated molten islands on the surface, leading to increased surface roughness. In a second time, we focused on Ge redistribution and the evolution of the strain in these regimes, and showed how relaxation is related to both the liquid/solid interface roughness and to the stored elastic energy. The rough l/s interface observed in partial or surface melt regimes facilitated the formation of strain relieving defects, leading partial relaxation in most layers. A smooth liquid/solid interface however enabled perfect regrowth unless the elastic energy stored in the layer exceeded  $750 \text{ mJ/m}^2$ . A last section is dedicated to the study of boron activation in  $\text{Si}_{0.7}\text{Ge}_{0.3}$  layers. The best results are obtained with laser annealing conditions leading to the exact melt and recrystallization of the whole 30 nm-thin SiGe layer. In this case, pseudomorphic layers with active dopant concentrations up to  $\sim 2.4 \times 10^{20} \text{ B/cm}^3$  and a strong Ge segregation toward the surface were obtained. These layers were observed to be stable up to  $600^\circ\text{C}$  for 20 minutes additional furnace anneals.

---

## Résumé

---

Le recuit laser nanoseconde est une méthode prometteuse pour l'activation de dopants jusqu'à de très fortes concentrations dans des jonctions fines à base de Si ou de Ge. Grâce à une absorption en surface et une durée d'impulsion extrêmement courte, cette technique permet de ne chauffer que l'extrême surface, ce qui est particulièrement favorable dans le cas d'une intégration 3D séquentielle. Les températures atteintes sont suffisantes pour conduire à la fusion d'une fine couche dans du Si ou du Ge, qui solidifie ensuite à des vitesses de l'ordre du mètre par seconde. Plusieurs études ont montré que le passage en phase liquide permet d'obtenir des concentrations de dopant actifs importantes, supérieures aux limites de solubilité en phase solide. Cette méthode, étudiée principalement dans le Si et le Ge, est en revanche trop peu connue dans le SiGe. Il reste de nombreuses inconnues sur le comportement de la contrainte et sur l'activation des dopants dans le SiGe. Ce travail a donc pour objectif d'étudier en profondeur l'effet du recuit laser nanoseconde sur des couches de SiGe dopées ou non dopées, avec des concentrations de Ge allant jusqu'à 40%. Une première partie de ce travail est dédiée à l'identification des régimes de recuit en fonction de la densité d'énergie laser. Une large partie est consacrée à l'étude de la fusion en surface, dans lequel on peut observer la formation d'îlots fondus séparés les uns des autres. L'observation de la ségrégation et sa simulation sont aussi un élément important de l'étude du SiGe, puisqu'elle cause la formation de gradients marqués et d'une zone riche en Ge à la surface. Une deuxième section est consacrée à l'étude de la contrainte dans le SiGe recuit par laser : il apparaît que la formation de défauts et la relaxation observée sont liées à la fois à la rugosité de l'interface liquide/solide et à l'énergie élastique causée par la déformation. Une interface rugueuse facilite la formation de défauts cristallins qui vont permettre la relaxation partielle ou totale de la couche. Dans le cas d'une interface lisse, la recrystallisation est parfaite si l'énergie élastique totale est inférieure à  $750 \text{ mJ/m}^2$ . Dans un dernier temps, l'activation du bore dans le  $\text{Si}_{0.7}\text{Ge}_{0.3}$  est étudiée. Les meilleurs résultats sont obtenus pour des conditions de recuit laser conduisant exactement à la fusion puis à la recrystallisation de toute la couche SiGe (30 nm). Dans ce cas, des couches pseudomorphes ont été obtenues, avec une concentration active de dopant allant jusqu'à  $2.4 \times 10^{20} \text{ B/cm}^3$  et une forte ségrégation du Ge vers la surface. Ces couches semblent être stables jusqu'à  $600^\circ\text{C}$  si des recuits supplémentaires sont réalisés.